1977

THE IMPACT OF A LIQUID DROP WITH A SOLID SURFACE and The Effects of the Properties of the Liquid on the Erosion of Solids

ROCHESTER, MICHAEL COLIN

http://hdl.handle.net/10026.1/1939

http://dx.doi.org/10.24382/4786
University of Plymouth

THE IMPACT OF A LIQUID DROP WITH A SOLID SURFACE

and

The Effects of the Properties of the Liquid on the Erosion of Solids

by

MICHAEL COLIN ROCHESTER

A dissertation submitted for the degree of Doctor of Philosophy in the University of Cambridge

Clare Hall,
Cambridge

September 1977

To

Anne, Andrew and James

CONTENTS

PREFACE

The work described in this dissertation was carried out between October 1970 and December 1973 in the Engineering Department, University of Cambridge, under the supervision of Dr J. H. Brunton.

I should like to thank Mr B. Butler and Mr R. Denston for technical assistance and advice throughout the course of the work, Mr R. Thorp, Mr H. Lowe and the staff of the Electronics Workshop for help with the design and construction of the high-speed camera, Mr A. A. K. Barker and the staff of the Engineering Workshop, particularly Mr J. Hautot, for help with the design and construction of the gas-powered gun and other pieces of equipment, Mr E. Nisbet and Mr J. Read for help with the preparation of the photographic plates, Dr J. J. Camus, of the Cavendish Laboratory, fo a number of useful discussions, and Dr J. H. Brunton for advice and encouragement since I started the work.

I should also like to thank the Science Research Council, the Westinghouse Electric Corporation and the Cambridge Philosophical Society for financial assistance.

The work is original, except where otherwise stated, and has not been submitted for a degree at any other university.

M. C. Rochester

Clare Hall,
Cambridge.

September 1977.

Notes on Symbols

All symbols are defined at the places where they are first used. The motion of the fluid is described with respect to a Cartesian coordinate system with origin at the point where the drop first strikes the solid. A fluid particle has coordinates x and y, where x is measured along the surface of the solid and y is measured perpendicular to it. Time t is reckoned from the instant of contact. Symbols that appear frequently in the book are as follows:

- p pressure
- V impact velocity
- V_j velocity of jets that flow out from under a drop
- R drop radius
- ϑ angle subtended at centre of drop by half-width of contact area
- ϑ_c magnitude of ϑ at which compression wave is released from edges of drop
- ϑ_e magnitude of ϑ at which flow appears from under drop
- x_c position of edge when compression wave released
- t_c time after impact at which compression wave released
- x_e position of edge when jets first appear from under drop
- t_e time after impact at which jets first appear from under drop
- ρ_0 fluid density
- c_0 sound speed in fluid
- μ fluid viscosity

In Chapter 3 x_1 is used in place of x and t_1 in place of t; x and t are then used to specify the edge of the drop. The following

non-dimensional variables appear:

$$x' = x/x_c,\ t' = t/t_c,\ x_1' = x_1/x_c \text{ and } t_1' = t_1/t_c.$$

In Chapter 6 the subscripts are dropped from the symbols for density and sound speed.

Footnotes are denoted by raised letters and notes appended to the chapters by raised numbers.

CHAPTER 1

INTRODUCTION

Why are sea-walls damaged by breaking waves? What is the load on the bottom of a ship when it slams down onto the surface of the sea? How are the leading edges of steam turbine blades damaged by water droplets? Is it safe to fly an aircraft through a rainstorm? These questions have one thing in common - they concern impact between a liquid and a solid. In the last fifty years or so they have inspired a large number of investigations.

1.1 Wave Impacts

Model studies of wave impacts against sea-walls have been carried out by Bagnold (1939) and Denny (1951). They measured wave loads and tried to relate them to the behaviour of the wave on impact. Results of experiments to measure wave loads on sea-walls at ports along the coasts of the Mediterranean Sea and the English Channel have been gathered together by Minikin (1946). The most significant fact that emerges from these studies is that there is little correlation between the laboratory results and the field measurements. Even today a satisfactory theory that can be tested in an independent series of experiments has not been developed. Nevertheless, in a work that is referred to by engineers who design sea-walls, it has been stated that water-hammer pressures, which arise when a moving liquid is suddenly stopped and compressed, are unlikely to occur in these impacts. (See Ippen (1966).) Although this conclusion does not conflict with experimental results that have been collected so far, severe corrosion damage to the legs of

gas-production platforms in the North Sea suggests that pressures of this magnitude may occur in wave impacts. (The damage has been described by Cottrill (1975).) At the time of writing experiments to measure wave slamming loads on this type of structure are being carried out by a group sponsored by the Department of the Environment. (See the anonymous article in the New Civil Engineer (1975).) The problems here are very similar to those that occur when ships and missiles slam into the surface of the sea, subjects that have been studied for many years.

1.2 Ship Slamming and Related Problems

The slamming problem has been investigated by von Karman (1929) and Wagner (1932) (seaplane floats), Shiffman and Spencer (1945), Nisewanger (1952) and Deragarabedian (1955) (missiles), Chu and Abramson (1961) and Ogilvie (1963) (ships) and Skalak and Feit (1966) (missiles), to mention only a few. Some of these were theoretical studies (for example, that of Deragarabedian), whereas others were experimental (for example, that of Nisewanger). The correlation between experiment and theory is very poor. For example, Deragarabedian predicted that the water-hammer pressure is generated at the centre of the liquid/solid interface when a rigid sphere strikes the surface of a liquid, but this is considerably greater than the pressure that was measured by Nisewanger when he fired spheres containing small pressure transducers into a basin of water. Over the years since this work was done there has been little effort to improve experimental techniques or to modify the theory to create a more comprehensive explanation of the impact process.

1.3 Turbine Blade Erosion and Rain Erosion of Aircraft

Systematic investigations of liquid impact erosion were begun in the early 1920's after it was noticed that rotor blades in the low pressure stages of steam turbines had been deeply pitted by impacts with water droplets. Over the years solutions to the problem have more or less kept pace with new developments such as the mercury steam turbine (Hatfield (1948)) and the metal vapour turbine (Pouchot (1968)). By the end of World War II military aircraft were flying fast enough to be damaged by rain, and from the early 1960's to the present day both problems have been studied together by the same groups of people, who have kept in close touch with one another through conferences and symposia. [1]

These studies have shown that erosion increases as a high power of the impact velocity, and that hardness and strain energy to fracture provide the best measures of erosion resistance. (See, for example, Honneger (1927) (turbines) and Fyall et al (1962) and Busch et al (1966) (aircraft).) They have made it possible for erosion resistant materials to be selected for specific applications, even though the reasons for this resistance were not understood; thus stellite shields have been forged on the leading edges of turbine blades to reduce the amount of pitting, and neoprene coatings have been glued to radomes on aircraft to reduce catastrophic failures of the structures.

The results of these investigations were difficult to interpret because the loads generated in the impacts were not known. This is common to all the topics discussed above. It is the main liquid impact problem today.

1.4 The Main Problem

What is the impact pressure when a liquid and a solid collide? This is the crucial question that must be answered before the problems discussed above can be understood more clearly. Despite the similarities between these problems they were studied in isolation from one another, so that a fruitful approach in one field was never used in another. Thus the pressure distribution under a spherical water drop when it collides with a solid could have been worked out as long ago as 1955 with a technique that was discussed by Deragarabedian, but his work seems to have gone unnoticed by the people who were studying aircraft and steam turbine blade erosion. Furthermore, mathematical methods that had been developed to solve analogous problems - the pressure distribution on wings in supersonic flow - were not applied to the impact problem at all. In fact it is an analogue technique that holds the key to the impact problem examined in this work. The method is outlined in Chapter 3.

1.5 The Present Study

It is possible that a realistic theory of drop impingement erosion could be developed if the magnitude and distribution of the pressure during impact were known. With this in mind, the following work needs to be done.

(i) Develop a theory for the impact of a liquid drop against a rigid surface. The theory should give at least an estimate of the following quantities: (a) the magnitude and duration of the mean impact pressure, (b) the pressure distribution under the drop at different positions and times, and (c) the outward flow velocity in the early stages of impact. The theory should be formulated so that

it can be applied to any liquid/solid geometry.

(ii) Measure the impact pressure distribution over a range of impact velocities for a number of different liquids and a number of solid surface profiles.

(iii) Compare the results of (ii) with the predictions of (i).

(iv) Develop a theory of erosion that includes liquid properties and compare the predictions of this theory with the results of erosion experiments carried out with a selection of liquids.

These topics are examined in the present work. A theory for the impact of a cylindrical liquid drop against a plane rigid solid is worked out in detail; estimates of the mean pressure and mean flow velocities are given as well as estimates of the pressure distribution under the drop at different positions and times. The results are compared with measurements of the impact pressure distribution made over a range of impact velocities with a variety of liquids. Measurements of the shear stress distribution under the drop and measurements of the pressure distribution within the drop are also presented. The calculations and measurements are related to events observed in photographs of the impact. Other results, showing the effect of drop size, drop shape, surface profile, liquid properties and acceleration of the solid on the pressure distribution, are given.

Experiments are described on the erosion of nickel by ten different liquids chosen so that the effects of density, acoustic impedance and viscosity could be investigated separately. Definite trends emerge from this work, and a dimensional analysis of the results leads to a general equation for the rate of erosion of the

material. An energy analysis of the erosion process is given, and an expression for the rate of erosion that is in reasonable agreement with experiment is developed.

Notes on Chapter 1

(1) Some of these have been reported in the documents listed below.

(i) Symposium on Erosion and Cavitation, ASTM STP 307, American Society for Testing and Materials, 1962.

(ii) Erosion by Cavitation or Impingement, ASTM STP 408, American Society for Testing and Materials, 1967.

(iii) Characterisation and Determination of Erosion Resistance, ASTM STP 474, American Society for Testing and Materials, 1970.

(iv) Erosion, Wear, and Interfaces with Corrosion, ASTM STP 567, American Society for Testing and Materials, 1974.

(v) A discussion on deformation of solids by the impact of liquids, and its relation to rain damage in aircraft and missiles, to blade erosion in steam turbines and to cavitation erosion, Philosophical Transactions of the Royal Society (London), Series A, Part Number 1110, Volume 260, pp. 73 - 315, 1966.

(vi) Proceedings of the international conferences on rain erosion and allied phenomena, 1 - 1965, 2 - 1967, 3 - 1970 and 4 - 1974. Copies can be obtained from the Royal Aircraft Establishment, Farnborough.

CHAPTER 2

A REVIEW OF PREVIOUS WORK

Detailed reviews of liquid impact erosion have been written (see, for example, the one by Heymann (1968a)), and work that has been done in recent years has been reported in documents that are easily obtained (see the list in Note 1, Chapter 1). For these reasons this review is brief and is largely culled from a report by Rochester (1977a).

2.1 Erosion

Liquid impact erosion has been studied in multiple impact machines that simulate conditions in rain or in steam turbines (Honneger (1927) (turbines) and Busch et al (1966) (aircraft)). This work has been done to evaluate materials, to determine the variation of erosion with impact velocity, to establish the effect of impact angle on erosion, and to examine the effect on erosion of a number of other variables, such as the size of the liquid drop and the shape of the solid surface.

2.1.1 The Pattern of Erosion

Erosion has been found to follow three well-defined stages (Hancox and Brunton (1966)). These are (i) an incubation period, during which no mass loss occurs (Stage 1); the surface of the material is covered with a random distribution of shallow depressions with diameters in the range from 1.0 to 20 μm; there is substantial evidence that these are caused when cavitation bubbles, formed at or near the liquid/solid interface during the early stages of impact,

collapse onto the surface of the solid (Camus (1971)); (ii) a period during which mass loss occurs at a more or less constant rate (Stage 2); material is removed from the pits formed during the incubation period; the pits grow as erosion proceeds, and towards the end of this stage they have joined up with one another, so that the entire surface is roughened; there is some evidence that erosion damage during Stages 1 and 2 is caused by a fatigue mechanism (Thomas and Brunton (1970)); (iii) a period during which mass loss occurs at a lower constant rate than that during the previous stage (Stage 3); there is some evidence that erosion occurs at a lower rate during this stage because liquid retained in the bottom of the pits cushions the surface against the impacts (Brunton (1967)).

2.1.2 Measurement of Erosion Damage

The erosion rate during Stage 2 and the reciprocal of the duration of Stage 1 have been suggested as measures of erosion damage for either grouping materials or determining relations between erosion damage and other variables (Heymann (1967a)).

2.1.3 The Effect of Impingement Conditions on Erosion

2.1.3.1 Impact Velocity

The erosion rate during Stage 2 can be expressed as either

$$E \sim (V - V_c)^{n_1}, \qquad 2.1$$

where V is the impact velocity, V_c is the impact velocity below which no mass loss occurs and n_1 is about 2.5 (see, for example, Baker et al (1966)), or

$$E \sim V^{n_2}, \qquad 2.2$$

where n_2 is about 5 (see, for example, Hoff et al (1967)). These relations do not hold for very brittle materials such as glasses, in which catastrophic failures can occur above certain velocities. They can usually be fitted to a set of results over different parts of the velocity range; the first generally fits results near the threshold velocity, whereas the second has been found to hold at velocities well above the threshold. There are no grounds for extrapolating either of these expressions outside the velocity range examined.

2.1.3.2 Impact Angle

The erosion rate during Stage 2 has been found to fit the relation

$$E \sim (V\cos\vartheta - V_c)^{n_1}, \qquad 2.3$$

where ϑ is the angle of impact (Fyall et al (1962)).

2.1.3.3 Drop Size

There is still much dispute on the effect of drop size. It would appear that the duration of Stage 1 increases as drop size decreases for drops with diameters less than about 2.5 mm, but that the rate of erosion during Stage 2 is not affected by drop size. The threshold velocity below which erosion does not occur varies with drop size according to

$$V_c^2 d = \text{constant}, \qquad 2.4$$

where d is the diameter of the drop (Heymann (1967a)).

2.1.3.4 Drop Shape

Erosion increases with the radius of curvature of the side of the drop which strikes the solid (de Haller (1933 and 1940)). This effect is the same as that due to drop size.

2.1.3.5 Surface Shape

Erosion has been found to increase on concave surfaces (de Haller (1933 and 1940)). Surface finish has been found to have no effect on erosion for scratch depths greater than 12 μm (Hancox and Brunton (1966)).

2.1.3.6 Liquid Layer

It has been demonstrated that a liquid layer can reduce both the total impact load and the damage caused by the outflowing fluid (Brunton (1967)). To be effective in this way the depth of the liquid layer must be similar to the diameter of the drop. There is some evidence that liquid retained in the pits is responsible for the fall in erosion rate that marks the end of Stage 2.

2.1.4 The Effect of Material Properties on Erosion

In general the erosion resistance of materials has been found to increase with hardness and strain energy to fracture (Honneger (1927) (hardness) and Thomas and Brunton (1970) (strain energy to fracture)). However, there are notable exceptions to both trends, and at the moment there does not appear to be a satisfactory material property that describes the erosion resistance of a material.

2.1.5 The Effect of Liquid Properties on Erosion

It has been found that the rate of erosion during Stage 2 increases with density and decreases with viscosity (Hancox and Brunton (1966) (density) and Canavelis (1966 and 1968) (viscosity)).

2.1.6 Theories of Erosion

At present there is no reliable theory of erosion that relates rate of erosion to either material properties or properties of the liquid and the impingement conditions (despite many attempts to develop one - see Heymann (1967b)).

2.2 Single Impact Damage

Detailed descriptions of damage caused by single impacts have been given, and attempts have been made to relate these findings to the behaviour of the drop on impact (Bowden and Brunton (1961), Hancox and Brunton (1966) and Thomas and Brunton (1970)). This work has shown that the damage is caused both by the initial high impact pressures that last for only a small fraction of the total impact time and by the erosive action of the liquid as it flows out at high speed from the centre of impact across the surface of the solid.

2.3 The Impact Pressure Distribution

There have been a few measurements of the average impact pressure during the initial stage of impact (Engel (1955), Bowden and Brunton (1961) and Hancox and Brunton (1966)), a detailed description of the initial stages of flow (Brunton and Camus (1970)), some attempts to measure the impact pressure distribution over the

impact surface (Vickers and Johnson (1973) and Rochester and Brunton (1974a, b)), and a few calculations of the pressure distribution (Engel (1955), Savic and Boult (1957), Bowden and Field (1964), Skalak and Feit (1966), Heymann (1969), Huang et al (1971) and Lesser (1973)), but much controversy still surrounds the results and conclusions of this work (Heymann (1974)). The history of the problem is summarised in Table 2.1. The last item marks the starting point of the present study.

Table 2.1

Impact Pressure Distribution at the Liquid/Solid Interface when a Liquid Drop Strikes a Plane Rigid Solid

Approach	Drop Shape	Pressure Distribution
Engel (1955)		
Theory and experiment.	Spherical drop.	Non-uniform. Maximum pressure not given, but assumed to be in ring around centre of impact. Mean pressure at this time $0.5\rho_0 c_0 V$.
Bowden and Field (1964)		
Theory.	Spherical drop.	Uniform. Equal to $\rho_0 c_0 V$.
Heymann (1969)		
Theory - wedge analogy.	Cylindrical drop.	Non-uniform. Maximum pressure about $3\rho_0 c_0 V$ at edge of contact region just before flow occurs.
Camus (1971)		
Theory - wedge analogy.	Cylindrical drop.	Non-uniform. Maximum pressure many times $\rho_0 c_0 V$ at edge of contact region just after flow starts.
Huang et al (1971)		
Theory.	Pin-cushion drop.	Non-uniform. Maximum pressure about $0.8\rho_0 c_0 V$ at centre of impact.
Lesser (1973)		
Theory.	Rectangular slug.	Non-uniform. Maximum pressure $\rho_0 c_0 V$ at centre of impact.
Johnson and Vickers (1973)		
Experiment.	Cylindrical jet.	Non-uniform. Maximum pressure $1.5\rho_0 c_0 V$ at edge of jet.
Rochester and Brunton (1974a)		
Experiment.	Cylindrical drop.	Non-uniform. Maximum pressure about $0.7\rho_0 c_0 V$ at centre of impact.

CHAPTER 3

THE THEORY OF DROP IMPACT

When a liquid drop strikes a solid surface, it is known that very high pressures are generated at the beginning of impact due to the compressibility of the fluid. Although detailed descriptions of the impact process have been given, satisfactory explanations of both the variation of the impact pressure and the flow of the drop during impact have not been developed. In this chapter a theory for the impact of a cylindrical liquid drop against a rigid solid is presented. Estimates of the mean impact pressure over the surface of contact between the liquid and the solid and the mean flow velocity from under the surface of the drop are given, as well as estimates of the pressure distribution under the drop at different positions and times.

3.1 The Mean Impact Pressure

Bowden and Field (1964) were able to show that the mean impact pressure over the contact surface up to the time when the pressure wave detaches from the edge of the drop is the water-hammer pressure. However, their argument was based on the unlikely supposition that the fluid particle velocity throughout the compressed region is constant and equal to the impact velocity. Skalak and Feit (1966) obtained the same result for the impact of a rigid solid with a plane liquid surface by using retarded potentials. Although their analysis is correct, and could be applied to the problem considered here, it is a complicated way to obtain a solution, since they begin by setting up an equation for the velocity potential within the

region of the disturbance. The simple result established through these calculations suggests that a more straightforward method exists. In fact the problem is easily solved by setting up a moving control volume around the flow; in this solution knowledge of what is happening inside the space occupied by the fluid is not required.

The problem that is considered here is illustrated in Fig. 3.1. A cylindrical liquid drop with a radius R is struck by a plane rigid solid at velocity V. After a time t the position of the edge of the drop is given by

$$x = [Vt(2R - Vt)]^{1/2}. \qquad 3.1a$$

If $Vt << 2R$, this reduces to

$$x = (2RVt)^{1/2}. \qquad 3.1b$$

The velocity with which the edge of the drop travels out across the surface of the solid is

$$dx/dt = [RV/(2t)]^{1/2} = RV/x, \qquad 3.2$$

and the angle subtended at the centre of the drop by the half-width of the area of contact between the liquid and the solid is given by

$$\sin\vartheta = x/R = (2Vt/R)^{1/2}. \qquad 3.3$$

The derivation of these equations is based on the assumption that flow from under the edges of the drop does not begin at the instant of first contact between liquid and solid. This is reasonable, since the edge of the drop is initially moving out across the surface of the solid faster than the pressure waves generated in the impact. Since the edge is decelerating as it travels out across the solid,

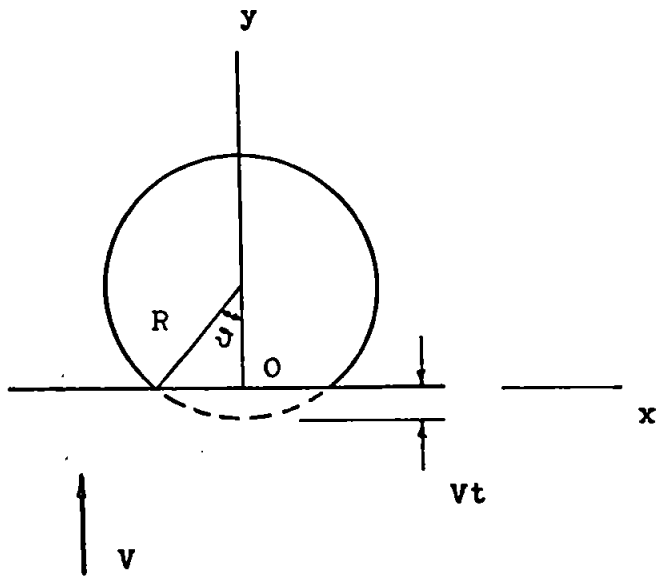

Fig. 3.1 The cylindrical liquid drop before outward flow begins.

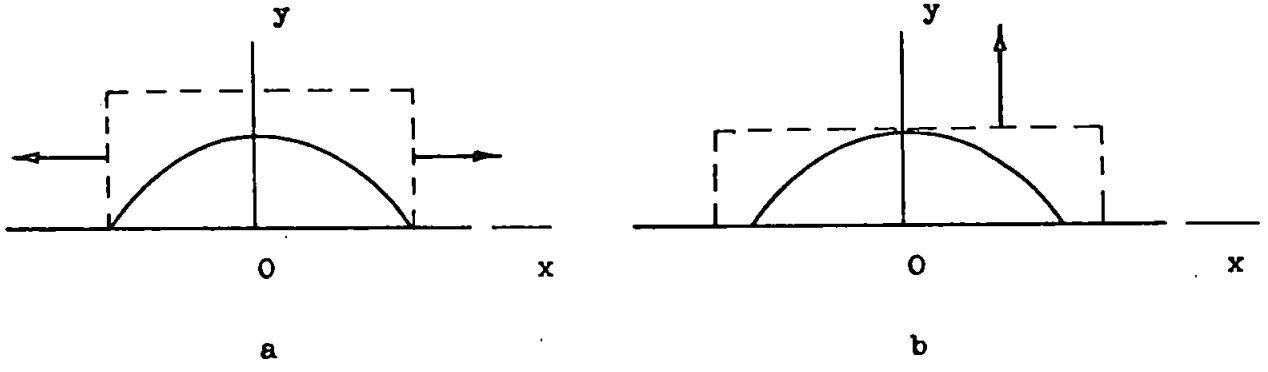

Fig. 3.2 Expanding volumes used to estimate the force exerted on the drop by the solid.

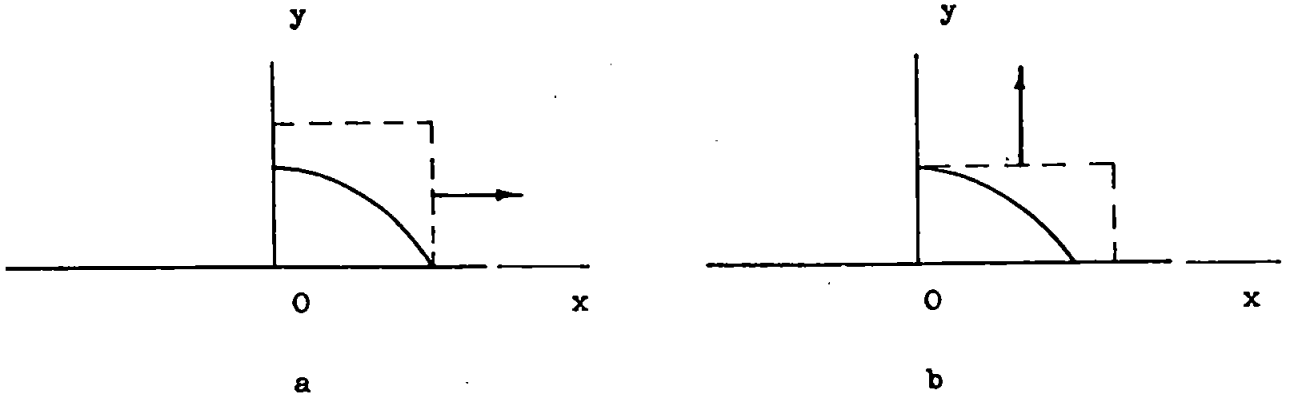

Fig. 3.3 Expanding volumes used to estimate the force exerted on the right hand side of the drop by the left hand side.

a place will be reached at which the wave velocity exceeds the edge velocity, the pressure inside the central compressed region will be released and the fluid will be free to move out across the surface of the solid beyond the edge of the drop. This will occur when

$$dx/dt = c_0 = [RV/(2t_c)]^{1/2} = RV/x_c. \qquad 3.4a$$

Here c_0 is the sound speed in the liquid, and x_c and t_c are the edge position and time after impact respectively at which the pressure wave overtakes the edge of the drop. Equation 3.4a is easily rearranged to give

$$x_c = RV/c_0, \text{ and } t_c = RV/(2c_0^2). \qquad 3.4b$$

It follows from Equation 3.3 that the flow angle at which this occurs is given by

$$\sin \vartheta_c = V/c_0. \qquad 3.4c$$

The analysis given below makes use of the following general result. The force $\underline{F}(t)$ on a fluid within a closed region with volume $v(t)$ and surface area $S(t)$ is

$$\underline{F}(t) = \rho_0 d/dt \int_{v(t)} \underline{q}\,dv + \rho_0 \int_{S(t)} \underline{q}(\underline{q}_S \cdot \underline{n})\,dS, \qquad 3.5a$$

where $\underline{q}$ is the fluid velocity at any position and time, $\underline{q}_S$ is the velocity of the surface and $\underline{n}$ is a unit vector normal to the surface (positive inwards). (See, for example, Jeffrey (1966).) If an average flow velocity is defined

$$\underline{q}_{av} = \left[\int_{v(t)} \underline{q}\,dv\right] / \left[\int_{v(t)} dv\right],$$

this equation can be written

$$\underline{F}(t) = \rho_0 d/dt[\underline{q}_{av} v(t)] + \rho_0 \int_{S(t)} \underline{q}(\underline{q}_s \cdot \underline{n}) dS. \qquad 3.5b$$

Consider the expanding control volumes illustrated in Fig. 3.2. They show the part of the fluid that contains the bow-shaped pressure wave generated at the beginning of the impact. In Fig. 3.2a the surface of the control volume that is normal to the y-axis is stationary at a distance $c_0 t_1$ above the x-axis, and the sides are moving out with the edges of the drop, to which the pressure wave remains attached. In Fig. 3.2b the sides normal to the x-axis are stationary, and the upper surface of the control volume is moving up the drop with the head of the pressure wave. The width of the control volume has been chosen so that the head of the wave will have travelled a distance $c_0 t_1$ along the y-axis when the edges of the drop reach the stationary boundaries of the control volume. At this time the forces on the control volumes will be the same because they will have the same shape. However, they have reached this shape in different ways, and this means that the equations for the forces will not have the same form. This leads to an expreesion for the force, as shown below.

Refer to Fig. 3.2a. At any time t the volume of the expanding control volume is

$$v = 2(2RVt)^{1/2} c_0 t_1,$$

therefore

$$dv/dt = (2RV/t)^{1/2} c_0 t_1.$$

These terms can now be substituted into Equation 3.5b, which becomes

$$F_y(t) = \rho_0[v_{av}(2RV/t)^{1/2}c_0t_1 + 2(2RVt)^{1/2}c_0t_1dv_{av}/dt], \qquad 3.6a$$

where $F_y(t)$ is the force exerted by the solid on the liquid, and v_{av} is the average fluid particle velocity inside the control volume in the y-direction.

Refer to Fig. 3.2b. At any time t the volume of the expanding control volume is

$$v = 2(2RVt_1)^{1/2}c_0t,$$

therefore

$$dv/dt = 2(2RVt_1)^{1/2}c_0.$$

These terms can now be substituted into Equation 3.5b, which becomes

$$F_y(t) = \rho_0[v_{av}2(2RVt_1)^{1/2}c_0 + 2(2RVt_1)^{1/2}c_0tdv_{av}/dt] + 2\rho_0c_0V(2RVt_1)^{1/2}. \qquad 3.6b$$

When $t = t_1$, Equations 3.6a and 3.6b give the same force. Therefore

$$\rho_0v_{av}(2RVt_1)^{1/2}c_0 = -2\rho_0c_0V(2RVt_1)^{1/2},$$

from which

$$v_{av} = -2V. \qquad 3.7$$

Equation 3.7 can now be substituted into either Equation 3.6a or Equation 3.6b to give

$$F_y(t) = -\rho_0c_0V2(2RVt)^{1/2}. \qquad 3.8a$$

This can be written

$$F_y(t) = - \rho_0 c_0 V A, \qquad 3.8b$$

where A is the area of contact between the liquid and the solid. The average pressure exerted on the solid by the fluid is therefore

$$p_{av} = - F_y(t)/A = \rho_0 c_0 V. \qquad 3.9$$

The average pressure on the surface of the solid during the period that the edge is travelling outwards faster than the pressure wave generated in the impact is therefore the water-hammer pressure. If the pressure is equal to $\rho_0 c_0 V$ at the centre of the contact area at the instant of impact and thereafter falls, it follows from Equation 3.9 that the pressure at the edge of the contact region increases as the impact proceeds.

Consider the control volumes illustrated in Fig. 3.3, in which the central plane of the drop is part of the surface. A discussion similar to that given above leads to an expression for the force exerted on the right hand side of the drop by the left hand side.

Refer to Fig. 3.3a. The force on the fluid within the control volume in the x-direction is

$$F_x(t) = (1/2)\rho_0 [u_{av}(2RV/t)^{1/2} c_0 t_1 + 2(2RVt)^{1/2} c_0 t_1 du_{av}/dt], \qquad 3.10a$$

where u_{av} is the average fluid particle velocity inside the control volume in the x-direction.

Refer to Fig. 3.3b. The force on the fluid within the control volume in the x-direction is

$$F_x(t) = (1/2)\rho_0 [u_{av} 2(2RVt_1)^{1/2} c_0 + 2(2RVt_1)^{1/2} c_0 t du_{av}/dt]. \qquad 3.10b$$

When $t = t_1$, Equations 3.10a and 3.10b give the same force,

therefore

$$u_{av} = 0. \qquad 3.11$$

Equation 3.11 can now be substituted into either Equation 3.10a or Equation 3.10b to give

$$F_x(t) = 0. \qquad 3.12$$

If the pressure is equal to $\rho_0 c_0 V$ at the centre of the contact area at the instant of impact and thereafter falls, it follows from Equation 3.12 that the pressure at some places along the central plane of the drop will be negative. Therefore cavitation is likely to occur just above the surface of the solid in the central region of the drop.

When the pressure wave overtakes the edge of the drop, the fluid will be free to move out across the surface of the solid. It is possible that the edge of the drop will still be moving out at a higher velocity than that imparted to the fluid particles by the release wave, so that a jet of fluid will not appear beyond the edge of the drop immediately. The edge position will still be given by Equation 3.1, and the analysis of the flow presented above will still hold. However, in the control volume illustrated in Fig. 3.2a, there will now be a contribution to the expression for $F_y(t)$ from the momentum flux across the sides. If the velocities of the particles along the boundaries of the control volume parallel to the y-axis are neglected, this term will be zero, and the average pressure exerted on the solid by the fluid will still be given by Equation 3.9. When flow beyond the edge of the drop occurs, the edge position will no longer be determined by the geometry of the impact, but will depend on the dynamics of the flow. Since the position of

the edge is not known beforehand, it does not seem possible that an analytical solution will be obtained to this part of the problem.

3.2 Outward Flow Velocity and Flow Angle

As discussed above, it does not follow that outward flow will occur from under the drop just because the edge is free. Since the average pressure over the contact area at the time when outward flow is able to occur is the water-hammer pressure, it is reasonable to suppose that fluid is driven out across the surface of the solid by this pressure. From the momentum equation the outward flow velocity should therefore be given by

$$(1/2)\rho_0 v_j^2 = \rho_0 c_0 V. \qquad 3.13a$$

(The unsteady term has been omitted.) The jet velocity is therefore

$$V_j = (2c_0 V)^{1/2}. \qquad 3.13b$$

This expression can be written as either

$$V_j/c_0 = (2V/c_0)^{1/2} \qquad 3.13c$$

or

$$V_j/V = (2c_0/V)^{1/2}. \qquad 3.13d$$

As the impact velocity is increased, the sound speed in the liquid increases according to the relation

$$c = c_0 + kV, \qquad 3.14$$

where k is a constant for a particular liquid (Heymann (1968b). For water k = 2, so that Equations 3.13c and 3.13d become

$$V_j/c_0 = [(2V/c_0)(1 + 2V/c_0)]^{1/2}, \qquad 3.15a$$

and

$$V_j/V = [2(2 + c_0/V)]^{1/2}. \qquad 3.15b$$

Graphs of V_j/c_0 and V_j/V versus V/c_0 are shown in Figs. 3.4 and 3.5 respectively. Note that when $V >> c_0$, $V_j/c_0 \rightarrow 2V/c_0$ (from Equation 3.15a), and $V_j/V \rightarrow 2$ (from Equation 3.15b).

Flow will appear beyond the edge of the drop when the edge velocity falls to V_j. This will occur when

$$dx/dt = V_j = [RV/(2t_e)]^{1/2} = RV/x_e. \qquad 3.16a$$

Here x_e and t_e are the edge position and time after impact respectively at which the jet overtakes the edge of the drop. Therefore

$$\sin\vartheta_e = x_e/R = V/V_j = [V/(2c_0)]^{1/2}. \qquad 3.16b$$

Also

$$x_e/x_c = [V/(2c_0)]^{1/2}/(V/c_0) = [c_0/(2V)]^{1/2}, \qquad 3.16c$$

and

$$t_e/t_c = c_0/(2V).^{a} \qquad 3.16d$$

When the equation of state is used, Equations 3.16b and 3.16c become

a Note that $x_e = [c_0/(2V)]^{1/2}RV/c_0 = R[V/(2c_0)]^{1/2}$, and $t_e = [c_0/(2V)][RV/(2c_0^2)] = R/(4c_0)$. These relations are used in Chapter 6.

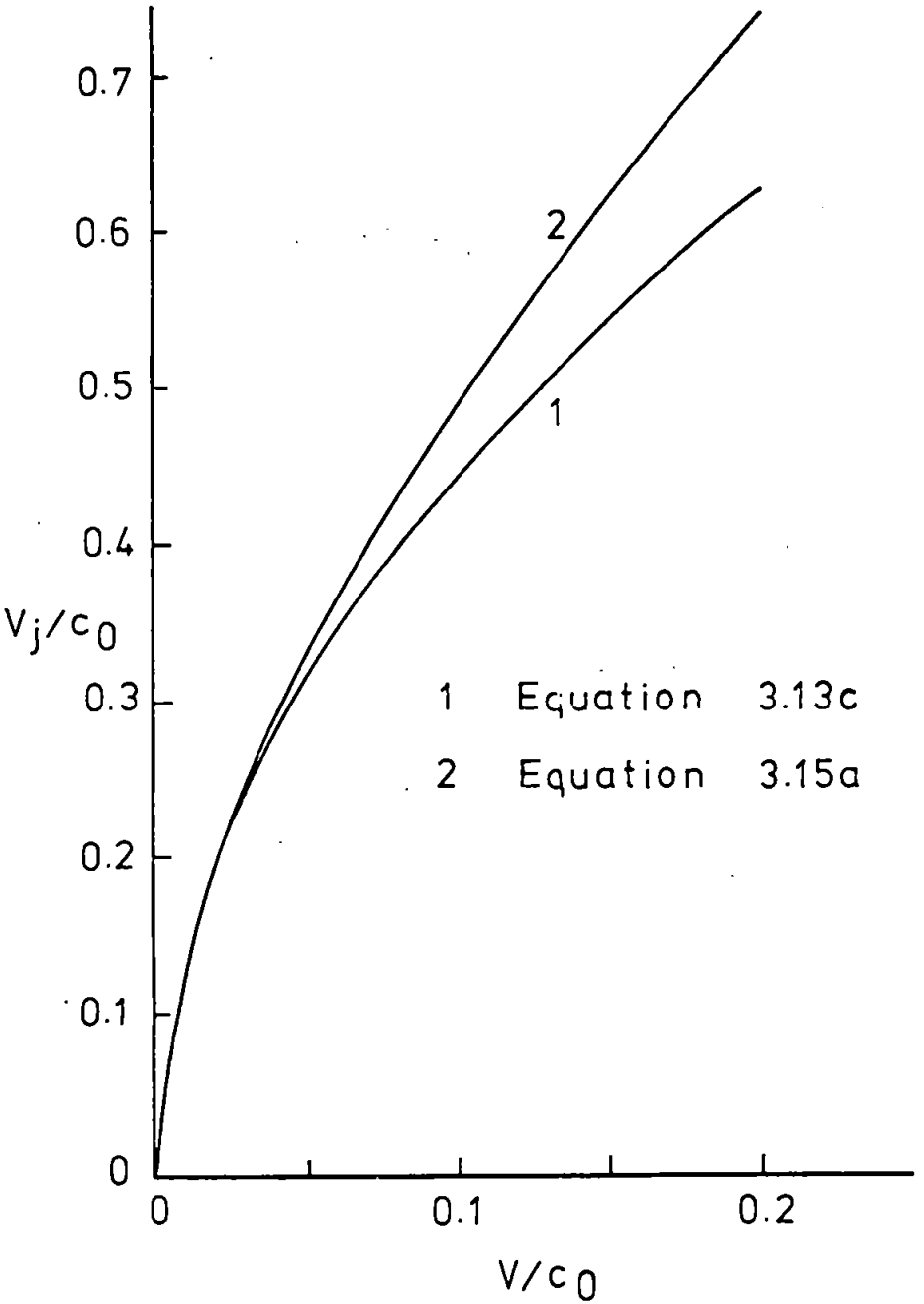

Fig. 3.4 V_j/c_0 versus V/c_0.

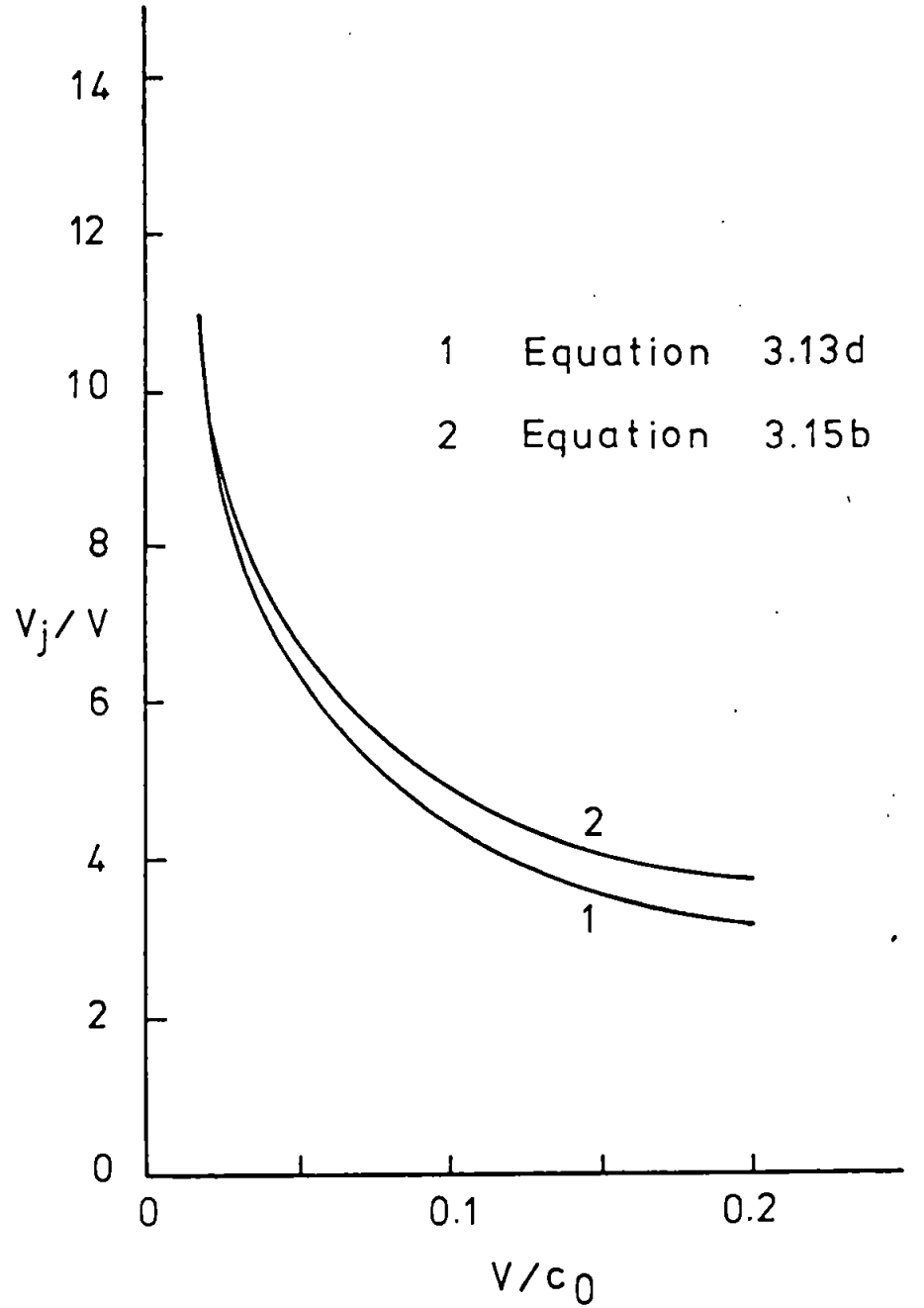

Fig. 3.5 V_j/V versus V/c_0.

$$x_e/R = 1/[2((c_0/V) + 2)]^{1/2}, \qquad 3.17a$$

and

$$x_e/x_c = [1 + c_0/(2V)]^{1/2}. \qquad 3.17b$$

Graphs of x_e/R and x_e/x_c versus V/c_0 are shown in Figs. 3.6 and 3.7 respectively. Note that when $V >> c_0$, $x_e/R \rightarrow 1/2$ (from Equation 3.17a), and $x_e/x_c \rightarrow 1$ (from Equation 3.17b).

3.3 The Impact Pressure Distribution

The pressure distribution under the drop during the impact can be obtained by solving the differential equations of fluid flow together with an equation of state and the appropriate initial and boundary conditions. It happens that both the equations of motion and the boundary conditions are non-linear, and in the present state of the art can only be solved by a numerical procedure. In the following sections the basic equations are written down and reduced to a single equation in terms of the velocity potential, the boundary and initial conditions are established for the particular problem that is investigated here and the equations are linearised. The pressure distribution is then calculated by an analytical technique that was used to solve an analogous problem in steady supersonic flow.

3.3.1 The Fundamental Equations

Consider the unsteady two-dimensional flow of an inviscid, non-heat conducting, compressible fluid.

The continuity equation is

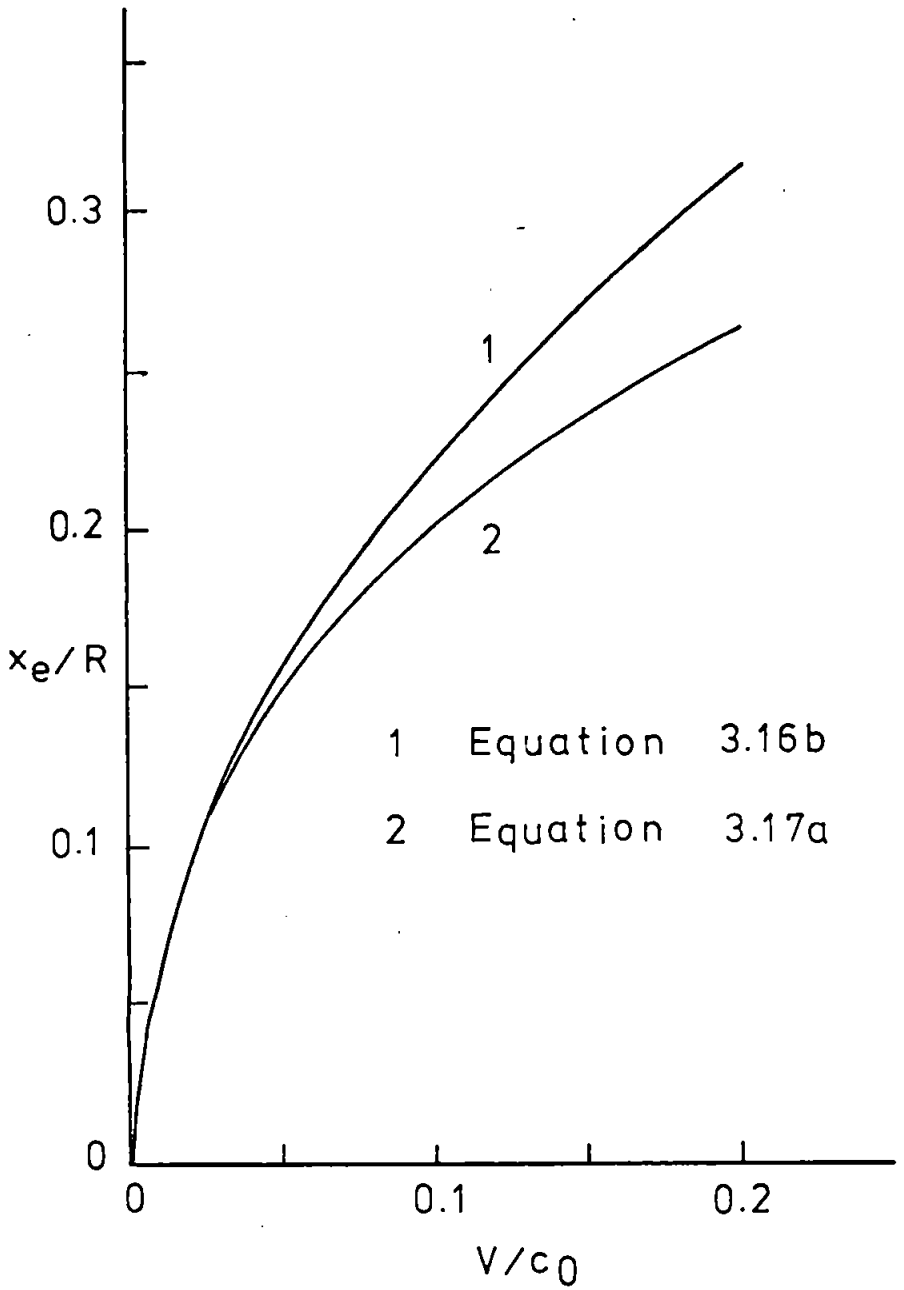

Fig. 3.6 x_e/R versus V/c_0.

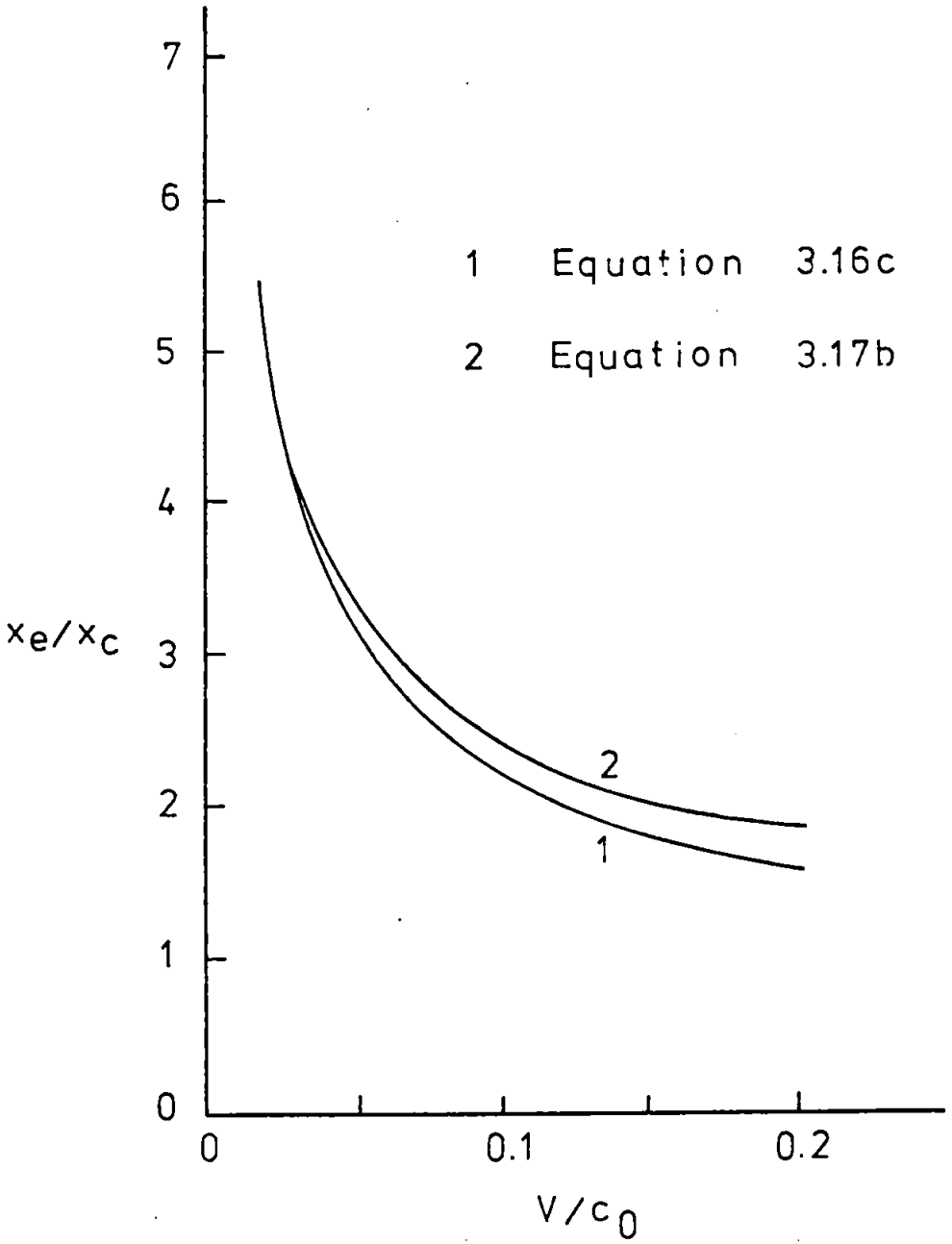

Fig. 3.7 x_e/x_c versus V/c_0.

$$\rho_t + (\rho u)_x + (\rho v)_y = 0, \qquad 3.18$$

where ρ is the density of the fluid and u and v are the particle velocity components in the x- and y-directions respectively at any time t.

The momentum equations are

$$u_t + uu_x + vu_y = -(1/\rho)p_x, \qquad 3.19a$$

$$v_t + uv_x + vv_y = -(1/\rho)p_y, \qquad 3.19b$$

where p is the pressure in the fluid at any position and time.

The energy equation is

$$s_t + us_x + vs_y = 0, \qquad 3.20$$

where s is the specific entropy of the fluid at any position and time.

The equation of state is

$$p = p(\rho, s). \qquad 3.21a$$

If the flow is homentropic (s constant everywhere), this becomes

$$p = p(\rho). \qquad 3.21b$$

The pressure and density are related to the sound speed c by the equation

$$dp/d\rho = c^2, \qquad 3.22$$

so that

$$\rho_t = (1/c^2)p_t, \ \rho_x = (1/c^2)p_x \text{ and } \rho_y = (1/c^2)p_y. \qquad 3.23$$

When these relations are substituted into Equation 3.18, it becomes

$$p_t + \rho c^2 u_x + u p_x + \rho c^2 v_y + v p_y = 0. \qquad 3.24$$

Equations 3.19a, 3.19b and 3.24 are three non-linear partial differential equations in three independent variables x, y and t, and three unknowns u, v and p.

Since the flow is homentropic, it must also be irrotational, so that the velocities can be derived from a potential φ. Thus

$$u = \varphi_x, \quad v = \varphi_y. \qquad 3.25$$

Equation 3.25 can be substituted into Equation 3.19a, which becomes

$$\varphi_{tx} + u u_x + v u_y = - (1/\rho) p_x. \qquad 3.26$$

Since the flow is irrotational, $u_y = v_x$, so that $v u_y = v v_x$, and Equation 3.26 can now be integrated with respect to x to become

$$\varphi_t + (1/2)(u^2 + v^2) + \int (1/\rho) dp = 0. \qquad 3.27a$$

This is Bernoulli's equation. It should be set equal to an arbitrary function of t and y, K(t,y) say. If Equation 3.25 is substituted into Equation 3.19b and the resulting equation integrated with respect to y, the same expression is obtained set equal to an arbitrary function of t and x, K'(t,x) say. Clearly K(t,y) = K'(t,x) = C(t), where C(t) is an arbitrary function of t. Since the addition of a function of time to φ does not affect the flow velocities calcualted with Equation 3.25, C(t) can be absorbed into φ_t, and the left hand side of Equation 3.27a can be set equal to zero.

When Equation 3.27a is differentiated with respect to t, it becomes

$$\varphi_{tt} + (1/2)(u^2 + v^2)_t + (1/\rho)p_t = 0. \qquad 3.28$$

This gives an expression for p_t.

Equation 3.25 can be substituted into Equation 3.19a and the result multiplied by u to become

$$uu_t + u^2\varphi_{xx} + uv\varphi_{yx} = -(1/\rho)up_x. \qquad 3.29a$$

This gives an expression for up_x.

Equation 3.25 can be substituted into Equation 3.19b and the result multiplied by v to become

$$vv_t + uv\varphi_{xy} + v^2\varphi_{yy} = -(1/\rho)vp_y. \qquad 3.29b$$

This gives an expression for vp_y.

When Equations 3.28, 3.29a and 3.29b are substituted into Equation 3.24, it becomes

$$\varphi_{tt} + (u^2 + v^2)_t + \varphi_{xx}(u^2 - c^2) + \varphi_{yy}(v^2 - c^2) + 2uv\varphi_{xy} = 0. \qquad 3.30a$$

This is a second order non-linear partial differential equation in three independent variables x, y and t, and one unknown φ. (The velocity components u and v are related to φ through Equation 3.25.) In principle a solution for φ can be obtained once the initial and boundary conditions on the flow are known.

3.3.2 Boundary and Initial Conditions

The general two-dimensional problem to be considered here is

illustrated in Fig. 3.8.

The kinematical boundary condition along the surface of contact between the solid and the liquid is

$$\varphi_n = \underline{V}.\underline{n}, \qquad 3.31a$$

where $\underline{V}$ is the impact velocity and $\underline{n}$ is a unit vector normal to the surface of the solid. This means that the velocity of a fluid particle at a point in contact with the solid is equal to the resolved component of the velocity of the solid normal to the contact surface at the point. Since the fluid is assumed inviscid, the solid is unable to impose a velocity component on it tangential to the contact surface. The fluid is free to slide over the solid (free-slip boundary condition). If it is assumed that first contact between liquid and solid occurs at $t = 0$, Equation 3.31a holds for $t > 0$.

Before contact occurs, the equation of the free surface is

$$y = y(x). \qquad 3.32a$$

If the surface is very shallow, this is approximately

$$y = 0. \qquad 3.32b$$

After contact occurs, the equation of the free surface is

$$y - Y(x,t) = 0. \qquad 3.32c$$

Equation 3.32c holds for $t > 0$ and $|x| > l(t)$, where $l(t)$ is the half-width of the solid at the level at which the solid surface intersects the free surface of the liquid. It is assumed that the solid is symmetrical about the y-axis.

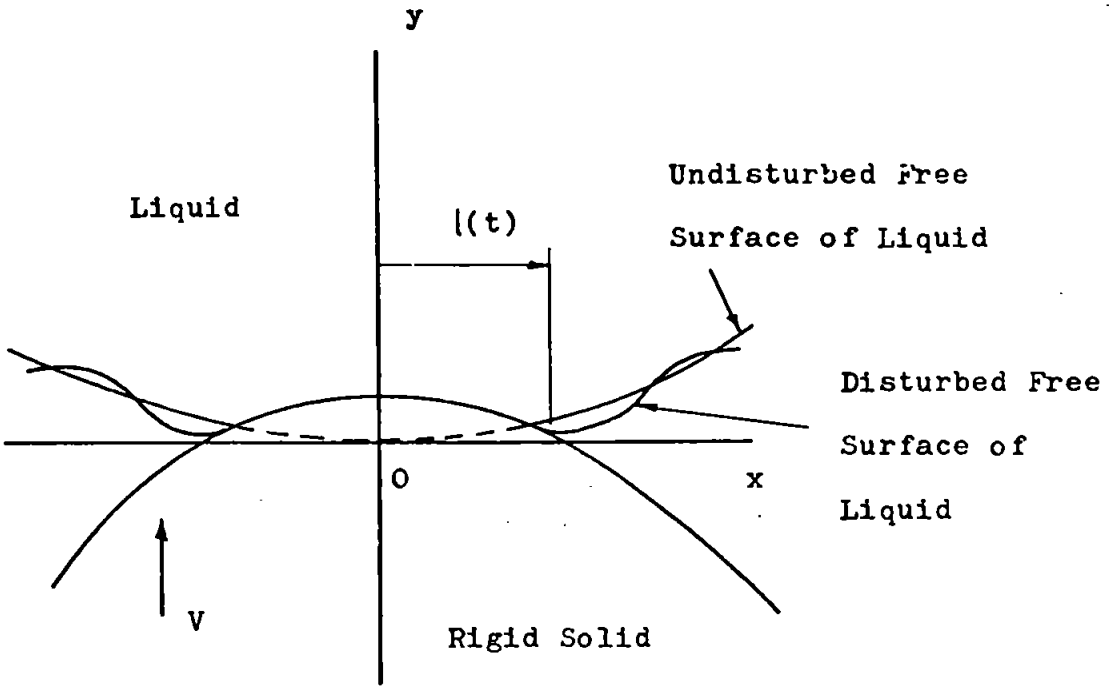

Fig. 3.8 The general impact problem.

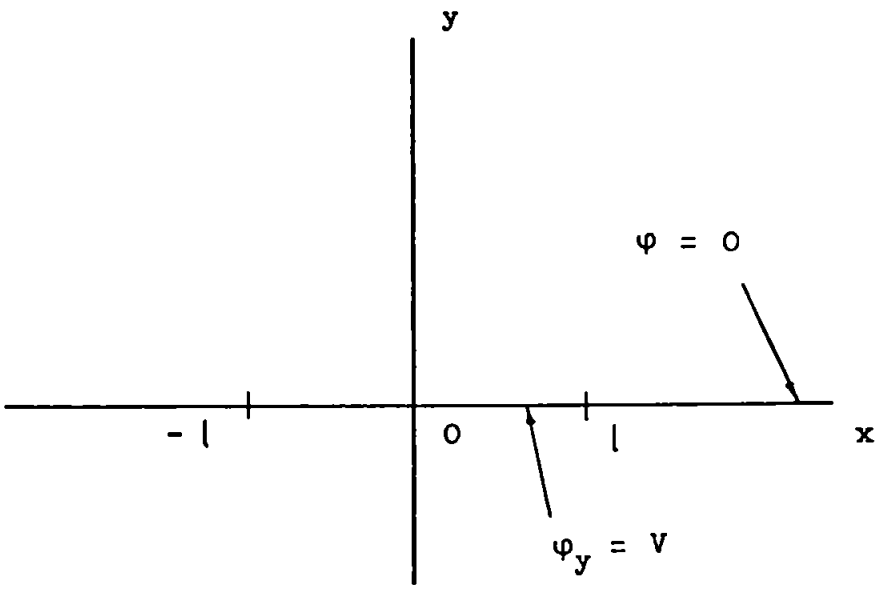

Fig. 3.9 Conditions at the interface between the liquid and the solid.

The kinematical boundary condition on the free surface is

$$D/Dt[(y - Y)] = 0 \text{ at } y = Y,$$

or

$$- Y_t - \varphi_x Y_x + \varphi_y = 0. \qquad 3.33$$

This means that a fluid particle in the free surface must remain there.

Bernoulli's equation (Equation 3.27a) at the free surface becomes

$$\varphi_t + (1/2)(u^2 + v^2) = 0, \qquad 3.34$$

since the pressure is constant and negligibly small at the free surface.

Instead of the boundary condition specified by Equation 3.31a, assume that the effect of the solid on the fluid can be specified by

$$\varphi_y = V(t), \qquad 3.31b$$

for $t > 0$ and $|x| < (t)$. This is illustrated in Fig. 3.9. The fluid has a velocity component on a section of the x-axis, rather than on the actual solid, and this component is normal to the x-axis, not to the solid.

Equation 3.31b is linear in φ, but the differential equation 3.30a and the boundary conditions given by Equations 3.33 and 3.34 are non-linear, and the free surface is specified by an unknown function which is also non-linear.

3.3.3 Linearisation and Final Statement of the Problem

In Equations 3.27a and 3.30a the non-linear terms are those that contain products of the velocity components. In the problem studied here these components change from zero to order V in the time that it takes a disturbance to reach the point under consideration. Consequently $\Delta u/\Delta x = O[V/(ct)]$ and $\Delta u/\Delta t = O[V/t]$, or $(\Delta u/\Delta x)/(\Delta u/\Delta t) = O[1/c]$, so that $u_x << u_t$. If $u << c$, it follows that $u_t >> uu_x$. Similarly $u_t >> vu_y$, $v_t >> uv_x$ and $v_t >> vv_y$. Therefore the term $(u^2 + v^2)$ in Equation 3.27a is small compared with φ_t and may be neglected, and the term $(u^2 + v^2)_t$ and those that contain u^2, v^2 and uv in Equation 3.30a are small compared with φ_{tt} and may be neglected.

When u and v are much less than c, the change in density is small, so that $\rho \simeq \rho_0$. Equation 3.22 may therefore be expanded as a Taylor series about the point on the p versus ρ curve at which $\rho = \rho_0$. Thus

$$dp/d\rho = c^2 = (dp/d\rho)_0 + (\rho - \rho_0)(d^2p/d\rho^2)_0 + \text{higher order terms} \simeq c_0^2.$$

The density ρ in Equation 3.27a and the sound speed c in Equation 3.30a may therefore be replaced by their undisturbed values ρ_0 and c_0 respectively.

Equation 3.27a therefore becomes

$$p = -\rho_0\varphi_t, \qquad 3.27b$$

and Equation 3.30a

$$\varphi_{tt} - c_0^2(\varphi_{xx} + \varphi_{yy}) = 0. \qquad 3.30b$$

The boundary conditions on the linear equation 3.30b are

$$\varphi_y = V, \qquad 3.31c$$

for $t > 0$ and $|x| < l(t)$, and

$$\varphi = 0, \qquad 3.35$$

for $t > 0$ and $|x| > l(t)$.

Equation 3.31c comes from Equation 3.31b by assuming that the velocity of the contact surface is constant throughout the impact, and Equation 3.35 comes from Equation 3.34 by neglecting the non-linear terms.

In Equation 3.33 φ_x and Y_x are of the same order as φ_y, and they are all much smaller than Y_t, so that the equation reduces to $Y_t = 0$, from which

$$Y(x,t) = 0 \qquad 3.36$$

on integration. The free surface is therefore undisturbed during the impact.

The pressure is zero before the impact, so that the initial conditions are

$$\varphi = 0 \text{ and } \varphi_t = 0. \qquad 3.37$$

The problem is to solve Equation 3.30b with the boundary conditions 3.31c and 3.35 and initial conditions 3.37 assuming no free surface disturbance 3.36. The velocity components can then be obtained from Equation 3.25 and the pressure from Equation 3.27b.

3.3.4 The Supersonic Flow Analogy

Write

$$t = z/[c_0(M^2 - 1)^{1/2}],$$

where $M > 1$. This can be substituted into Equation 3.30b, which becomes

$$\varphi_{xx} + \varphi_{yy} - (M^2 - 1)\varphi_{zz} = 0.$$

This is the linearised equation for steady high speed flow over an aerofoil, with flow at infinity in the positive z-direction; M is the Mach number of the flow. If the aerofoil is flat, the normal component of flow velocity at the surface of the wing is constant and equal to $U\alpha$, where U is the flow velocity a long way from the wing and α is the angle of attack. The method of solving this problem is discussed in detail by Ward (1955).[a] Since the wing is thin (in the linearised theory), the boundary data are given in the plane $y = 0$. Thus $\varphi_y = U\alpha$ on the wing and $\varphi = 0$ off the wing. In the impact problem the boundary data are also given in the plane $y = 0$. This is illustrated in Fig. 3.10. The region inside the contact edge corresponds to the planform of the wing. There is thus a complete analogy between the impact of a liquid mass with a solid and the supersonic flow of air over an aerofoil. From this it follows that if the solution for one of these problems is known the solution for the other can be written down at once. Unfortunately, the solution of the supersonic flow problem for the pressure distribution over the surface of an aerofoil which has a planform with the same boundary shape as the contact edge in the impact problem that is studied here has not been worked out, so that the

a A lucid discussion of the problem is given by Heaslet and Lomax (1948). It is also discussed in many current text-books on compressible flow. (See, for example, Curle and Davies (1971).)

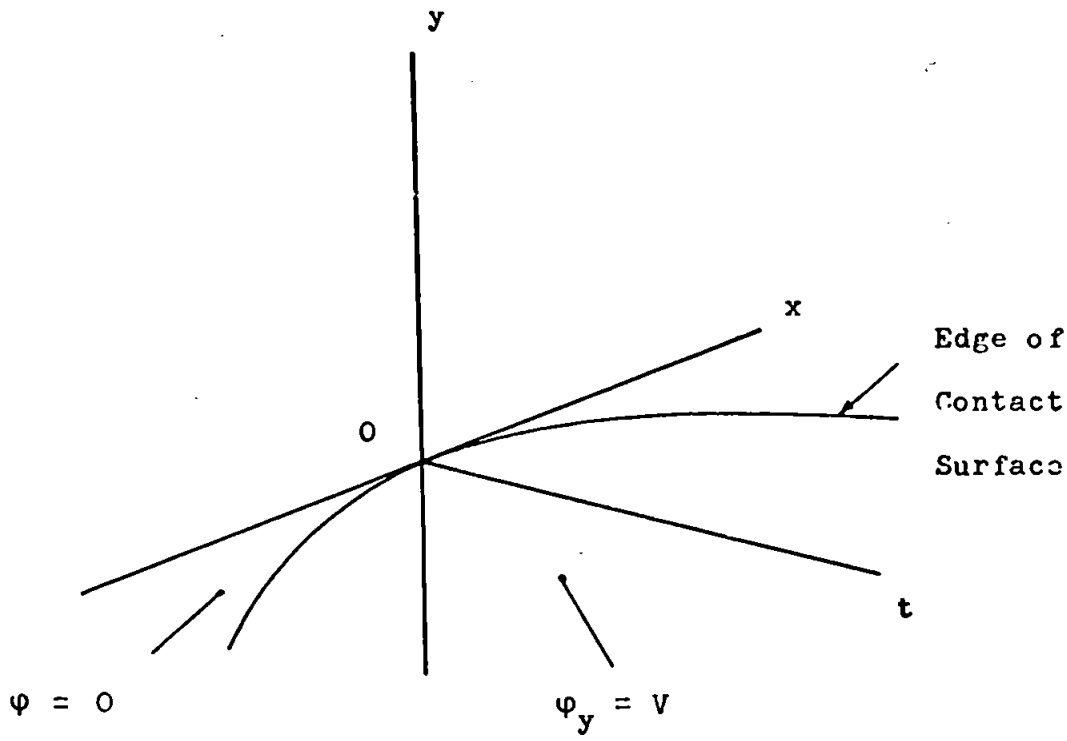

Fig. 3.10 The impact problem in the x-y-t space.

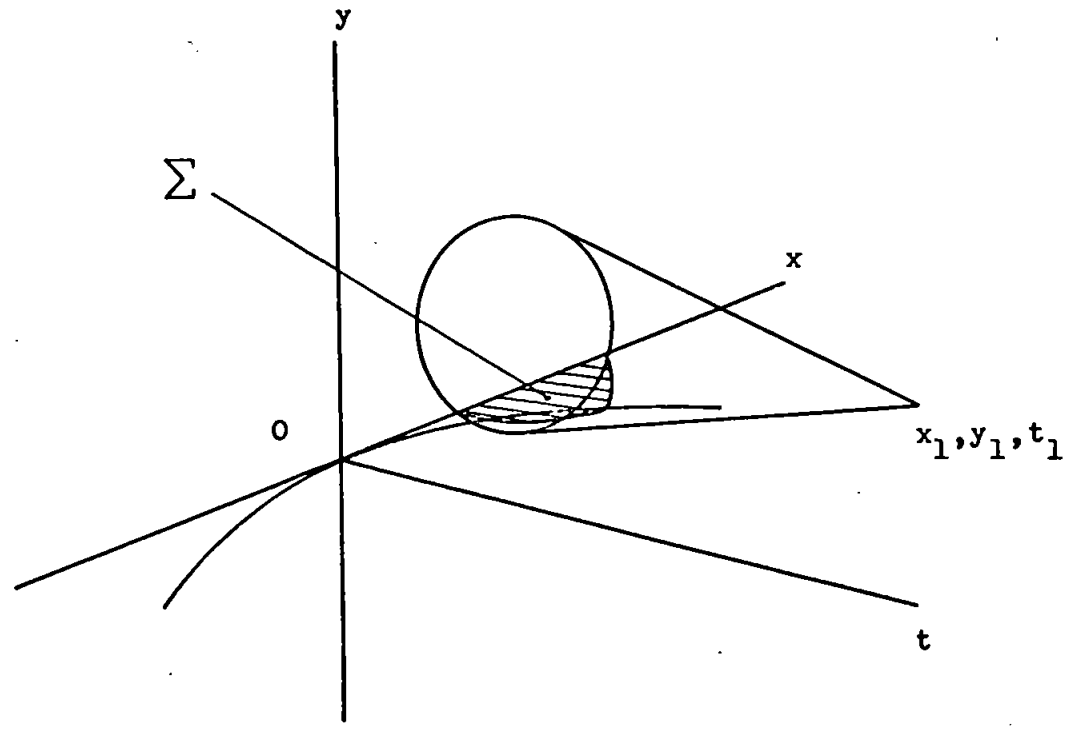

Fig. 3.11 The domain of dependence of the point x_1, y_1, t_1 in the x-y-t space.

analogy cannot be used directly. However, the general method that is used to solve the supersonic flow problem is easily adapted to solve the impact problem, as shown below.

3.3.5 Solution for the Impact Pressure Distribution

The problem is to determine the potential at any point x_1, y_1, t_1 in the x-y-t space. (See Fig. 3.11.) From the general theory of hyperbolic equations, it is known that the value of any quantity at x_1, y_1, t_1 depends only on the values that it has at points within the characteristic cone

$$c_0 t < c_0 t_1 - [(x - x_1)^2 + (y - y_1)^2]^{1/2}.$$

Since nothing happens in the fluid for $t < 0$, the cone is the finite region shown in Fig. 3.11. This conical region is known as the domain of dependence of the point through which it passes.

It can be shown that the potential at any point x_1, y_1, t_1 in the x-y-t space can be expressed as an integral of either φ_y or φ over the region Σ in the $y = 0$ plane (Ward (1955)). (This region is shown shaded in Fig. 3.11.) Since φ_y is known over part of Σ, the formulation in terms of φ_y will be used here. It is

$$\varphi(x_1, y_1, t_1) = - (c_0/\pi) \iint_{\Sigma} (\varphi_y)_{y=0} dt dx / [c_0^2 (t - t_1)^2 - (x - x_1)^2 - y_1^2]^{1/2}. \quad 3.38$$

Since only the pressure distribution over the contact region between liquid and solid is required, it is sufficient to determine the potential at points in the $y = 0$ plane, for which Equation 3.38 reduces to

$$\varphi(x_1,0,t_1) =$$

$$-(c_0/\pi)\iint_{\Sigma}(\varphi_y)_{y=0}dtdx/[c_0^2(t-t_1)^2-(x-x_1)^2]^{1/2}, \qquad 3.39$$

where Σ is the triangular area in $y = 0$ for which

$$0 < c_0t < c_0t_1 - (x - x_1).$$

The integrand has a simpler form in characteristic coordinates. Let

$$\xi = c_0t_1 - x_1 + K, \quad \eta = c_0t_1 + x_1 + K,$$

and

$$\xi' = c_0t - x + K, \quad \eta' = c_0t + x + K,$$

where K is a constant; ξ',η' are characteristic coordinates in the x-t plane; the characteristic lines ξ' = constant and η' = constant make the Mach angle with the t-axis.

The Jacobian of the transformation is

$$\partial(t,x)/\partial(\xi',\eta') = 1/(2c_0).$$

Write

$$N(\xi',\eta') = -(\varphi_y)_{y=0}/(2\pi), \text{ and } \varphi(\xi,\eta) = \varphi(x_1,0,t_1),$$

so that Equation 3.39 becomes

$$\varphi(\xi,\eta) = \iint_{\Sigma}N(\xi',\eta')d\xi'd\eta'/[(\xi-\xi')(\eta-\eta')]^{1/2}, \qquad 3.40$$

where Σ is the region $\xi' \leq \xi$, $\eta' \leq \eta$.

The problem in the x-t plane is illustrated in Fig. 3.12. The origin of the characteristic coordinates is at the point O', so that

$$A \quad (0,\eta_0), \quad G \quad (\xi_0,0),$$

and the equation of the contact edge is either

$$GAC \quad \xi' = H_1(\eta'), \quad JG \quad \xi' = H_2(\eta'),$$

or

$$JGA \quad \eta' = F_1(\xi'), \quad AC \quad \eta' = F_2(\xi').$$

Expressions are now obtained for the potential in the regions of the x-t plane shown in Fig. 3.12.

Potential in Region 1

This region is shown isolated in Fig. 3.13a. The boundary conditions are

$$N(\xi',\eta') = 0 \text{ for } \xi' < 0, \ \eta' < 0,$$

and

$$N(\xi',\eta') = -V/(2\pi) \text{ for } \xi' > 0, \ \eta' > 0.$$

From Equation 3.40 the integration over the shaded part Σ is therefore

$$\varphi(\xi,\eta) = -(V/(2\pi)) \int_{H_1(\eta)}^{\xi} d\xi'/(\xi - \xi')^{1/2} \int_{F_1(\xi')}^{\eta} d\eta'/(\eta - \eta')^{1/2}.$$

(See Fig. 3.13b.)

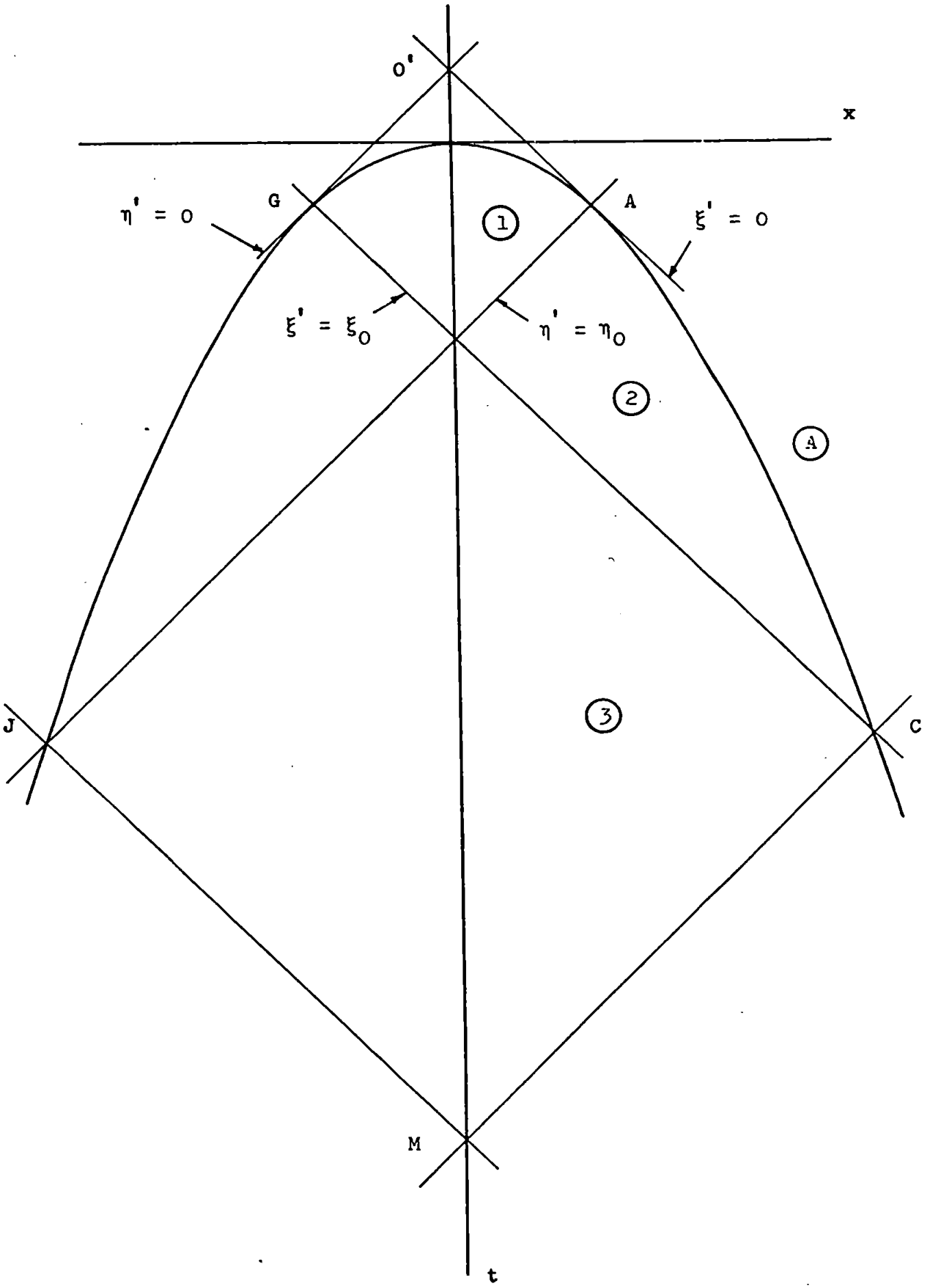

Fig. 3.12 Characteristics in the x-t plane.

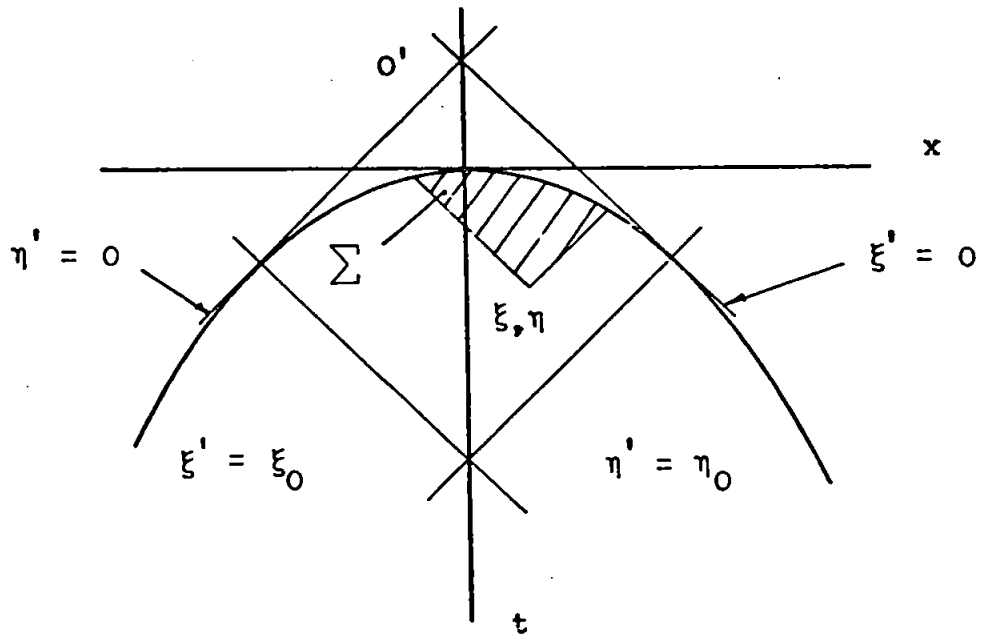

Fig. 3.13a Domain of integration for ξ,η in Region 1.

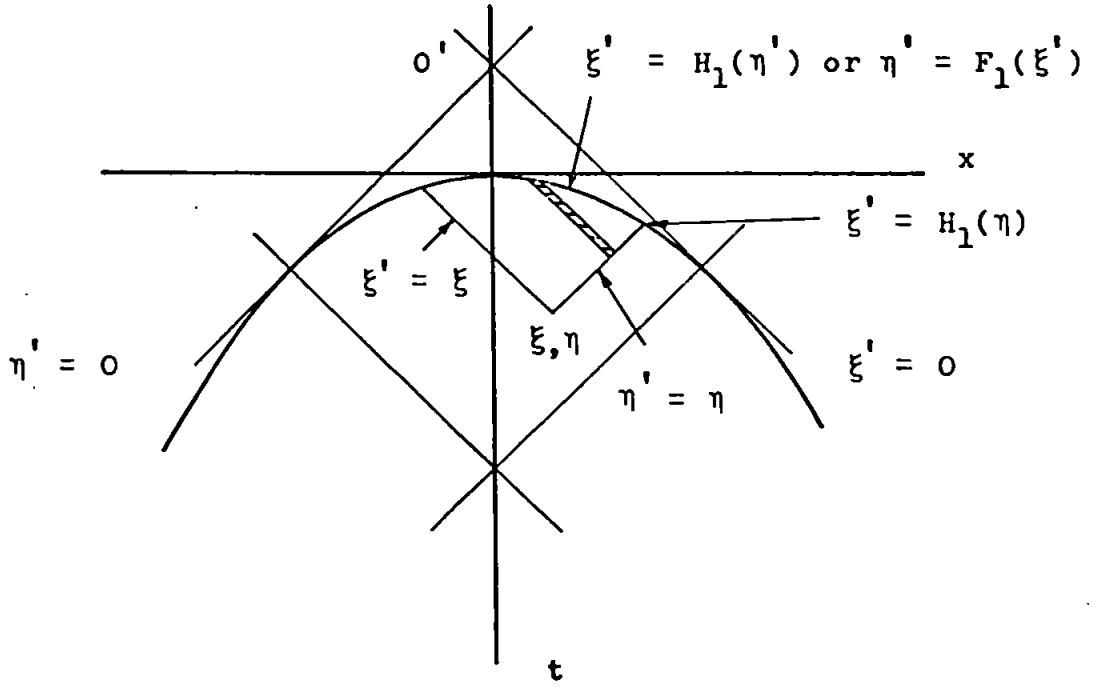

Fig. 3.13b Limits of integration for ξ,η in Region 1.

The first part is easily integrated.

$$\int_{F_1(\xi')}^{\eta} d\eta'/(\eta - \eta')^{1/2} = -2(\eta - \eta')^{1/2}\Big|_{F_1(\xi')}^{\eta} = 2[\eta - F_1(\xi')]^{1/2}.$$

The expression for the potential in Region 1 therefore becomes

$$\varphi(\xi,\eta) = -(V/\pi)\int_{H_1(\eta)}^{\xi} [(\eta - F_1(\xi'))/(\xi - \xi')]^{1/2} d\xi'. \qquad 3.41a$$

The solution is continued below.

Potential in Region A

This region is shown in Fig. 3.14. Note that

(i) $N(\xi',\eta') = 0$ for $\xi' < 0$, $\eta' < 0$;

(ii) $N(\xi',\eta')$ is unknown in Region A; call it $g(\xi',\eta')$; and

(iii) $\varphi(\xi,\eta) = 0$ in Region A.

From Equation 3.40 and (iii) above the integration over the shaded part Σ is therefore

$$\varphi(\xi,\eta) = \left[\int_0^{\xi} d\xi'/(\xi - \xi')^{1/2}\right]\left[\int_{F_2(\xi')}^{\eta} (g(\xi',\eta')/(\eta - \eta')^{1/2})d\eta' - (V/(2\pi))\int_{F_1(\xi')}^{F_2(\xi')} d\eta'/(\eta - \eta')^{1/2}\right] = 0. \qquad 3.42$$

This is satisfied if the part between the second brackets is zero. Since $g(\xi',\eta')$ is not needed here, there is no need to obtain an expression for it.

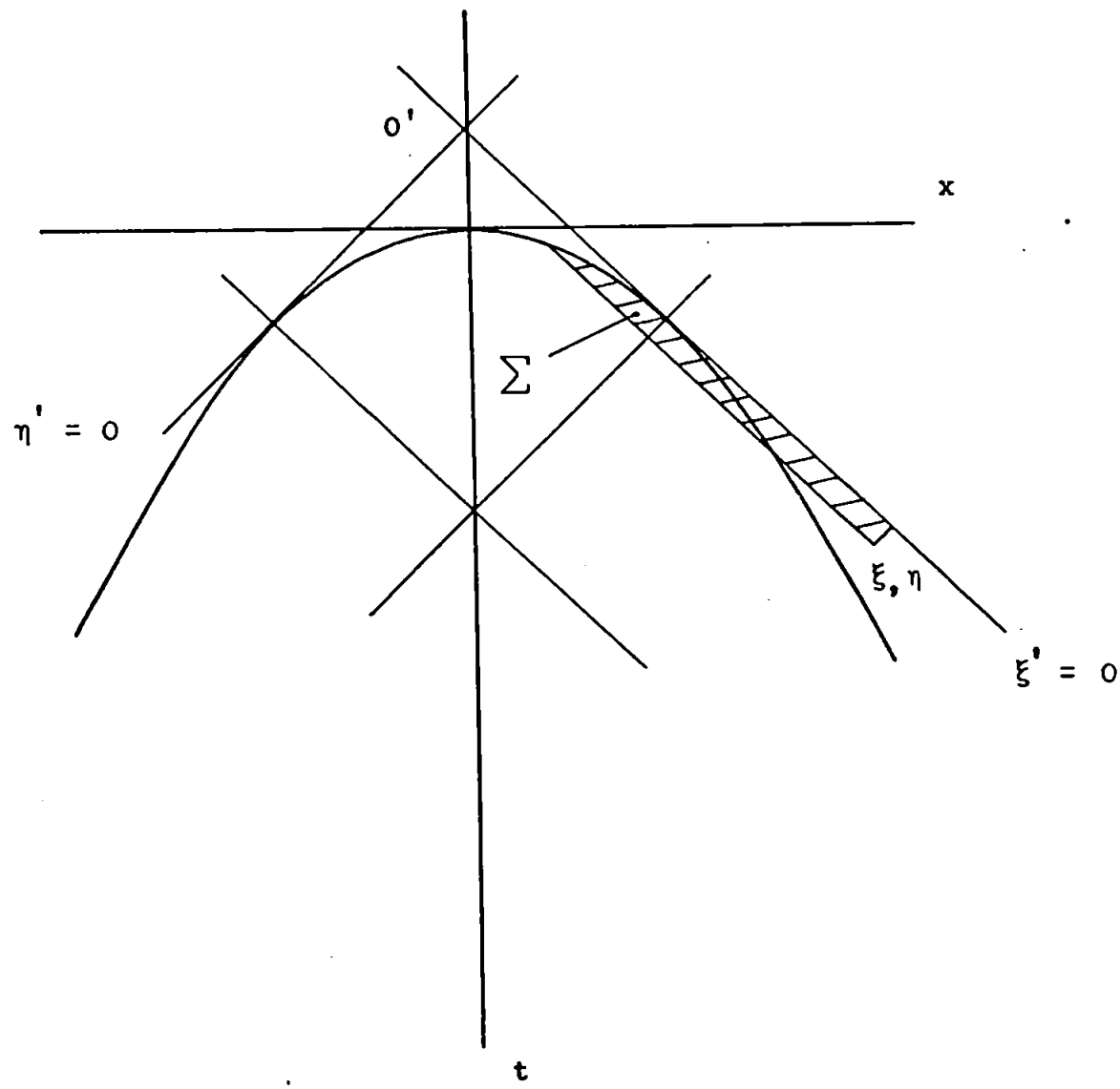

Fig. 3.14 Domain of integration for ξ,η in Region A.

Potential in Region 2

This region is shown in Fig. 3.15. From Equation 3.40 the integration over the shaded areas Σ and Σ' is

$$\varphi(\xi,\eta) = -(V/(2\pi)) \int_{H_1(\eta)}^{\xi} d\xi'/(\xi - \xi')^{1/2} \int_{F_1(\xi')}^{\eta} d\eta'/(\eta - \eta')^{1/2}$$

$$+ \left[\int_{0}^{H_1(\eta)} d\xi'/(\xi - \xi')^{1/2} \right] \left[\int_{F_2(\xi')}^{\eta} (g(\xi',\eta')/(\eta - \eta')^{1/2}) d\eta' \right.$$

$$\left. - (V/(2\pi)) \int_{F_1(\xi')}^{F_2(\xi')} d\eta'/(\eta - \eta')^{1/2} \right] = 0.$$

The last part of this expression is zero from Equation 3.42, therefore

$$\varphi(\xi,\eta) = -(V/(2\pi)) \int_{H_1(\eta)}^{\xi} d\xi'/(\xi - \xi')^{1/2} \int_{F_1(\xi')}^{\eta} d\eta'/(\eta - \eta')^{1/2}.$$

This is the same as the relation found for Region 1, so that

$$\varphi(\xi,\eta) = -(V/\pi) \int_{H_1(\eta)}^{\xi} [(\eta - F_1(\xi'))/(\xi - \xi')]^{1/2} d\xi'. \qquad 3.43a$$

The solution is continued below.

Potential in Region 3

This region is shown in Figs. 3.16a and 3.16b. A result can be found in Region B similar to that found in Region A, so that the

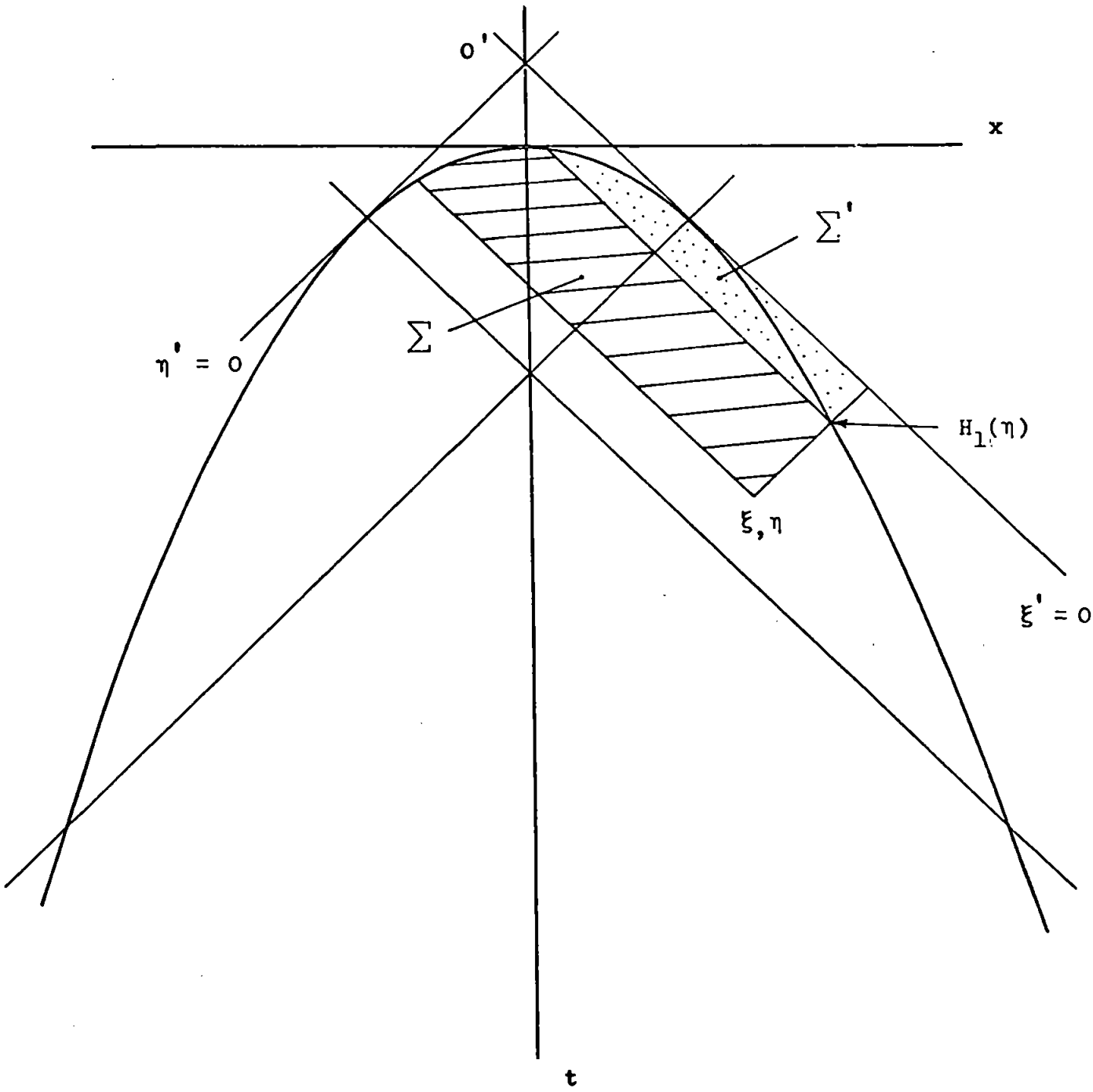

Fig. 3.15 Domain of integration for ξ,η in Region 2.

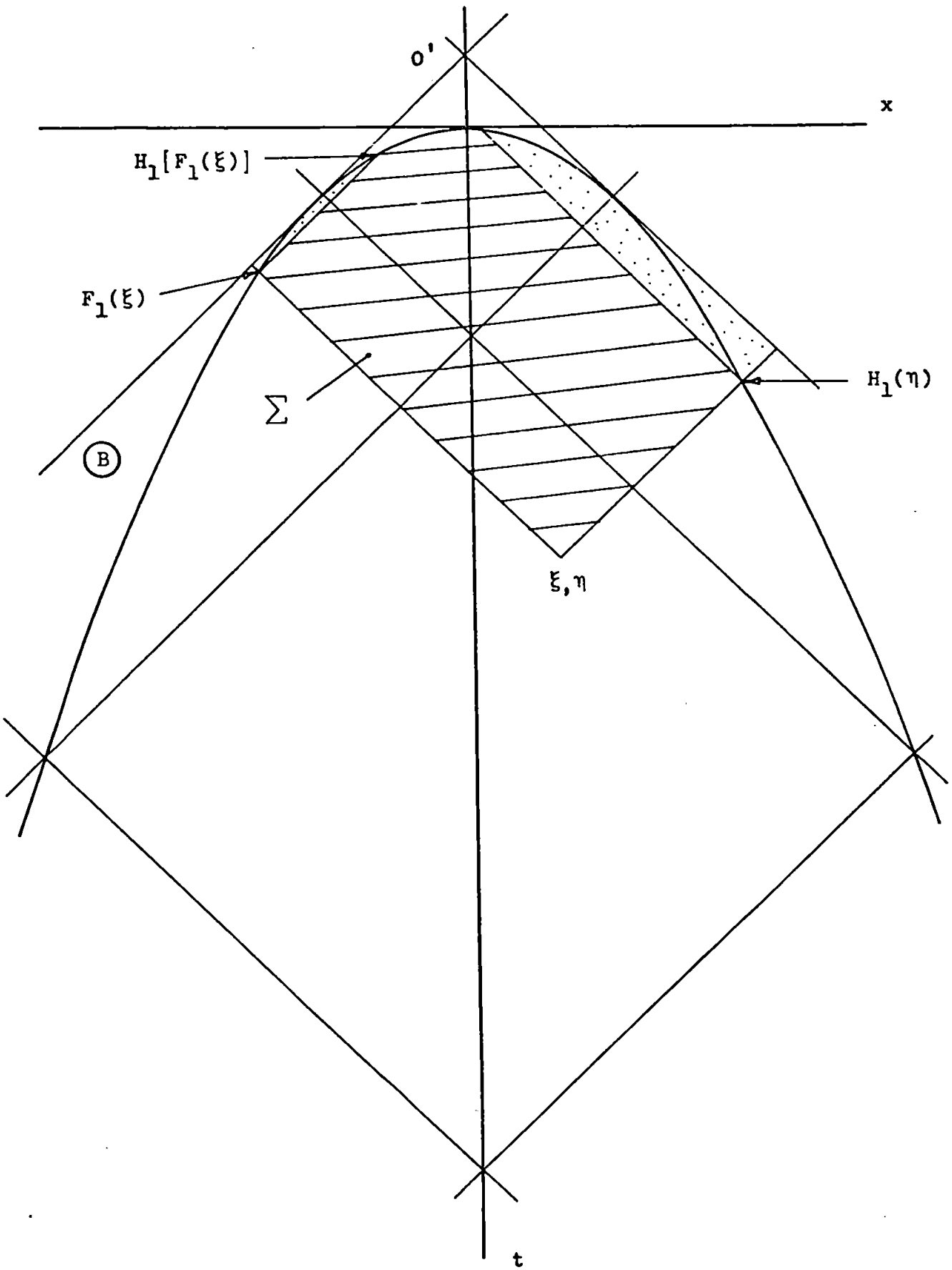

Fig. 3.16a Domain of integration for ξ,η in Region 3.

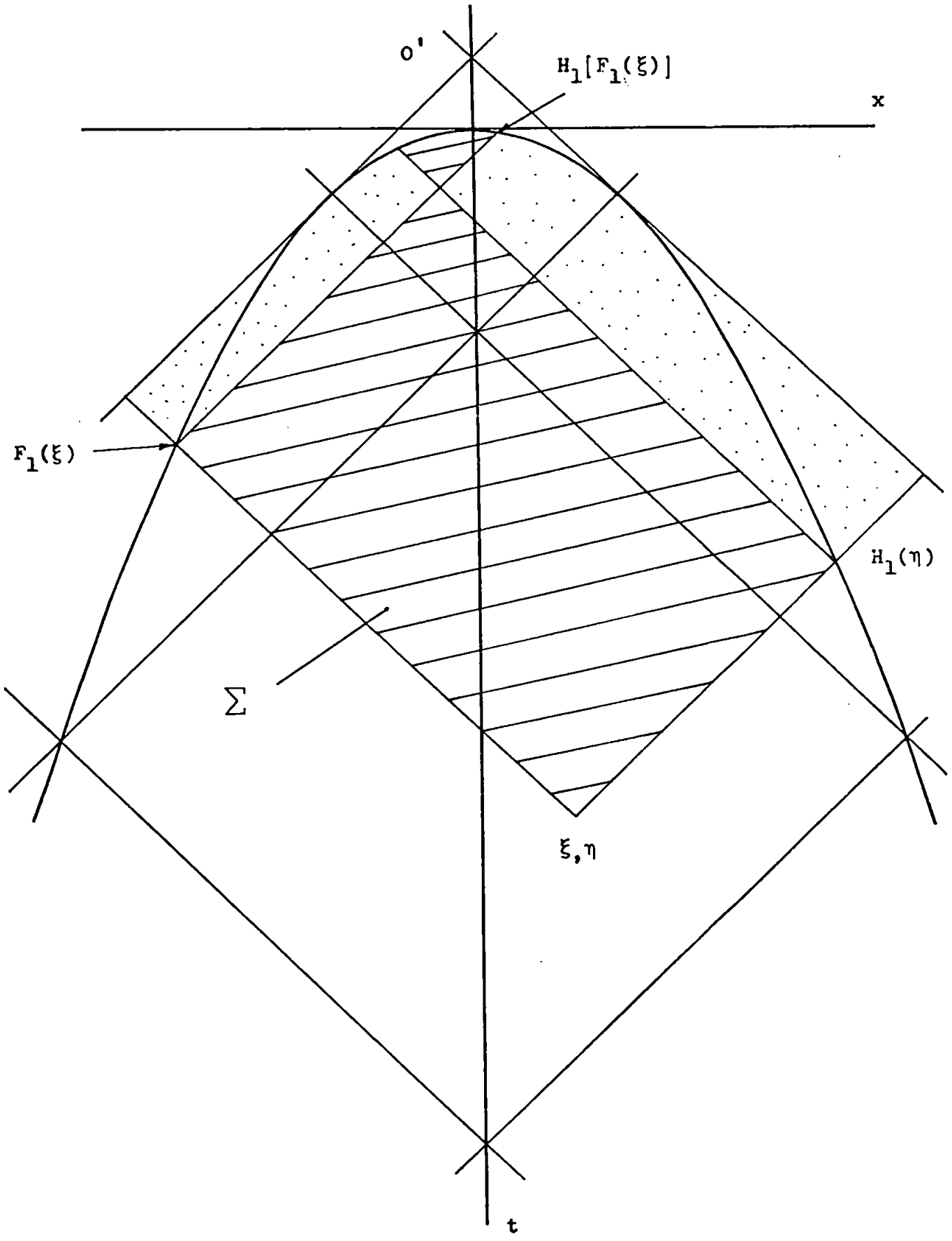

Fig. 3.16b Domain of integration for ξ,η in Region 3.

expression for the potential in Region 3 becomes

$$\varphi(\xi,\eta) = -(V/(2\pi)) \int_{H_1(\eta)}^{\xi} d\xi'/(\xi - \xi')^{1/2} \int_{F_1(\xi')}^{\eta} d\eta'/(\eta - \eta')^{1/2}$$

$$+ (V/(2\pi)) \int_{H_1[F_1(\xi)]}^{\xi} d\xi'/(\xi - \xi')^{1/2} \int_{F_1(\xi')}^{F_1(\xi)} d\eta'/(\eta - \eta')^{1/2},$$

therefore

$$\varphi(\xi,\eta) = -(V/\pi) \int_{H_1(\eta)}^{\xi} [(\eta - F_1(\xi'))/(\xi - \xi')]^{1/2} d\xi'$$

$$+ (V/\pi) \int_{H_1[F_1(\xi)]}^{\xi} [(F_1(\xi) - F_1(\xi'))/(\xi - \xi')]^{1/2} d\xi'. \qquad 3.44a$$

The solution is continued below.

The solution can be continued beyond Region 3. However, $g(\xi',\eta')$ must now be determined by solving the integral equation between the second brackets in Equation 3.42. This leads to a complex expression for $N(\xi',\eta')$ in Region A. The calculations will be terminated at points along the upper boundary of Region 3.

The integrals in the expressions for potential throughout the x-t plane can only be evaluated if the functions that describe the contact edge are specified. These functions are illustrated in Figs. 3.17a and 3.17b. It can be seen that they are single-valued functions of the characteristic coordinates ξ',η'. At the points

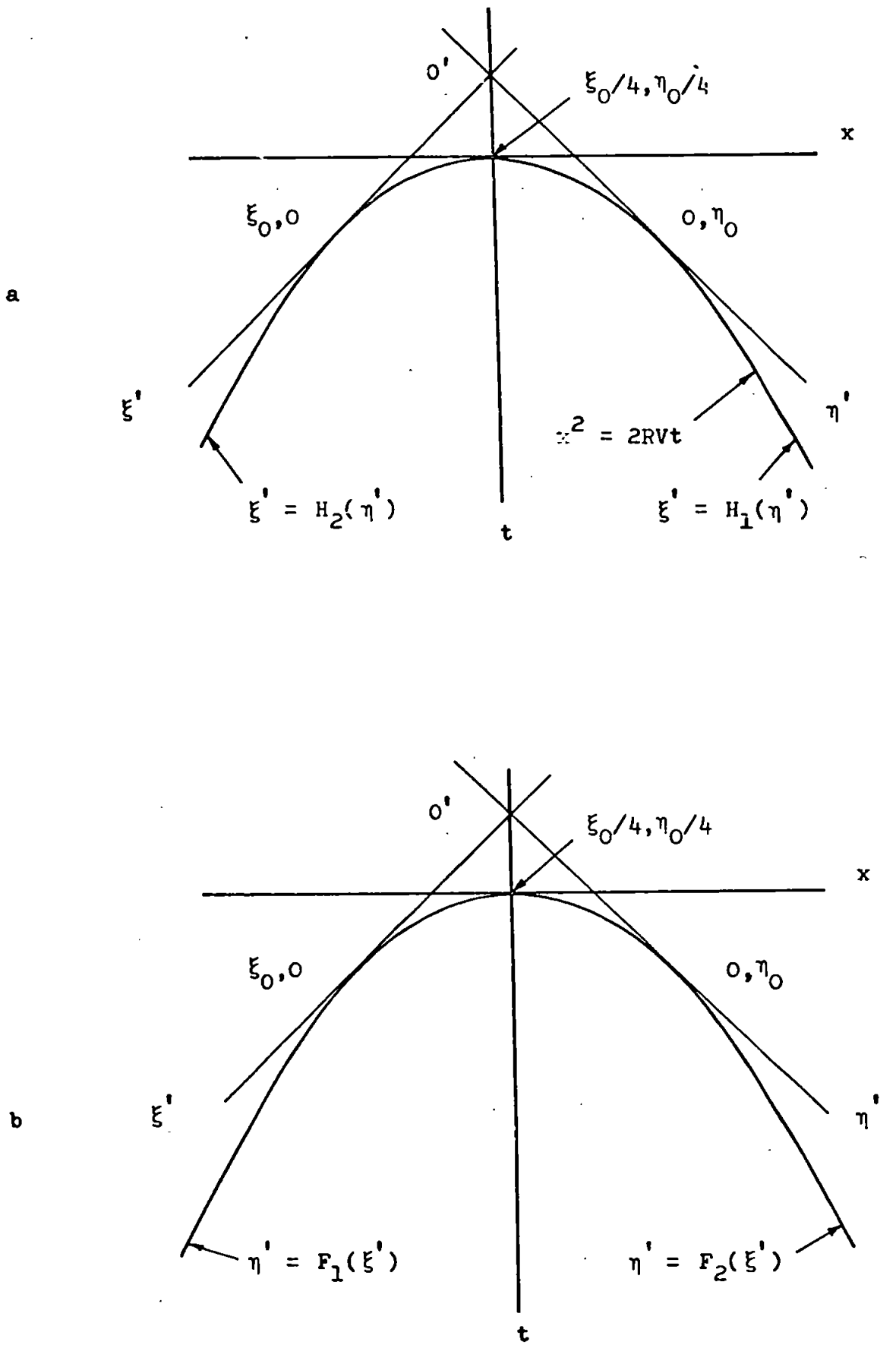

Fig. 3.17 The contact edge as a function of the characteristic coordinates.

specified by the coordinates ξ_0,0 and 0,η_0, where the characteristic lines $\eta' = 0$ and $\xi' = 0$ respectively are tangent to the curve that defines the contact edge, the pressure waves generated in the impact overtake the edges of the contact region between the liquid and the solid. The fronts of the reflected waves that are in contact with the solid propagate into the liquid along the characteristic lines $\eta' = \eta_0$ and $\xi' = \xi_0$.

The problem that is considered here is the impact of a cylindrical liquid drop with a plane rigid solid (see Fig. 3.1). Since the free surface of the liquid remains undisturbed during the impact (Equation 3.36), the equation of the contact edge as a function of x and t is given by Equation 3.1b [a]. The coordinates of the points in the x-t plane that correspond to the edge positions at which pressure waves generated in the impact are just able to overtakes the edges of the drop are given by Equation 3.4b. These coordinates can be used to determine the value of the constant K in the transformation equations. (This constant, which determines the position of the origin O' of the characteristic coordinates, can only be fixed when the equation of the contact edge is specified.) Thus $\xi' = 0$, $\eta' = \eta_0$ when $x = x_c = RV/c_0$, $t = t_c = RV/(2c_0^2)$, therefore $K = RV/(2c_0)$ and $\eta_0 = \xi_0$ (by symmetry) $= 2RV/c_0 = 4K$. The transformation equations therefore become

a At some time during the impact jets of liquid squirt out from under the edges of the drop, after which the contact edge is no longer defined by Equation 3.1b. It turns out that this occurs at times which correspond to points on the contact edge beyond Region 3 (see below).

$$\xi = c_0 t_1 - x_1 + RV/c_0, \quad \eta = c_0 t_1 + x_1 + RV/c_0,$$

and

$$\xi' = c_0 t - x + RV/c_0, \quad \eta' = c_0 t + x + RV/c_0.$$

The second pair of equations are easily rearranged to give x and t as functions of ξ' and η'. Thus

$$x = (\eta' - \xi')/2, \quad t = (\xi' + \eta')/(2c_0) - RV/(2c_0^2).$$

These relations can then be substituted into the equation that defines the contact edge (Equation 3.1b) to give

$$(\eta' - \xi')^2/4 = 2RV[(\xi' + \eta')/(2c_0) - RV/(2c_0^2)].$$

This is easily simplified to give an explicit expression for η' in terms of ξ' and vice versa. Thus

$$\eta' = \xi' + \xi_0 \pm 2(\xi'\xi_0)^{1/2},$$

and

$$\xi' = \eta' + \eta_0 \pm 2(\eta'\eta_0)^{1/2}.$$

The equations that define the contact edge are therefore either

$$\xi' = H_1(\eta') = \eta' + \eta_0 - 2(\eta'\eta_0)^{1/2}, \qquad 3.45a$$

$$\xi' = H_2(\eta') = \eta' + \eta_0 + 2(\eta'\eta_0)^{1/2}, \qquad 3.45b$$

or

$$\eta' = F_1(\xi') = \xi' + \xi_0 - 2(\xi'\xi_0)^{1/2}, \qquad 3.45c$$

$$\eta' = F_2(\xi') = \xi' + \xi_0 + 2(\xi'\xi_0)^{1/2}. \qquad 3.45d$$

Also

$$F_1(\xi) - F_1(\xi') = \xi - \xi' - 2\xi_0^{1/2}(\xi^{1/2} - \xi'^{1/2}), \qquad 3.46a$$

$$H_1(\eta) = \eta + \eta_0 - 2(\eta\eta_0)^{1/2}, \qquad 3.46b$$

and

$$H_1[F_1(\xi)] = F_1(\xi) + \eta_0 - 2[F_1(\xi)\eta_0]^{1/2}. \qquad 3.46c$$

Equation 3.41a for the potential in Region 1 therefore becomes

$$\varphi(\xi,\eta) = -(V/\pi)\int_{H_1(\eta)}^{\xi} [(\eta - (\xi' + \xi_0 - 2(\xi'\xi_0)^{1/2}))/(\xi - \xi')]^{1/2} d\xi'. \qquad 3.41b$$

Since Equation 3.43a for the potential in Region 2 is the same as Equation 3.41a, Equation 3.41b also gives the potential in Region 2.

Equation 3.44a for the potential in Region 3 becomes

$$\varphi(\xi,\eta) = -(V/\pi)\int_{H_1(\eta)}^{\xi} [(\eta - (\xi' + \xi_0 - 2(\xi'\xi_0)^{1/2}))/(\xi - \xi')]^{1/2} d\xi' + (V/\pi)\int_{H_1[F_1(\xi)]}^{\xi} [(\xi - \xi' - 2\xi_0^{1/2}(\xi^{1/2} - \xi'^{1/2}))/(\xi - \xi')]^{1/2} d\xi'. \qquad 3.44b$$

The ultimate aim of the analysis is to obtain an expression for the pressure distribution across the surface of contact between the liquid and the solid. In principle this can be carried out by

evaluating the integrals for the potential in the various regions, transforming the resulting expressions back into the original variables x_1 and t_1, and using Equation 3.27b to obtain the pressure distribution. However, it is simpler to transform Equation 3.27b from x_1, t_1 to ξ, η, differentiate the integrals for $\varphi(\xi, \eta)$ under the integral sign with respect to ξ and η, then evaluate the resulting expressions to get the pressure distribution directly.

Since the potential is a function of ξ and η and both ξ and η are functions of x_1 and t_1, $\varphi_{t_1} = \varphi_\xi \xi_{t_1} + \varphi_\eta \eta_{t_1}$. The transformation equations then give

$$\varphi_{t_1} = c_0(\varphi_\xi + \varphi_\eta),$$

so that the pressure at any point ξ, η is

$$p = -\rho_0 c_0(\varphi_\xi + \varphi_\eta), \qquad 3.27c$$

from Equation 3.27b.

Pressure Distribution in Regions 1 and 2

Equations 3.41b and 3.27c give

$$p = (\rho_0 c_0 V/\pi)\left[(\eta - (\xi^{1/2} - \xi_0^{1/2})^2)^{1/2}/(\xi - H_1(\eta))^{1/2}\right.$$

$$- (\eta - ((H_1(\eta))^{1/2} - \xi_0^{1/2})^2)^{1/2}(1 - (\eta_0/\eta)^{1/2})/(\xi - H_1(\eta))^{1/2}$$

$$+ (1/2)\int_{H_1(\eta)}^{\xi} d\xi'/\left[(\eta - (\xi'^{1/2} - \xi_0^{1/2})^2)(\xi - \xi')\right]^{1/2}$$

$$\left. - (1/2)\int_{H_1(\eta)}^{\xi} [(\eta - (\xi'^{1/2} - \xi_0^{1/2})^2)^{1/2}/(\xi - \xi')^{3/2}]d\xi' \right.$$

$$+ (1/2) \int_{H_1(\eta)} [(\eta - (\xi^{1/2} - \xi_0^{1/2})^2)/(\xi - \xi')^{3/2}]d\xi' \,. \quad a,\ b \qquad 3.47a$$

The integrals can be simplified by making the substitutions

$$u = \xi'^{1/2},\ k = \xi^{1/2},\ a = \eta^{1/2} + \xi_0^{1/2},\ b = \eta^{1/2} - \xi_0^{1/2}.$$

They become

$$\int_{b^2}^{k^2} u\,du/[(a - u)(b + u)(k^2 - u^2)]^{1/2}$$

$$- \int_{b^2}^{k^2} [((a - u)(b + u))^{1/2}/(k^2 - u^2)^{3/2}]u\,du$$

$$+ \int_{b^2}^{k^2} [((a - k)(b + k))^{1/2}/(k^2 - u^2)^{3/2}]u\,du.$$

a The term $\xi' + \xi_0 - 2(\xi'\xi_0)^{1/2}$ has been written $(\xi'^{1/2} - \xi_0^{1/2})^2$.

b The general result

$$\partial/\partial a \int_b^a f(x)dx/(a - x)^{1/2} = - (1/2) \int_b^a [f(x) - f(a)]dx/(a - x)^{3/2}$$

$$+ f(a)/(a - b)^{1/2}$$

has been used, since the integrand approaches infinity at the upper limit. (See Ward (1955).)

The last two integrals are easily integrated by parts to become

$$- [((a - u)(b + u))^{1/2} - ((a - k)(b + k))^{1/2}]/(k^2 - u^2)^{1/2}\Big|_{b^2}^{k^2}$$

$$+ (1/2)\int_{b^2}^{k^2} (a - b - 2u)du/[(a - u)(b + u)(k^2 - u^2)]^{1/2}.$$

Therefore the integrals reduce to

$$- [((a - u)(b + u))^{1/2} - ((a - k)(b + k))^{1/2}]/(k^2 - u^2)^{1/2}\Big|_{b^2}^{k^2}$$

$$+ ((a - b)/2)\int_{b^2}^{k^2} du/[(a - u)(b + u)(k^2 - u^2)]^{1/2}. \qquad 3.48$$

When the limits are inserted into the first part of Equation 3.48 and it is transformed back into ξ,η, it becomes

$$(\eta - ((H_1(\eta))^{1/2} - \xi_0^{1/2})^2)^{1/2}/(\xi - H_1(\eta))^{1/2}$$

$$-(\eta - (\xi^{1/2} - \xi_0^{1/2})^2)^{1/2}/(\xi - H_1(\eta))^{1/2},$$

since it is zero at the upper limit.

The non-integral parts in Equation 3.47a therefore reduce to

$$(\eta - ((H_1(\eta))^{1/2} - \xi_0^{1/2})^2)^{1/2}(\eta_0/\eta)^{1/2}/(\xi - H_1(\eta))^{1/2}, \qquad 3.49$$

and the integral parts to the integral in Equation 3.48.

The integral in Equation 3.48 is an elliptic integral of the first kind. (See the detailed discussion of elliptic integrals in

Smirnov (1964).) It is evaluated as follows.

Let

$$u = a + 1/t.$$

When this is substituted into the integral in Equation 3.48, it gives

$$- \int dt/[\{(b + a)t + 1\}\{(a - k)t + 1\}\{(k + a)t + 1\}]^{1/2}.$$

(The limits of the integral and the factor $(a - b)/2$ have been omitted.) The roots of the cubic in the denominator of the integrand are

$$\alpha = - 1/(b + a), \beta = - 1/(a - k), \gamma = - 1/(k + a),$$

where $\gamma > \alpha > \beta$. [a] Now let

$$t = \beta + (\alpha - \beta)\sin^2\vartheta.$$

When this is substituted into the above integral, it gives

$$2(\alpha\beta\gamma/(\beta - \gamma))^{1/2} \int d\vartheta/(1 - k_1^2\sin^2\vartheta)^{1/2},$$

where

$$k_1^2 = (\alpha - \beta)/(\gamma - \beta).$$

This is an elliptic integral of the first kind with modulus k_1.

a The expressions $(b + a) = 2\eta^{1/2}$, $(a - k) = (\eta^{1/2} + \xi_0^{1/2}) - \xi^{1/2}$ and $(k + a) = \xi^{1/2} + (\eta^{1/2} + \xi_0^{1/2})$ are positive. But $(k + a) > (a - k)$, therefore $\gamma > \beta$, $(b + a) > (a - k)$, therefore $\alpha > \beta$, and $(b + a) < (k + a)$, therefore $\gamma > \alpha$. Therefore $\gamma > \alpha > \beta$.

Therefore in terms of ξ,η the integral in Equation 3.48 becomes

$$(\xi_0^{1/2}/(\xi\eta)^{1/4})\int_{\vartheta_2}^{0} d\vartheta/(1 - k_1^2\sin^2\vartheta)^{1/2}, \qquad 3.50a$$

where

$$k_1^2 = ((\xi^{1/2} + \eta^{1/2})^2 - \xi_0)/(4\xi^{1/2}\eta^{1/2}), \qquad 3.51$$

$$\sin^2\vartheta = 2\eta^{1/2}(\xi'^{1/2} - \xi^{1/2}) \times 1/[(\xi^{1/2} + \eta^{1/2} - \xi_0^{1/2})(\xi'^{1/2} - \eta^{1/2} - \xi_0^{1/2})], \qquad 3.52$$

$$\vartheta_2 = \sin^{-1}[2\eta^{1/2}((H_1(\eta))^{1/2} - \xi^{1/2}) \times 1/((\xi^{1/2} + \eta^{1/2} - \xi_0^{1/2})((H_1(\eta))^{1/2} - \eta^{1/2} - \xi_0^{1/2}))]^{1/2}. \qquad 3.53$$

Equation 3.50a can be written

$$(\xi_0^{1/2}/(\xi\eta)^{1/4})F(k_1, \vartheta_2), \qquad 3.50b$$

where $F(k_1, \vartheta_2)$ is an incomplete elliptic integral of the first kind, modulus k_1 and amplitude ϑ_2.

When Equations 3.49 and 3.50b are substituted into Equation 3.47a, the expression for the pressure distribution in Regions 1 and 2 becomes

$$p = (\rho_0 c_0 V/\pi)[(\eta - ((H_1(\eta))^{1/2} - \xi_0^{1/2})^2)^{1/2}(\eta_0/\eta)^{1/2}/(\xi - H_1(\eta))^{1/2} + (\xi_0^{1/2}/(\xi\eta)^{1/4})F(k_1, \vartheta_2)]. \qquad 3.47b$$

In Region 1 $\eta < \eta_0$, and since $(H_1(\eta))^{1/2}$ is always positive, it must be written $(\eta_0^{1/2} - \eta^{1/2})$, from Equation 3.46b. Therefore the first part of Equation 3.47b reduces to zero and, from Equation 3.53, the amplitude of the elliptic integral becomes $\pi/2$. The expression for the pressure distribution in Region 1 is therefore

$$p = (\rho_0 c_0 V/\pi)(\xi_0^{1/2}/(\xi\eta)^{1/4})F(k_1,\pi/2), \qquad 3.54$$

where $F(k_1,\pi/2)$ is a complete elliptic integral of the first kind with modulus k_1.

Pressure Distribution in Region 3

Equations 3.44b and 3.27c give

$$p = (\rho_0 c_0 V/\pi)[\text{Equation 3.47b} - ((\xi^{1/2} - \xi_0^{1/2})/\xi^{1/2})^{1/2}$$
$$+ ((\xi^{1/2} + (H_1[F_1(\xi)])^{1/2} - 2\xi_0^{1/2})/(\xi^{1/2} + (H_1[F_1(\xi)])^{1/2}))^{1/2}$$
$$\times dH_1[F_1(\xi)]/d\xi$$
$$- \int_{H_1[F_1(\xi)]}^{\xi} (1/2)(\xi_0/\xi)^{1/2} d\xi'/((\xi^{1/2} + \xi'^{1/2} - 2\xi_0^{1/2})^{1/2} \times (\xi^{1/2} + \xi'^{1/2})^{3/2})]. \text{ a} \qquad 3.55a$$

In Region 3 $F_1(\xi) < \eta_0$, and since $(H_1\ F_1(\xi)\ )^{1/2}$ is always positive, it must be written $(\eta_0^{1/2} - (F_1(\xi))^{1/2})$, from Equation 3.46c. But $(F_1(\xi))^{1/2}$ is always positive, and since $\xi > \xi_0$

a The integrand in the second integral in Equation 3.44b has been written $((\xi^{1/2} + \xi'^{1/2} - 2\xi_0^{1/2})/(\xi^{1/2} + \xi'^{1/2}))^{1/2}$.

in this region, it must be written $(\xi^{1/2} - \xi_0^{1/2})$, from Equation 3.45c, where ξ' has been put equal to ξ. Therefore the third term in Equation 3.55a reduces to zero.

The integral can be simplified by making the substitutions

$$u = \xi'^{1/2},\ k = \xi^{1/2},\ a = \eta^{1/2} + \xi_0^{1/2},\ b = \eta^{1/2} - \xi_0^{1/2}.$$

It becomes

$$\int 2u\,du/[(k - (a - b) + u)^{1/2}(k + u)^{3/2}].$$

(The factor $-(1/2)(\xi_0/\xi)^{1/2}$ and the limits have been omitted.) This can be simplified further with the substitution

$$u = -k + 1/t.$$

It becomes

$$\int 2(kt - 1)dt/[t((b - a)t + 1)^{1/2}].$$

The two parts of this integral are easily integrated to give

$$(4k/(b - a))((b - a)t + 1)^{1/2} + 4\tanh^{-1}((b - a)t + 1)^{1/2}.$$

(The second part is integrated by means of the substitution $z^2 = (b - a)t + 1$.) When this expression is transformed back into coordinates ξ,η and the limits are inserted, the integral term in Equation 3.55a becomes

$$((\xi^{1/2} - \xi_0^{1/2})/\xi^{1/2})^{1/2}$$
$$- ((\xi^{1/2} + (H_1[F_1(\xi)])^{1/2} - 2\xi_0^{1/2})/(\xi^{1/2} + (H_1[F_1(\xi)])^{1/2}))^{1/2}$$
$$- 2(\xi_0/\xi)^{1/2}\tanh^{-1}((\xi^{1/2} - \xi_0^{1/2})/\xi^{1/2})^{1/2}$$

$$+ 2(\xi_0/\xi)^{1/2}\tanh^{-1}$$

$$((\xi^{1/2} + (H_1[F_1(\xi)])^{1/2} - 2\xi_0^{1/2})/(\xi^{1/2} + (H_1[F_1(\xi)])^{1/2}))^{1/2}.$$

In this expression the second and fourth terms are zero, as discussed above, the first term cancels with the second term in Equation 3.55a, so that finally the pressure distribution in Region 3 is given by

$$p = (\rho_0 c_0 V/\pi)[\text{Equation 3.47b}$$

$$- 2(\xi_0/\xi)^{1/2}\tanh^{-1}((\xi^{1/2} - \xi_0^{1/2})/\xi^{1/2})^{1/2}].$$

3.55b

The equations for the pressure distribution can be simplified by introducing the non-dimensional quantities

$$P = p/(\rho_0 c_0 V),\ X = \xi/\xi_0,\ Y = \eta/\eta_0.$$

In terms of these variables the pressure distribution in Region 1 is

$$P = (1/\pi)(1/(XY)^{1/4})F(k_1, \pi/2), \qquad 3.56a$$

the pressure distribution in Region 2 is

$$P = (1/\pi)[(4(Y^{1/2} - 1)/(X - Y - 1 + 2Y^{1/2}))^{1/2}(1/Y^{1/2})$$

$$+ (1/(XY)^{1/4})F(k_1, \vartheta_2)\ ], \qquad 3.57a$$

and the pressure distribution in Region 3 is

$$P = (1/\pi)[\text{Equation 3.57a} - (2/X^{1/2})\tanh^{-1}(1 - (1/X^{1/2}))^{1/2}],$$

3.58a

where

$$k_1 = (1/2)\,[((X^{1/2} + Y^{1/2})^2 - 1)/(X^{1/2}Y^{1/2})]^{1/2}, \qquad 3.59a$$

$$\vartheta_2 = \sin^{-1}[Y^{1/2}(1 + X^{1/2} - Y^{1/2})/(X^{1/2} + Y^{1/2} - 1)]^{1/2}. \qquad 3.60a$$

If the non-dimensional quantities x_1' and t_1' are defined

$$x_1' = x_1/x_c = x_1/(RV/c_0),\quad t_1' = t_1/t_c = t_1/[RV/(2c_0^2)],$$

the transformation equations become

$$X = (1/4)(t_1' + 1 - 2x_1'),\quad Y = (1/4)(t_1' + 1 + 2x_1').$$

The equations for the pressure distribution in the three regions, written in terms of x_1' and t_1', are shown in Table 3.1. Graphs of P versus x_1' at various t_1' are shown in Fig. 3.18, and of P versus t_1' at various x_1' in Fig. 3.19. (The elliptic integral was evaluated from tables in the book by Abramowitz and Stegun (1965).) Before these results are discussed, the geometry of the impact will be examined in more detail.

The equation of the contact edge and the equations of the characteristic lines between the various regions in the x-t plane can be written in terms of either $X' = \xi'/\xi_0$, $Y' = \eta'/\eta_0$ or $x' = x/x_c = x/(RV/c_0)$, $t' = t/t_c = t/[RV/(2c_0^2)]$. These equations are listed in Table 3.2 and illustrated in Fig. 3.20.

A graph of dx'/dt' versus x' is shown in Fig. 3.21. When $x' > 2$, that is when the edge of the drop is almost half way across Region 2, it can be seen that the edge of the drop is moving out across the surface of the solid at an almost constant velocity. The flow should therefore begin to approach a steady state in this region.

Table 3.1

The Impact Pressure Distribution

$P = p/(\rho_0 c_0 V)$, $x_1' = x_1/x_c = x_1/(RV/c_0)$, $t_1' = t_1/t_c = t_1/(RV/(2c_0^2))$.

Region 1

$$P = (1/\pi)\left(2/\left((t_1' + 1)^2 - (2x_1')^2\right)^{1/4}\right)F(k_1, \pi/2). \qquad 3.56b$$

Region 2

$$P = (1/\pi)\left[\left(2\left(2 - (t_1' + 1 + 2x_1')^{1/2}\right)/(x_1' + 1 - (t_1' + 1 + 2x_1')^{1/2}\right)\right)^{1/2} \times 2/(t_1' + 1 + 2x_1')^{1/2} + \left(2/\left((t_1' + 1)^2 - (2x_1')^2\right)^{1/4}\right)F(k_1, \vartheta_2)\right]. \qquad 3.57b$$

Region 3

$$P = (1/\pi)\left[\text{Equation 3.57b} - \left(4/(t_1' + 1 - 2x_1')^{1/2}\right)\tanh^{-1}\left(1 - 2/(t_1' + 1 - 2x_1')^{1/2}\right)^{1/2}\right]. \qquad 3.58b$$

In these equations

$$k_1 = \left[(1/2)\left(1 + (t_1' - 1)/\left((t_1' + 1)^2 - (2x_1')^2\right)^{1/2}\right)\right]^{1/2}, \qquad 3.59b$$

$$\vartheta_2 = \sin^{-1}\left[(1/2)\left((t_1' + 1 + 2x_1')^{1/2}\left(2 + (t_1' + 1 - 2x_1')^{1/2} - (t_1' + 1 + 2x_1')^{1/2}\right)\right) \times 1/\left((t_1' + 1 - 2x_1')^{1/2} + (t_1' + 1 + 2x_1')^{1/2} - 2\right)\right]^{1/2}. \qquad 3.60b$$

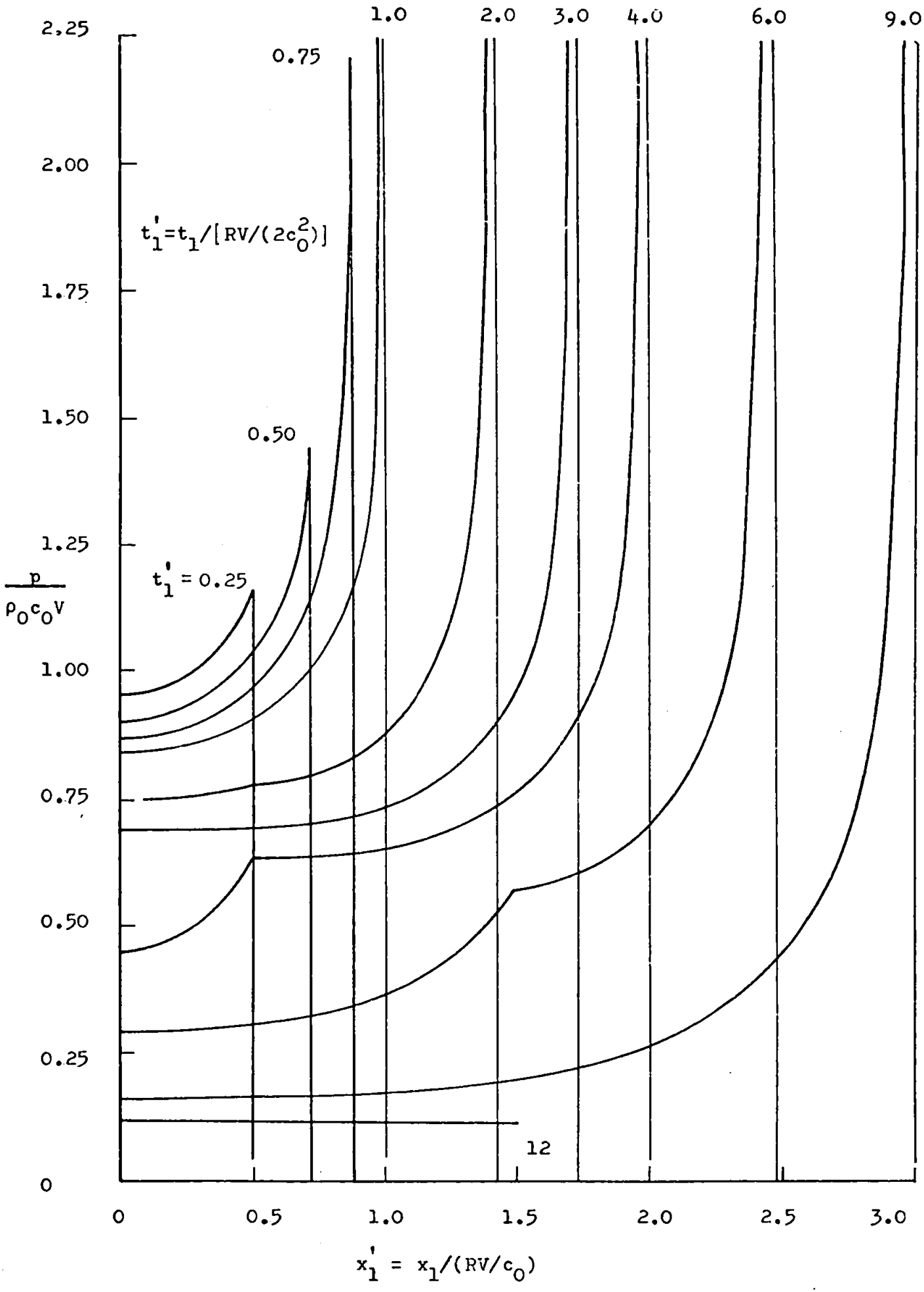

Fig. 3.18 Impact pressure distribution under a cylindrical liquid drop at several times after impact.

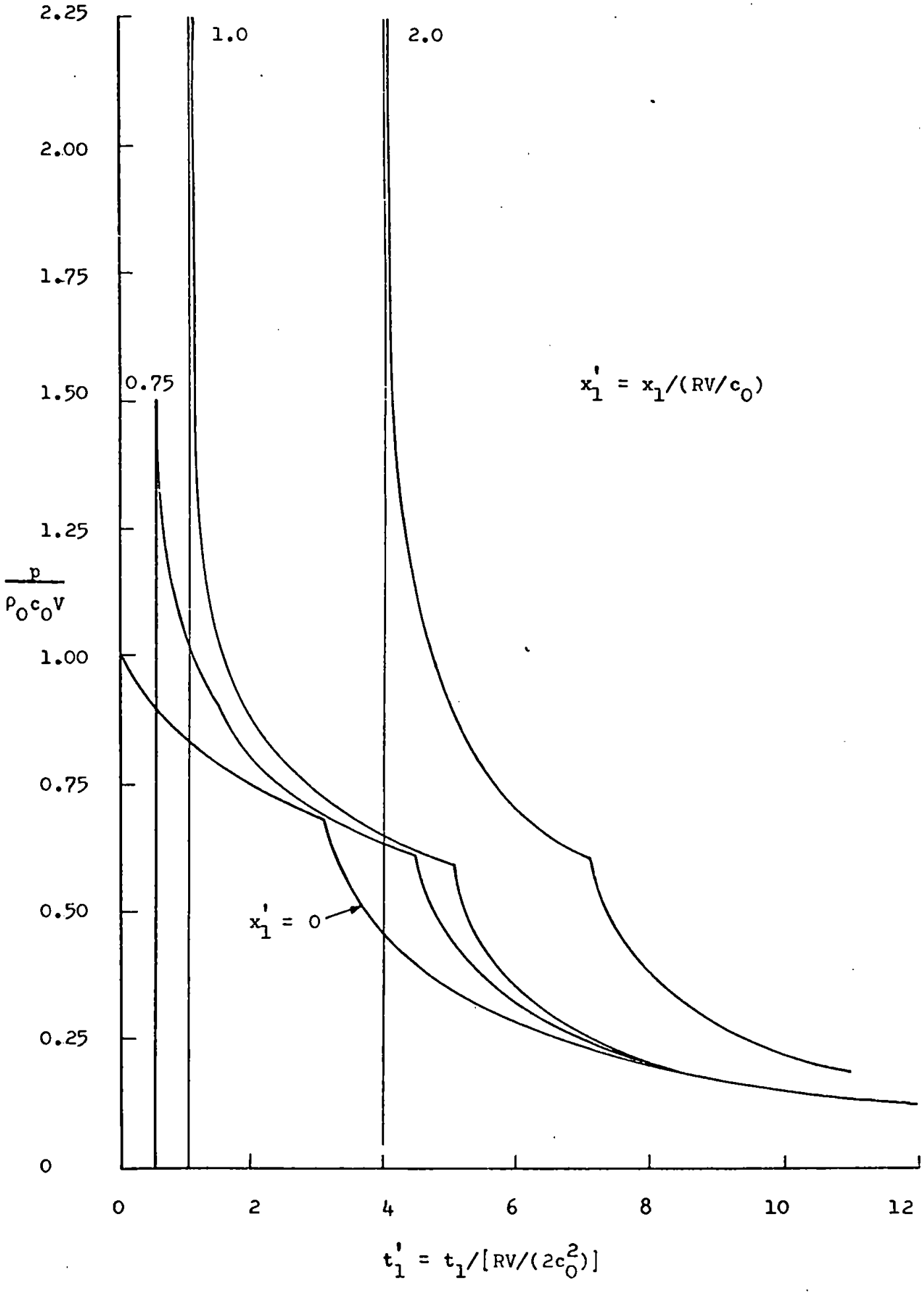

Fig. 3.19 Impact pressure under a cylindrical liquid drop at several places on the contact surface.

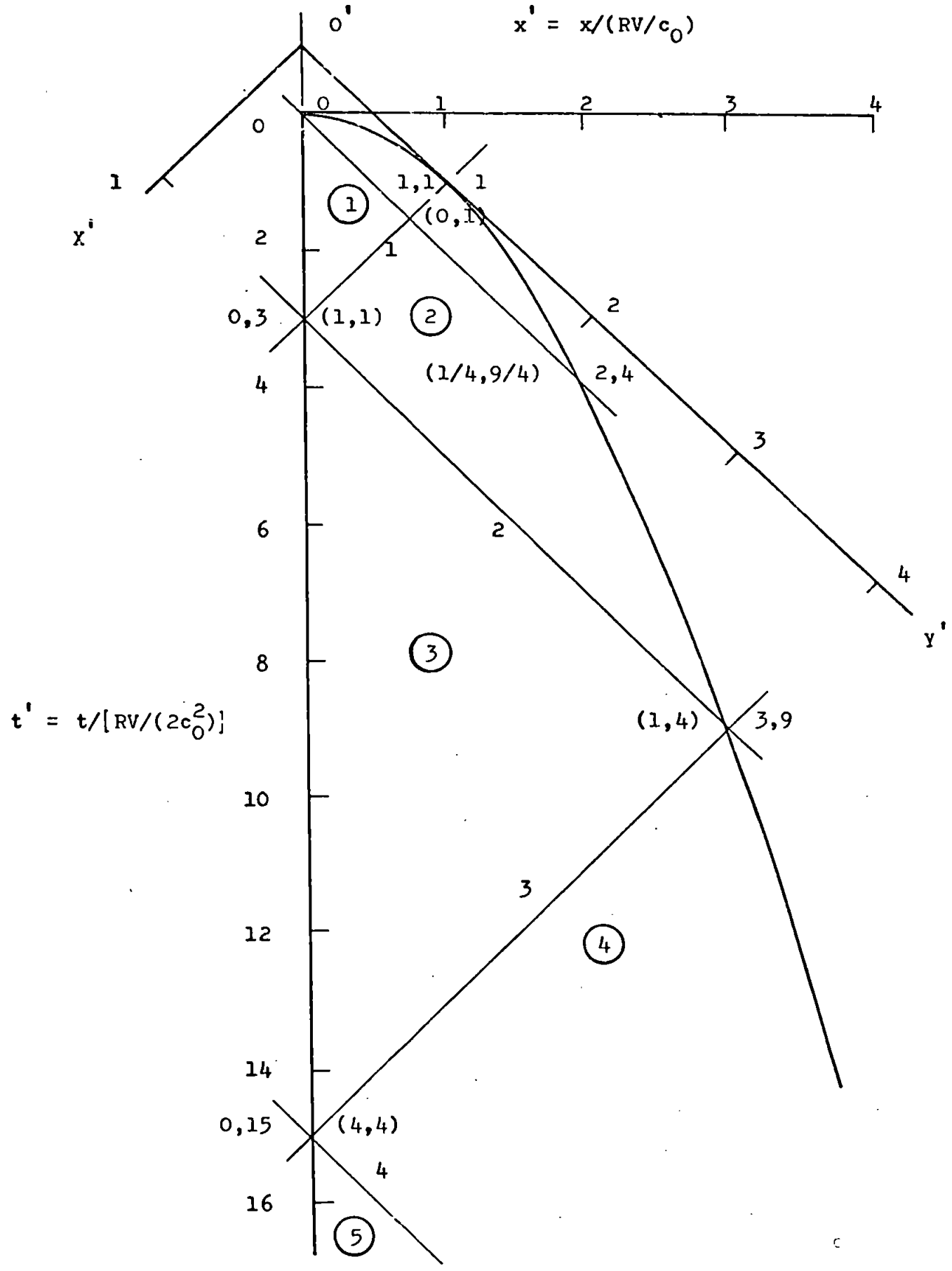

Fig. 3.20 Characteristics in the x'-t' plane. The coordinates of points where the characteristics intersect the curve describing the liquid-solid boundary are given with respect to both x', t' and the non-dimensional characteristic coordinates X', Y' (in brackets).

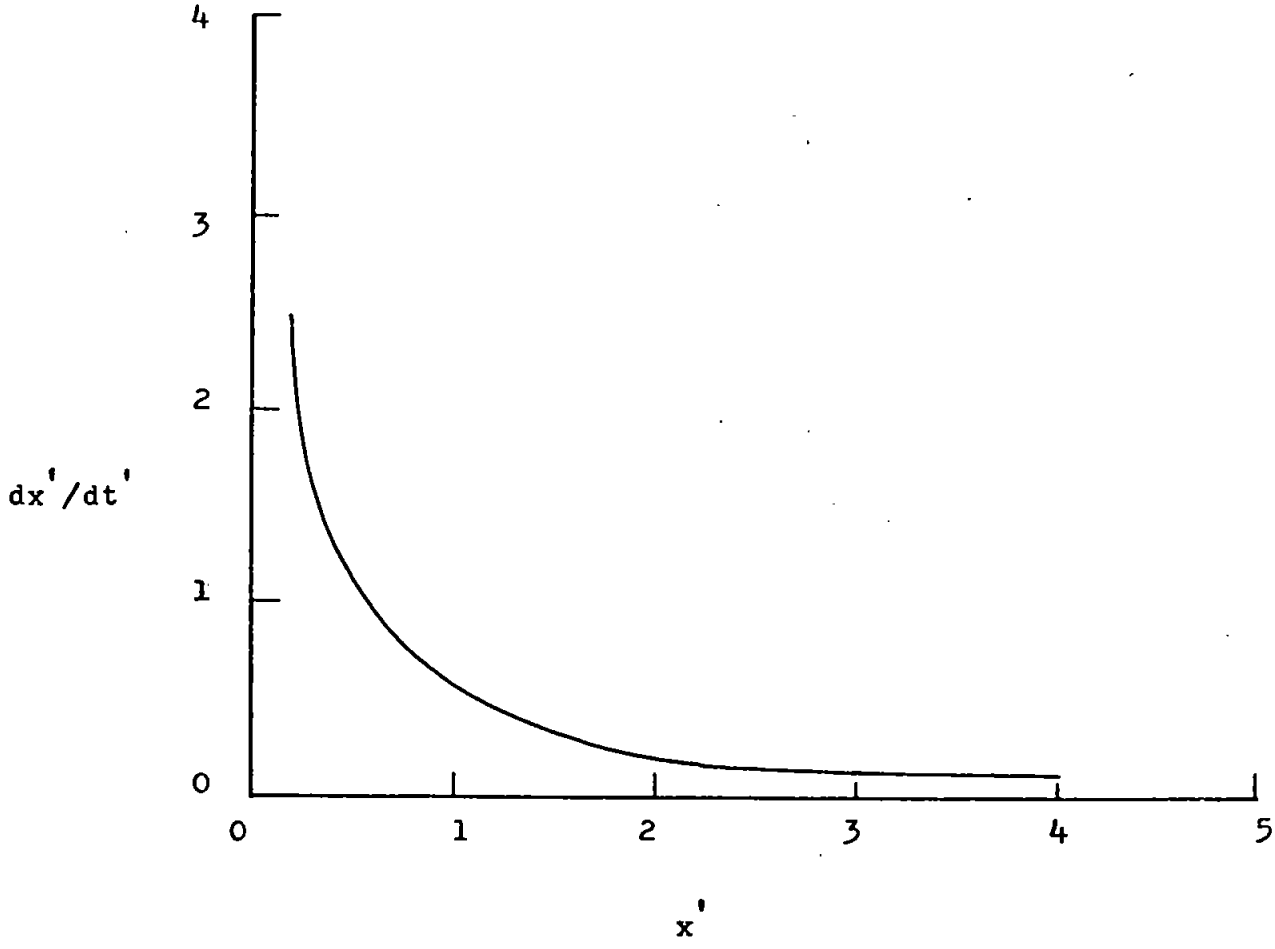

Fig. 3.21 dx'/dt' versus x'.

Table 3.2

Equations of the Contact Edge and the Characteristic Lines

	x',t'	X',Y'
Contact Edge	$x'^2 = t'$	$X' = (1 - Y'^{1/2})^2$
Line between Regions 1 and 2 (1)	$x' = (1/2)(3 - t')$	$Y' = 1$
Line between Regions 2 and 3 (2)	$x' = (1/2)(t' - 3)$	$X' = 1$
Line between Regions 3 and 4 (3)	$x' = (1/2)(15 - t')$	$Y' = 4$
Line between Regions 4 and 5 (4)	$x' = (1/2)(t' - 15)$	$X' = 4$

The numbers in brackets refer to the lines in Fig. 3.20.

3.3.6 Discussion on the Impact Pressure Distribution

Figs. 3.12 and 3.20 show what is happening along the surface of contact at any time during the impact. Disturbances travel along characteristic lines parallel to OA and OG. In Region 1 the velocity at a point on the edge of contact is greater than the velocity at which disturbances are propagated along the characteristics. An observer travelling with a disturbance along a characteristic line would think that this region was unbounded. However, the edge of contact is decelerating and at point A, where the characteristic

OA is tangent to the path of the edge of contact, its velocity is equal to the velocity at which disturbances are propagated through the fluid. A relief wave travels along AJ, informing the fluid that an edge has been reached. At the same time a wave starts out from the other edge at point G and travels along GC. Region 2 is bounded by these lines and the path of the contact edge; it describes conditions at any point along the surface of contact between the edge of the drop and the front of the advancing relief wave before the arrival of the wave from the opposite edge of the drop. The wave initiated at A reaches the opposite edge at J and is reflected back into the drop along the characteristic JM. At the same time the wave initiated at G reaches C and is reflected along the characteristic CM. Region 3 is bounded by the path of the relief wave and the path of its reflection in the edge of the drop. At any point along the contact surface the calculations have been terminated when the relief wave returns after reflection in the edge of the drop.

To fix ideas in the physical space, the wave geometry within a drop at three times after impact is illustrated in Fig. 3.22. The drawing represents a 5.0 mm diameter water drop that strikes a rigid plane surface at a velocity of 100 m/s. The wave-fronts are the envelopes of wavelets centred on the place where they were initiated. (This is Huyghens' construction.) In (a) $t_1 = t_c$ and the compression wave is about to detach from the edge of the drop. In (b) $t_1 = 3t_c$ and the relief wave from the edge has just reached the centre of the drop. In (c) $t_1 = 6t_c$ and the relief wave has passed through the centre of the drop, where it began to interfere with the relief wave from the opposite edge. The relief wave will reach the edge of the drop at a time $t_1 = 9t_c$. (See Fig. 3.20.)

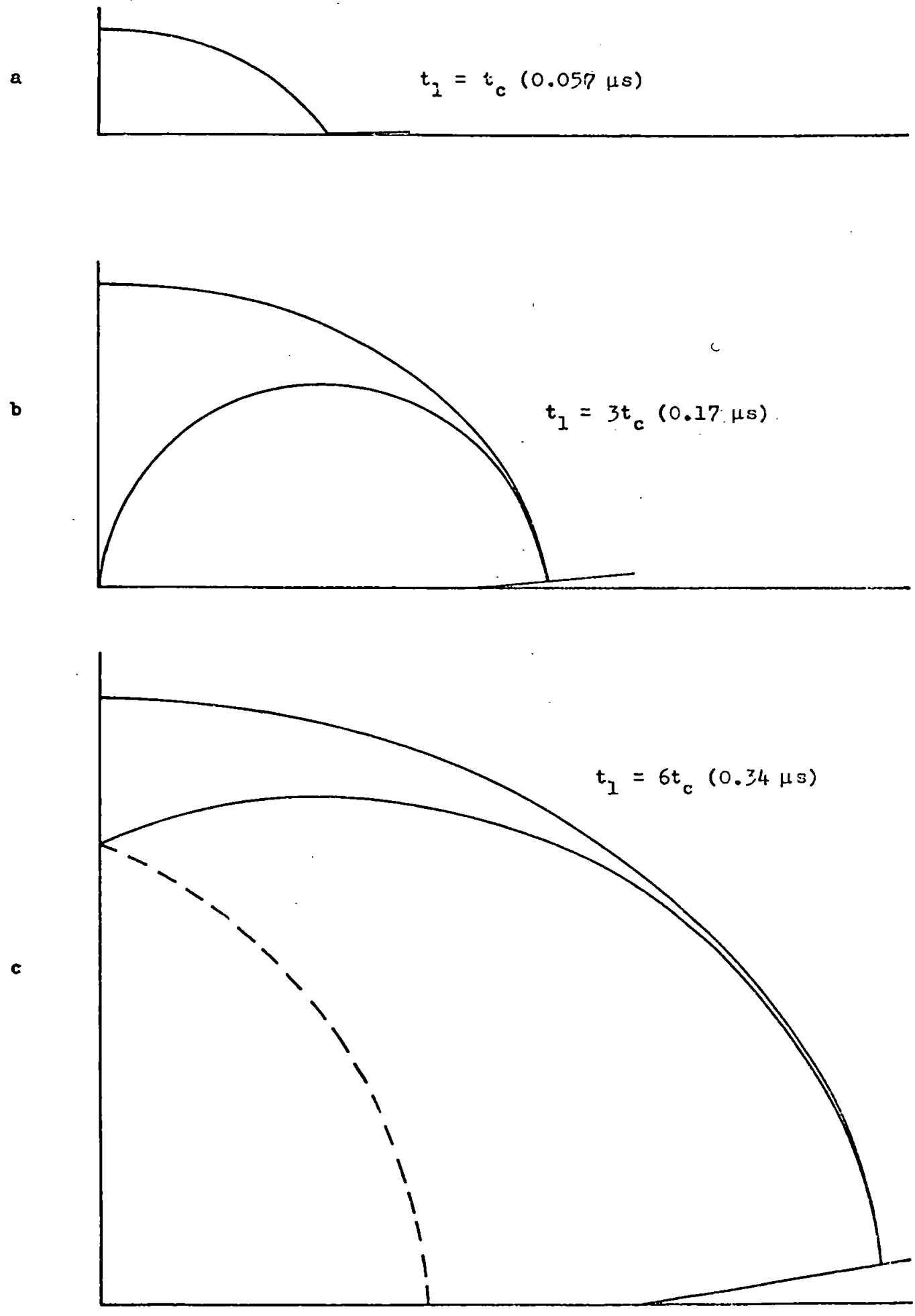

Fig. 3.22 Pressure wave geometry when a 5.0 mm diameter water drop strikes a plane rigid surface at 100 m/s. (It is 250 times actual size.)

Since it is a tensile pulse it will reflect in the free edge of the drop as a pulse of compression. As it passes back into the drop it will increase the pressure at any position behind it above that to which it has fallen. Therefore the pressure at any position on the contact surface that corresponds to points in the x-t plane that lie beyond the boundary between Regions 3 and 4 probably fluctuates about a slowly-decreasing low level. This is discussed further below.

In the calculations presented above it was assumed that the position of the edge of the drop during the impact was fixed by the geometry of the flow and was given by Equation 3.1b. But it has been argued that flow from under the edge of the drop will overtake the contact edge at positions and times given by Equations 3.16c and 3.16d respectively. For a water drop it follows from Equation 3.6d that t_e will be greater than $9t_c$ when the impact velocity is less than about 80 m/s. At higher impact velocities than this t_e will be less than $9t_c$, but it can never be less than t_c - see the discussion at the end of Section 3.2. The appearance of a jet from under the edge of the drop would obviously upset the calculations for the impact pressure distribution and it was partly for this reason that the analysis was concluded at points in the x-t plane that lie along the characteristic that divides Regions 3 and 4.

Refer now to Fig. 3.18. The pressure at the centre of the contact surface at the instant of impact is equal to P. As the impact proceeds the pressure rises at the contact edge and falls at the centre. These profiles have similar shapes to those of blast waves in air that move out across the ground from the centre of an

explosion. The main difference between these waves and blast waves is that the magnitude of the pressure at the front of the wave increases as the wave travels through the fluid. The reason for this is that energy is continuously supplied to the fluid as different parts of it are brought into contact with the moving solid. The waves are thus generated as though by a series of explosions set off one after another along the path of the wave. The magnitude of the pulses add together as the wave proceeds through the fluid. [a] At $t_1' = 1$ the pressure is infinite at the edge, and remains so for the rest of the impact. An infinite pressure will not occur in an actual impact, since gross yielding of any real material will occur long before this is reached. The infinity in the pressure is a direct result of the linearisation of the equations of motion, and is analogous to the leading edge singularity that occurs in the theory of thin aerofoils in subsonic flow. In aerofoil theory the singularity is removed by rounding the edge of the wing. The boundary conditions must then be applied off the plane of the wing to give a finite pressure at the leading edge stagnation point. However, the linearised equations cannot be used to obtain the solution in this region because the perturbation in the mean velocity of the flow near the stagnation point cannot be small in comparison with the mean flow velocity.

In the impact problem studied here the expressions for the pressure distribution depicted in the above graph were derived by assuming that the particle velocities imposed on the fluid by

a It is not quite as simple as this in two dimensions, since Huyghens' principle of superposition does not apply. (See Courant and Hilbert (1962).)

the motion of the boundary were small compared with the velocity of sound in the fluid, and changes in both fluid density and sound speed could be neglected. This made it possible to linearise the equation of motion, which was then solved analytically. Since the x-component of particle velocity at the centre of impact is always zero (from symmetry) and the average velocity in the x-direction is zero up to the time when the initial compression wave is released (Section 3.1), it is reasonable to assume that the x-component of particle velocity at any point on the contact surface is zero until that point is reached by the front of the relief wave, which propagates into the drop from the free edge. From the equation of state (Equation 3.21b), it follows that very large changes of pressure mean very large changes of density, which violates one of the assumptions on which the calculations of the impact pressure distribution were based. (The variable sound speed term would have to be retained in the equation for φ_{tt} (Equation 3.30a), and the integral would have to be retained in Bernoulli's equation (Equation 3.27a).) As the relief wave passes through the fluid, the fluid behind it will be free to move out across the surface of the solid, and even at quite low impact velocities particle velocities of a similar magnitude to the sound speed will occur (Section 3.2). Therefore near the edge of the drop high pressures imply either large density changes in the drop or large particle velocities parallel to the surface of the solid, so that in this zone the full non-linear equations must be solved to get the correct pressure distribution. As mentioned previously, there does not appear to be an analytical method of solving the non-linear equations, and the numerical methods that have been tried give pressure distributions that decrease towards the edge of the drop

(Huang et al (1971)), in contrast to those given by the linearised solution above. Such a trend is not expected and implies that a mistake was made when the numerical scheme was set up. (This is discussed in detail by Rochester (1977a).)

In Fig. 3.19, P versus t_1' curves are shown for four positions under the drop. Changes of slope occur at times which correspond to points in the x'-t' plane which lie on the characteristic lines. Towards the end of the period for which results have been obtained, the pressure is more or less the same at all positions under the drop - about 0.1P. This is also shown very clearly in Fig. 3.18, where the curves for times towards the end of the period studied are almost parallel to the x_1'-axis over most of their width. At $x_1' = 0$ there is only one change of slope; it occurs when the relief waves from the edges of the contact surface reach the centre of the drop. At $x_1' = 0.75$ there are two changes of slope; they occur when the relief waves from the edges arrive, the first from the near edge and the second from the far edge of the drop. The change of slope in curves for points on the contact surface beyond $x_1' = 1$ occurs when the relief wave from the edge farthest away from the point arrives. As discussed above, it is probable that the pressure begins to rise again at times beyond those calculated for here. The pressure pulses will therefore have oscillating tails.

More detailed discussion of these curves will be deferred until the results of experiments to measure the impact pressure distribution have been presented.

3.3.7 Impact Pressure Distribution on Curved Surfaces

In a number of practical problems impact takes place not against

a plane surface but against one that is curved. If the surface of the solid over the region of contact between liquid and solid can be assumed to have a constant radius, the impact can be treated as though the solid surface is plane and the radius of the drop is changed from R_l to

$$R = R_l R_s/(R_l + R_s), \qquad 3.61$$

where R_s is the radius of the solid. (Convex surfaces in both liquid and solid are positive.)

3.3.8 Impact Pressure Distribution when the Flow is Incompressible

As the impact proceeds the solution for compressible flow should approach that for incompressible flow, since the pressure waves reflect back and forth within the drop as time passes, evening out any slight changes of density within the fluid. It can be shown that there is little difference between the solutions for times after impact greater than about $5t'$. [1] An interesting application of incompressible flow theory to the problem of wave impacts against sea-walls is given in Appendix 1.

3.4 Summary

A detailed discussion of the impact of a cylindrical liquid drop against a rigid solid has been given. It has been shown that the mean impact pressure under the drop during the early stage of impact is given by the water-hammer equation, and that the duration of the stages of impact at any point increase with the radius of the drop and the impact velocity but decrease with the sound speed in the fluid. Equations for the impact pressure distribution under

the drop have been developed. It has been shown that the pressure at the instant of impact is equal to the water-hammer pressure, and that as the impact proceeds the pressure at the edge of the drop increases above this value and the pressure at the centre falls below it. The shape of the pressure pulses have been related to changes of the wave geometry within the drop. A pictorial summary of the results is given in Fig. 3.23. It remains now to compare the predictions of the theory with experimental results on drop impact.

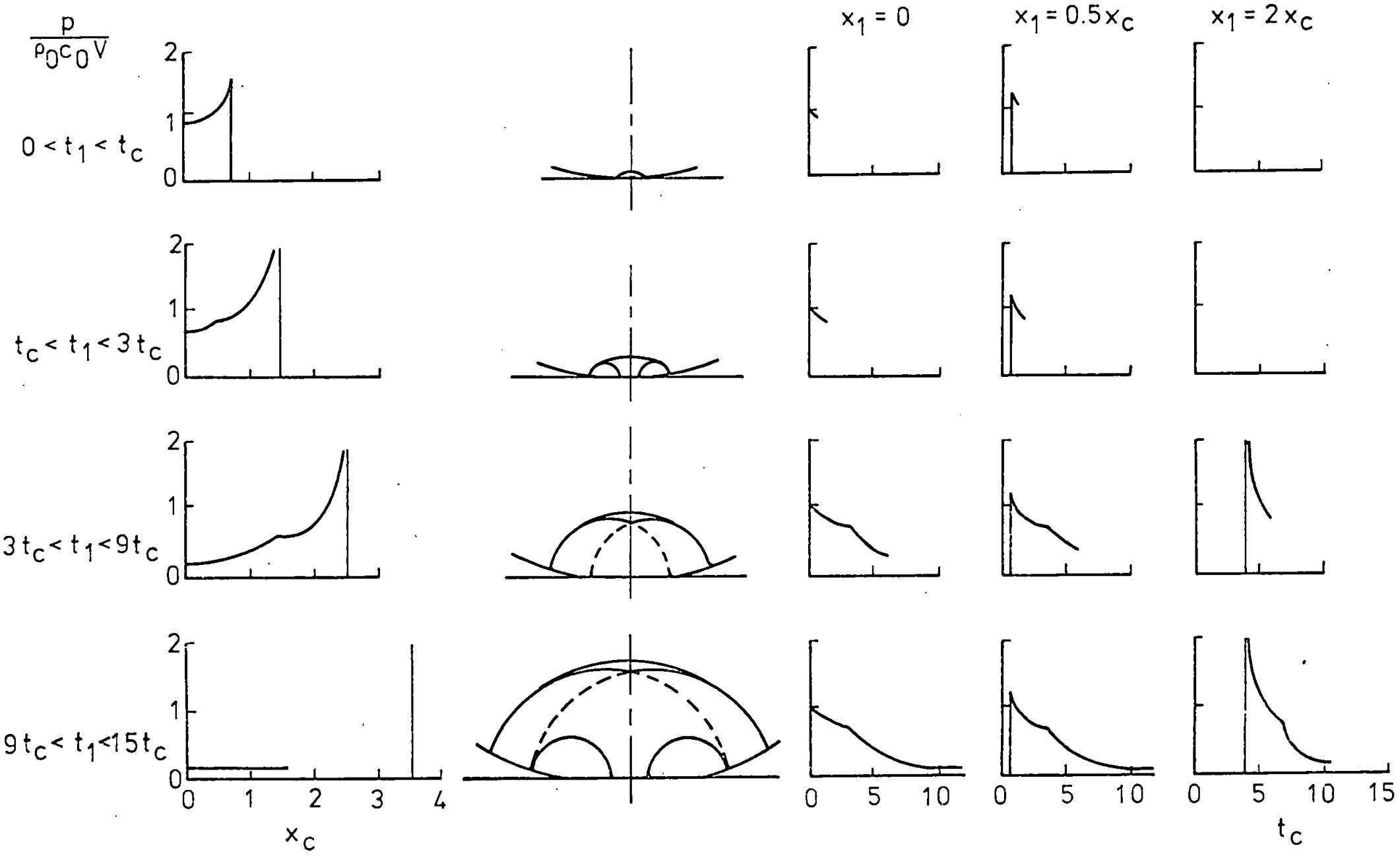

Fig. 3.23 The impact of a cylindrical liquid drop with a plane rigid solid - summary.

Notes on Chapter 3

(1) When the flow is incompressible, the velocity potential satisfies Laplace's equation. The boundary and initial conditions are the same as before. In this note an expression for the pressure at the centre of the contact area is developed. This solution is then compared with the one for compressible flow given above.

For incompressible flow it can be shown that the velocity potential at the centre of the contact area is given by

$$\varphi = (1/\pi) \oint_s \ln(1/r)\varphi_n ds, \qquad 3.(i)$$

where s is the distance around the edge of the drop, φ_n is the velocity normal to the edge of the drop (positive outwards) and r is the distance from the centre of the contact area to a point on the edge of the drop. (This result follows from an application of Green's theorem - see either Courant and Hilbert (1962) or Copson (1975). It is double that given in these works because the impact point lies on the boundary of the drop.)

Outside the contact edge φ_n is zero and over the contact surface it is constant and equal to the impact velocity V, so that Equation 3.(i) becomes

$$\varphi = -(V/\pi) \int_{-(2RVt)^{1/2}}^{(2RVt)^{1/2}} \ln(1/x)dx. \qquad 3.(ii)$$

Equation 3.(ii) is easily integrated to give

$$\varphi = -(2V/\pi)(2RVt)^{1/2}. \qquad 3.(iii)$$

Now $p = -\rho_0\varphi_t$. When φ_t is evaluated from Equation 3.(iii) and substituted into this expression, an equation for the pressure at the centre of the contact area is obtained. It is

$$p/(\rho_0 c_0 V) = (2/\pi)(1/t'^{1/2}). \qquad 3.(iv)$$

Equation 3.(iv) is plotted in Fig. 3.(i), together with the previous result for compressible flow. For incompressible flow the pressure at the instant of first contact is infinite, since deceleration of a finite mass of fluid is assumed to have occurred over an infinitessimally small area. It can be seen that the two solutions are very close to one another for times after impact longer than about $5t'$.

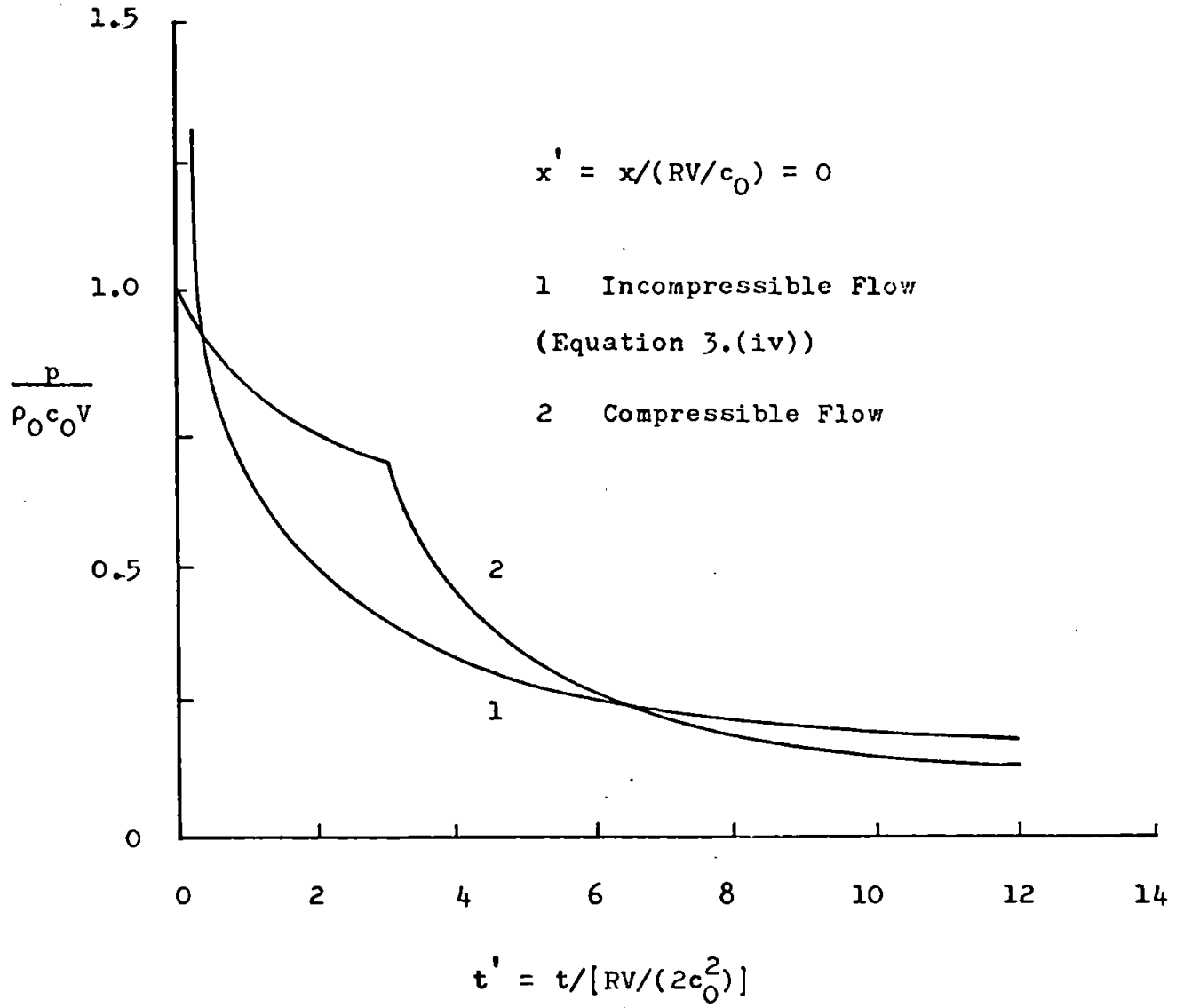

Fig. 3.(i) Impact pressure under a cylindrical liquid drop at the centre of the contact area.

CHAPTER 4

EXPERIMENTAL TECHNIQUES USED IN THE STUDY OF DROP IMPACT

One of the principal aims of the experimental work was to measure the impact pressure distribution under a liquid drop when it collides with a solid. At the start of the project it was hoped that this could be done by firing a liquid jet at a solid which contained a pressure transducer, since a simple technique for producing high velocity liquid jets had already been developed by Brunton (1959) and Bowden and Brunton (1961). This proved to be unfeasible and a new technique, in which a solid containing a small pressure transducer was fired at a stationary liquid drop, had to be developed. Before this method is described the reasons why it was not possible to use the high velocity liquid jets to do the work will be examined.

4.1 High Velocity Liquid Jets

The principle of the method that was used by Bowden and Brunton to produce high velocity liquid jets is illustrated in Fig. 4.1. The liquid is contained in a small steel chamber which is closed at the back with a thin neoprene disc. A slug from an airgun is fired into the back of the chamber whereupon the liquid squirts out of the nozzle at high velocity. (The jet velocity is usually about four times the slug velocity - see Brunton (1959).) A cross-sectional view of a typical chamber is shown in Fig. 4.2, and a photograph of the apparatus is shown in Fig. 4.3.

A shadow picture of a 1.0 mm diameter jet produced by this method is shown in Fig. 4.4. The jet is moving to the right at

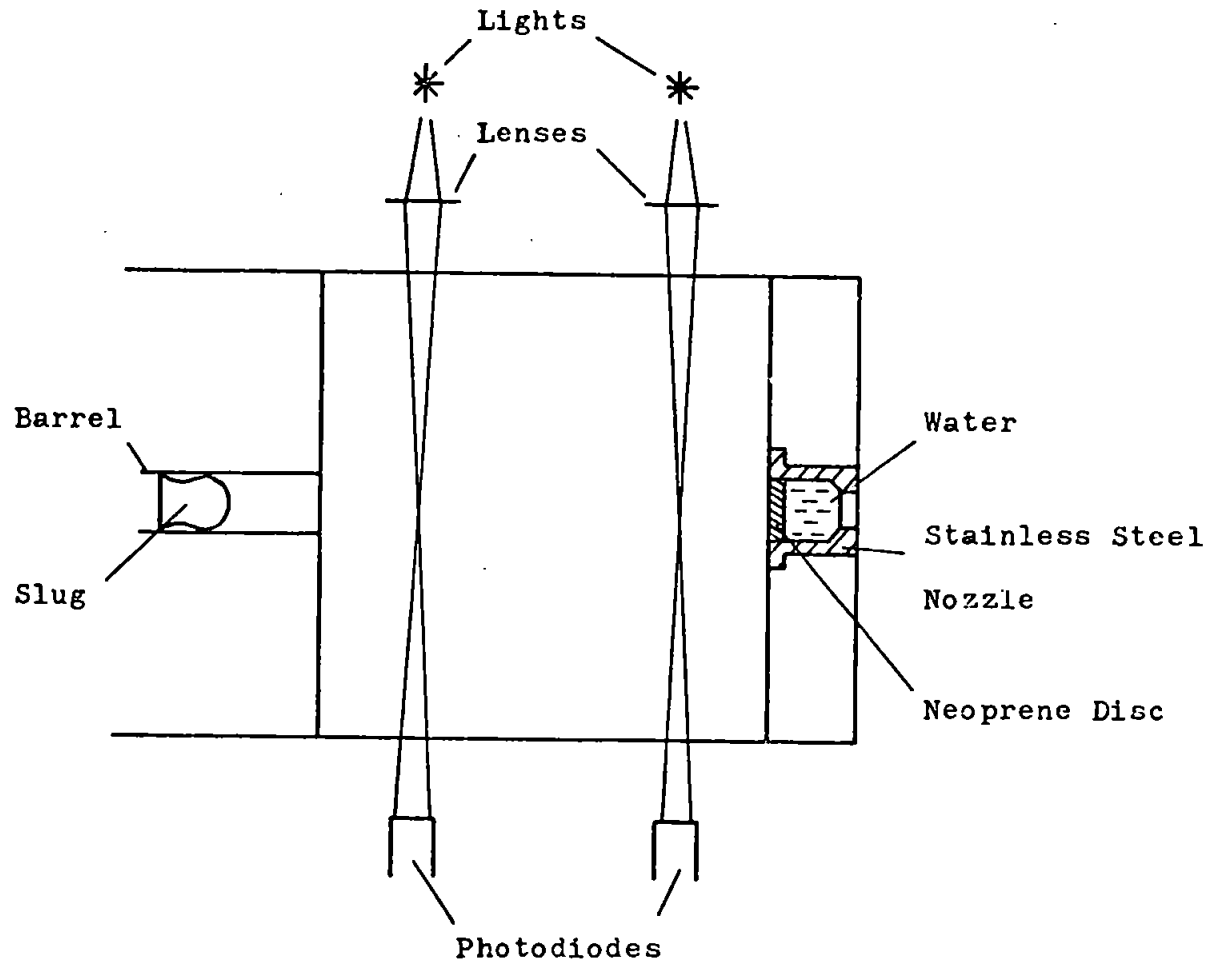

Fig. 4.1 Principle of the method used to produce high velocity liquid jets.

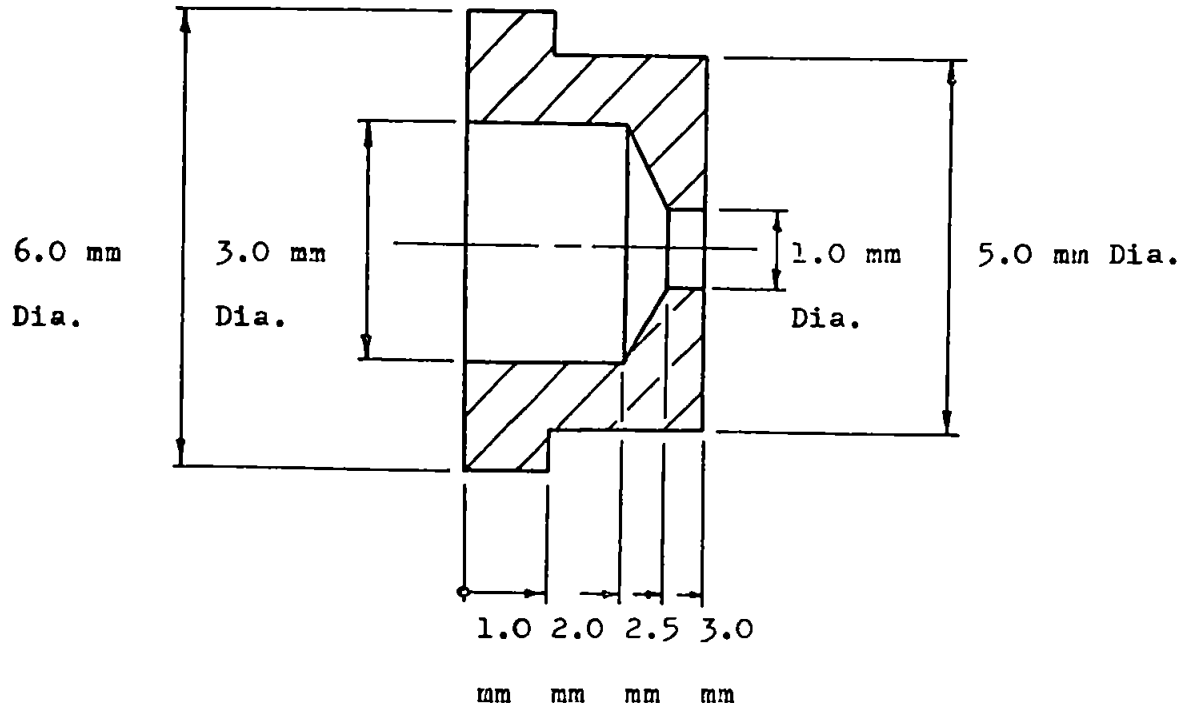

Fig. 4.2 Cross-sectional view of a chamber used in the production of high velocity liquid jets.

Fig. 4.3 (Opposite page, top.) Gun used for the production of high velocity liquid jets.

Fig. 4.4 (Opposite page, middle.) Shadow picture of a 1.0 mm diameter water jet moving through air at 600 m/s.

Fig. 4.5 (Opposite page, bottom.) Shadow pictures of a 1.0 mm diameter water jet striking a thick perspex block at 600 m/s. The time between the frames is 4.2 μs. The water is flowing out across the surface of the block at about 700 m/s.

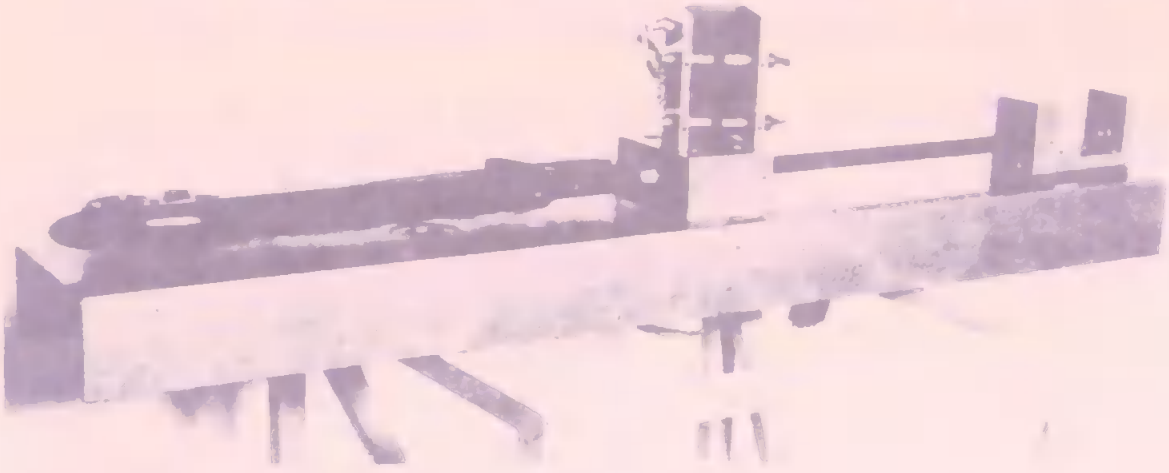

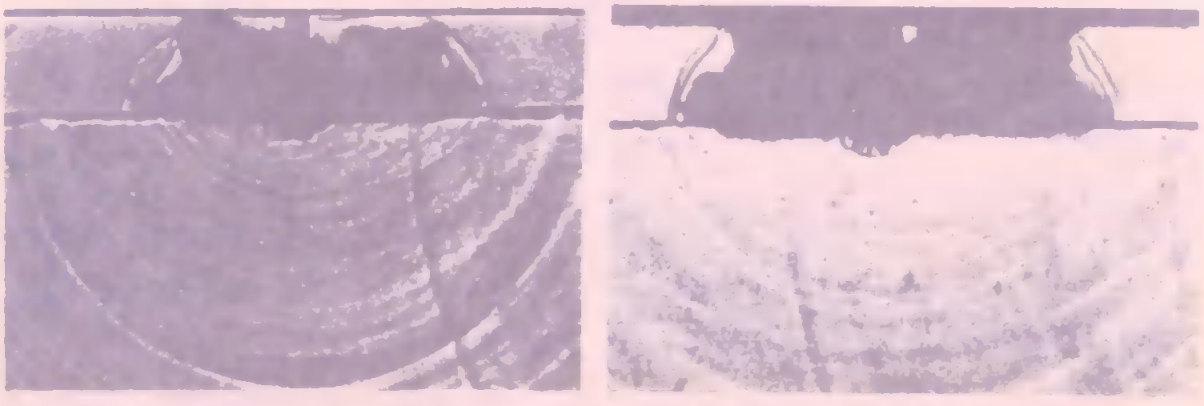

a b

5 mm

about 600 m/s. (This picture is one of a sequence of six. The average time between the frames was 1.8 μs. The velocity was determined by measuring the displacement of the jet head between the first and the fourth frames and dividing the result by the time interval.) The core of the jet is visible at the nozzle outlet. Other pictures have shown that the core remains coherent for very large distances from the nozzle. (For a 1.0 mm diameter water jet stable cores have been photographed at distances greater than 200 mm from the nozzle.) It can be seen that the head of the jet has an irregular shape. This is observed to change as the jet drives through the air, and, at any particular distance from the nozzle, it is found to vary from one jet to another. For these reasons, and also because the flow in the jet head is not known, it was decided that these jets could not be used in experiments to measure the impact pressure distribution.

One further point - the high velocity jets damaged the materials from which the gauges were to be made (tufnol, perspex, quartz and various piezoelectric ceramics) in a single impact. This point is illustrated in Fig. 4.5. This shows two shadow pictures of a 1.0 mm diameter water jet striking the edge of a 6.0 mm thick perspex block at about 600 m/s. The deep pit which was cut in the top surface of the block in the early stages of the impact is clearly visible. A complex system of stress waves can also be seen. The one moving across the block from the right has an average velocity of about 2,100 m/s. It is a longitudinal wave that has been been reflected from the corner of the block. (See Kolsky (1963).)

It was therefore not feasible to measure the pressure

distribution under a drop by firing a jet at a stationary target for the following reasons: (i) low velocity jets could not be produced easily; (ii) control of the jet velocity was not possible; (iii) the shape of the jet head was very irregular and varied from one jet to another; (iv) the flow in the jet head was not known; and (v) high velocity jets damaged gauge materials in a single impact.

There was now only one other way in which the work could be done - the solid would have to be fired at the liquid. This method has been used by a number of investigators to study the way in which the drop behaves during the impact. Fyall (1967) fired projectiles from a gas-powered gun against 2.0 mm diameter water drops at velocities up to 300 m/s; from a series of photographs of the impacts he was able to determine the stage at which flow from under the drop began and to measure the velocities at which the water flowed out across the surface of the solid. Brunton and Camus (1970) and Camus (1971) developed a technique for studying details of the pressure wave structure within a drop during an impact. A cylindrical drop about 5.0 mm in diameter was held between two glass plates and an aluminium projectile was fired between the plates at the drop with detonators. The impact was photographed with a high-speed camera. This method had four limitations: (i) it was difficult to control the velocity of the projectile (the maximum velocity was about 100 m/s); (ii) both the projectile and the impact chamber were damaged in the impact, particularly the back of the plate; (iii) details of the flow were hidden behind the meniscus; and (iv) each experiment took a long time to complete. However it had one advantage over the method that was used by Fyall - the drop could be placed in any

desired position relative to a point on the surface of the projectile. For this reason it was decided to develop the technique further, to use it to measure the pressure distribution under a drop, and, in a parallel series of experiments, to take shadow and schlieren photographs of the impact with a high-speed camera.

4.2 The Basic Experimental Method

4.2.1 Principle of the Method

The method is illustrated in Fig. 4.6a. A thin, oblong-sectioned bullet, 20 mm long, 15 mm wide and 1.5 mm deep, was fired from a special gas-powered gun at a stationary liquid drop held between two perspex windows. A piezoelectric ceramic, about 0.3 mm wide and 0.5 mm deep, was mounted at the front surface of the bullet. The signal generated in the impact was fed into an oscilloscope through an arrangement of sliding contacts between the bullet and the inside surface of one of the windows. The bullet velocity was measured with a photoelectric system. Two photodiodes were mounted 20 mm apart in the side of the barrel about 30 mm in front of the drop. They were illuminated by light beams from small holes in the opposite side of the barrel. Signals produced in the photodiodes when the beams were cut by the leading edge of the bullet operated a digital counter through an amplifier. A photograph of the impact region is shown in Fig. 4.6b.

The shear stress distribution under the drop was measured with an oblong-sectioned gauge in which the ceramic was electroded in such a way that it responded to shear stress only.

The pressure within the drop was measured with a piezoelectric

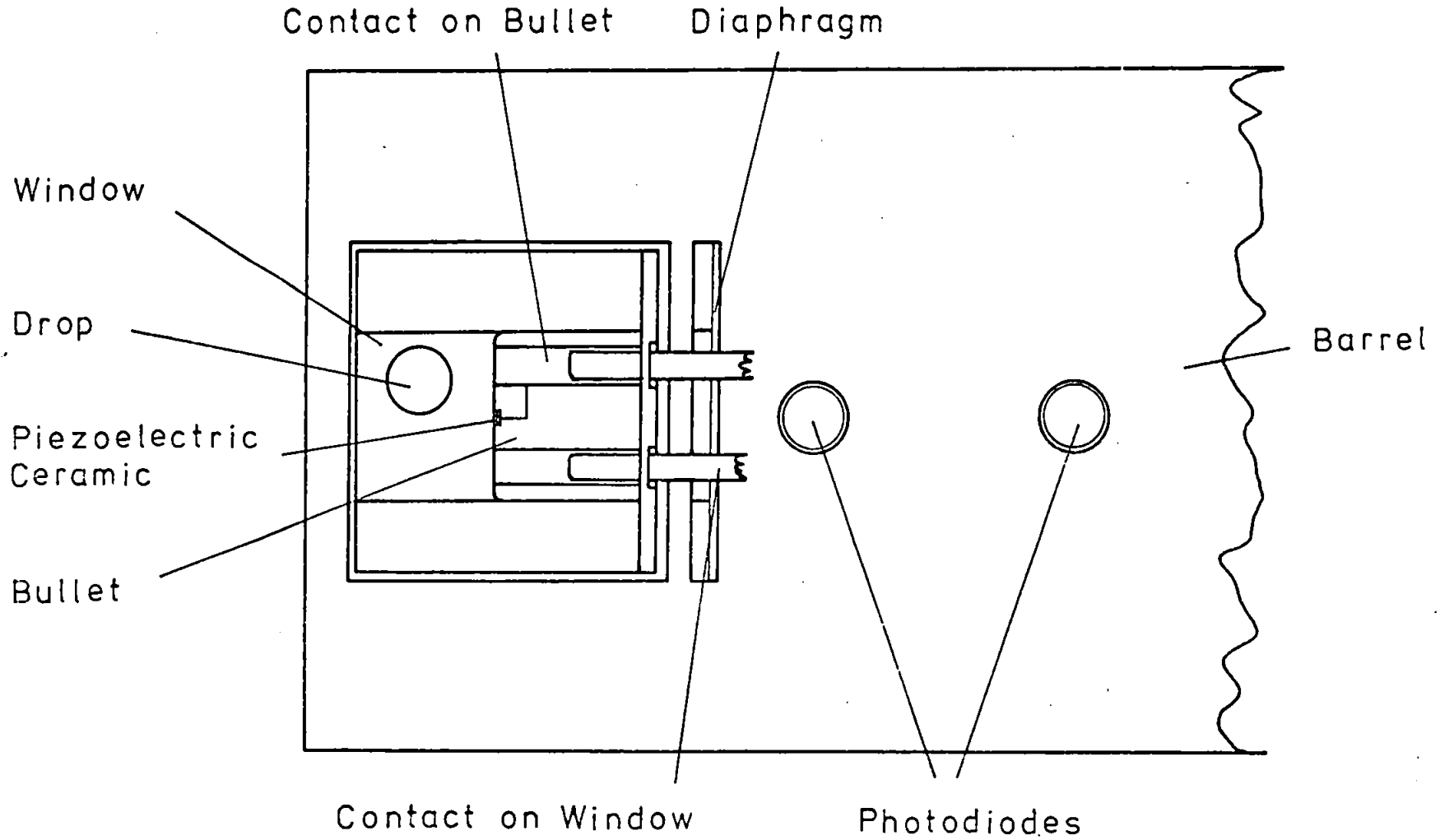

Fig. 4.6a (Above.) Principle of the method used to measure the impact pressure and shear stress distributions under a drop.

Fig. 4.6b (Below.) Detail of the impact region in the working section of the oblong-sectioned barrel.

ceramic mounted in the middle of the inside face of an insulating block. The block replaced one of the windows in the working section of the gun.

Descriptions of the gun and the pickup arrangement are given in Rochester (1977b) and Rochester et al (1977). The gauges are described in Rochester (1977c).

4.2.2 Calibration of the Gauges

The pressure gauges were calibrated by a method similar to that developed by Crook (1952). The gauge was held tightly in a heavy clamp and a steel ball was placed in contact with the ceramic. Another steel ball was swung against this arrangement from a known height and the output from the gauge was displayed on an oscilloscope.

It can be shown that

$$M[2g(h_1 + h_2)]^{1/2} = (2/3)(C/d)V_{max}t, \qquad 4.1$$

where M is the mass of the ball, h_1 is the height from which it falls, h_2 is the height to which it rebounds, g is the acceleration due to gravity, V_{max} is the maximum output of the gauge, t is the duration of the impact, d is the effective piezoelectric constant of the ceramic, and C is the combined capacitance of the ceramic, the pickup, the leads and the oscilloscope input.

M and C were measured and h_2, V_{max} and t were noted for a range of h_1. A graph of $M[2g(h_1 + h_2)]^{1/2}$ versus $(2/3)V_{max}t$ was plotted, from which the effective piezoelectric constant of the ceramic was calculated.

The above procedure was carried out for all the pressure gauges that were used in the experiments. It was repeated after a broken

gauge had been repaired and at the end of a long series of experiments. The effective piezoelectric constant was about 260×10^{-12} C/N.

It can be shown that the pressure on the gauge during an impact is

$$p = CV/(dA), \qquad 4.2$$

where V is the output of the gauge and A is the area of the ceramic.

The area of the ceramic in each gauge was measured and substituted into Equation 4.2 with the values of C and d obtained in the above experiments. The calibration constants for the gauges used in the work, together with the dimensions and surface areas of the ceramics, are given in Table 4.1. (The calibration constant is C/(dA).)

The shear gauge was calibrated with the same apparatus, but this time the impulse was applied to the ceramic as a shear load - a piece of copper, glued to the surface of the ceramic, was struck from the side by the steel ball. The effective piezoelectric constant was calculated in a similar way to that described above. The shear stress on the gauge was found to be

$$\tau = 1.3 \pm 0.1V \quad MN/m^2. \qquad 4.3$$

The stresses measured in the experiments were derived solely from forces on the face of the ceramic. This was established by applying a large force to the surface of the gauge adjacent to the ceramic. The output was only a small fraction of that obtained when the ceramic was loaded directly.

Table 4.1

Specification of the Pressure Gauges Used in the Drop Impact Experiments with the Oblong-Sectioned Gun

Number	Dimensions of Ceramic		Surface Area of Ceramic	Calibration Constant
	Length	Width		
	mm		mm^2	$MN^{-2}V^{-1}$
Flat Bullet Gauges				
1	0.42	0.88	0.46	2.1 ± 0.2
6 (Large hole.)	1.17	0.29	0.34	2.9 ± 0.3
7 (Small hole.)	1.17	0.29	0.34	2.9 ± 0.3
12 *	0.46	0.33	0.15	6.4 ± 0.6
15 *	0.52	0.31	0.16	6 ± 1
Sidewall Gauge				
1	0.42	0.29	0.12	8 ± 2

The gauges marked with an asterik contain a copper backing bar.

In all gauges the ceramic was PZT-4, manufactured by Brush Clevite. The bullets and the housing for the sidewall gauge were made from tufnol, a cloth-laminated plastic manufactured by Tufnol. The numbers refer to a more comprehensive list of gauges in Rochester (1977c). Number 15 flat bullet gauge was made by sandwiching a sheet of duralumin between two sheets of tufnol. The gauges had a rise-time of about 0.1 μs.

Experiments with a pressure gauge mounted in the end-wall of a shock tube showed that there was some overshoot to a step change in pressure. The output signal contained small amplitude oscillations with a frequency of about 5 MHz due to longitudinal vibration of the ceramic plate and very small amplitude oscillations with a frequency of about 10 MHz due to the radial vibration of the plate. It was concluded from this that oscillations on a typical pressure pulse from a drop impact could not have been caused by vibrations of the ceramic, but had to represent changes that had occurred in the liquid during the impact. (See Rochester (1977c).)

4.2.3 Procedure for Doing the Experiments

A photograph of the experimental set-up is shown in Fig. 4.7. The measurements of peak impact pressure and peak shear stress under the drop were made as follows. The gun was clamped on its side and a drop was inserted between the windows at some predetermined position against a graticule. (The gun was clamped on its side to stop the drop sliding about in the impact chamber.) An elastic diaphragm was placed across the barrel through a slit behind the working section to prevent the air blast from disturbing the drop before the bullet arrived. The signal generated in the impact was recorded on the oscilloscope and the time that the bullet took to pass between the photodiodes was registered on the counter. (The trace on the oscilloscope was photographed with a camera mounted in front of the tube.) Four firings were made at each position. The pulse heights were measured and the stresses were calculated. Measurements were made across the drop from - 2.0 mm to 3.5 mm. Between - 0.75 mm and 0.75 mm these were made

Fig. 4.7 Experimental arrangement for measuring the impact pressure distribution under a drop using the gas-powered gun fitted with the oblong-sectioned barrel.

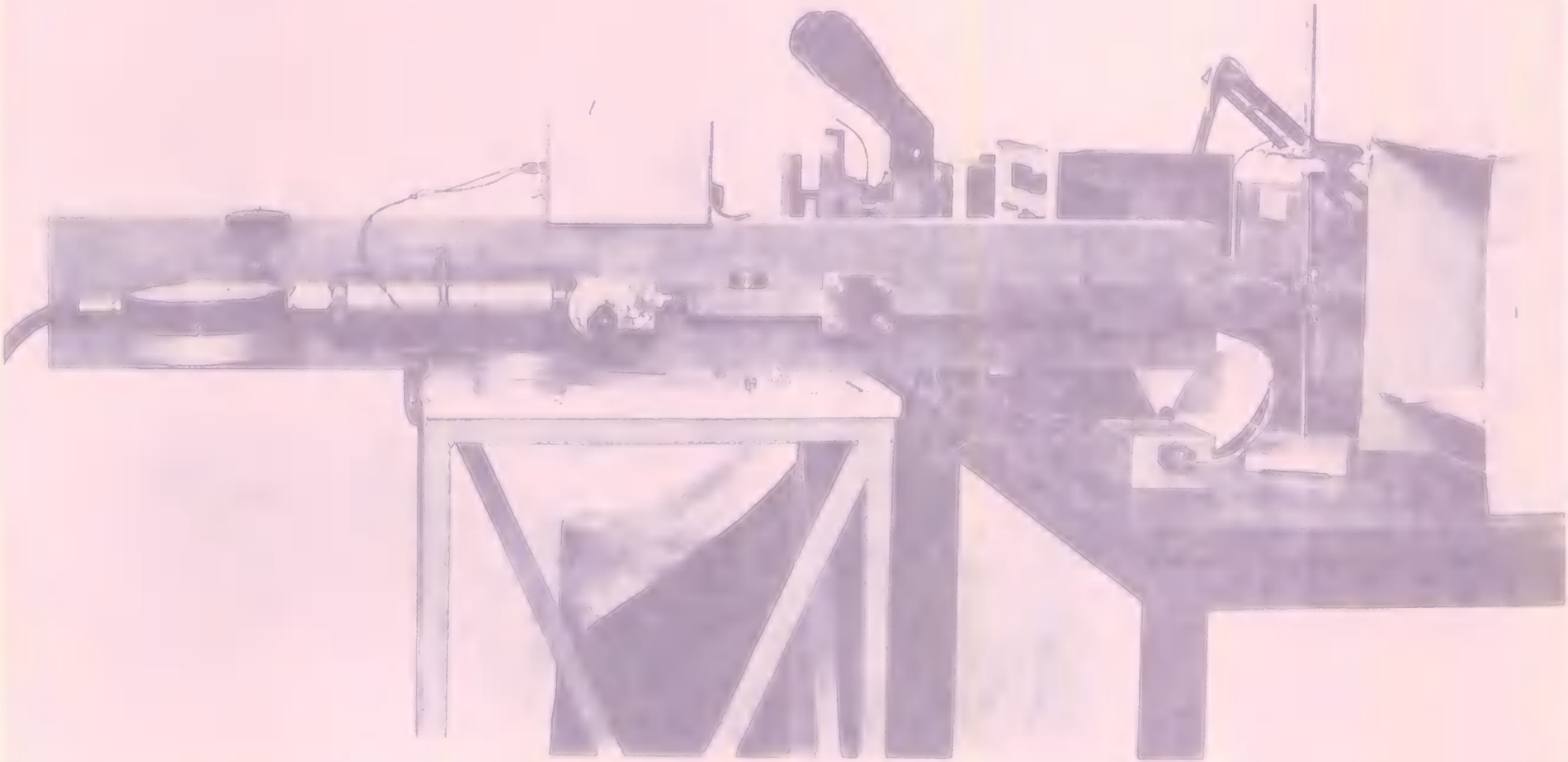

in 0.25 mm steps, and outside this region they were made in 0.5 mm steps.

The measurements of peak pressure within the drop were made in a simialr way. They were made along the central axis of the drop in 0.5 mm steps.

4.2.4 Photographs of the Impact

The impact was photographed in a separate series of experiments with a Cranz-Schardin high-speed camera. A drawing of the optical arrangement that was used in the work is shown in Fig. 4.8, and a photograph of the experimental set-up is shown in Fig. 4.9. A detailed description of the camera is given in Rochester (1977d).

4.3 Further Experimental Methods

It was essential to be able to measure the impact pressure distribution in other ways. For this purpose two independent techniques were developed. The first is illustrated in Figs. 4.10, 4.11a and 4.11b. A cylindrical bullet, 30 mm long and 15 mm in diameter, was fired into the side of a vertical jet of water. A small piezoelectric ceramic was mounted at the front surface of the bullet. As before the signal generated in the impact was picked up by an arrangement of sliding contacts. The pressure was calculated from

$$p = 6.0 \pm 0.6V \quad MN/m^2. \qquad 4.4$$

The second technique is illustrated in Figs. 4.12 and 4.13. The gauge was bolted to the rim of a rotating disc and driven into the side of a vertical jet of water. The signal generated in

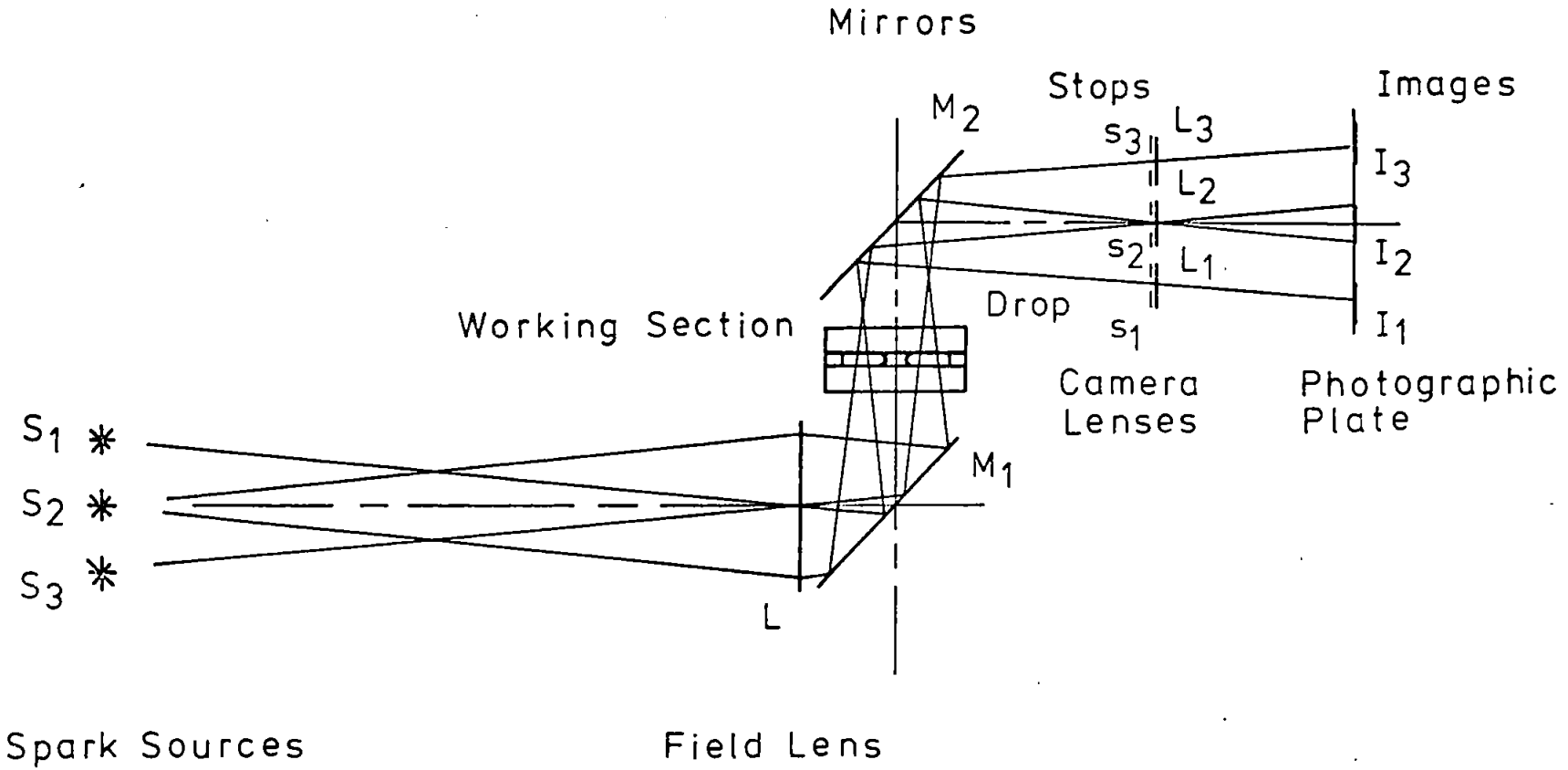

Fig. 4.8 Experimental arrangement for photographing drop impact with the Cranz-Schardin high-speed camera.

Fig. 4.9 (Opposite page, top.) The Cranz-Schardin high-speed camera set up for photographing drop impact.

Fig. 4.14 (Opposite page, bottom.) A typical sequence of shadow pictures taken with the high-speed camera. The average time between the frames is 2.6 μs.

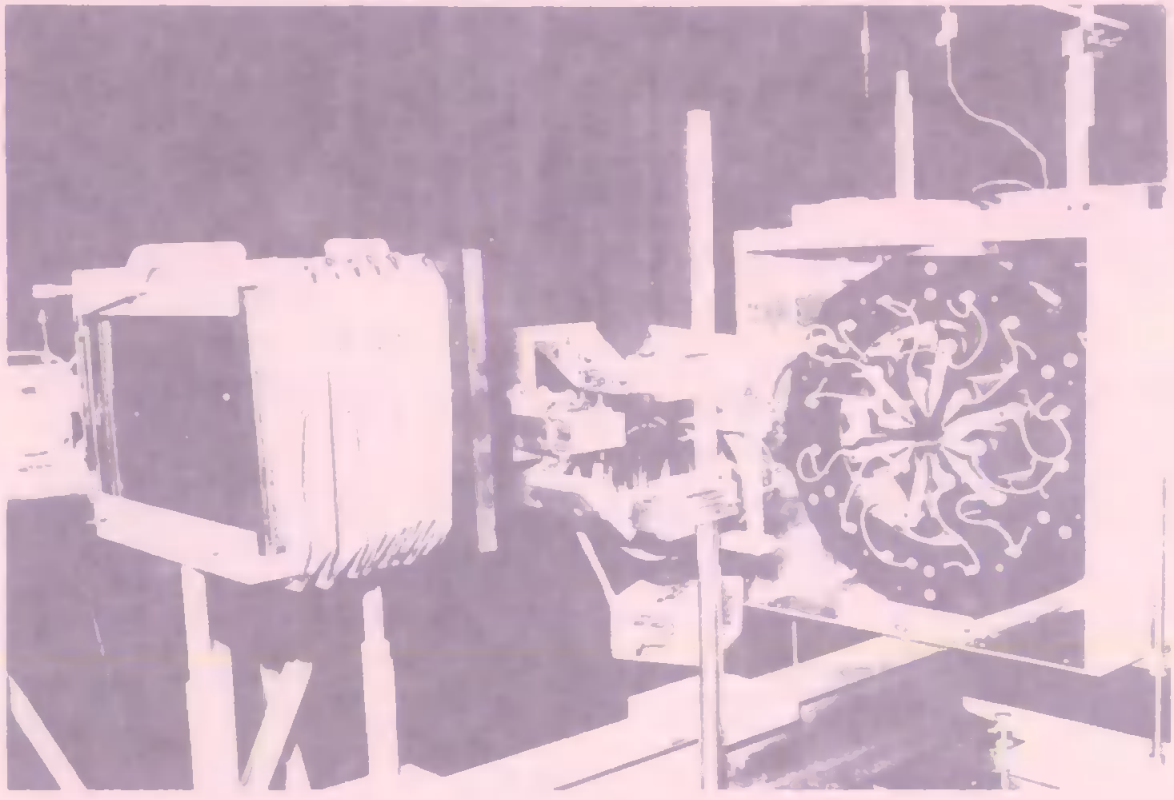

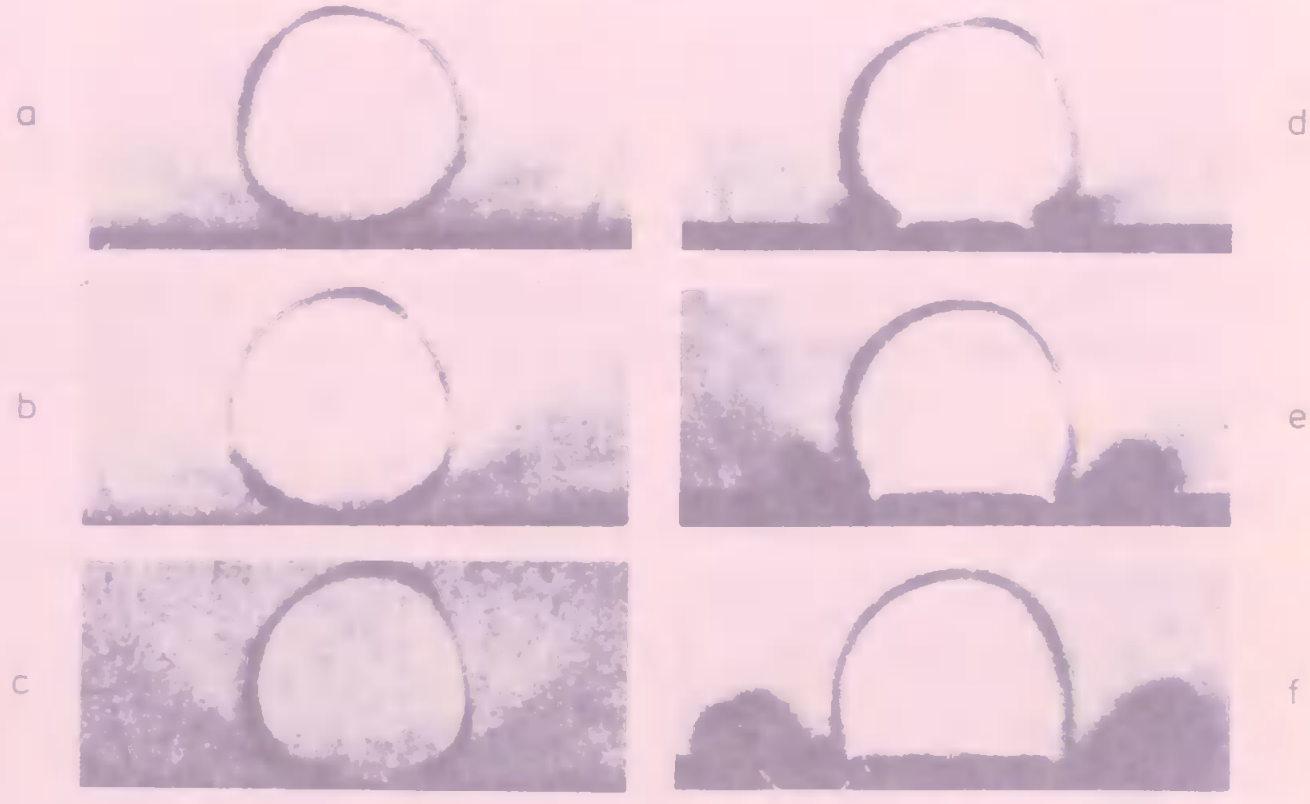

2 mm

Fig. 4.10 Experimental arrangement for measuring the impact pressure distribution under a drop using the gas-powered gun fitted with the cylindrical barrel.

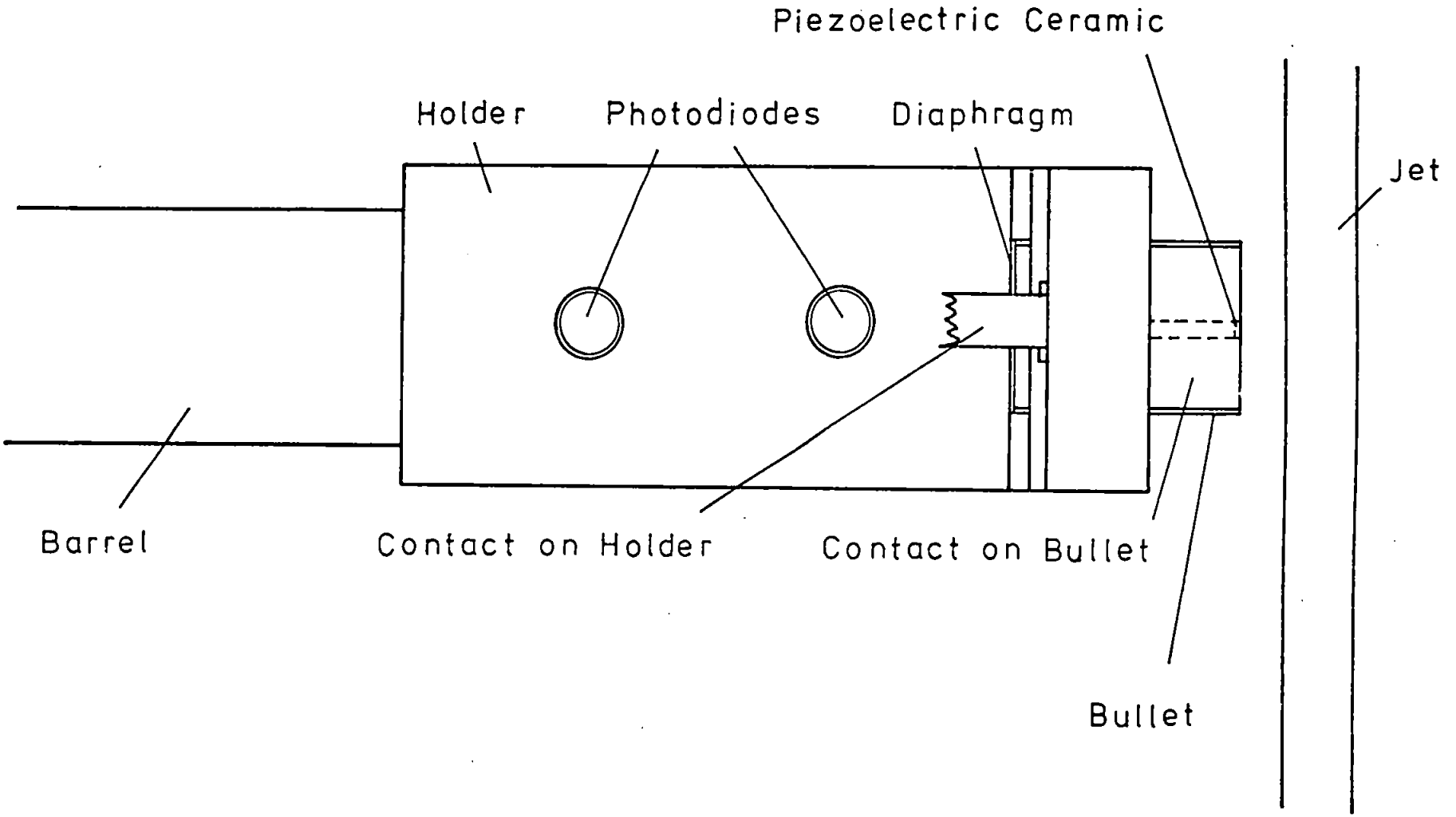

Fig. 4.11a (Above.) Principle of the second method used to measure the impact pressure distribution under a drop.

Fig. 4.11b (Below.) Detail of the impact region at the end of the cylindrical barrel.

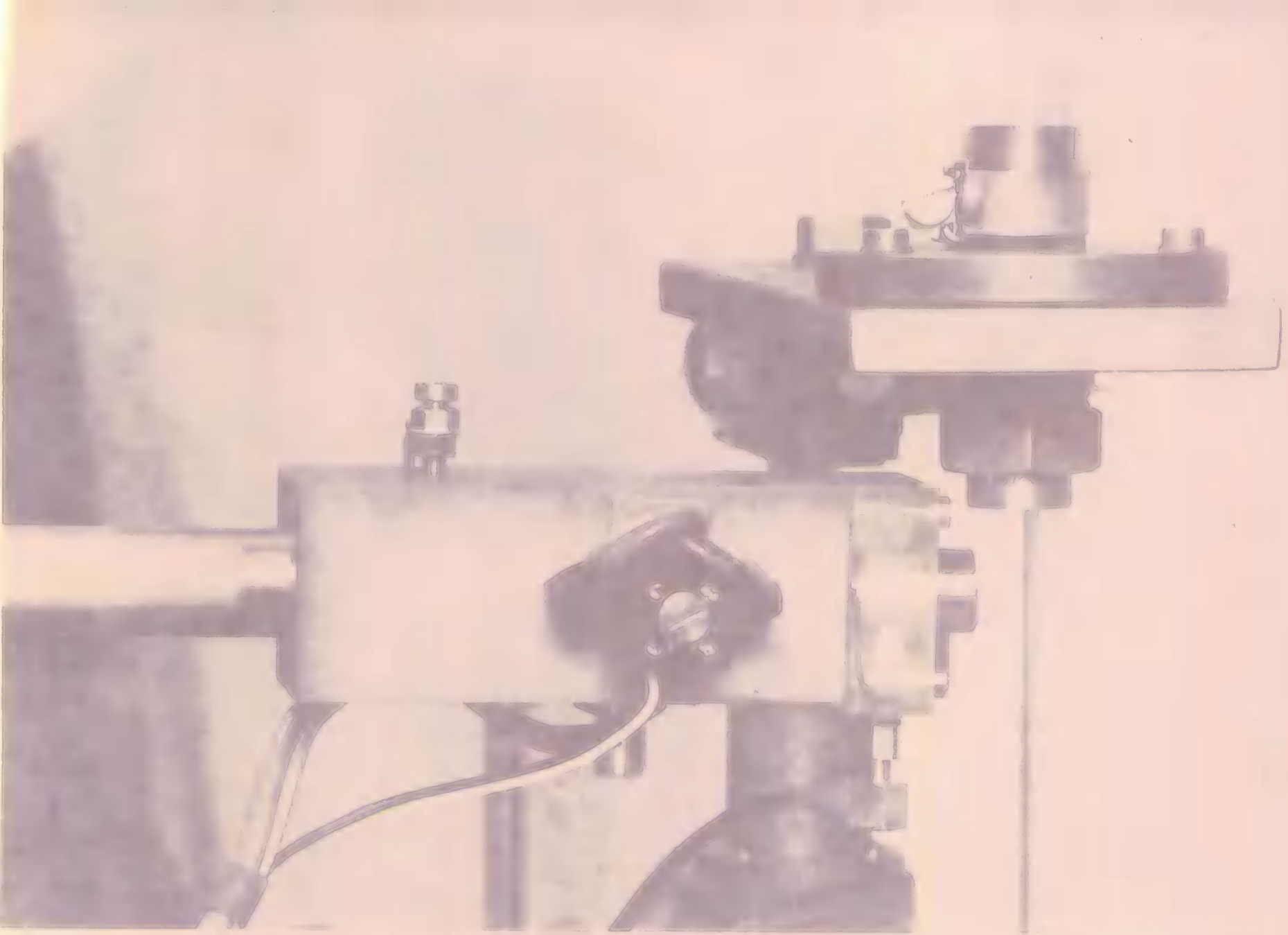

Fig. 4.12 Experimental arrangement for measuring the impact pressure distribution under a drop using the rotating rig.

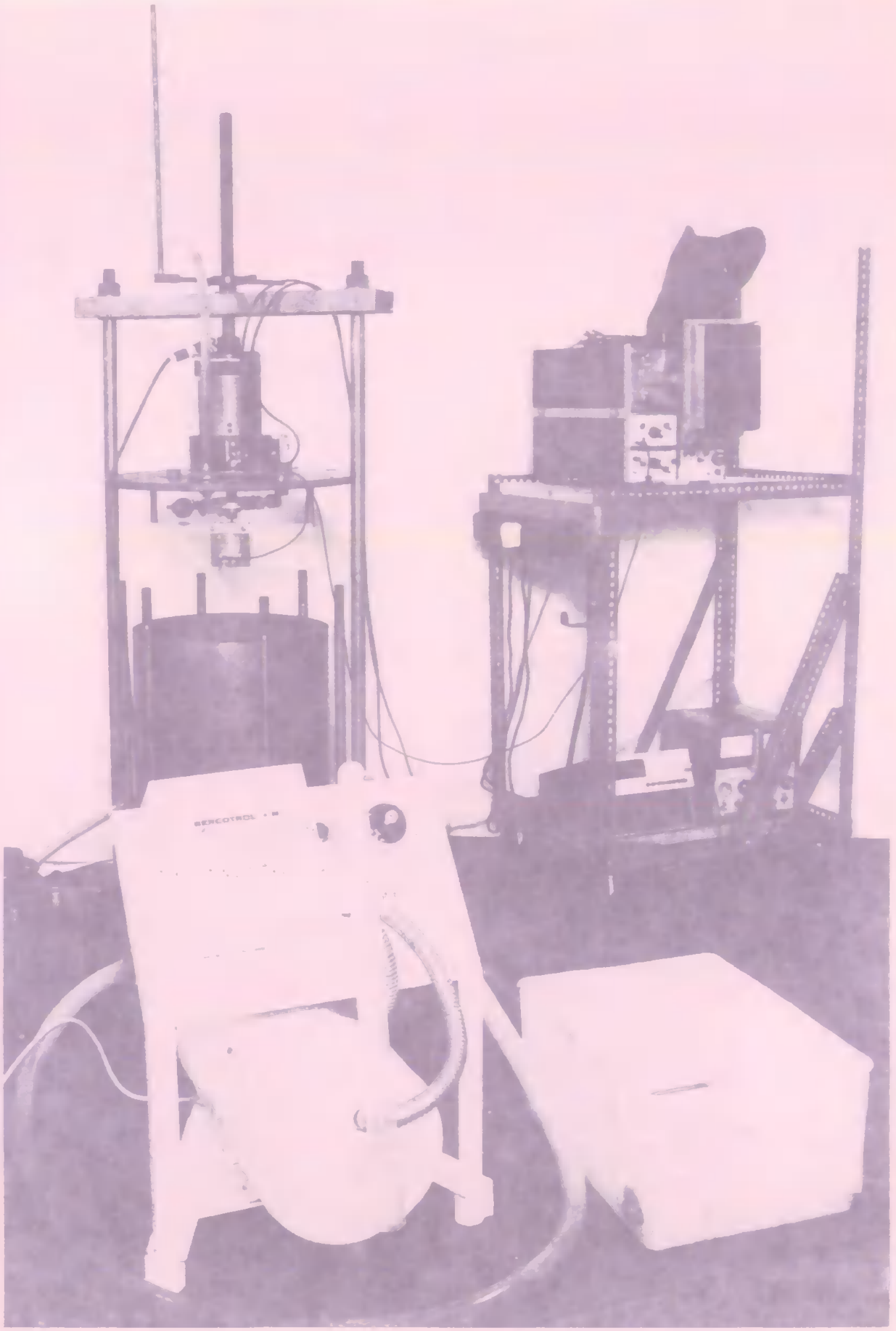
SERCOTROL

Fig. 4.13 Detail of the impact region in the rotating rig.

the impact was picked off the gauge through mercury slip-rings, and the pressure was calculated from

$$p = 6.4 \pm 0.6V \quad MN/m^2. \qquad 4.5$$

4.4 Some Typical Results [1, 2, 3]

A typical sequence of shadow pictures is shown in Fig. 4.14. It shows a bullet striking a 5.0 mm diameter water drop at 96 m/s. In (c) flow is about to start and a slight fuzziness can be seen in the corners of the drop. (The system was thrown out of focus to accentuate any pressure changes, and a 6.0 mm diameter stop was inserted in front of each lens to avoid double exposures, so that some features of these pictures are similar to those obtained with a schlieren system.) The fuzziness is a region of intense pressure change, which remains at the edge as the drop begins to flow out across the surface of the solid. (See (d) and (e).) In (e) a pressure wave can be seen returning to the impact face after reflection in the top surface of the drop. Shock waves can be seen in the air ahead of the outward flowing jets. The outward flow velocity is about 600 m/s, and the angle that the edge of the drop makes with the solid surface when lateral flow begins is about 10°. These points will be discussed in more detail in Chapter 5.

Some typical pressure pulses are shown in Fig. 4.15. Numbers (a), (b) and (c) were obtained with an oblong-sectioned bullet, and (d) was obtained in an experiment with the rotating disc. A few comments on each of these pulses are given below. The matter will be discussed in more detail in Chapter 5.

Fig. 4.15a This pulse was produced when a 5.0 mm diameter water

a A 5.0 mm diameter water drop was struck by a flat bullet gauge at an impact velocity of 121 m/s. The peak pressure is approximately 270 MN/m^2.

b A 5.0 mm diameter water drop was struck by a flat bullet gauge at an impact velocity of 101 m/s. The peak pressure is approximately 40 MN/m^2.

c A 5.0 mm diameter water drop was struck by a bullet at an impact velocity of 100 m/s. The peak pressure is approximately 40 MN/m^2.

d A 6.0 mm diameter water jet was struck from the side at an impact velocity of 20 m/s by the gauge used in the rotating rig. The peak pressure is approximately 10 MN/m^2.

Fig. 4.15 A selection of pressure pulses obtained in the drop impact experiments.

a 120 MN / m^2

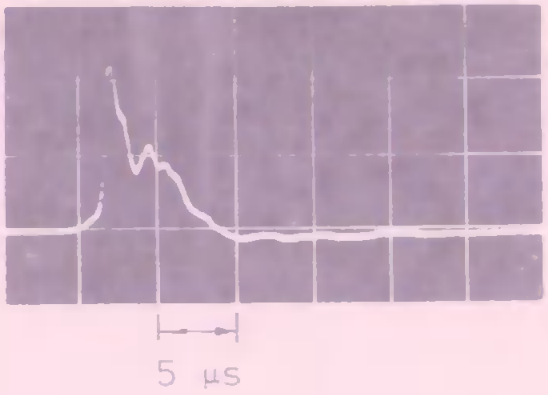

x = 0.5 mm

b 30 MN / m^2

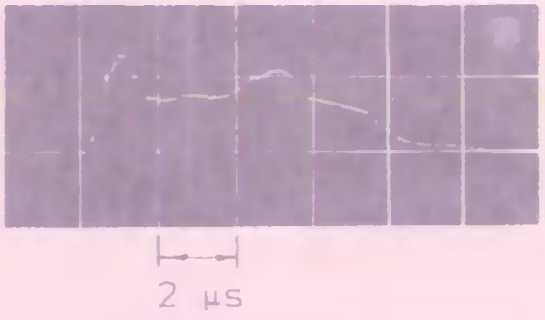

x = - 1.5 mm

c 16 MN / m^2

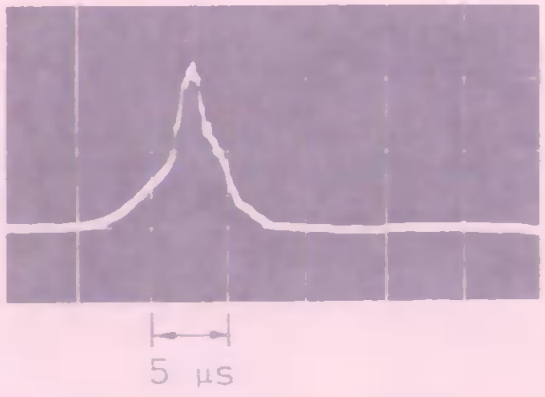

y = 1.0 mm

d 13 MN / m^2

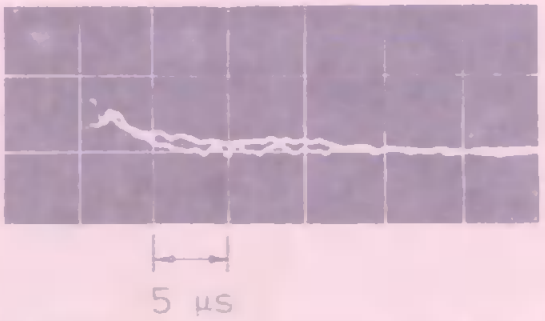

x = - 1.0 mm

drop was struck by a flat bullet gauge at 121 m/s. It shows the pressure changes that occurred at a position 0.5 mm from the centre of impact. The peak pressure was about 270 MN/m^2. The curved step at the foot of the pulse built up as the bullet passed through the meniscus. (For a water drop the width of the meniscus is about 0.1 mm, so that the bullet should take a little less than a microsecond to pass through it - this is the same as the duration of the step.) The maximum pressure was attained about 0.25 μs later. This was about the time that the drop took to roll over the ceramic. (Since the ceramic is 0.31 mm wide the time required for the drop to roll over it at a position 0.5 mm from the centre of impact is approximately 0.2 μs. The rise-time of the gauge is about 0.1 μs, so that the duration of the leading edge of the pulse should be about 0.3 μs. This is in good agreement with the measured value.) The pressure fell from the peak to a lower level in two stages before it rose again to a second peak. The first change took place between 0.5 μs and 0.75 μs after the peak, and the second change occurred about 1.0 μs later. The first change of slope occurred when a release wave from the edge of the drop reached the position of the gauge. (See discussion in Chapter 5.) The total duration of the pressure was about 8.0 μs. At the end of this period the pressure fell to a level beyond the resolution of the system.

Fig. 4.15b This pulse was produced when a 5.0 mm diameter water drop was struck by a flat bullet gauge at 101 m/s. It shows the pressure changes that occurred at a position 1.5 mm from the centre of impact. The peak pressure was about 40 MN/m^2. The trace was triggered when the bullet struck the drop. (A switch, similar to that used for examining the effectiveness of the pickup arrangement,

was used to trigger the oscilloscope as soon as the bullet touched the drop. See Rochester (1977b).) This technique was extremely difficult to use and was never successfully applied to a wide range of problems. The pressure began to build up about 5.4 μs after contact. This was about the time that the edge of the drop took to reach a point 1.5 mm from the centre of impact. (It takes about 1.0 μs for the bullet to cut through the meniscus and 4.5 μs for the edge of the drop to flow out across the surface of the bullet to the centre of the gauge.) The total duration of the pressure was about 10 μs.

Fig. 4.15c This pulse was produced when a 5.0 mm diameter water drop was struck by a bullet at 100 m/s. It shows the pressure changes that occurred at a position 1.0 mm from the centre of impact along the central axis of the drop. The pressure built up slowly because the disturbance was dispersed as it travelled through the drop.

Fig. 4.15d These pulses were produced when a gauge bolted to the rim of a rotating disc was driven through the side of a 6.0 mm diameter water jet at 20 m/s. They show the pressure changes that occurred in thee consecutive runs at a position 1.0 mm from the centre of impact. Note that the pulses have more or less the same magnitude and shape.

Notes on Chapter 4

(1) For taking schlieren pictures 1.5 mm diameter stops were placed in front of the camera lenses and the light from the spark sources was focussed in the plane of the stops. The images of all regions of density gradient then appeared darker than the background, since any displacement of the source image resulted in decreased illumination. Note that the direction of the density gradient could not be found by this method. (See Howarth (1953), Ladenburg et al (1955), Liepmann and Roshko (1957) and Holder and North (1963) for more details of schlieren methods.) No attempt was made to design the system. A piece of stressed perspex was simply introduced into the field of view to ensure that reasonable schlieren images could be obtained. The sensitivity of the system was increased by moving the stops to one side thereby covering up part of the images of the sources. This was done in such a way that the plate received adequate illumination when there was no deflection of the beam.

(2) Errors that occur when photographs of drop impact are analysed - (i) measurements from the negatives ($\pm$ 0.05 mm), (ii) estimation of the frame intervals ($\pm$ 0.1 μs), (iii) estimation of the magnification ($\pm$ 0.01), (iv) estimation of the impact velocity ($\pm$ 2 m/s), and (v) interpretation of (a), (b), (c) and (d) below.

(a) The width of the meniscus in a water drop is 0.1 mm. In other liquids it is approximately 0.8 mm.

(b) The double images that can be seen on some frames were caused by internal reflection of light in the windows of the gun.

(c) In some frames the front of the drop is hidden by the edge of the bullet (Frames 3 and 4). This was caused by refraction of light through the windows of the gun.

(d) The depressions that can be seen in most of the frames were caused by refraction of light through the liquid.

As a result of these errors drop diameters are given to the nearest 0.1 mm, impact velocities to the nearest 10 m/s, outward flow velocities to the nearest 100 m/s and flow angles to the nearest degree.

(3) Errors that occur when photographs of stress pulses are analysed - (i) calculations with the gauge (typically about 10 percent), and (ii) estimation of the position of the drop (± 0.05 mm from - 1.0 mm to 1.0 mm and ± 0.1 mm outside this region). These errors are not indicated on the photographs of the pulses. The error in the peak pressure at any particular position was computed from a number of observations in the usual way. (See Braddick (1963), Ch. 2.)

CHAPTER 5

EXPERIMENTS ON DROP IMPACT

The experimental techniques described in the previous chapter have been used to study the impact of a liquid drop with a solid surface. The main aim of the experiments was either to confirm or to determine the limitations of the theory that was presented in Chapter 3. In this chapter a description of the flow of a drop when it strikes a solid surface is given, based upon sequences of photographs taken with the high-speed camera. Measured values of flow angle and outward flow velocity are then compared with the values predicted with the formulae developed in Chapter 3. Measurements of the pressure distribution under a drop are presented and compared with theory, and a comprehensive view of the impact of a liquid drop with a solid is developed, based upon both the results of these experiments and the theory discussed above. Experimental results for the shear stress distribution under a drop and the pressure distribution within a drop, both of which have not been examined theoretically, are also presented and discussed.

5.1 The Flow of a Drop during Impact

The principal aims of the work were to observe the development and propagation of pressure waves within the drop, to determine the angle that the edge of the drop makes with the solid surface when lateral flow begins, and to measure the outward flow velocity. These problems were studied at impact velocities in the range from about 60 m/s to about 160 m/s.

5.1.1 Description of the Impact - Change in Drop Shape, Pressure Wave Geometry and Cavitation Bubbles

A sequence of shadow pictures taken with the high-speed camera is shown in Fig. 5.1. It shows a bullet striking a 5.1 mm diameter water drop at 66 m/s. The average time between the frames is 1.0 μs. Contact with the solid has been made in (a), and flow from under the edges of the drop has already begun in (b), 1.2 μs later. The angle that the edge of the drop makes with the solid surface when lateral flow begins is about 9°, and the jets in (f) are moving out across the surface of the solid at about 400 m/s. Too much light reached the photographic plate in this sequence, so that details of the pressure wave geometry within the drop were obliterated.

A fuzzy black dot can be seen in the base of the drop in contact with the surface of the solid. It has a maximum width of about 0.2 mm (Frame (a)). As the impact proceeds, it changes in both shape and volume. This is particularly clear in Frames (d), (e) and (f). In (d) the dot is much smaller than it was in (a), and it no longer seems to be resting on the surface of the solid. In (e) it has increased in volume, and in (f) it has increased in volume even more and is now about the same size that it was at the beginning of the impact. The time between Frames (a) and (f) is 4.6 μs, so that the dot appears to collapse and grow again in this period of time. It could be a cavitation bubble. These bubbles are expected to appear along the central axis of the drop just above the surface of the solid, as discussed in Section 3.1. If cavitation bubbles were formed when the pressure in this region fell below zero, they would collapse again in the pressure field set up around them, generating very high pressures near the

Fig. 5.1 Shadow pictures of a bullet striking a 5.1 mm diameter water drop at 66 m/s. The intervals between the frames are (a) and (b) 1.2 μs, (b) and (c) 0.8 μs, (c) and (d) 0.8 μs, (d) and (e) 1.0 μs and (e) and (f) 0.8 μs. Contact is first made in (a), and flow from under the edges of the drop has already begun in (b). The angle that the edge of the drop makes with the solid surface when lateral flow begins is about 9°. The jets in (f) are moving out across the surface of the solid at about 400 m/s.

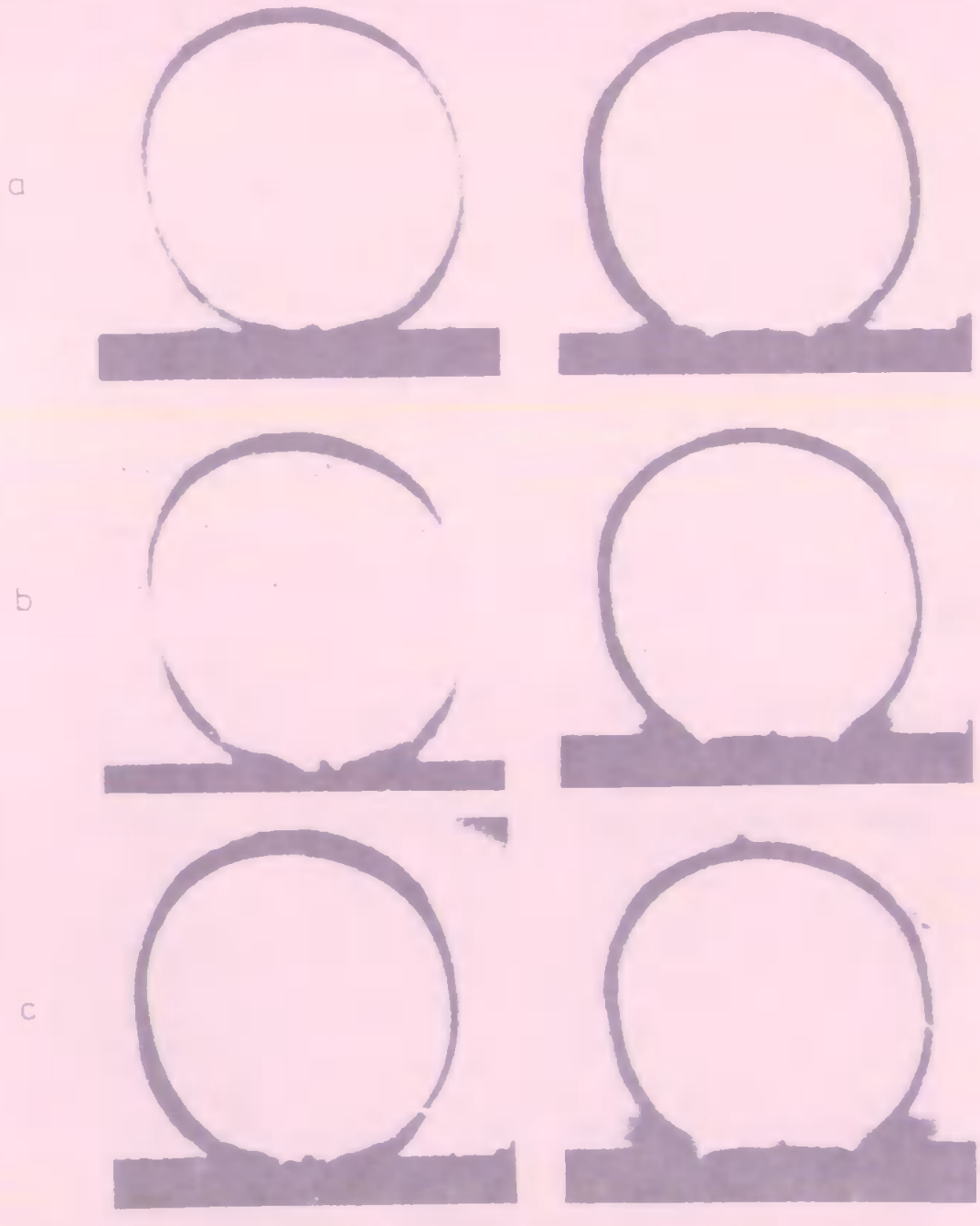
a
d
b
e
c
f
2 mm

collapse point. A number of people (see, for example, Benjamin and Ellis (1966), Brunton (1970) and Camus (1971)) have shown that when this happens the bubble can oscillate in and out several times, until it eventually collapses completely, after breaking up into smaller and smaller volumes. It is also possible that the dot is a pocket of air trapped between the drop and the surface of the solid in the early stage of the impact. This could easily occur here, since the drop has a large meniscus, which could collapse inwards onto the surface of the solid and trap the air that lies between the two sides of the drop.

Whether the dot is a pocket of trapped air or a cavitation bubble filled with saturated water vapour, it will still collapse and rebound in the pressure field inside the drop. If it has air inside it, it will collapse more slowly than when it is filled with the saturated water vapour only, and the air will reduce the very high pressures that can be generated in the later stages of collapse.

These bubbles can also be seen in the sequence of shadow pictures shown in Fig. 4.14. Here the entire surface of the solid under the drop is covered with them, particularly in Frames (d), (e) and (f). This was a common feature of most of the impacts.

Three consecutive frames from a sequence of shadow pictures are shown in Fig. 5.2. They show a bullet striking a 5.0 mm diameter water drop at 97 m/s. The time between (a) and (b) is 3.2 μs, and the time between (b) and (c) is 2.0 μs. The system was thrown out of focus to accentuate any pressure changes within the drop. In (a) flow from under the drop has not begun, and there are two distinct dark regions in the edges. These are regions of

Fig. 5.2 Shadow pictures of a bullet striking a 5.0 mm diameter water drop at 97 m/s. The interval between (a) and (b) is 3.2 μs, and the interval between (b) and (c) is 2.0 μs. The camera was thrown out of focus so that the pressure gradients within the drop would be accentuated. In (a) intense pressure gradients can be seen near the edges of the drop.

Fig. 5.3 Shadow pictures of a bullet striking a 4.7 mm diameter water drop at 137 m/s. The interval between (a) and (b) is 1.0 μs, and the interval between (b) and (c) is 0.8 μs. The jets in (c) are moving out across the surface of the solid at about 800 m/s.

Fig. 5.4 Schlieren pictures of a bullet striking a 5.0 mm diameter water drop at 97 m/s. The time between the frames is 2.4 μs. Intense pressure gradients exist in the edges of the drop even after outward flow of the liquid is well established. The direction of the pressure gradients could not be determined from the photographs because circular stops had been used.

Fig. 5.5 Schlieren picture of a bullet striking a 5.0 mm diameter water drop at 100 m/s. There is a region of intense pressure change near the free surface of the drop. Trapped pockets of air can be seen in the drop on the surface of the solid.

a b c

2 mm

a b c

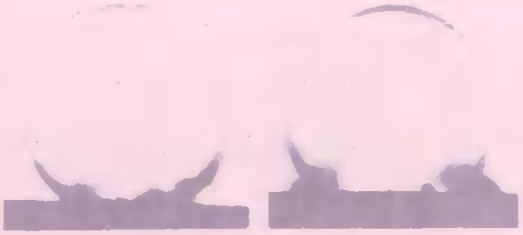

a b

2 mm

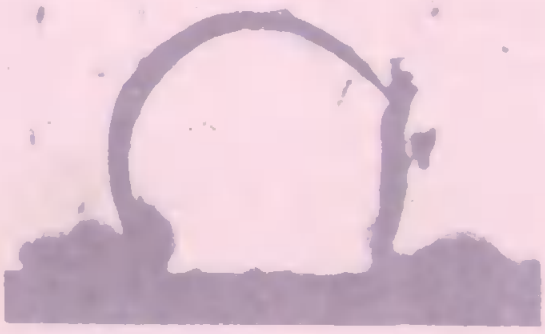

2 mm

intense pressure change. This was to be expected from the analysis in Chapter 3, where it was shown that the pressure, and hence the pressure gradient, increases towards the edge of the drop as the impact proceeds. However, large pressure gradients would also exist in the edges of the drop if the pressure distribution were bow-shaped, so that these pictures cannot be taken as evidence for a pressure distribution in which the pressure is lower at the centre of impact than at the edge of the contact surface. The region is not just restricted to the surface of the drop in contact with the solid, but occurs both inside the drop away from the edges as well as along the free surface. In (b) outward flow has started, and the region of intense pressure change has remained with the edges of the drop as they have moved out across the surface of the solid. The pressure wave can be seen near the top of the drop. (In the 3.2 μs between (a) and (b) the leading edge of the wave should have covered about 4.7 mm, as observed here.) In (c) this wave can be seen returning to the impact face after reflection in the top surface of the drop.

Three consecutive frames from a sequence of shadow pictures are shown in Fig. 5.3. They show a bullet striking a 4.7 mm diameter water drop at 137 m/s. The time between (a) and (b) is 1.0 μs, and the time between (b) and (c) is 0.8 μs. Two pockets of trapped air can be seen in (a) and these change shape as the impact proceeds. Flow has already begun in (a), and regions of intense pressure change can be seen in the edges of the drop. As before they persist even after outward flow has become established. In (c) the front of a crescent-shaped pressure wave can be seen about half way across the drop on its way to the top surface.

The pressure wave geometry is more pronounced in the schlieren pictures shown in Fig. 5.4. They are two consecutive frames from a sequence of six. The diameter of the drop is 5.0 mm, the impact velocity is 97 m/s and the time between the frames is 2.4 μs. In (a) a crescent-shaped pressure wave inside the drop and regions of intense pressure change in the edges of the drop can be seen. A little water can just be seen on the right-hand side about to flow outwards from under the drop. In (b) outward flow has been established, and regions of intense pressure change still exist in the edges. The surface of the solid inside the drop away from the edges is uneven, covered with either cavitation bubbles or pockets of air trapped during the impact. These details can be seen even more clearly in the single schlieren picture in Fig. 5.5.

Despite many attempts, shadow pictures of the impact before the pressure wave was released from the edges of the drop were not obtained, so that it was not possible to estimate the flow angle at which this occurred and so check the validity of Equation 3.4c. However, it is clear from the photographs described above that outward flow from under the drop does not occur until the pressure wave initiated in the beginning of the impact has detached from the edges and has moved some distance into the drop. It remains to determine whether the outward flow velocities and the flow angles predicted with the equations in Chapter 3 agree with the experimental values estimated from both the sequences of photographs described above and others like them.

5.1.2 Outward Flow Velocity and Flow Angle

The outward flow velocities and flow angles were estimated from

measurements on the negatives. Impact velocities were in the range from about 60 m/s to about 160 m/s, and all drop diameters were about 5.0 mm. A graph of V_j/c_0 versus V/c_0 is shown in Fig. 5.6, and a graph of x_e/R ($= \sin\vartheta_e$) versus V/c_0 is shown in Fig. 5.7. The points (a) were obtained from the sequence of pictures shown in Fig. 5.1, the points (b) were obtained from a sequence of pictures not shown here, the points (c) were obtained from the sequence shown in Fig. 4.14, and the points (d) were obtained from the sequence from which the pictures shown in Fig. 5.3 were selected. The other points were obtained from sequences of pictures in which only one of the two quantities could be determined. In both figures the theoretical results derived in Section 3.2 are shown as dashed lines. In Fig. 5.6 a result from the work of Fyall (1967), who fired perspex bullets at 2.0 mm diameter water drops, and another from the work of Camus (1971), who fired duralumin bullets at 5.0 mm diameter water drops, are shown. It can be seen that the experimental results are very close to the theoretical ones over a wide velocity range, so that confidence can be placed in the simple theory developed in Section 3.2, where the formulae for flow velocities and flow angles were derived without knowing any details of the flow within the drop.

The flow velocities at (b) and (d) are higher than the predicted ones. In both cases the flow velocity was obtained from measurements on the last two frames of the sequence, just after flow had started. In the early stages of flow there is some evidence that outward flow velocities are higher than those given by the equations developed in Section 3.2. For example, the point (e) was obtained from a sequence of photographs in which outward flow was visible on all frames except the first one; the impact velocity was 96 m/s and the outward

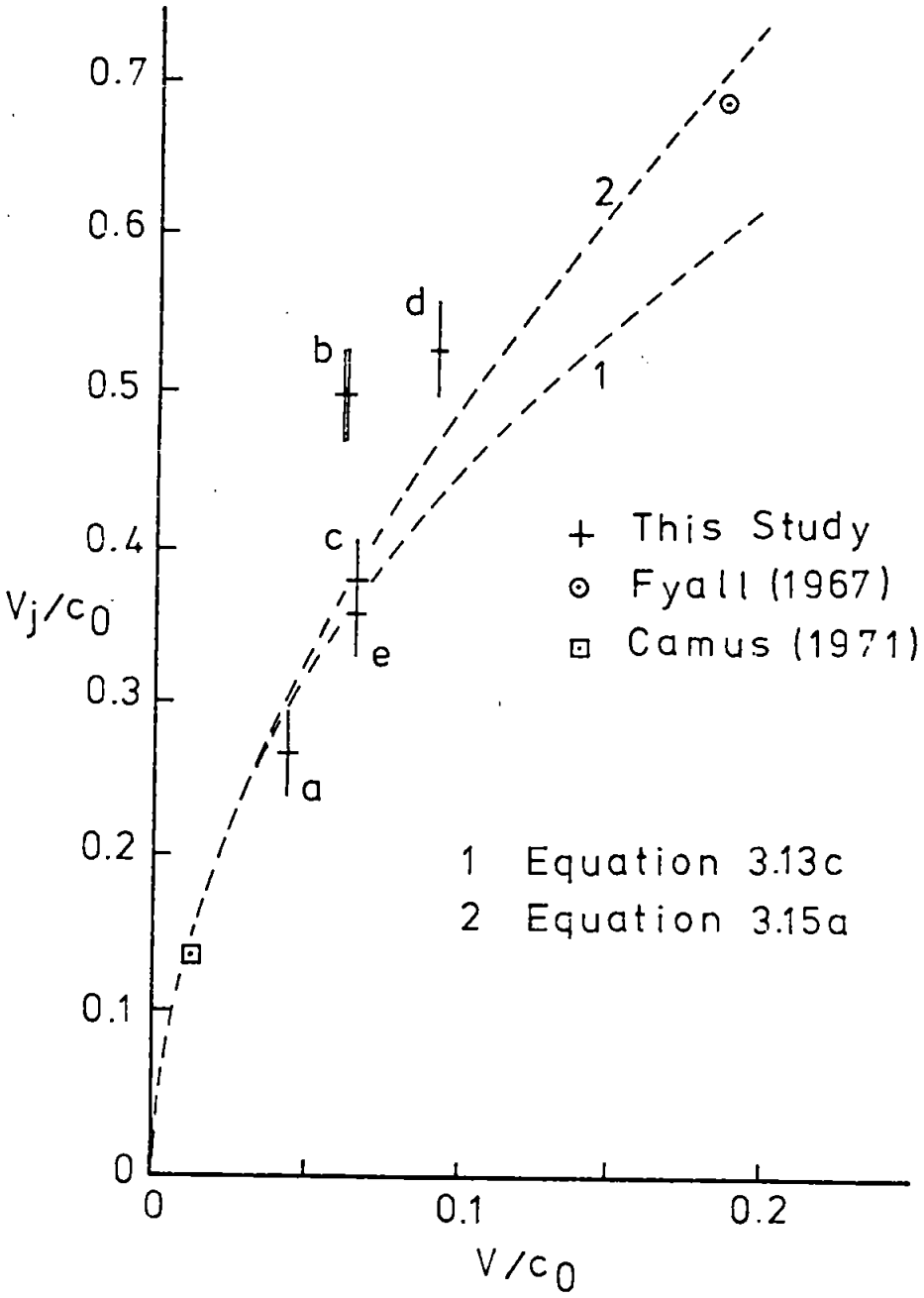

Fig. 5.6 V_j/c_0 versus V/c_0.

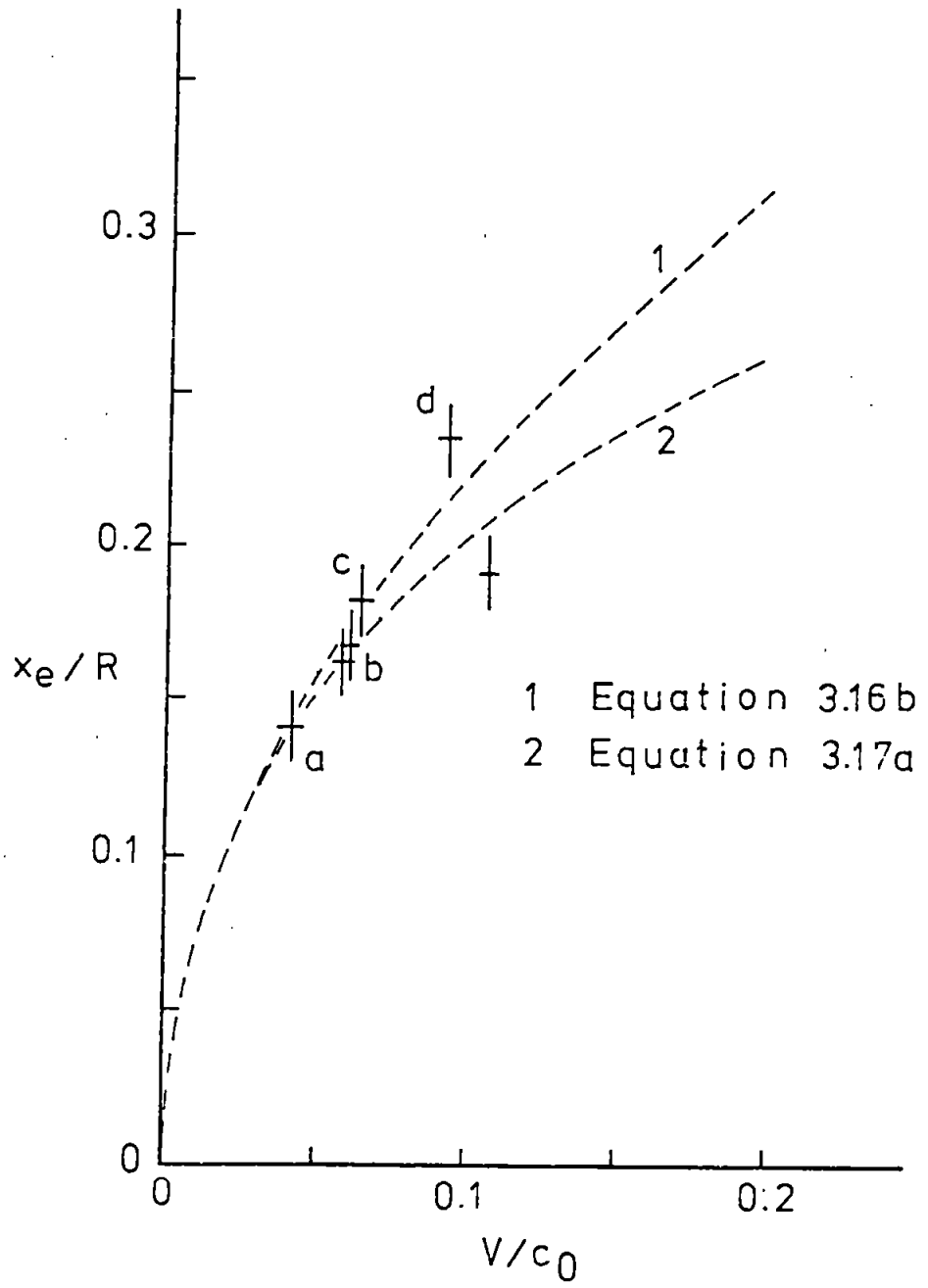

Fig. 5.7 x_e/R versus V/c_0.

flow velocity decreased from about 700 m/s to about 400 m/s over a period of 9.8 μs; the average flow velocity in this interval, which was used to plot the point in Fig. 5.6, was 500 m/s.

An outward flow velocity at a much higher impact velocity than those that were studied here has been measured by Brunton (1961). He fired a 2.2 mm diameter water jet against a flat perspex block at 680 m/s, and from a sequence of photographs of the impact he estimated that the outward flow velocity was 1,560 m/s (about 2.3 times the impact velocity). Thus $V_j/c_0 = 1.05$ when $V/c_0 = 0.46$. Equation 3.13c gives $V_j/c_0 = 0.96$, and Equation 3.15a gives $V_j/c_0 = 1.33$. Therefore the experimental result lies between the predicted values. This is to be expected, since the perspex deforms during the impact and this causes a reduction in the impact velocity with respect to the solid surface.

5.2 The Mean Impact Pressure under a Drop

The mean impact pressure under a 5.0 mm diameter water drop was measured with a gauge in which the sensing element had a large surface width. (This was Number 1 flat bullet gauge - when the impact velocity was 100 m/s the width of the sensing element was about the same as the width of the drop in contact with the solid at the time when outward flow began.) The pressure pulses obtained in this experiment were similar to those that were described in the previous chapter. (See Fig. 4.15.) At a particular impact velocity the peak pressure obtained when the drop was placed symmetrically with respect to the sensing element was taken to be the average pressure over the contact surface in the early stage of impact. (It was also the greatest pressure measured with this gauge,

no matter where the drop was placed in relation to the position of the sensing element.) A graph of average pressure versus impact velocity is shown in Fig. 5.8. It can be seen that the average pressure varies linearly with impact velocity in the range from 60 m/s to 140 m/s. It has a magnitude of about $0.7\rho_0 c_0 V$, smaller than the water-hammer pressure deduced in Section 3.1 (Equation 3.9).

What is the reason for the difference between these results and the values given by the water-hammer equation? The impact surface must deform slightly when it strikes the drop (otherwise it would not be possible to measure the pressure) and this will reduce the impact velocity with respect to the solid. The impact velocity will be reduced from V to $V/[1 + \rho_0 c_0/(\rho_s c_s)]$, where ρ_s is the density of the solid and c_s is the sound speed in the solid. (The impact has been treated as equivalent to the collision of two elastic rods - see Gardner (1932) and de Haller (1933).) Therefore the average impact pressure will become

$$p_{av} = \rho_0 c_0 V/[1 + \rho_0 c_0/(\rho_s c_s)]. \qquad 5.1a$$

For tufnol the density is 1.35×10^3 kg/m^3 and the sound speed is 2,500 m/s, and for water the density is 1.00×10^3 kg/m^3 and the sound speed is 1,483 m/s. [a] When these values are substituted into Equation 5.1a, it becomes

$$p_{av} = 0.70\rho_0 c_0 V. \qquad 5.1b$$

a The density of tufnol was taken from an anonymous report published by Tufnol Ltd. (1954), and the sound speed was measured in the laboratory. The physical properties of water and other liquids used in the work are given in Chapter 6. (See Table 6.1.)

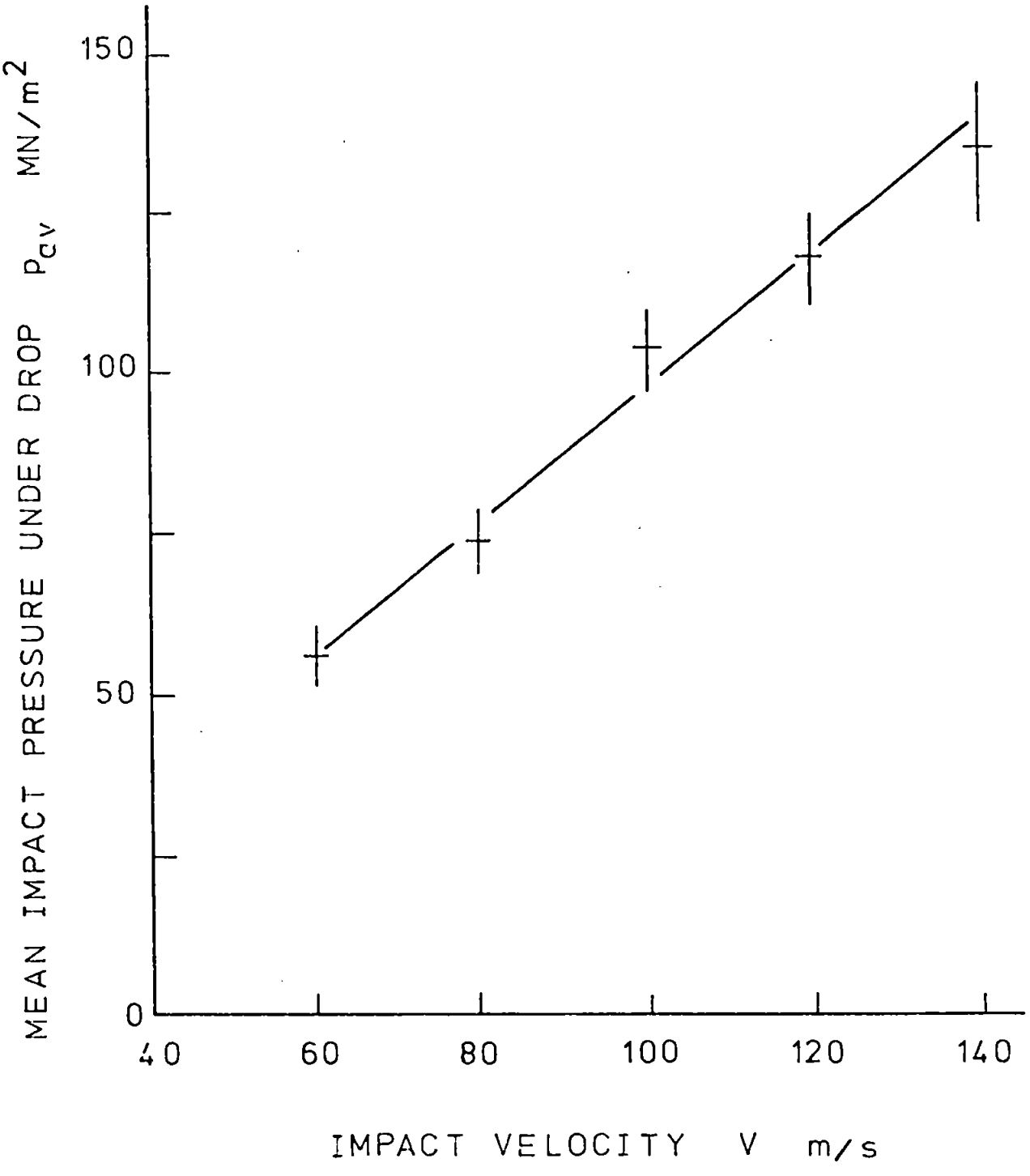

Fig. 5.8 Mean impact pressure under a cylindrical water drop, p_{av}, versus impact velocity, V. The drop diameter was 5.0 mm.

This is the same as the result obtained in the experiment.

5.3 The Pressure Distribution under a Drop

5.3.1 Peak Pressure Distribution under a Drop

A graph showing the variation of peak impact pressure with position under a 5.0 mm diameter water drop when it is struck by a bullet at 100 m/s is shown in Fig. 5.9. (Number 12 flat bullet gauge was used to obtain one set of results (disc). The other set (cylinder) was obtained with the cylindrical bullet gauge.) The pressure distribution is symmetrical about the centre of impact. The maximum pressures during the impact occur at positions 0.5 mm either side of the centre. The pressure at the centre is approximately 110 MN/m^2 ($0.7\rho_0 c_0 V$). At the edges it is approximately 260 MN/m^2 ($1.8\rho_0 c_0 V$).

The results for positions $x > 0$ are shown plotted to a larger scale in Fig. 5.10. Two dashed lines are shown in the same figure. Line 1 is the locus of peak pressures under the drop based on the calculations in Chapter 3. (See Fig. 3.18.) Line 2 comes from a theory developed by Camus (1971). [a] This theory goes somewhat as follows. When flow from under the drop has begun the edge region at any instant is equivalent to a sheet of liquid striking the solid with velocity V at an angle ϑ. Flow takes place from a point that is moving across the surface of the solid with velocity $V\cot\vartheta$. In a coordinate system moving with the edge of the drop the flow is steady, so that the steady form of Bernoulli's equation can be used

a The development follows an idea of Taylor (1966). See Appendix 1.

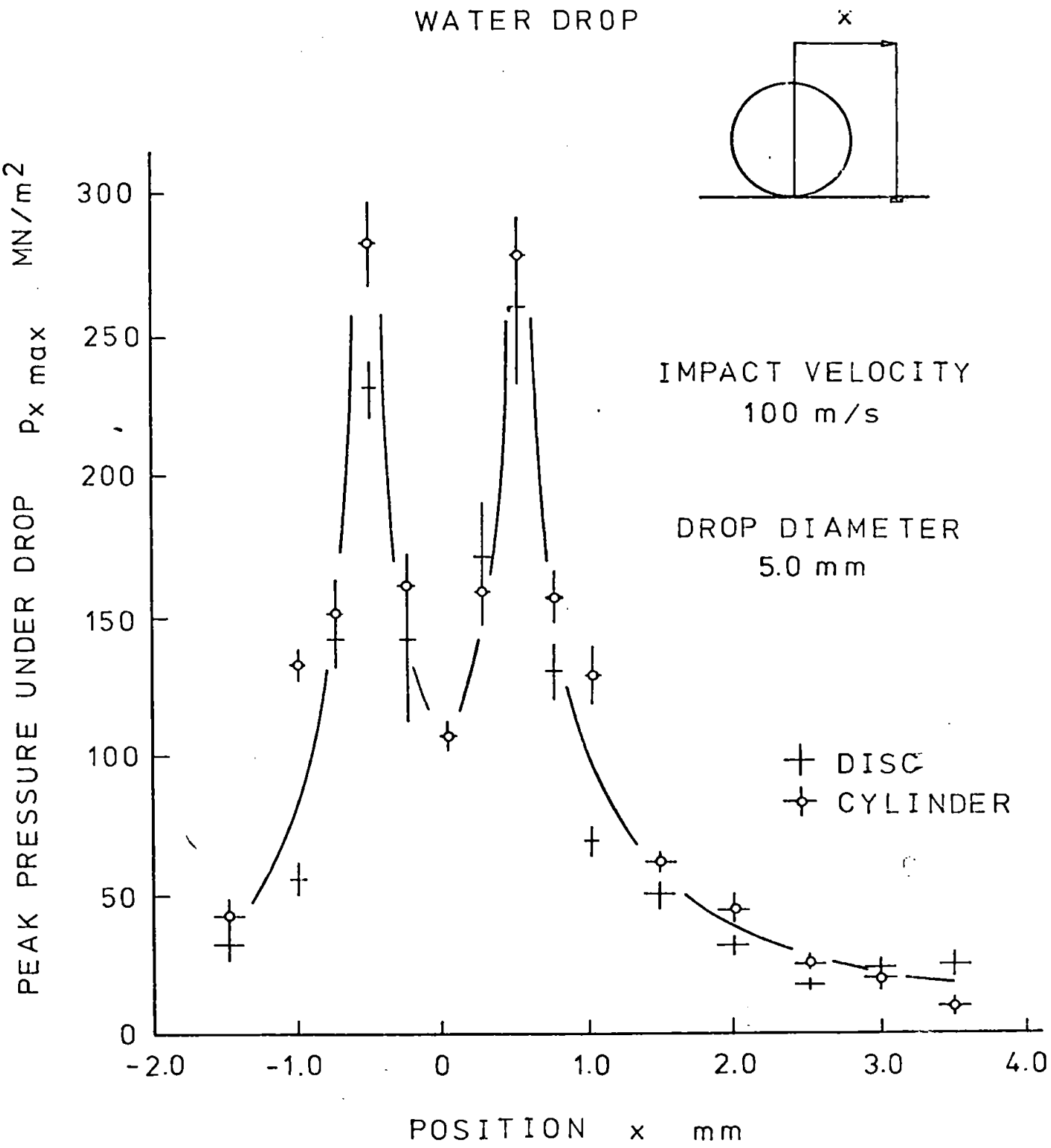

Fig. 5.9 Peak pressure under a cylindrical water drop, $p_{x\,max}$, versus position, x.

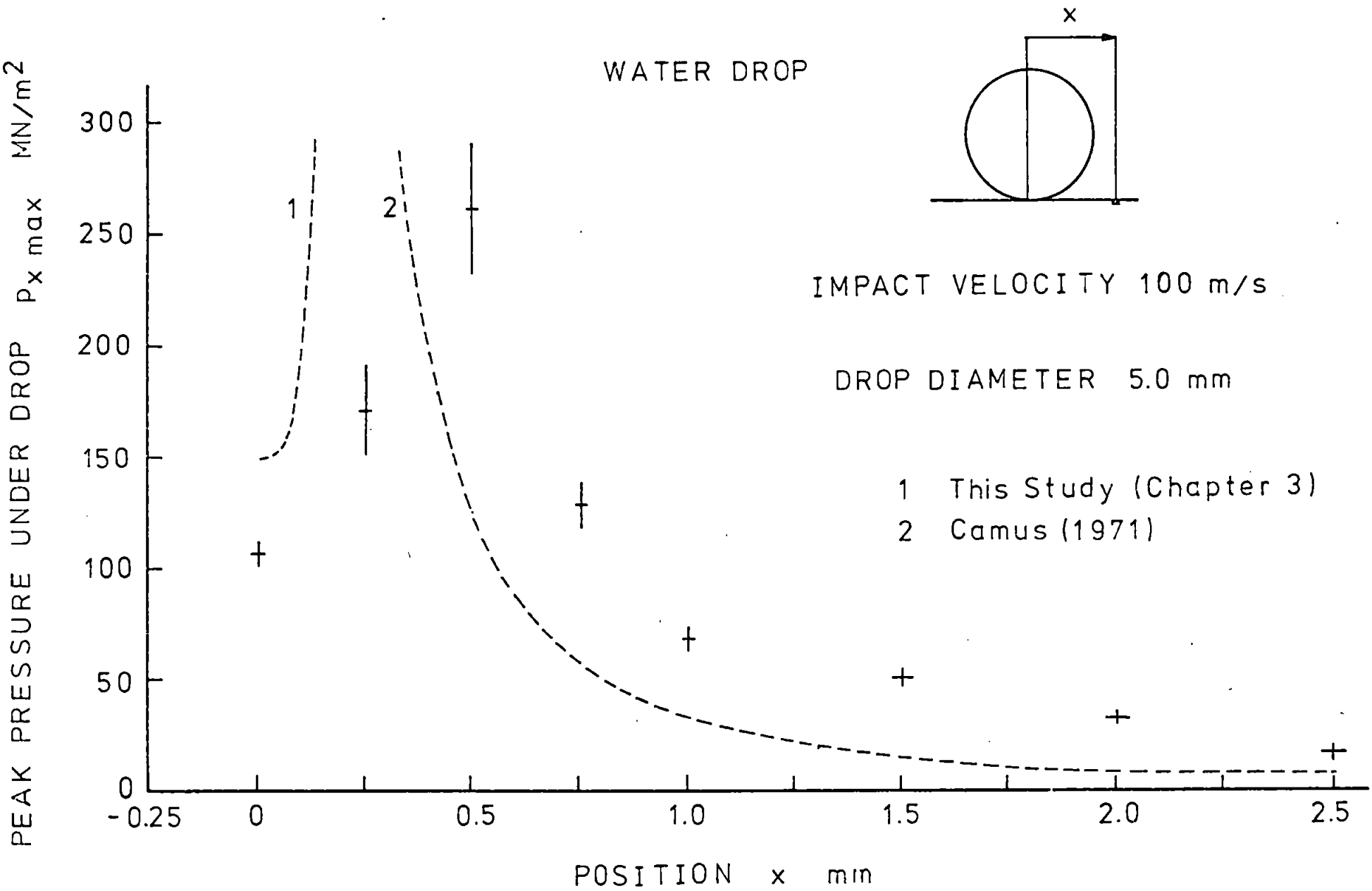

Fig. 5.10 Peak pressure under a cylindrical water drop, $p_{x\,max}$, versus position, x (x>0).

to determine the pressure. When this is done, the pressure at the edge (a stagnation point in the moving system) turns out to be

$$p = \rho_0 V^2 \mathrm{cosec}^2 \vartheta/2. \qquad 5.2$$

At any instant this is the greatest pressure on the surface of the solid, since it is a stagnation pressure. The flow angle and the position of the edge of the drop are related through Equation 3.3. Equations 3.3 and 5.2 were used to plot Line 2 in Fig. 5.10. Although the deceleration of the edge of the drop has been neglected in this analysis and the flow has been assumed incompressible, the agreement between experiment and theory in the later stages of flow is quite good. (At distances from the centre of impact greater than say 1.0 mm.)

In Chapter 3 it was shown that the peak pressure at the centre of impact is equal to $\rho_0 c_0 V$; as the impact proceeds the peak pressures at the edges of the drop rise until they become infinite at the places where the edges are overtaken by the pressure waves generated in the impact. When a 5.0 mm diameter water drop is struck by a rigid solid at 100 m/s this should occur at distances of approximately 0.17 mm from the centre of impact (at x_c - see Fig. 3.20 and Equation 3.4b). In fact the greatest peak pressures occur at distances of 0.5 mm from the centre, and the peak pressure at the centre is only $0.7\rho_0 c_0 V$ (Fig. 5.9). As discussed in Section 5.2 above, the pressure is reduced at the centre of impact because the surface of the bullet deforms slightly during the impact. The implication of this here is that the pressures in the early stages of impact for impact against a rigid surface would be approximately 1.4 times those measured in the experiments. Therefore in an impact against a rigid surface (a metal is more or less rigid in impacts at the velocities used

here) the pressure at the centre would be $\rho_0 c_0 V$ and the pressures at distances of 0.5 mm from the centre would be $2.5\rho_0 c_0 V$. It is clear that the linear theory does not give the pressures that occur close to the edges of the drop. This is illustrated further below, where the high pressure regions are examined in more detail.

5.3.2 Shape of the Pressure Pulses. Variation of Pressure under a Drop with Position and Time

A typical set of pressure pulses obtained in an experiment with a water drop is shown in Figs. 5.11a and 5.11b. These pulses (and others) were used to plot the points in Fig. 5.9. It can be seen that the majority of them consist of an initial pulse, typically about a microsecond wide, followed by a number of oscillations. (The curved step at the front of a pulse built up as the bullet passed through the meniscus, and the slope of the leading edge was formed as the drop rolled over the ceramic - see Chapter 4.) The height of the first pulse indicates the pressure under the edge of the drop at the instant the water reaches the position of the gauge. It may be inferred that changes in pulse shape after this time occur when waves reflected in the edges of the drop pass over the gauge. Evidence for this idea is given below.

When a 5.0 mm diameter water drop is struck by a bullet at 100 m/s flow from under the drop begins at distances of 0.46 mm either side of the centre of impact 0.42 μs after contact (see Equations 3.4b, 3.16c and 3.16d). Pressures have been calculated up to distances of 0.51 mm from the centre of impact ($3x_c$ - see Fig. 3.20 and Equation 3.4b). Measurements have only been made at

Fig. 5.11a A selection of pressure pulses obtained in an impact experiment with a water drop. (Number 12 flat bullet gauge was used.) The diameter of the drop was 5.0 mm and the impact velocity was 100 m/s. The time scale is 5 μs a division and the pressure scale is 64 MN/m^2 a division. The positions at which the pulses occurred and the magnitudes of the peak pressures are shown below.

Letter	Position x	Peak Pressure $p_{x\ max}$
	mm	MN/m^2
a, f	0, 0	110, 101
b, g	0.25, - 0.25	165, 165
c, h	0.5, - 0.5	261, 220
d, i	0.75, - 0.75	128, 141
e, j	1.0, - 1.0	64, 55

These pulses (and others) were used to plot the points in Fig. 5.9.

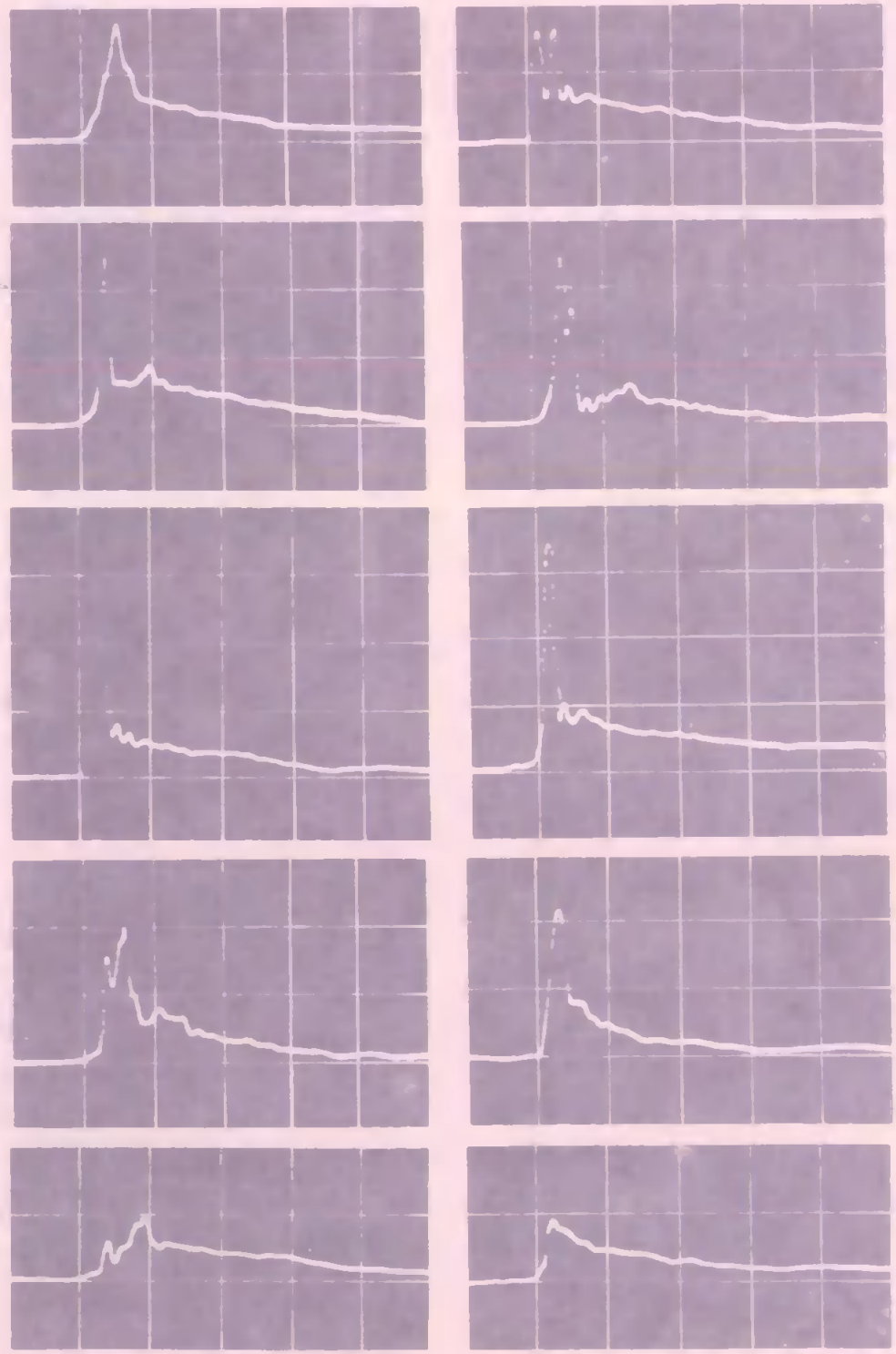
a
b
c
d
e
f
g
h
i
j

Fig. 5.11b As for Fig. 5.11a. The magnitudes of the peak pressures are (a) 50 MN/m^2, (b) 32 MN/m^2, (c) 18 MN/m^2 and (d) 22 MN/m^2.

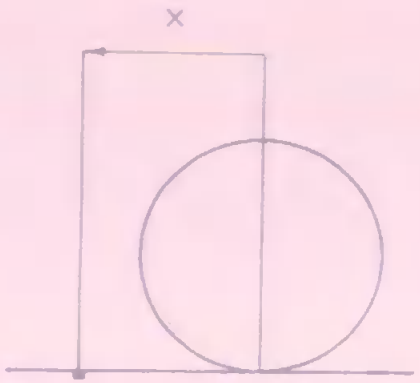
x

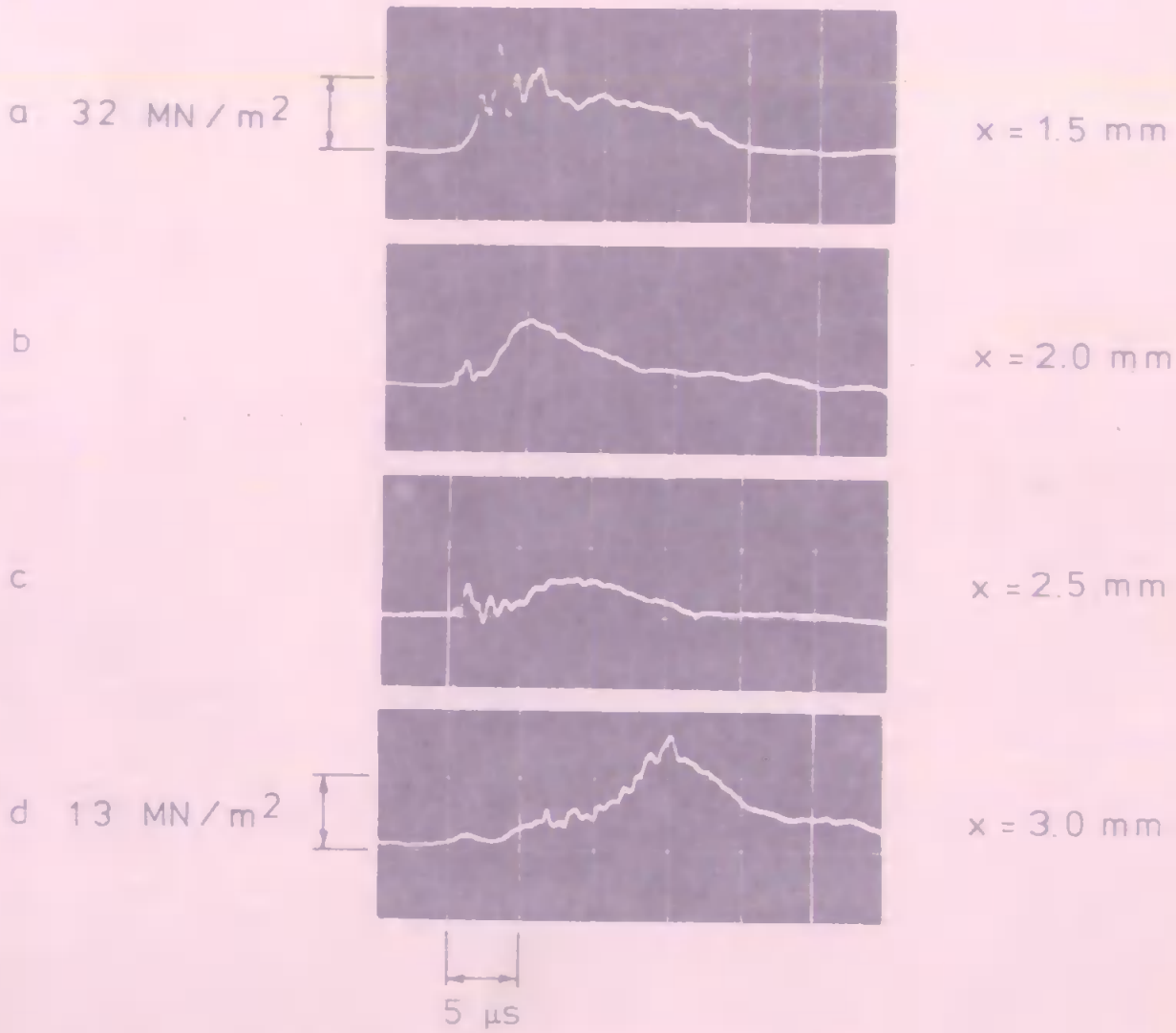
a 32 MN / m2
x = 1.5 mm
b
x = 2.0 mm
c
x = 2.5 mm
d 13 MN / m2
x = 3.0 mm
5 µs

five places inside this region - at x = 0 mm, 0.25 mm, - 0.25 mm, 0.5 mm and - 0.5 mm. Only a small part of the pulse at x = 0.5 mm (and of the one at x = - 0.5 mm) has been calculated, since the position is crossed by the front of a compression wave from the edge of the drop soon after the pulse is formed. Furthermore, the edges of the drop will have been overtaken by the outflowing jets when this position is reached. Therefore only the pressure pulses at the centre of impact and those at positions 0.25 mm either side of the centre of impact may be compared with the theory developed in Chapter 3.

In Fig. 5.12a the calculated shape of the pulse that occurs at the centre of impact is shown as a dashed line. The first change of slope occurs 0.17 μs ($3t_c$) after impact when the release waves from the edges of the drop reach the centre of the contact area. On the same graph three points measured from Pulse (f) in Fig. 5.11a are plotted. Times have been measured from a line through the top of the first pulse since the leading edge shows only what is happening as the bullet penetrates the meniscus and rolls over the ceramic. The first point is the maximum pressure measured at the centre of impact, the second point occurs about 0.4 μs later at a level where there is a change in the slope of the falling edge of the first part of the pulse, and the third point occurs about 0.5 μs after impact at the base of the first pulse. There is quite good agreement between experiment and theory. The maximum pressure at the centre of impact is lower than that calculated with the equation in Chapter 3 because the surface of the gauge deforms during the impact. (See discussion above.)

The top of the second peak (in Pulse (f)) is reached about 1.0 μs after contact, the top of the third peak is reached about

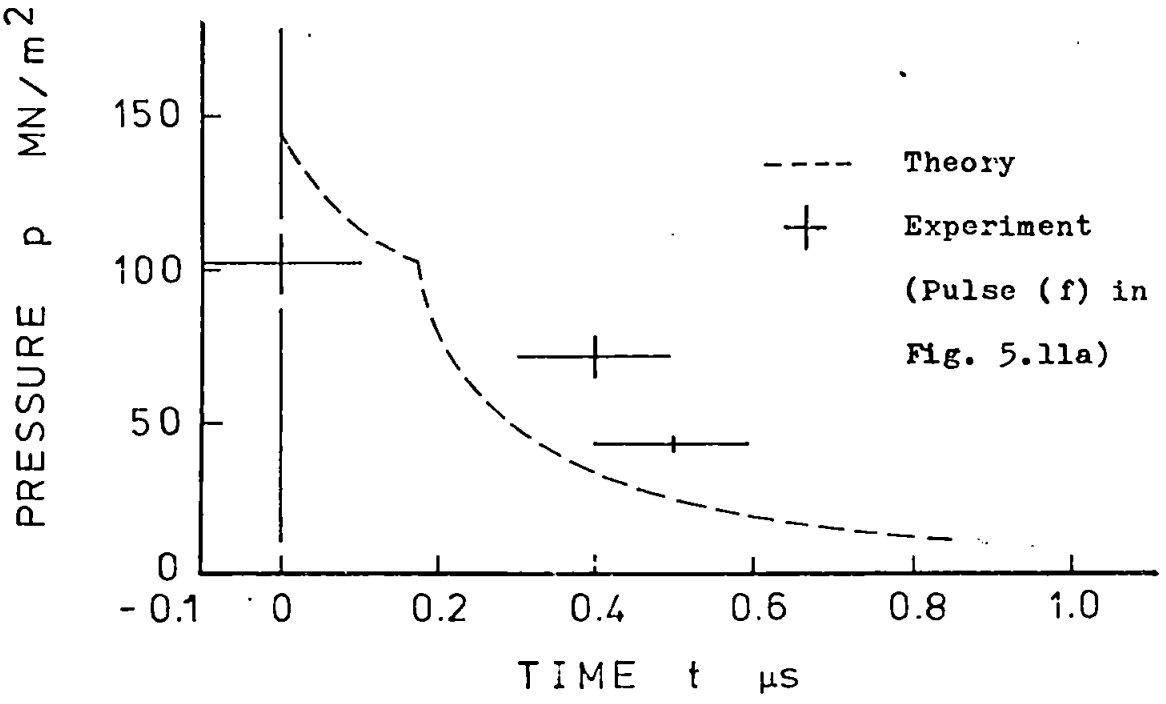

Fig. 5.12a Pressure under a 5.0 mm diameter water drop at the centre of impact. The impact velocity was 100 m/s.

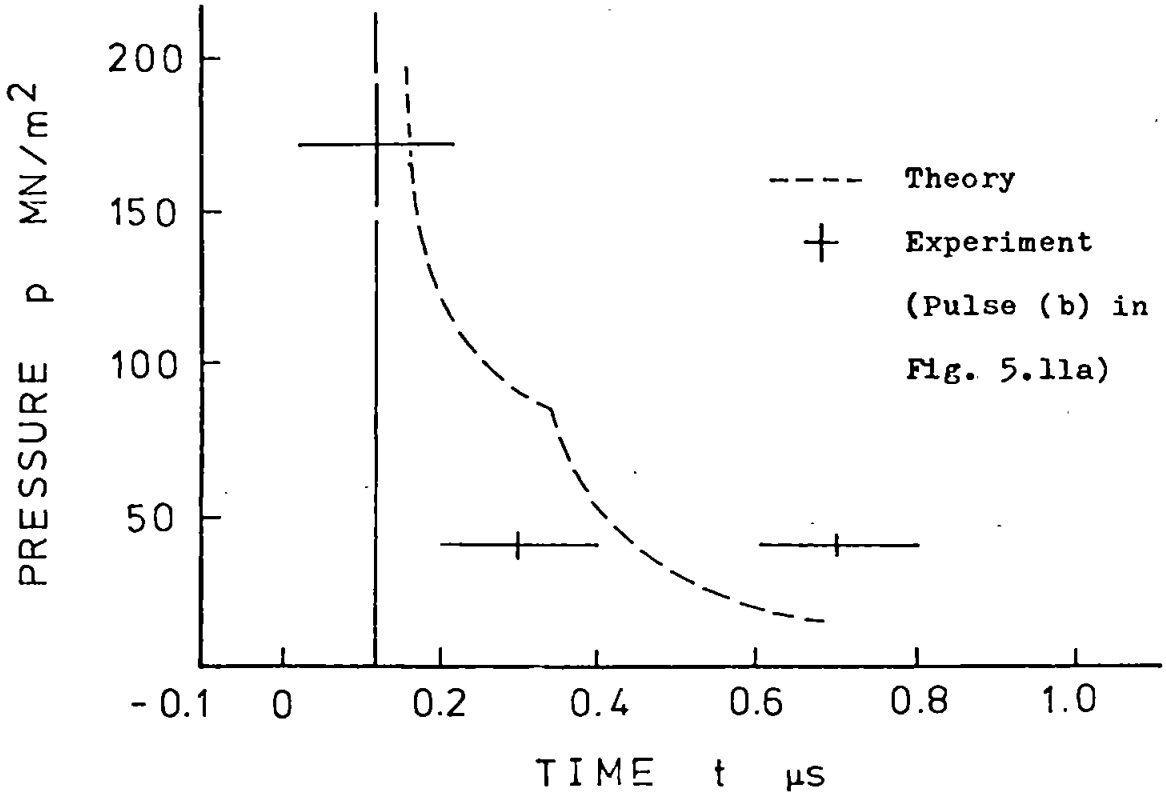

Fig. 5.12b Pressure under a 5.0 mm diameter water drop at a position 0.25 mm from the centre of impact. The impact velocity was 100 m/s.

2.2 μs after contact, and the top of the fourth peak is reached about 3.6 μs after contact. In Chapter 3 it was surmised that oscillations would occur as a result of wave reflections in the drop; it was shown that the pressure at any point will begin to increase rather than continue to decrease when a compression wave from the edge arrives. Although the magnitudes of the peaks cannot be estimated with the theory developed in this work, the times at which they occur can be determined from the geometry of the pressure waves within the drop and the positions of the free surface of the drop.

There is, however, a complication here. By the time the first compression waves have been initiated the jets will have been formed and the edge positions will no longer be given by Equation 3.1b - the particle flow behind the jets will have taken the edges of the drop out across the surface of the solid to greater distances from the centre of impact than those estimated with this equation. Nevertheless, in a first approximation this may be neglected, since the photographs of the impact show quite clearly that the jets travel out much faster than the edges - the distances between the fronts of the jets and the inside edges of the drop increase as the impact proceeds rather than stay constant. (See, for example, the sequence of pictures shown in Fig. 4.14.) Thus the positions of the free surfaces seen by the pressure waves as they approach the edges of the drop will still be given by Equation 3.1b.

The first compression waves will reach the centre of the drop 0.85 μs ($15t_c$) after contact. They will reach the far edges of the drop 1.42 μs ($25t_c$) after impact, where they will reflect as waves of tension. These waves will reach the centre of the drop about

2.0 μs ($35t_c$) after impact. This is very close to the time that the top of the third peak (in Pulse (f)) is reached.

It can be seen, then, that pressures measured at the centre of the drop up to the time the compression waves from the edges arrive is in reasonable agreement with theory, and that the frequency of the pressure oscillations after this period can be estimated by assuming that positions of the edges of the drop behind the jets continue to be given by Equation 3.1b.

In Fig. 5.12b the calculated shape of the pulse that occurs at positions 0.25 mm either side of the centre of impact is shown as a dashed line. The edges of the drop reach these points 0.125 μs after contact. The change of slope occurs about 0.34 μs after impact when the release wave from the edge of the drop on the side opposite to the gauge arrives. The points plotted on the graph are taken from the falling edge of the leading pulse in Fig. 5.11a (b). It can be seen that there is quite good agreement between experiment and theory once the edge of the drop has passed a little way beyond the point. As expected, the pressure at the edge is not infinite.

In Fig. 5.13a a graph showing the variation of pressure with position under the drop at a time of 0.125 μs after impact (when the edge is at a position 0.25 mm from the centre of contact) is shown. The dashed line is taken from the theory developed in Chapter 3. The point at the centre is taken from Pulse (f) in Fig. 5.11a 0.125 μs from the top, and the second point is the peak pressure at a position 0.25 mm from the centre of contact given by Pulse (b) in Fig. 5.11a. If it had been possible to measure pressures at points within this region it is reasonable to suppose that they would have increased outwards with distance from the centre, so that

Fig. 5.13a (Opposite page, top.) Pressure distribution under a 5.0 mm diameter water drop 0.125 μs after impact. The impact velocity was 100 m/s.

Fig. 5.13b (Opposite page, bottom.) Pressure distribution under a 5.0 mm diameter water drop 0.5 μs after impact. The impact velocity was 100 m/s.

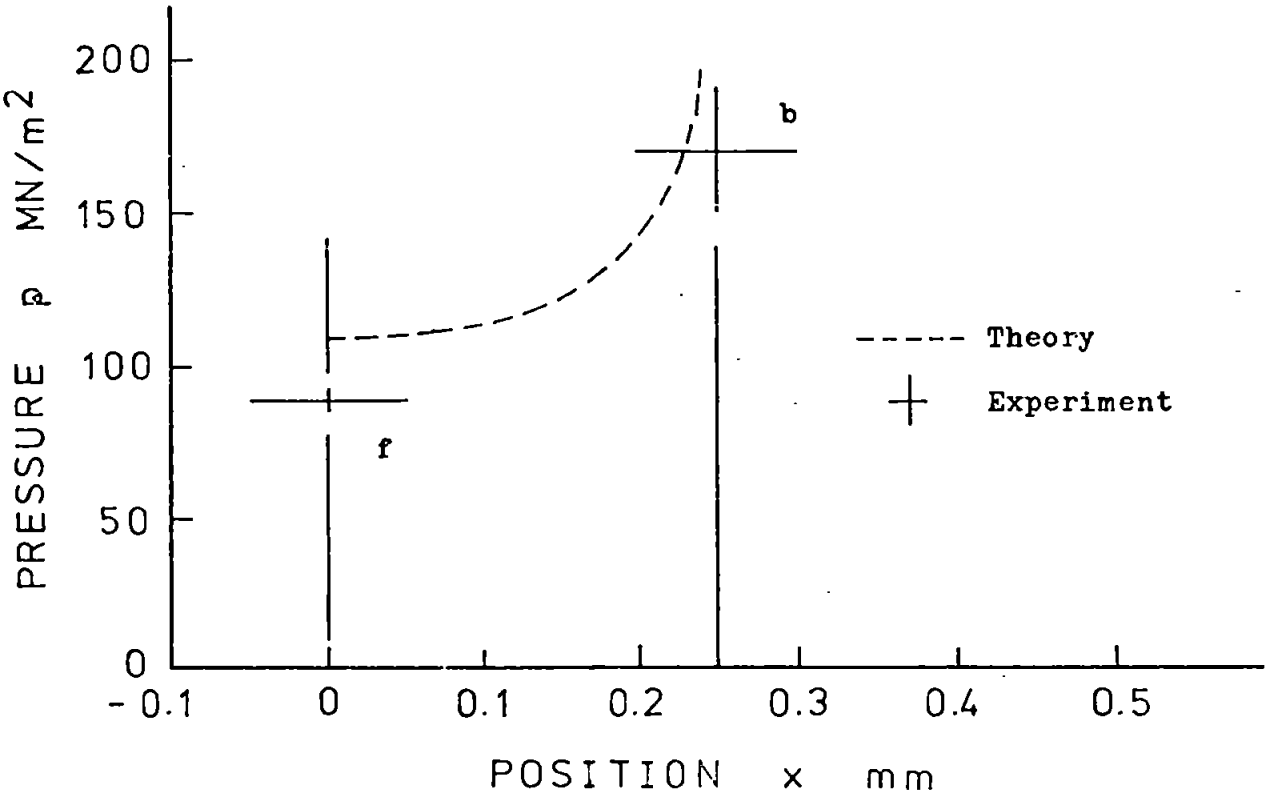
200
150
100
50
0
PRESSURE p MN/m2
b
f
Theory
Experiment
- 0.1
0
0.1
0.2
0.3
0.4
0.5
POSITION x mm

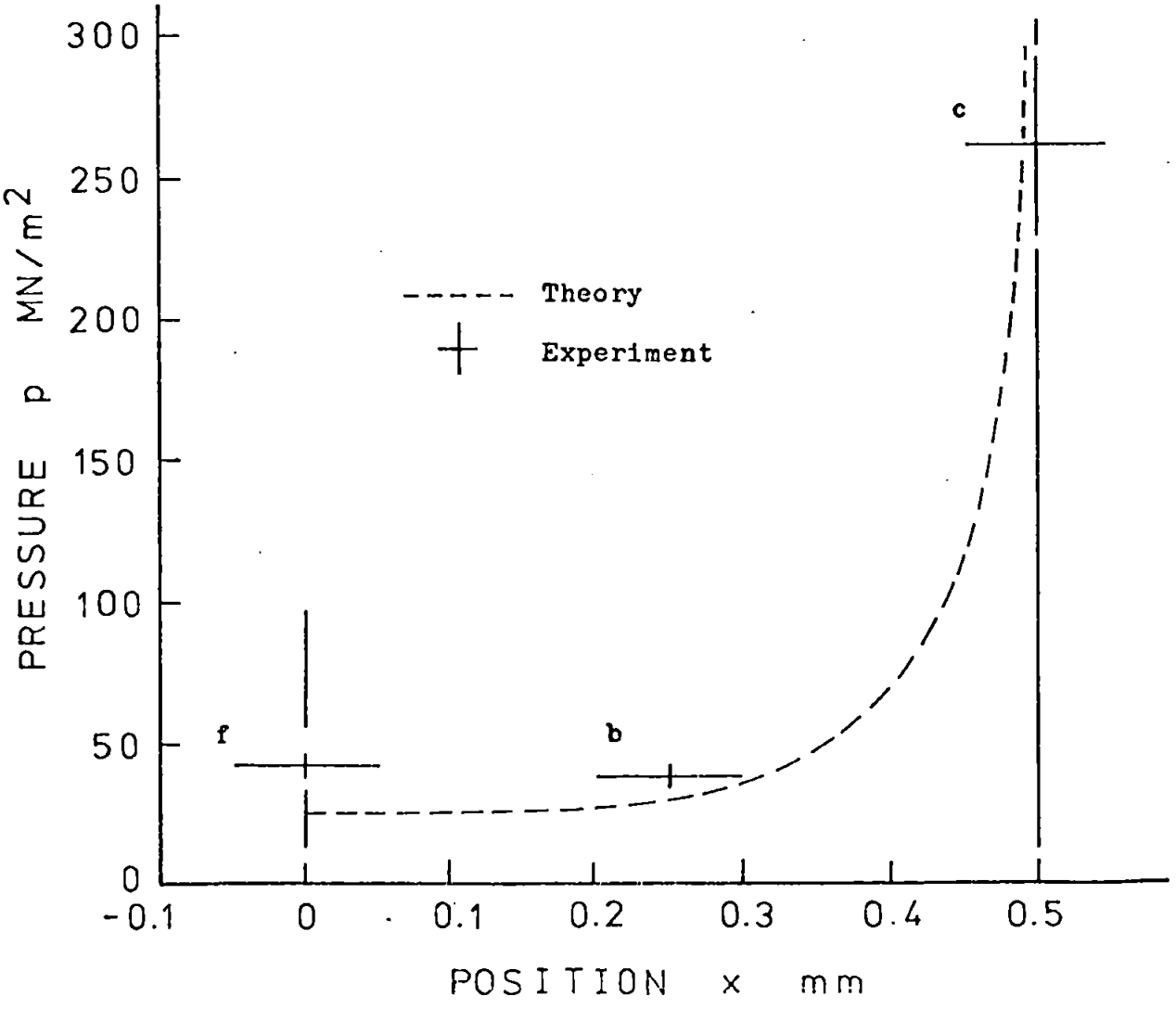
300
250
200
150
100
50
0
PRESSURE p MN/m2
c
Theory
Experiment
f
b
- 0.1
0
0.1
0.2
0.3
0.4
0.5
POSITION x mm

it may be concluded that experiment and theory are in good agreement until very close to the edge of the drop. This pattern is illustrated even more clearly in Fig. 5.13b, which shows the variation of pressure under the drop when the edge is at a position 0.5 mm from the centre of impact. (This occurs 0.50 μs after contact.) The centre point is taken from Pulse (f) 0.50 μs after contact, the second point is taken from Pulse (b) and the third point is the peak pressure at a position 0.5 mm from the centre of impact given by Pulse (c). The agreement between experiment and theory is very striking. It is clear that significant differences between experiment and theory will only occur very close to the edge of the drop. (At distances less than about 0.01 mm from the edge, say - see Fig. 5.13b.)

At distances from the centre of impact greater than 1.0 mm the first pulse of pressure is smaller than some of the following ones. This happens because the points where these pulses were taken are reached when the pressure within the region is falling, that is the point lies behind a tension front. For example, the point $x = 1.5$ mm is reached just before a wave of tension arrives from the far edge of the drop. This wave is reflected in the edge close to the point and returns as a wave of compression; the second pulse (after the reflection) is therefore greater than the first. (See Pulse (a) in Fig. 5.11b.) It is to be noted that negative pressures do not occur anywhere on the contact surface, although at some places the pressure almost falls to zero. (See, for example, (b) and (c) in Fig. 5.11b.)

5.4 The Pressure Distribution within a Drop

5.4.1 Peak Pressure Distribution along the Central Axis of a Drop

A graph showing the variation of peak pressure with position along the central axis of a 5.0 mm diameter water drop when it is struck by a bullet at 100 m/s is shown in Fig. 5.14. A selection of pressure pulses, upon which this graph is based, is shown in Fig. 5.15. The maximum pressure that it was possible to measure in the experiment occurs at a distance of 1.5 mm above the impact point. It was not possible to measure the pressure close to the impact surface, but at a point only 0.5 mm above it the pressure was only 14 MN/m^2, compared with about 40 MN/m^2 1.0 mm above this and, from Fig. 5.9, about 110 MN/m^2 at the impact surface itself.

There is clearly a steep dip in the peak pressure just above the impact surface, beyond the resolution of the gauge. The front of the initial compression wave will have reached a position 0.5 mm above the surface about 0.34 μs after contact. At this time the release waves will have begun to travel into the drop and will have passed through the centre of the contact area. The jets will not have appeared from under the edges of the drop. The dip in the peak pressure therefore implies that a very low, possibly even a negative, pressure is generated along the central axis of the drop close to the surface of the solid. This was deduced from general considerations in Section 3.1, and the above evidence supports the argument presented there. Attempts were made to explore the region close to the contact point, but either very small signals or no signals at all were obtained. More detailed study of this region would require a gauge with a smaller sensitive area than the one

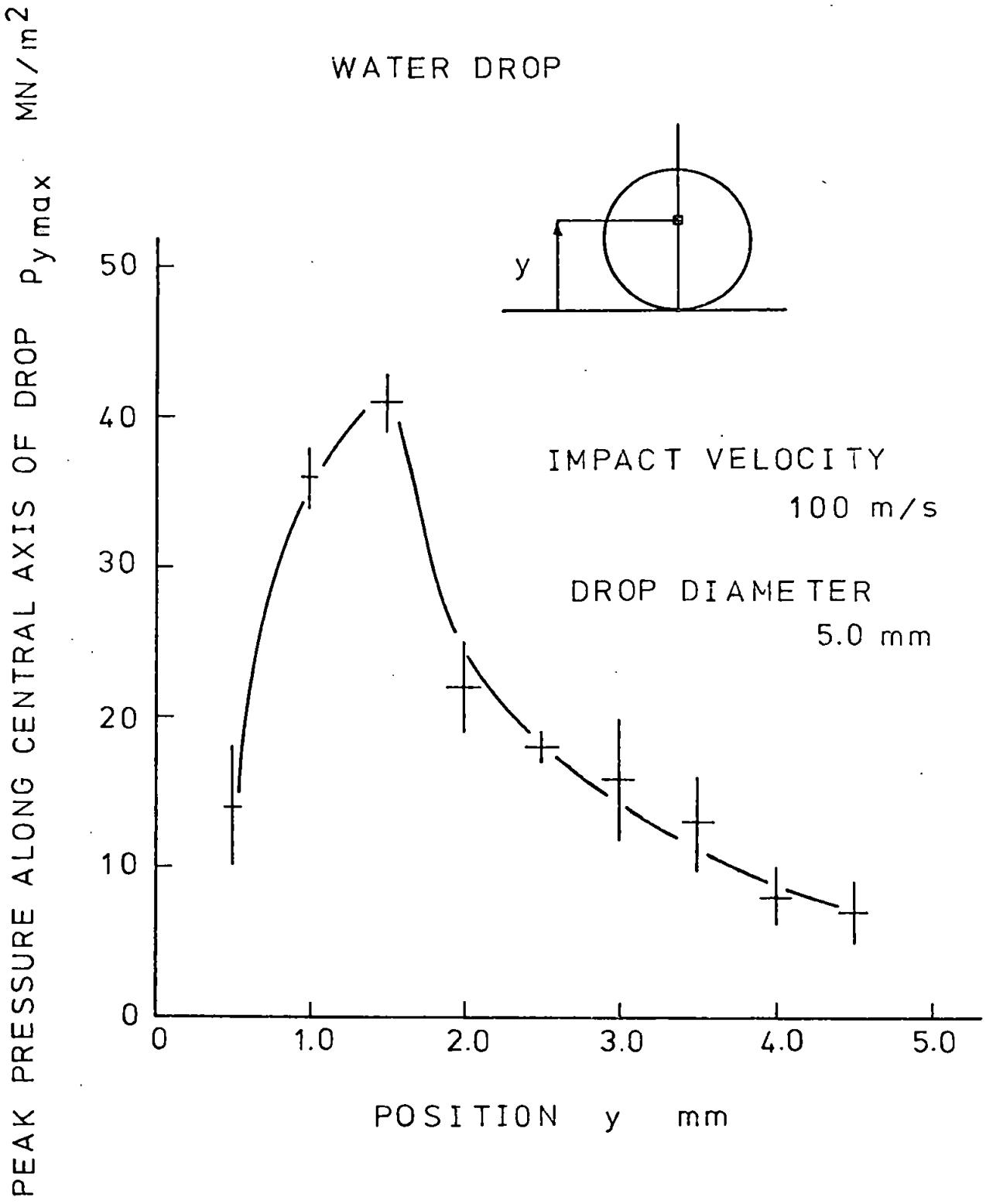

Fig. 5.14 Peak pressure along the central axis of a cylindrical water drop, $p_{y\,max}$, versus position, y.

Fig. 5.15 A selection of pressure pulses obtained at positions along the central axis of a 5.0 mm diameter water drop when it was struck by a bullet at 100 m/s. The magnitudes of the peak pressures are (a) 41 MN/m^2, (b) 43 MN/m^2, (c) 16 MN/m^2, (d) 8 MN/m^2 and (e) 7 MN/m^2. These pulses (and others) were used to plot the points in Fig. 5.14. In (e) negative pressures occur. They were produced when the pressure wave initiated at the impact surface was reflected in the top surface of the drop. (See Fig. 5.2.) Both this pulse and the one at (d) contain high frequency oscillations. They could have been caused by the collapse and expansion of cavitation bubbles, which would have been formed in a negative pressure zone. In (e) the negative pressure is 4 MN/m^2, quite sufficient for this to have happened.

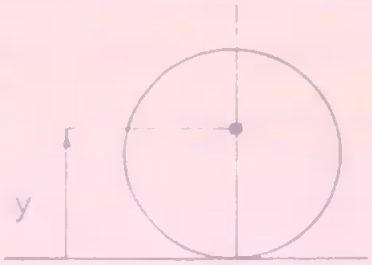
y

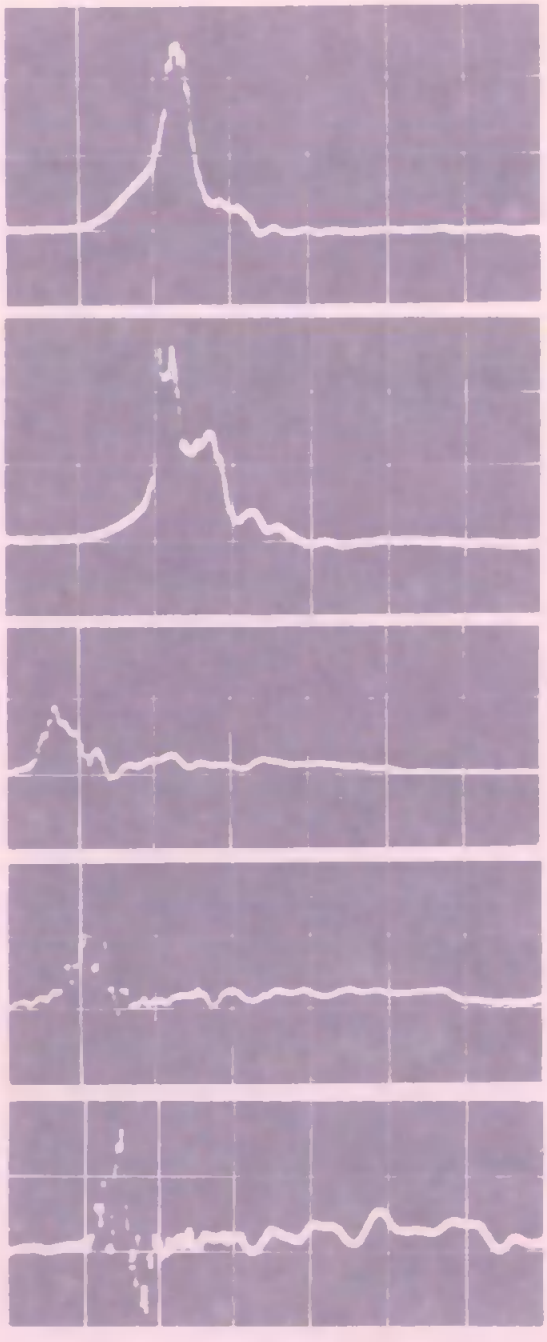
a 15 MN/m2
y = 1.0 mm
b
y = 1.5 mm
c
y = 3.0 mm
d 8 MN/m2
y = 4.0 mm
e 4 MN/m2
y = 4.5 mm
5 µs

used here.

Negative pressures occur close to the top surface of the drop. (See Pulse (e) in Fig. 5.15.) They were produced when the pressure wave initiated at the impact surface was reflected as a wave of tension in the top surface of the drop. (See, for example, Frame (c) in Fig. 5.2.) Very high frequency oscillations can be seen superimposed on the pulses. They could have been caused by the collapse and expansion of cavitation bubbles, which would have been formed in a negative pressure zone. In (e) the negative pressure is approximately 4 MN/m^2, quite sufficient for this to have happened. Unfortunately, in this study cavitation bubbles have not been observed in the upper part of the drop. However, Camus (1971) has photographed cavitation bubbles in this region at lower impact velocities than those that were used here.

5.4.2 Peak Pressure Distribution across a Drop

A graph showing the variation of peak pressure with position across a 5.0 mm diameter water drop at a distance of 1.0 mm above the contact surface when it is struck by a bullet at 100 m/s is shown in Fig. 5.16. The interesting point to observe here is that the peak pressure distribution across the contact area retains its shape at sections above the impact point.

5.5 The Shear Stress Distribution under a Drop

A graph showing the variation of peak shear stress with position under a 5.0 mm diameter water drop when it is struck by a bullet at 100 m/s is shown in Fig. 5.17. A selection of shear stress pulses is shown in Fig. 5.18. The shear stress distribution is symmetrical

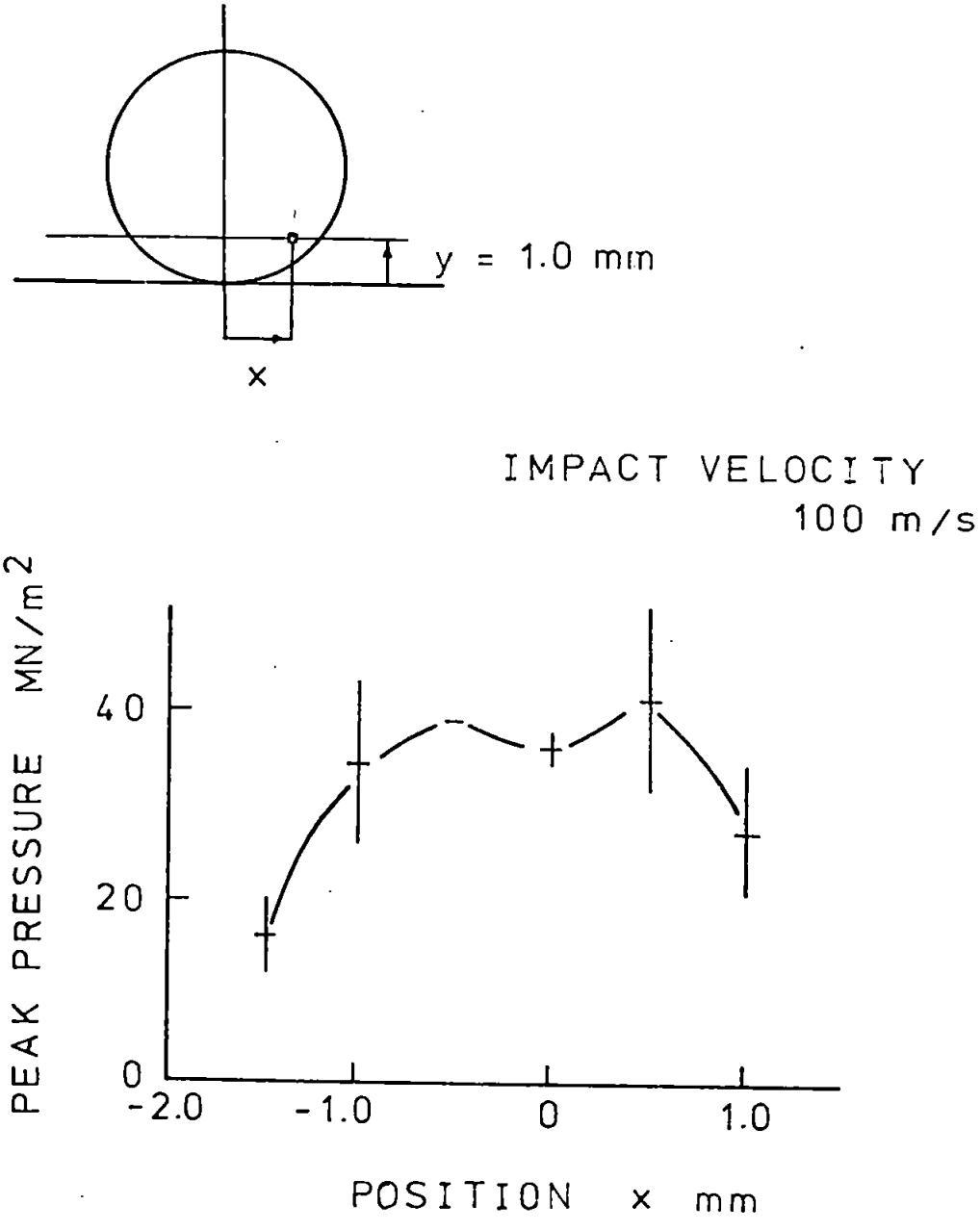

Fig. 5.16 Peak pressure across a cylindrical water drop. The drop diameter was 5.0 mm.

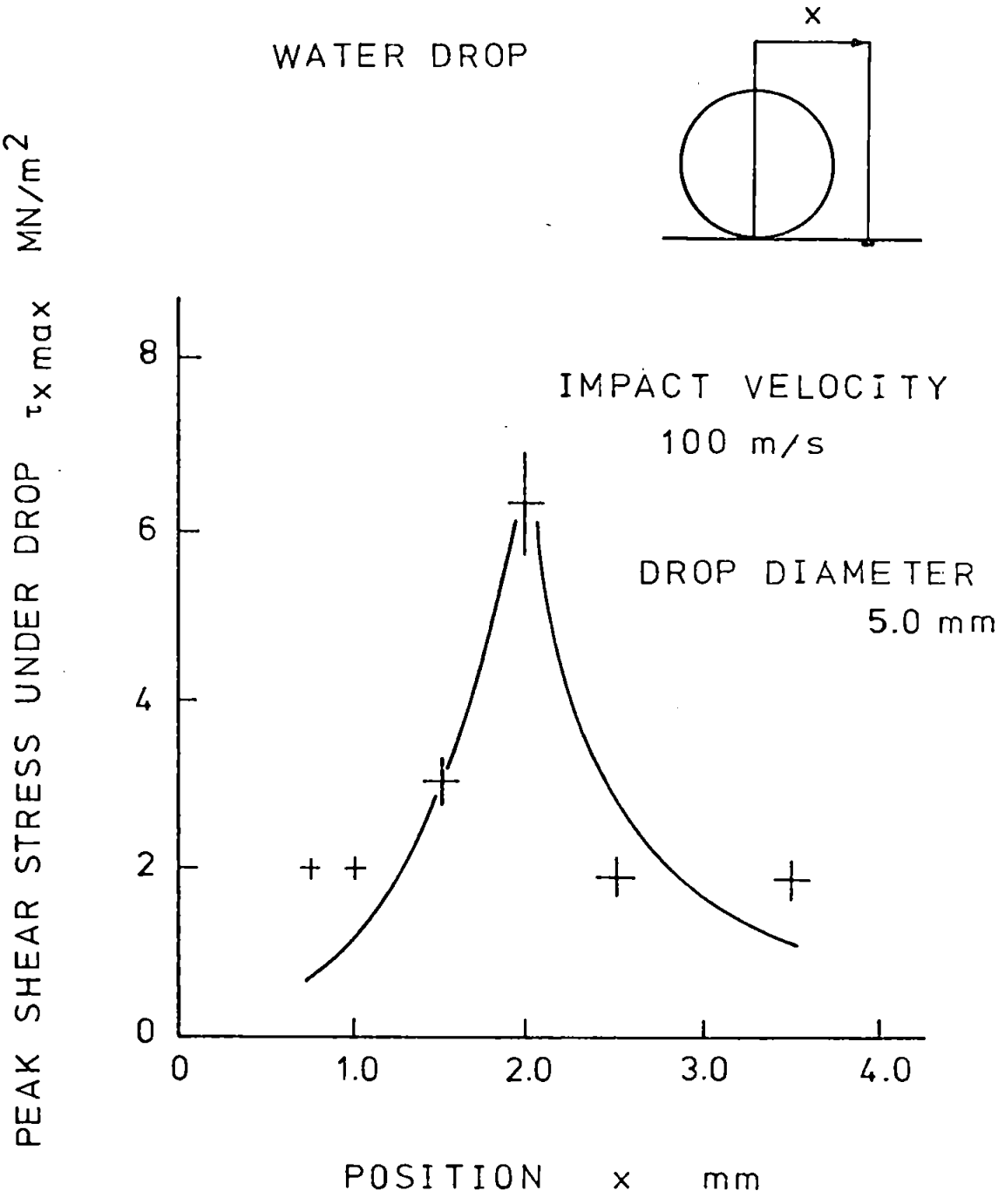

Fig. 5.17 Peak shear stress under a cylindrical water drop, $\tau_{x\,max}$, versus position, x.

Fig. 5.18 A selection of shear stress pulses obtained in an experiment with a water drop. The diameter of the drop was 5.0 mm and the impact velocity was 100 m/s. The peak stresses are (a) 2.0 MN/m^2, (b) 3.0 MN/m^2 and (c) 7.4 MN/m^2. These pulses (and others) were used to plot the points in Fig. 5.17.

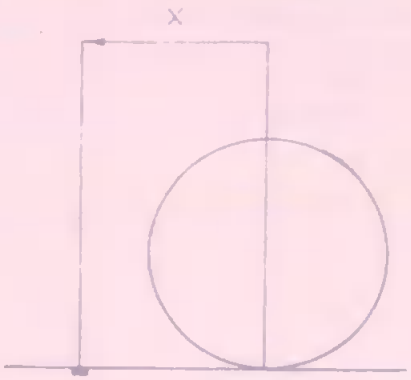
x

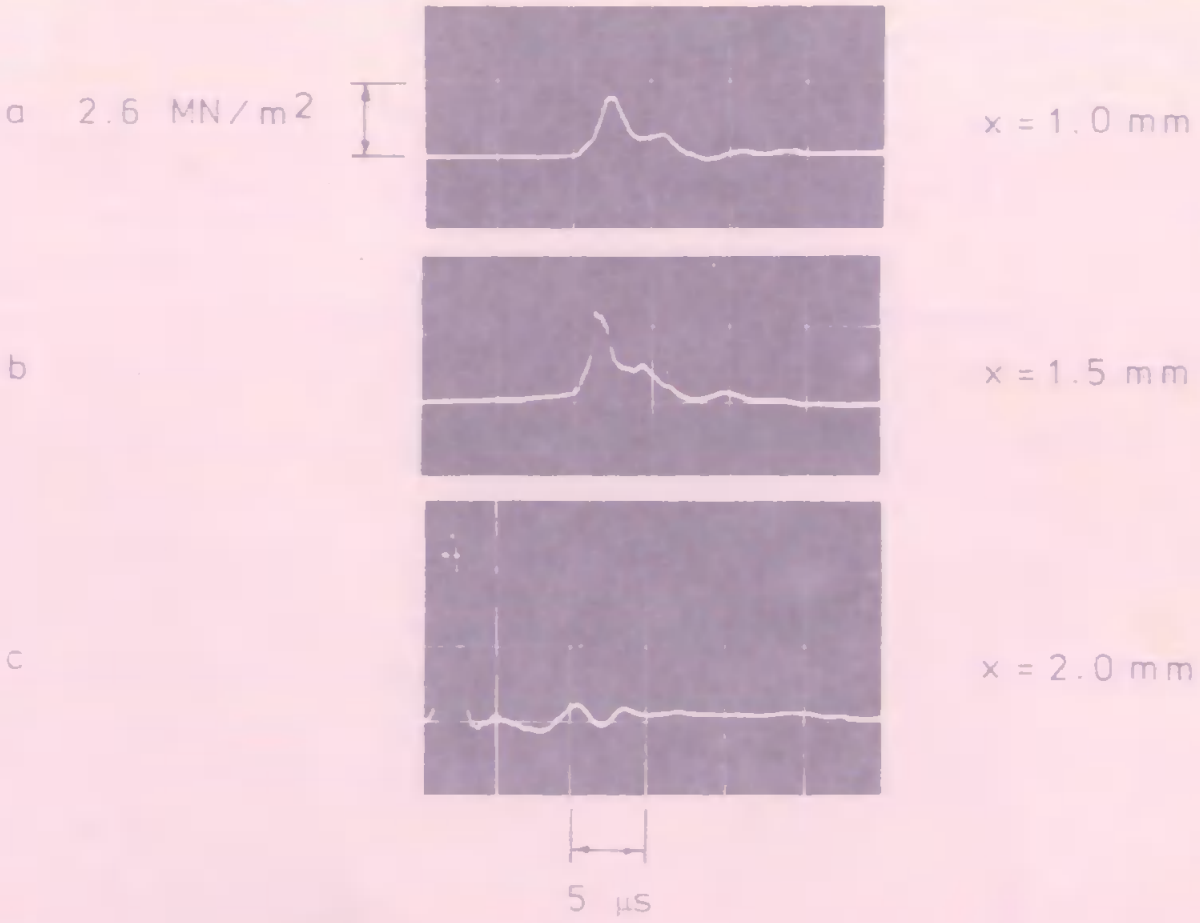
a 2.6 MN/m2
x = 1.0 mm
b
x = 1.5 mm
c
x = 2.0 mm
5 µs

about the centre of impact. (Only results for one side of the contact region are given here.) The stress at the centre is zero. It rises to a peak of about 6.0 MN/m^2 at a distance of 2.0 mm from the centre of impact. It then falls to a more or less constant level of about 2.0 MN/m^2.

The shear stresses develop as flow from under the drop is established. The maximum shear stresses occur in the edges of the drop when the contact region has expanded to about a width equal to the diameter of the drop. They are associated with the very high velocity gradients that exist there. (Over a very short distance - of the order of the half-width of the contact area at the most - particles of water are accelerated from rest to velocities of about the same magnitudes as those of the jets.) The gradients only exist for a short time, since the pulses only last about 5 μs. (See Fig. 5.18.)

5.6 The Effect of Liquid Properties on the Peak Pressure Distribution under a Drop

Results for two liquids - bromobenzene with a density 1.5 times that of water and oil 2 with a viscosity about 16 times that of water - have been obtained. Graphs of peak pressure versus position under the drops are shown in Figs. 5.19 and 5.20 and some typical pressure pulses are shown in Figs. 5.21 and 5.22. Both results are for an impact velocity of 100 m/s. Those for bromobenzene (Figs. 5.19 and 5.21) were obtained with Number 15 flat bullet gauge (and need not be corrected to give the pressure that would have been generated in an impact against a rigid surface) and those for oil 2 (Figs. 5.20 and 5.22) were obtained with Number 12 flat bullet gauge (and must

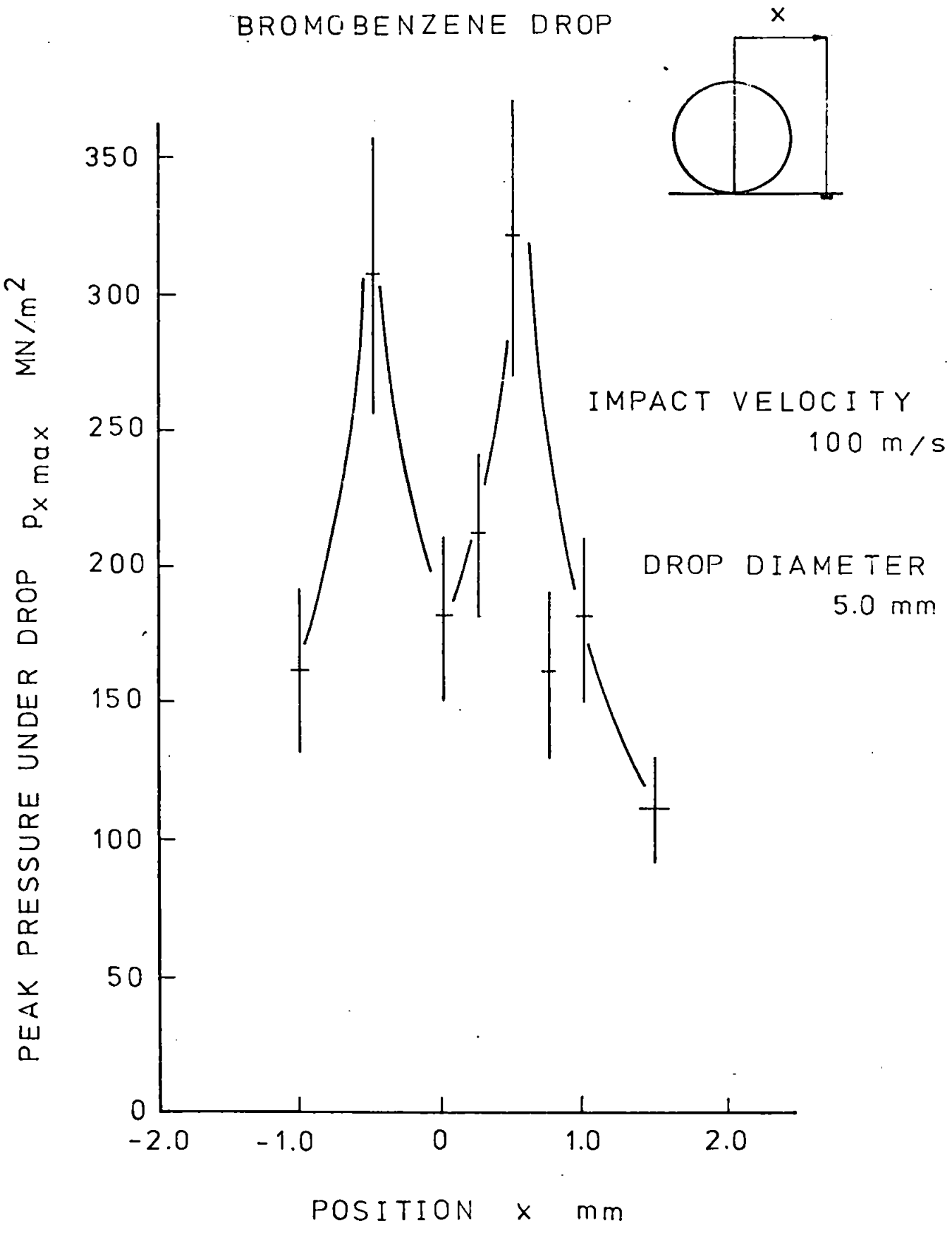

Fig. 5.19 Peak pressure under a cylindrical drop of bromobenzene, $p_{x\,max}$, versus position, x.

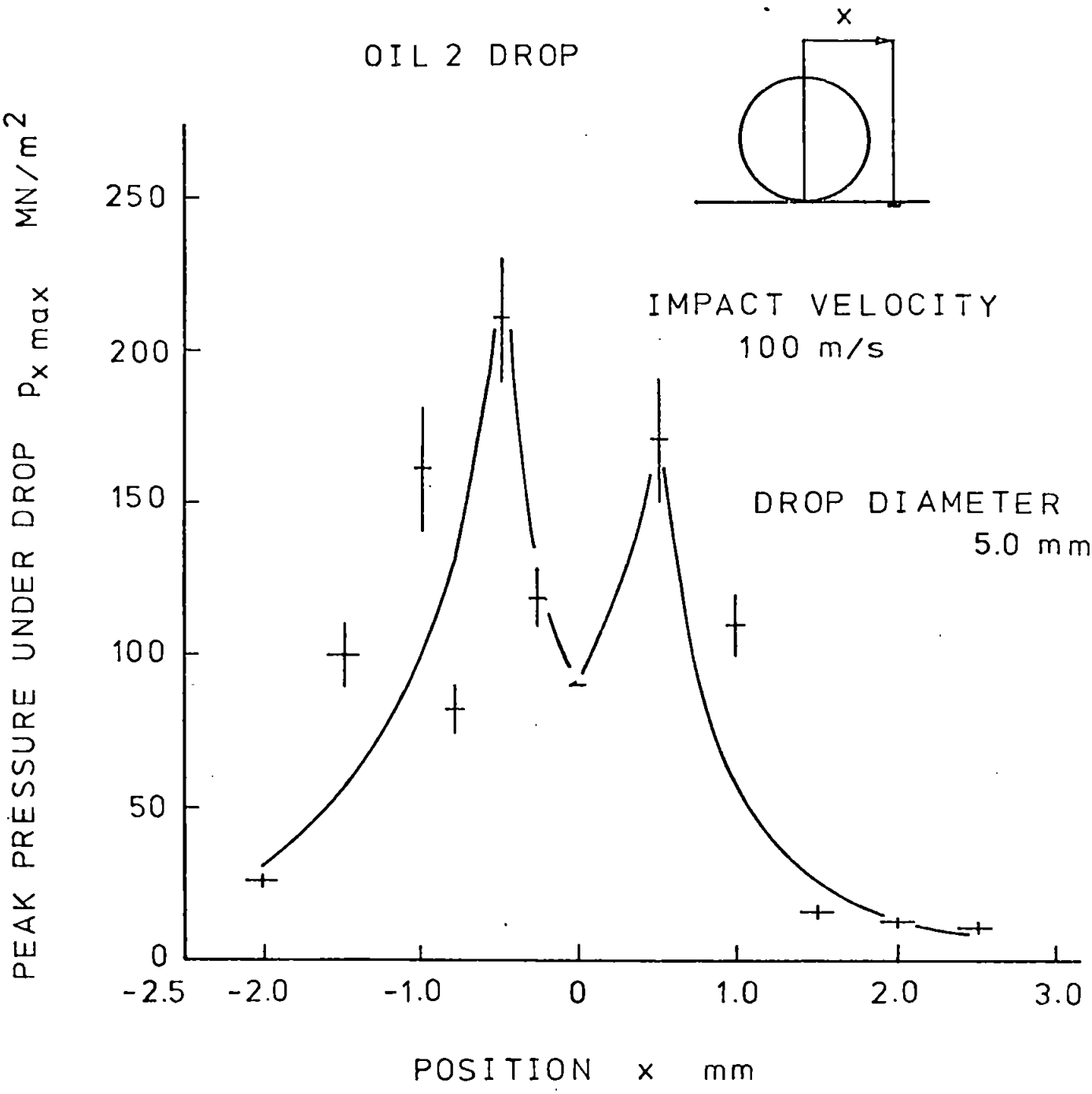

Fig. 5.20 Peak pressure under a cylindrical drop of oil 2, $p_{x\,max}$, versus position, x.

Fig. 5.21 A 5.0 mm diameter drop of bromobenzene was struck by a flat bullet gauge at an impact velocity of 100 m/s. The peak pressures are (a) 180 MN/m^2 and (b) 257 MN/m^2.

Fig. 5.22 A 5.0 mm diameter drop of oil 2 was struck by a flat bullet gauge at an impact velocity of 100 m/s. The peak pressure is 211 MN/m^2.

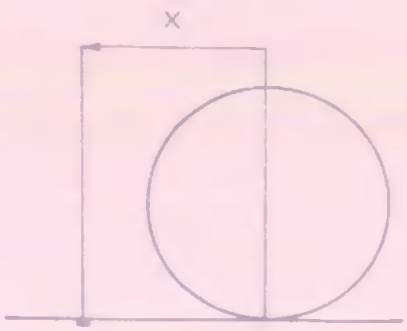

a 120 MN / m^2

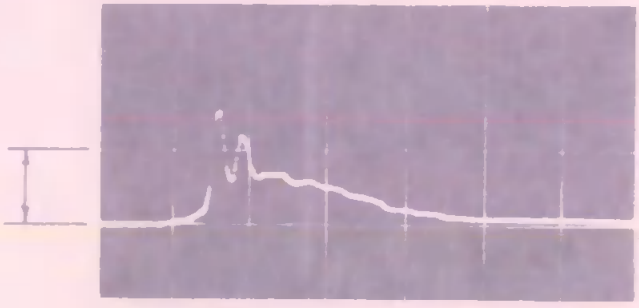

x = 0 mm

b

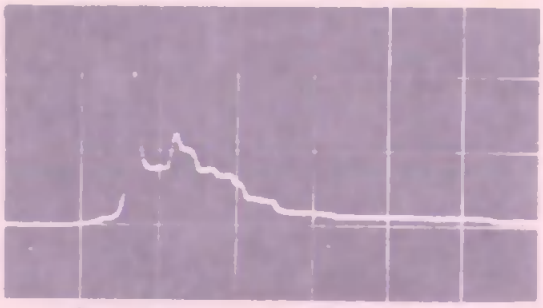

x = 0.25 mm

64 MN / m^2

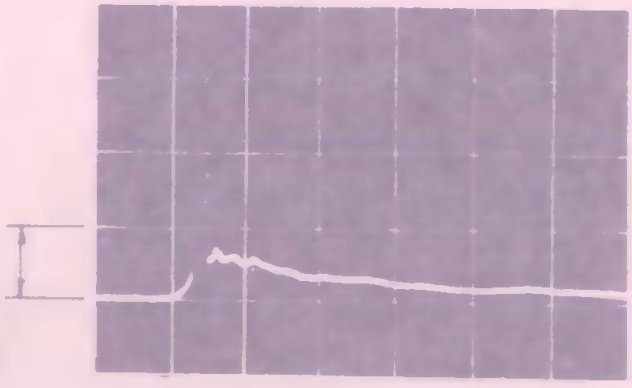

x = - 0.5 mm

be corrected).

It can be seen that the pulse shapes and the pattern of the pressure distribution curves are the same as they were with a water drop. The maximum pressures during the impact occur at positions 0.5 mm either side of the centre of impact. For bromobenzene the pressure at the centre is approximately 180 MN/m^2 ($1.1\rho_0 c_0 V$), and the maximum pressures are approximately 300 MN/m^2 ($1.9\rho_0 c_0 V$). For oil 2 the pressure at the centre is approximately 90 MN/m^2 ($0.7\rho_0 c_0 V$), and the maximum pressures are approximately 200 MN/m^2 ($1.6\rho_0 c_0 V$); when these are corrected to give the magnitudes that they would have in an impact against a rigid solid they become $\rho_0 c_0 V$ at the centre of impact and about $2.2\rho_0 c_0 V$ at the edges.

In the form $p_{x\ max}/(\rho_0 c_0 V)$ the magnitudes of both the pressures at the centre of impact and the maximum pressures at the edges of the drop appear to be much the same for the three liquids studied here. It seems reasonable to infer that this will be true for all liquids. (Note that the maximum pressures observed in the edges of the drop are not necessarily the maximum pressures generated in the impact, since the pressures could only be measured at specific places on the impact surface.)

Some shadow pictures are shown in Figs. 5.23 and 5.24. One important point here - the very high viscosity of oil 4 (more than 60 times that of water) has no influence on the flow of the drop during the early stages of impact.

5.7 Further Results

The effects on the pressure distribution of drop size, drop

Fig. 5.23 (Opposite page, top.) Shadow pictures of a bullet striking a 6.3 mm diameter drop of oil 4 at 93 m/s. The intervals between the frames are (a) and (b) 3.2 μs and (b) and (c) 2.0 μs. The jets in (c) are moving out across the surface of the solid at about 700 m/s. A bow-shaped pressure wave can be seen in (a), about half way across the drop. It has detached from the edges, where a slight fuzziness can be seen, indicating large pressure gradients there. In (a) it is probable that flow is hidden behind the meniscus, so that the flow angle cannot be estimated. With V_j = 700 m/s and V = 93 m/s, V_j/c_o is about 0.8, rather higher than the value of about 0.5 given by Equation 3.13c. This is in keeping with the remarks made earlier in the text that outward flow velocities near the beginning of flow are larger than those that occur later. In (c) a globule of air in the right hand top corner of the drop has started to collapse under the pressures set up around it when the pressure wave passed by.

Fig. 5.24 (Opposite page, bottom.) Shadow pictures of a bullet striking a 5.0 mm diameter drop of bromobenzene at 94 m/s. The intervals between the frames are (a) and (b) 3.2 μs and (b) and (c) 2.0 μs. The jets in (c) are moving out across the surface of the solid at about 600 m/s. This is slightly larger than the value given by Equation 3.13c (about 450 m/s).

a b c

a b c

2 mm

shape, surface profile, acceleration of the surface during impact and impact velocity have been studied. The main trends are described below.

5.7.1 Drop Size

Experiments were carried out with 2.0 mm and 10.0 mm diameter water drops. (Number 15 flat bullet gauge was used.) The impact velocity was 100 m/s. With 2.0 mm diameter drops the highest pressures occurred at distances of 0.25 mm either side of the centre of impact. They were about 450 MN/m^2 ($3\rho_o c_o V$). With 10.0 mm diameter drops the highest pressures were observed at distances of 1.0 mm either side of the centre of impact. The pressure at the centre was about 170 MN/m^2 ($1.1\rho_o c_o V$) and the pressures at the edges were about 200 MN/m^2 ($1.4\rho_o c_o V$).

5.7.2 Drop Shape

Experiments were carried out with an oval water drop in which the major axis was 6.0 mm long and the minor axis was 3.0 mm long. (Number 15 flat bullet gauge was used.) The impact velocity was 100 m/s. When the major axis was perpendicular to the impact surface pressures of about 460 MN/m^2 ($3.1\rho_o c_o V$) were observed at positions 0.25 mm either side of the centre of impact. When the minor axis was perpendicular to the impact surface the highest pressures occurred at positions 1.0 mm either side of the centre of impact and were about 210 MN/m^2 ($1.4\rho_o c_o V$).

5.7.3 Surface Profile

When flat bullet gauges with either 5.0 mm or 1.0 mm diameter

holes in the impact face were fired against 5.0 mm diameter water drops at 100 m/s the maximum pressures at the centre of impact were about 100 MN/m^2. On a rigid surface this would have been about $\rho_0 c_0 V$. In the experiments with the 5.0 mm diameter hole negative pressures were often observed about 5 μs after contact. Why should this have happened? The impact is equivalent to a flat-bottomed drop striking a plane surface. It is known in this case that the pressure goes negative at points on the surface reached by the second reflection of the release wave (Ogilvie (1963) [a]). This wave will reach the centre of impact after a time given by $3R/c_0$; in the present problem this is about 5 μs, as observed. It is significant that no concentration of the impact pressure occurs at the base of the holes, so that this cannot be used to explain the increase in erosion rate that is often observed on pitted surfaces. (This idea has been used by many people - see, for example, Heymann (1968a).)

5.7.4 Acceleration of the Surface during Impact

Pressure measurements were made in a rig similar to that used in a number of erosion experiments. (The apparatus is described in Chapter 4.) The gauge was attached to a rotating disc and struck the side of a jet of water once every revolution. There was therefore a large acceleration perpendicular to the direction of impact. No high edge pressures were observed below 10 m/s, possibly on account of the large size of the ceramic, but as the impact velocity was inceased a zone of high edge pressure appeared that was a maximum on the edge away from the centre of rotation. At 30 m/s a pressure of about 170 MN/m^2 ($3.8\rho_0 c_0 V$) was observed.

a Ogilvie studied the impact of a flat-bottomed solid with a plane liquid surface. This is similar to the present problem at the beginning of impact.

5.7.5 Impact Velocity

Experiments were carried out with 5.0 mm diameter water drops at impact velocities in the range from 80 m/s to 120 m/s. (Number 15 flat bullet gauge was used.) Pressures at the centre of impact were about $\rho_0 c_0 V$ and those at the edges were about $1.6\rho_0 c_0 V$. At 80 m/s maximum pressures occurred at positions somewhere between 0.25 mm and 0.5 mm from the centre of impact; at 120 m/s they moved out to positions about 0.75 mm from the centre.

5.8 The High Edge Pressures

The agreement between experiment and theory is good apart from the fact that the largest impact pressures under a drop do not occur at the positions on the surface where the release waves are formed. In the above paragraphs results for water drops at impact velocities in the range from 80 m/s to 120 m/s and results for two different liquids at 100 m/s have been given, so that it should be possible to determine where these high pressures occur in relation to the wave geometry in the drop and the flow from under it across the surface of the solid.

Consider first the results of the experiments with water drops. For a 5.0 mm diameter water drop struck by a bullet at 100 m/s these pressures occur about 0.5 mm either side of the centre of impact. A very short distance beyond this, at a position 0.51 mm from the centre, reached only about 0.01 μs later, the release wave reflects as a wave of compression in the edge of the drop - could this be the place where the highest pressures occur? They cannot be associated with the jets since these first moved out beyond the edges of the drop when the edges were about 0.46 mm from the centre

of impact, about 0.2 μs earlier.

The places where the high edge pressures were observed in the above experiments are shown in Table 5.1, together with the positions of the edges when the release waves are initiated (x_c), the positions of the edges when the release waves catch up with them ($3x_c$) and the positions of the edges when the jets are formed (x_e).

Table 5.1

Geometry of the Impact

Liquid	x_c	$3x_c$	x_e	Observed Position of High Edge Pressure
	mm	mm	mm	mm
R = 2.5 mm, V = 100 m/s				
Water	0.17	0.51	0.46	0.5
Bromobenzene	0.23	0.70	0.54	0.5
Oil 2	0.18	0.53	0.47	0.5
R = 1.0 mm, V = 100 m/s				
Water	0.07	0.20	0.18	0.25
R = 2.5 mm, V = 80 m/s				
Water	0.13	0.40	0.41	Between 0.25 and 0.5
R = 2.5 mm, V = 120 m/s				
Water	0.20	0.61	0.50	About 0.75

On the evidence presented in this table it is difficult to decide

whether the high pressures are associated with the jets or with the release waves. In fact it looks as though the high edge pressures are not associated with either of them. For the moment, then, it must remain a mystery, to be cleared up when the full equations describing the impact are solved. One small deduction can, however, be made. If the jets have already formed before the release waves have caught up with the edges (as they have for all the impacts in Table 5.1 except for the one at 80 m/s) the jets will be given a boost soon after the waves are reflected in the edges because of the sudden increase in pressure there. There is some evidence that this happens; in Fig. 4.14 the jets in Frame (e) have a velocity of about 500 m/s, but in Frame (f), 2.0 μs later, they have increased to 600 m/s.

5.9 Significance of the Results in Relation to the Erosion of Solids

It has been shown that the pressures generated during drop impingement are as high as $3\rho_0 c_0 V$. This is much larger than previously realised. Even at moderate impact velocities (say about 200 m/s) this pressure would be greater than the yield stress of some of the toughest materials. Furthermore, the very high velocity jets that flow out from under the drop will strike any grain boundaries exposed by the impact. Very high stresses tangential to the surface will arise in these impacts, and it is likely that they will be sufficient to tear large pieces of the material out of the surface, perhaps in an undamaged condition.

The presence of cavitiation bubbles on the surface of a solid could lead to very high local pressures, which could be responsible for the tiny indentations that mark the onset of erosion.

5.10 Summary

The peak pressure distributions under 5.0 mm diameter drops of water, bromobenzene and oil 2 for an impact velocity of 100 m/s have been presented. They were symmetrical about the centre of impact. The maximum pressures occurred 0.5 mm either side of the centre. The pressures at the centre were about $\rho_0 c_0 V$, and the pressures at the edges were as high as $2.5\rho_0 c_0 V$ (after allowance for deformation of the gauge).

The peak shear stress distribution under a 5.0 mm diameter water drop and the peak pressure along the central axis of a 5.0 mm diameter water drop for impact velocities of 100 m/s have been presented. The shear stress distribution was symmetrical about the centre of impact. The stress at the centre was zero. It rose to peaks of about 6.0 MN/m^2 at distances of 2.0 mm either side of the centre, and fell to a constant level of about 2.0 MN/m^2 beyond this region. The peak pressure close to the surface of the solid was very small. It was thought that negative pressures may have occurred there.

Other results, showing the effect on the pressure distribution of drop size, drop shape, surface profile, impact velocity and the acceleration of the surface during impact, have also been presented. On rotating surfaces, such as occur in many rain erosion simulators, very high pressures were observed at the edge of the drop away from the centre of rotation.

The results were related to the theory developed in the work and to events observed in photographs of the impact. The positions of the high edge pressures were not correctly estimated with the

theory; they could not be related to the geometry of the impact.

The significance of the results in relation to the mechanism of erosion damage was discussed.

CHAPTER 6

THE INFLUENCE OF THE PHYSICAL PROPERTIES OF THE LIQUID ON THE EROSION OF SOLIDS

There have been very few investigations of the effect of liquid properties on erosion, not only because the eroding fluid has usually been water, but also because theories of erosion that involve liquid properties have only been proposed in recent years. From the results of the work that has been done it may be concluded that erosion damage increases as the density of the eroding liquid is increased, and that it decreases as viscosity is increased. There is not enough information here to assist the engineer working on the design of turbines, so that a more detailed study of the problem is needed. In this chapter experiments are described on the erosion of a typical ductile metal by a number of liquids chosen so that the effects of density, acoustic impedance and viscosity could be investigated separately. Definite trends emerge from this work, and a dimensional analysis of the results leads to a general equation for the rate of erosion of the metal during Stage 2. An energy analysis of the erosion process is given, and an expression for the rate of erosion during Stage 2 that is in reasonable agreement with experiment is developed.

6.1 The Erosion Experiments

Nickel specimens were eroded by several liquids in a wheel-and-jet machine. The liquids that were used in the work are listed in Table 6.1, together with their relevant physical properties. They are divided into two groups. In the first group the densities and sound speeds vary but the viscosities have more or less the same low

values. In the second group the densities and sound speeds are almost the same but the viscosities vary over a wide range.

Table 6.1

Physical Properties of Liquids Used in Erosion Experiments *

Liquid	Density kg/m^3	Sound Speed m/s	Acoustic Impedance $kg/m^2\text{-}s$	Viscosity Ns/m^2
Group 1 [a]				
Ethyl alcohol	0.79×10^3	1,162	0.92×10^6	1.20×10^{-3}
Paraffin	0.80	1,325	1.06	1.36
Water	1.00	1,483	1.48	1.00
Bromobenzene	1.50	1,074/50	1.61	1.49
Carbon tetrachloride	1.63	938	1.53	0.97
Mercury	13.5	1,454	19.7	1.55
Group 2 [b]				
Oil 1	0.825	1,430	1.23	5.5 ± 0.1
Oil 2	0.870	1,420	1.23	16.5 ± 0.5
Oil 3	0.870	1,430	1.25	24 ± 1
Oil 4	0.870	1,460	1.27	64 ± 2

* All values measured at room temperature unless otherwise indicated.

a Kaye and Laby (1966).

b Alexander Duckham Ltd.

The nickel specimens, 20 mm long, 6 mm wide and 3 mm deep, were

machined from cold-rolled bar stock. They were annealed in a vacuum furnace at 900°C for one hour. The target surfaces were polished on a range of silicon carbide papers and a diamond-impregnated cloth to give a CLA surface roughness of the order of 1 μm. The mean hardness of the polished face was measured and from this figure the approximate tensile strength of the material was calculated. These values, and other relevant physical properties of nickel, are collected together in Table 6.2.

Table 6.2

Physical Properties of Nickel Specimens Used in Erosion Experiments

Composition	Density [a]	Sound Speed [a]	Acoustic Impedance	Hardness	Tensile Strength * (approx.)
%	kg/m^3	m/s	kg/m^2-s	kg/mm^3	MN/m^2
99.995	8.9×10^3	4,974	44.3×10^6	66 ± 4	220

a Kaye and Laby (1966).

* In a standard tensile test the 0.2% proof strength of the nickel was found to be about 120 MN/m^2, and the tensile strength (UTS) about 290 MN/m^2.

The wheel-and-jet machine was a modified version of an earlier design (Thomas and Brunton (1970)). A photograph of the rig is shown in Fig. 6.1. Two specimens were bolted opposite one another to the rim of a duralumin disc, which was rotated at high speed by an electric motor. The disc was enclosed in a heavy steel tank. A view inside the tank is shown in Fig. 6.2. Once every revolution the

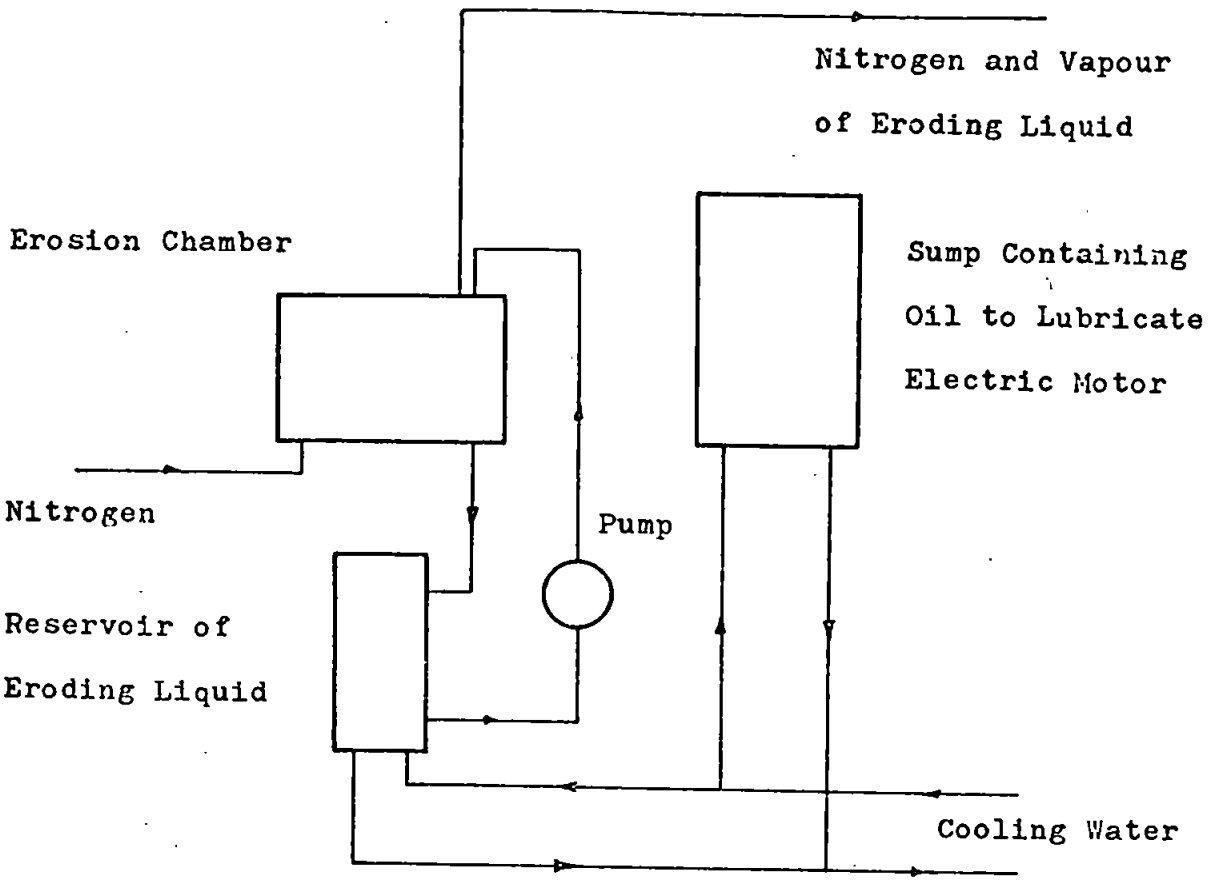

Fig. 6.1 The rig used in the erosion experiments.

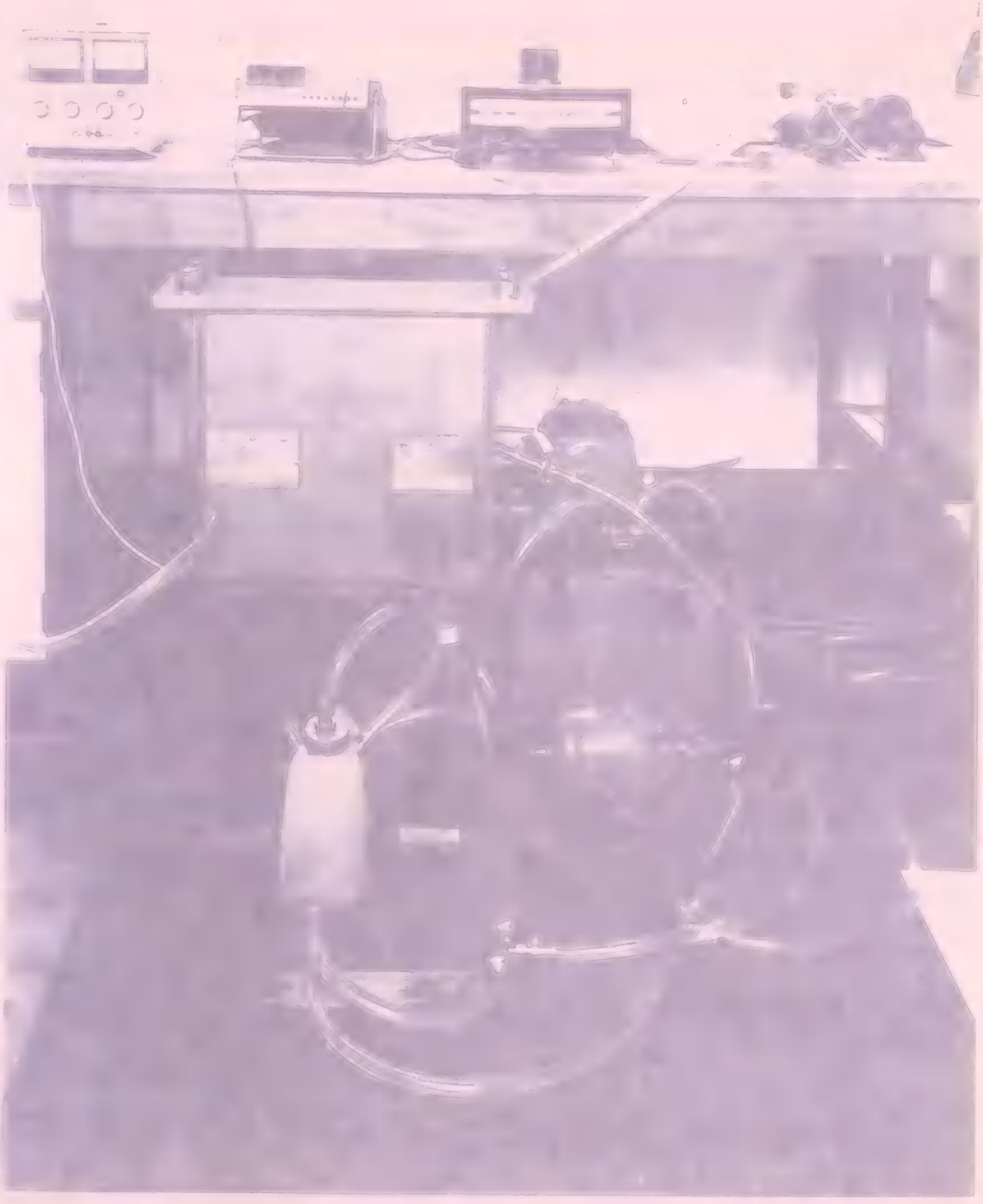

Fig. 6.2 View inside the erosion chamber showing the nozzle, the liquid jet and a duralumin disc with two specimens bolted in place.

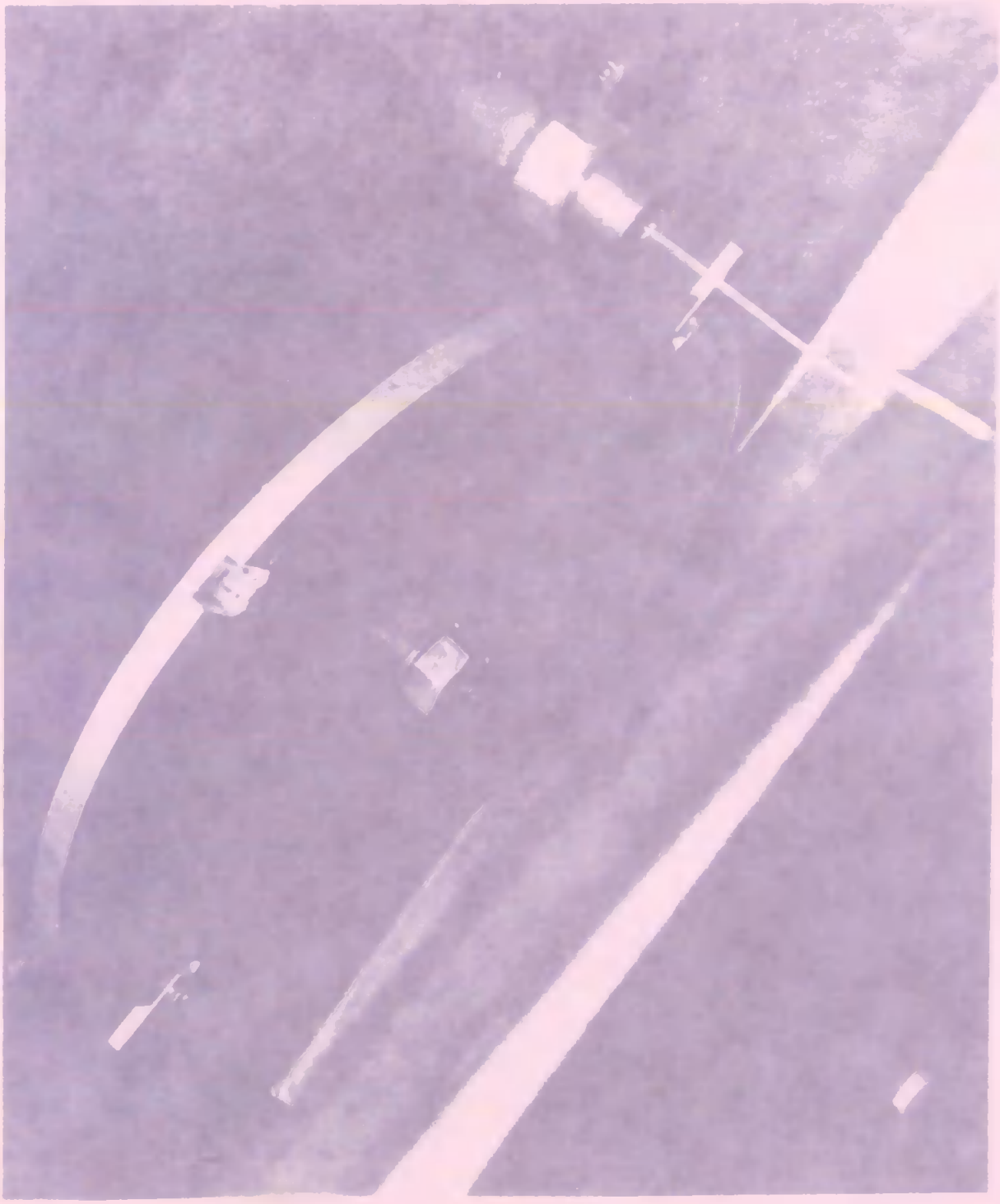

target faces of the specimens cut across a steady jet of liquid which issued from a nozzle screwed into the side of the tank. The nozzle was cast in araldite inside a brass shield, which protected the jet from the air flow set up by the rotating disc. There was a small clearance between the edge of the shield and the sides of the specimens (about 7 mm). It was found that the jet was deformed if this gap were too large and that this had a significant effect on the erosion of the material. The impact frequency was measured with a phototransistor system and a digital counter. The frequency could be varied between 80 and 600 Hz and the impact velocity between 50 and 280 m/s.

The liquid was pumped through the system. The temperature was measured with a thermocouple placed in the line upstream from the nozzle. Good temperature control was essential when the oils were used because their viscosities changed rapidly with temperature. For this purpose the oil reservoir in the circuit was water-cooled. Throughout the experiments the temperature was 20 $\pm$ 1°C.

The jet velocity was maintained at a speed sufficient to ensure that the jet axis remained parallel to the axis of rotation of the disc and that the jet re-formed between impacts. These things were checked with a stroboscope.

When mercury was used as the eroding fluid the pump and reservoir were replaced by a steel tube from which the mercury was forced by a stream of compressed air. The disc which carried the specimens and all other components within the tank were made of steel.

During an experiment the erosion chamber was purged with nitrogen. This reduced any danger of explosions and carried toxic fumes out of

the laboratory. The lid was sealed with a neoprene washer and the axle with a felt washer soaked in oil.

Experiments at an impact velocity of 100 m/s were carried out with all the liquids and at impact velocities in the range from 100 m/s to 210 m/s with water and carbon tetrachloride. Experimental details are given in Table 6.3.

Table 6.3

The Erosion Experiments

Impact Velocity	Impact Frequency	Jet Diameter	Specimen Width
m/s	Hz	mm	mm
100 ± 2	166 ± 4	1.5	3.0
140 ± 2	232 ± 4	1.5	3.0
180 ± 4	188 ± 4	1.5	3.0
210 ± 4	217 ± 4	1.5	3.0

Two specimens were eroded in each experiment, during which mass loss measurements were made at regular intervals.

6.2 Measurement of Erosion Damage

In many investigations of erosion it has been usual to plot graphs of mass loss against either time or number of impacts. Although this is convenient, it makes comparison of results obtained under different experimental conditions difficult. Therefore, for the purpose of correlation of these results with those of other studies of erosion, it seems reasonable to follow Heymann (1967a, 1970)

by using two parameters, the mean depth of erosion, Y_e, and the mean height of impingement, H_i. They are defined as follows:

$$Y_e = \frac{\text{Volume of Material Removed}}{\text{Projected Area of Impact}}$$

$$= \frac{\text{Mass Loss}}{\text{Solid Density} \times \text{Jet Diameter} \times \text{Specimen Width}};$$

$$H_i = \frac{\text{Volume of Liquid Impinged}}{\text{Projected Area of Impact}}$$

$$= \frac{\text{Volume of Cylinder Cut by Jet in Single Impact} \times \text{Impact Frequency} \times \text{Time}}{\text{Jet Diameter} \times \text{Specimen Width}}.$$

It is clear that Y_e is proportional to mass loss and H_i to number of impacts.

6.3 Pattern of Erosion

Graphs of Y_e versus H_i for a selected number of liquids are shown in Figs. 6.3 and 6.4. With the exception of the result for mercury (not shown) and those for carbon tetrachloride at the higher impact velocities, there are three clearly defined stages. These are set out in Fig. 6.5. Stage 1 was not observed with carbon tetrachloride at 210 m/s and Stages 1 and 3 were not observed with mercury. As the density of the fluid increases, the difference in the slopes of the curve during Stages 2 and 3 tends to disappear. In general, the results show that the physical properties of the fluid influence the duration of Stages 1 and 2 and the magnitude and rate of change of the mean depth of erosion during Stages 2 and 3; thus the duration of Stages 1 and 2 decreases with density and increases with viscosity, and the level of damage at the end of Stage 2 and the rate of change

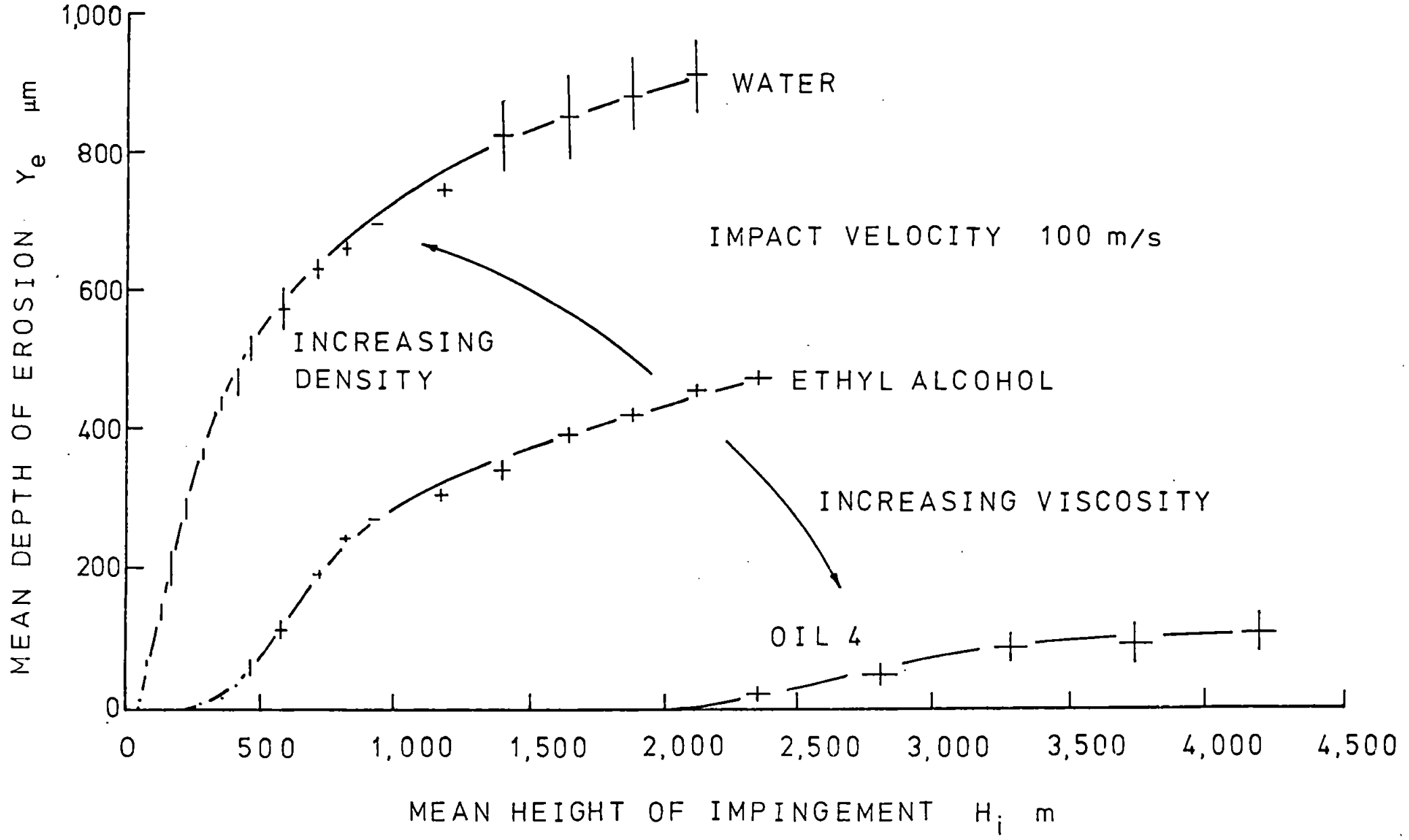

Fig. 6.3 Mean depth of erosion, Y_e, versus mean height of impingement, H_i.

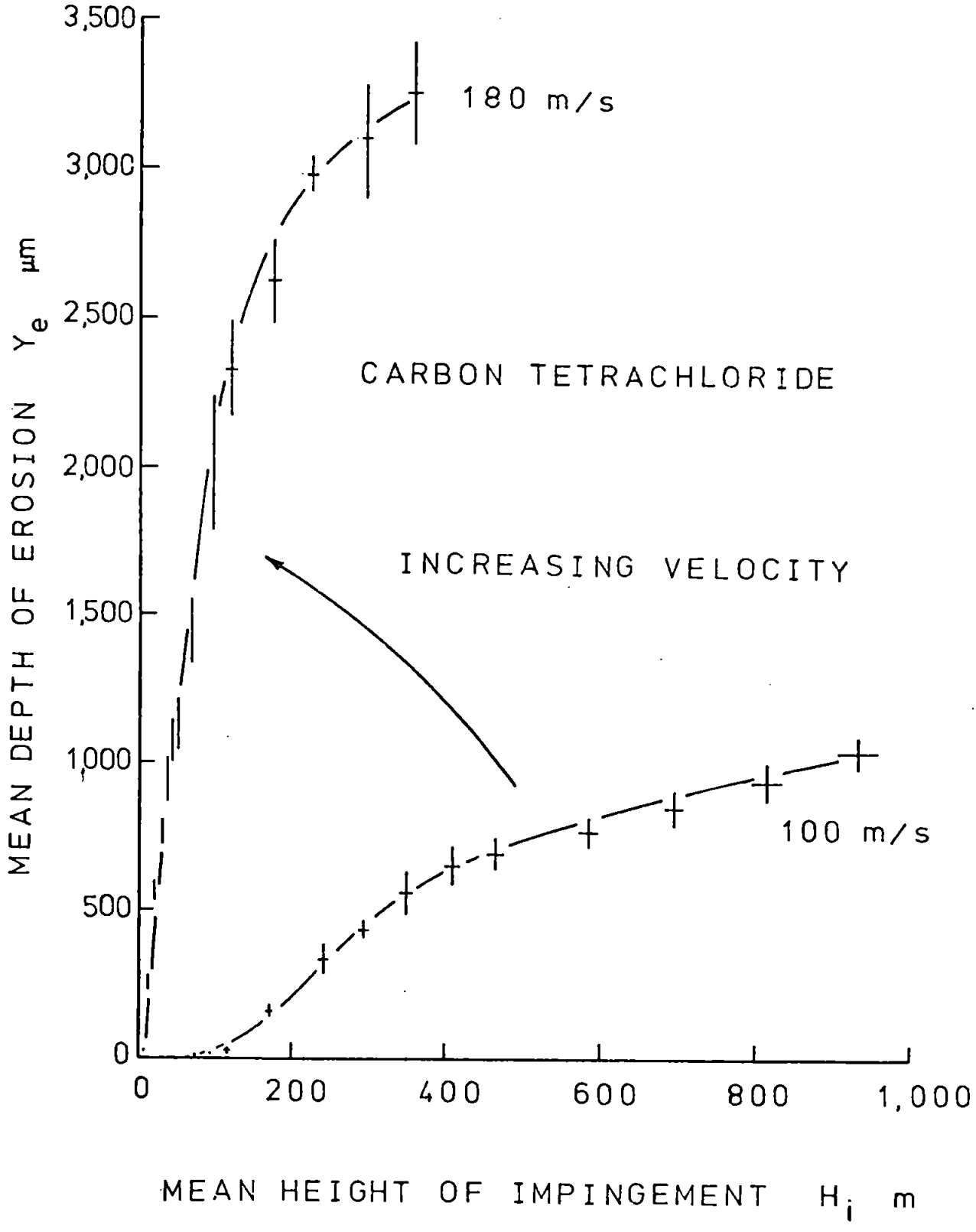

Fig. 6.4 Mean depth of erosion, Y_e, versus mean height of impingement, H_i, for carbon tetrachloride at two impact velocities.

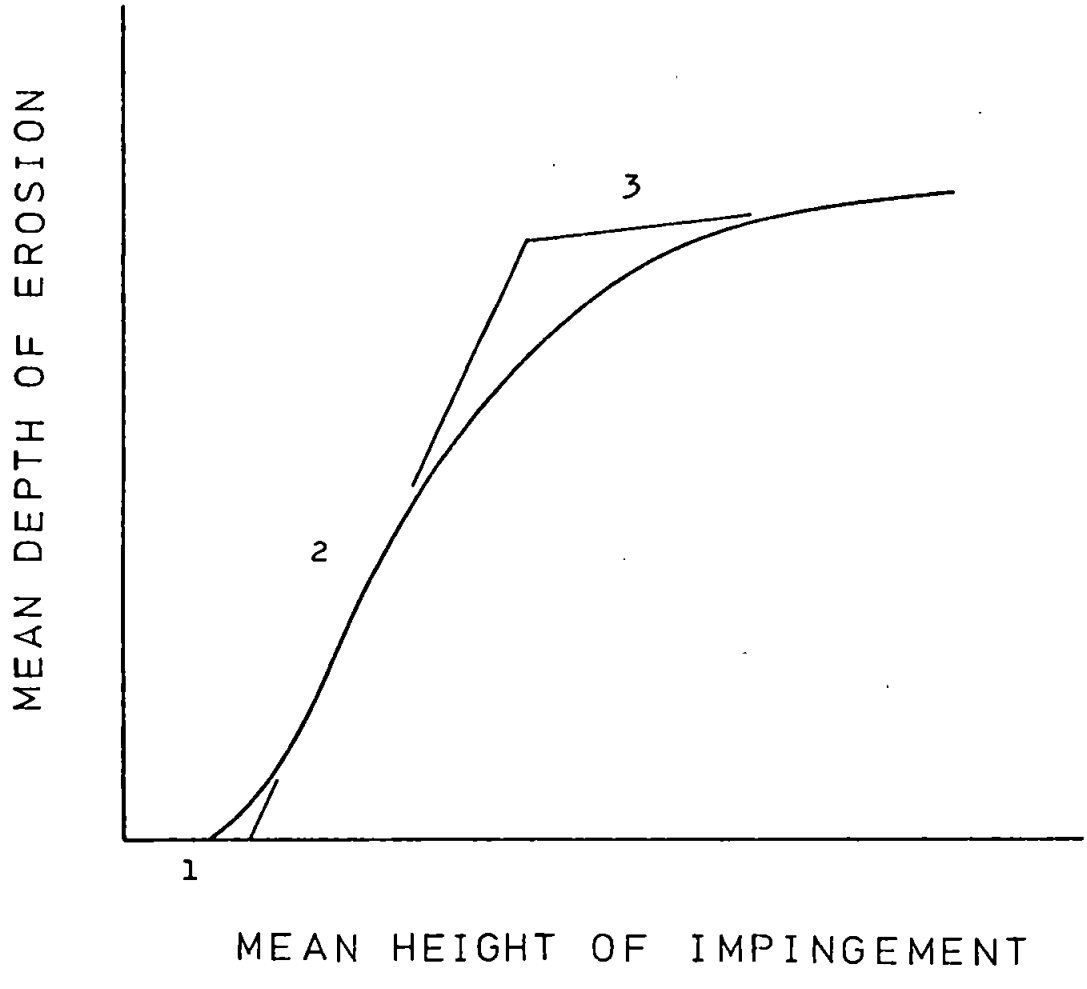

Fig. 6.5 Stages in the erosion process.

of the mean depth of erosion during Stages 2 and 3 increase with density and decrease with viscosity.

The appearance of the surface during erosion followed the pattern described in other investigations (Hancox and Brunton (1966) and Thomas and Brunton (1970)).

Stage 1

The surface was plastically deformed, but no mass loss occurred. At the beginning of this stage the surface was covered with shallow depressions. The depressions grew as the stage progressed. Towards the end of the stage the surface was uniformly covered with these depressions, and the impact force had tilted grain boundaries, so that individual grains were clearly visible. In addition the edges of the specimen bulged out.

Stage 2

The surface was heavily pitted, and material was lost at a more or less constant rate. At the beginning of the stage a few of the depressions formed during Stage 1 developed into large pits. Most of the mass was lost from these places. The areas between the pits, particularly when oil was used to erode the material, had the same appearance during this stage as during the previous one. Towards the end of the stage some of the larger pits had joined up, so that a deep, pitted groove was formed across the specimen.

Stage 3

There was no obvious change in the appearance of the surface, and material was lost at a lower, almost steady rate.

The main differences were for mercury and for carbon tetrachloride at 210 m/s, where deformation and mass loss occurred after only a few impacts. Readings were taken after 2 seconds (after about 300 impacts) for mercury and after 30 seconds (after about 7,500 impacts) for carbon tetrachloride; in both instances a significant mass loss had occurred.

Photographs of nickel specimens at the end of tests in which they had been eroded by a water jet at an impact velocity of 140 m/s are shown in Fig. 6.6. Note that some of the specimens have begun to splay out at the edges of the erosion pits. Material was probably removed from these areas by the cleaved front of the jet as it cut through the specimens. At higher impact velocities it was observed that the specimens had begun to bend, so that fresh surfaces must have been opened up to the impinging fluid at the bottom of the eroded pits. The liquid had also begun to undercut the edges of the erosion pits. These factors could have led to an increase in the rate of erosion damage.

6.4 Relations between Liquid Properties and Erosion Damage

In order to look for relations between liquid properties and erosion damage, suitable measures of damage must be chosen. Since the shapes of the erosion curves are similar to one another (see Fig. 6.5), it was decided to use equivalent points on the curves as a basis for measurements of erosion damage. One such point corresponds to the end of Stage 1 and another to the end of Stage 2. When these points are used, the following measures of erosion damage may be defined: (1) the mean height of impingement at the end of Stage 1, H_1; (2) the mean height of impingement at the end of Stage 2, H_2;

Fig. 6.6 Eroded specimens of nickel at the end of tests using water at an impact velocity of 140 m/s seen from (a) the top and (b) the side.

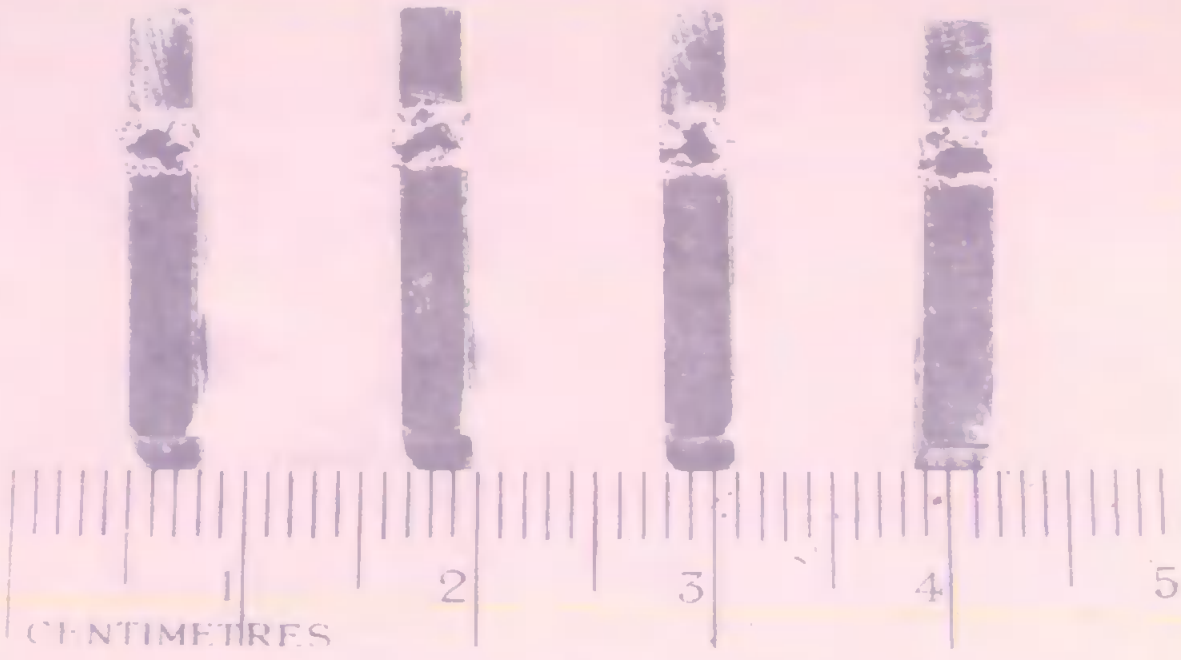

a

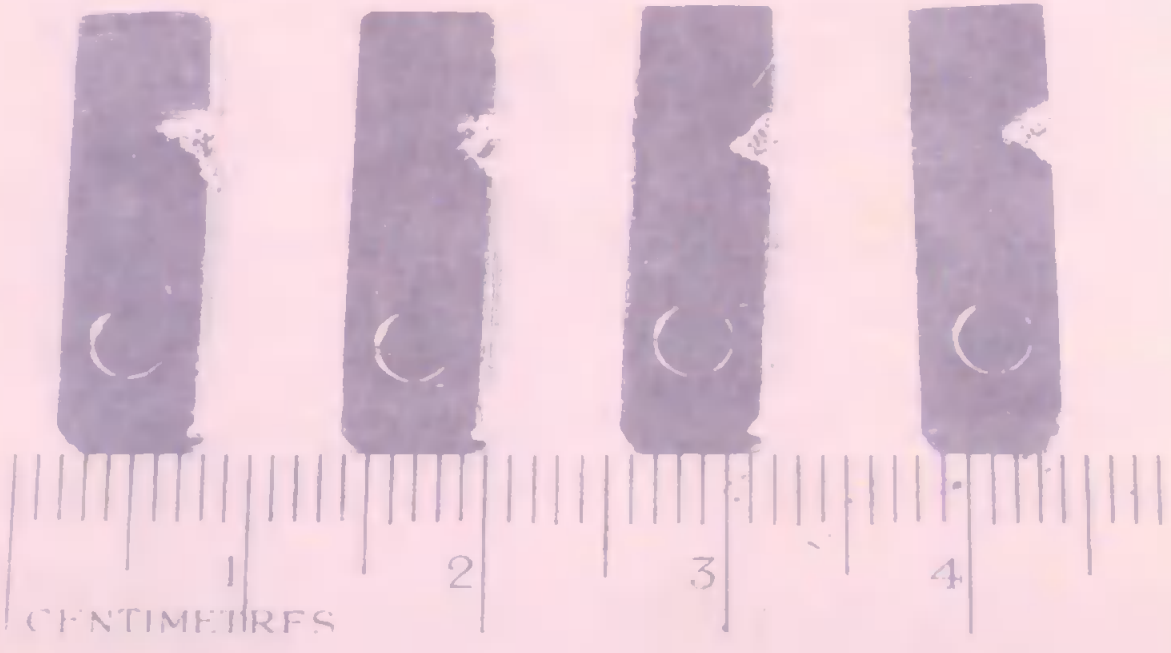

b

(3) the difference between the mean height of impingement at the end of Stages 1 and 2, $H_2 - H_1$; (4) the mean depth of erosion at the end of Stage 2, Y_2; (5) the mean depth of erosion during Stage 3 at an arbitrary mean height of impingement, Y_H; (6) the rate of change of the mean depth of erosion during Stage 2, Y_2'; and (7) the rate of change of the mean depth of erosion during Stage 3, Y_3'. These definitions are illustrated in Fig. 6.7.

The parameters (1) to (7) were measured for each liquid from the curves shown in Fig. 6.3 and from those for the other liquids. Graphs of each of these parameters were then plotted against functions of density, ρ, acoustic impedance, Z, and viscosity, μ. These are shown in Figs. 6.8a to 6.8g. The main findings are summarised in Table 6.4.

From the erosion curve for mercury it was only possible to measure Y_2'. It was $200 \pm 30 \times 10^{-6}$. This result was not used when the straight line in Fig. 6.8f was fitted to the results for the other liquids. For mercury the equation obtained from this graph ($Y_2' = A\rho^2$ - see Table 6.4) gives $Y_2' = 220 \pm 20 \times 10^{-6}$, in excellent agreement with the measured value. It can be concluded from this that the relation between Y_2' and ρ holds over a wide range of density.

Density is related to the energy of the impinging fluid and acoustic impedance to the magnitude of the impact pressure. Since H_1 is not correlated with density but strongly with acoustic impedance, and since both Y_2' and Y_3' are correlated with density and acoustic impedance, it may be concluded that the physical processes occurring during Stage 1 are governed by the impact pressure and that those occurring during Stages 2 and 3 are connected with both energy transfer from the impinging fluid and with the impact pressure. It can be seen that the viscosity of the liquid has a significant

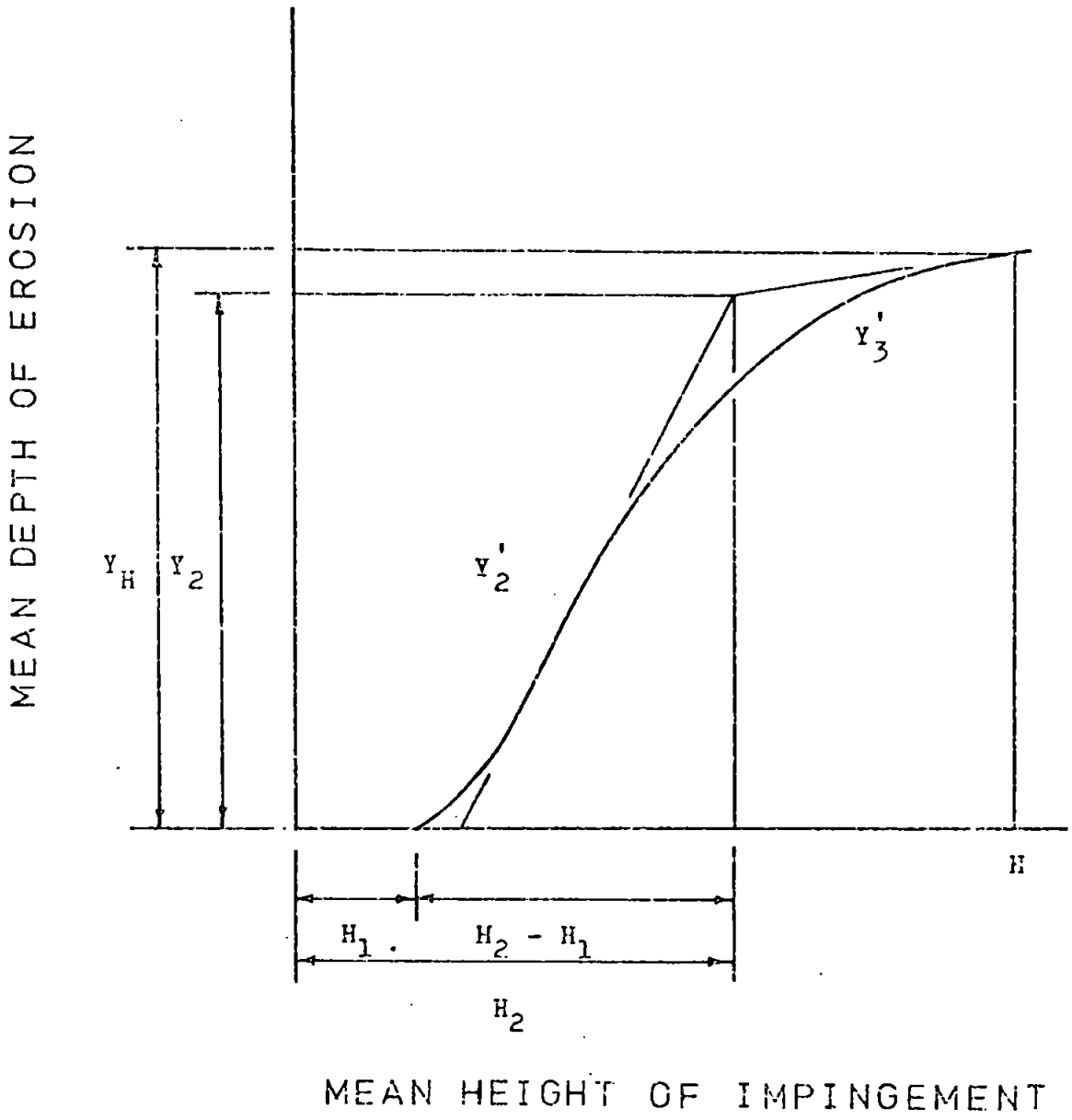

Fig. 6.7 Measures of erosion damage.

Fig. 6.8 Damage parameters versus functions of density, ρ, acoustic impedance, Z, and viscosity, μ. The impact velocity was 100 m/s.

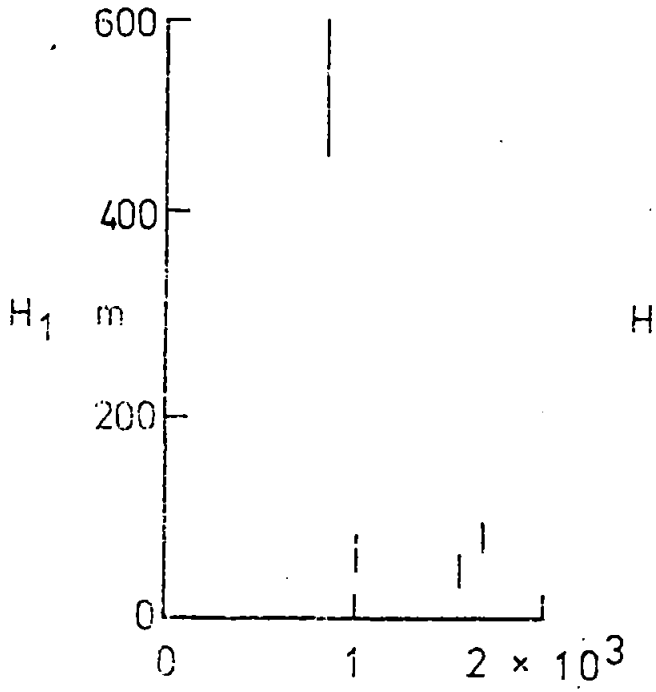
600
400
200
0
H_1 m
0
1
2 × 10³
ρ kg/m³

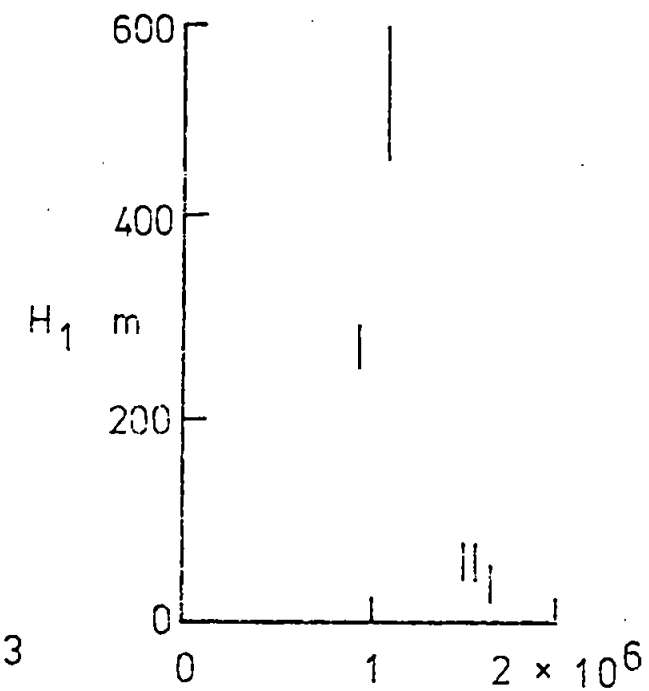
600
400
200
0
H_1 m
0
1
2 × 10⁶
Z kg/m²s

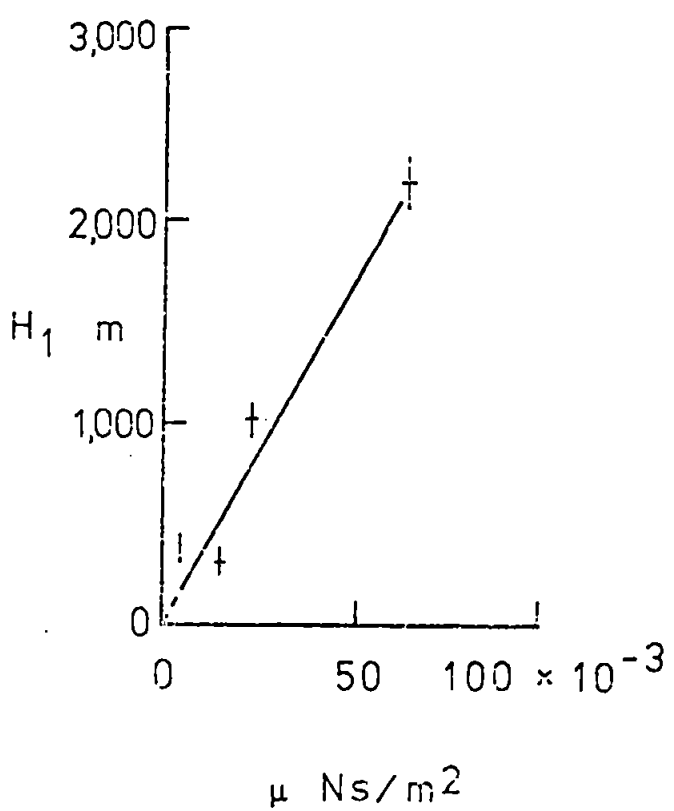
3,000
2,000
1,000
0
H_1 m
0
50
100 × 10⁻³
μ Ns/m²

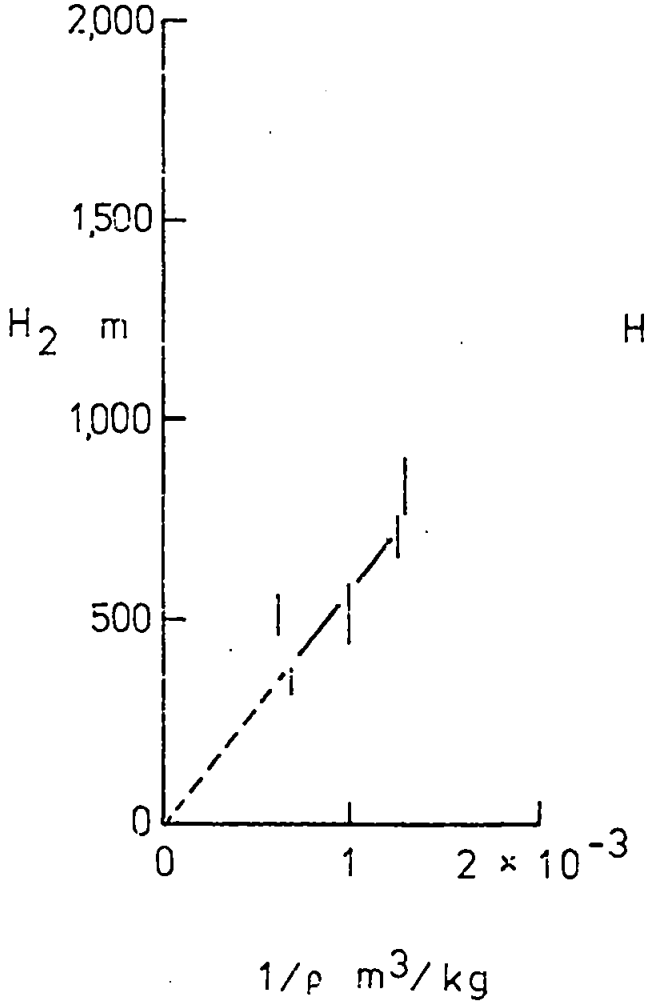
2,000
1,500
1,000
500
0
H_2 m
0
1
2×10^{-3}
$1/\rho$ m^3/kg

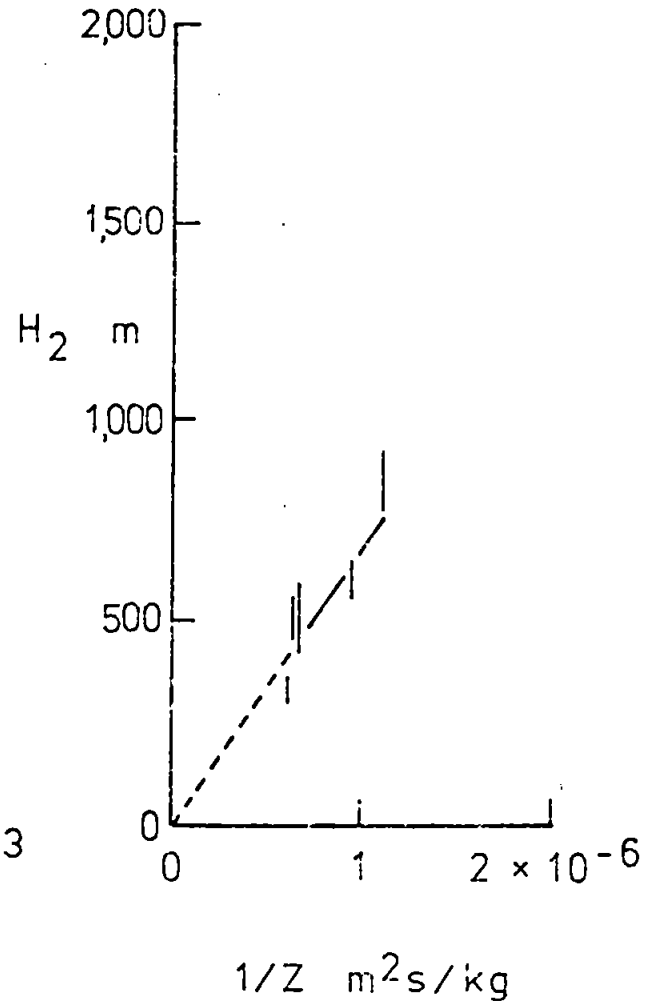
2,000
1,500
1,000
500
0
H_2 m
0
1
2×10^{-6}
$1/Z$ m^2s/kg

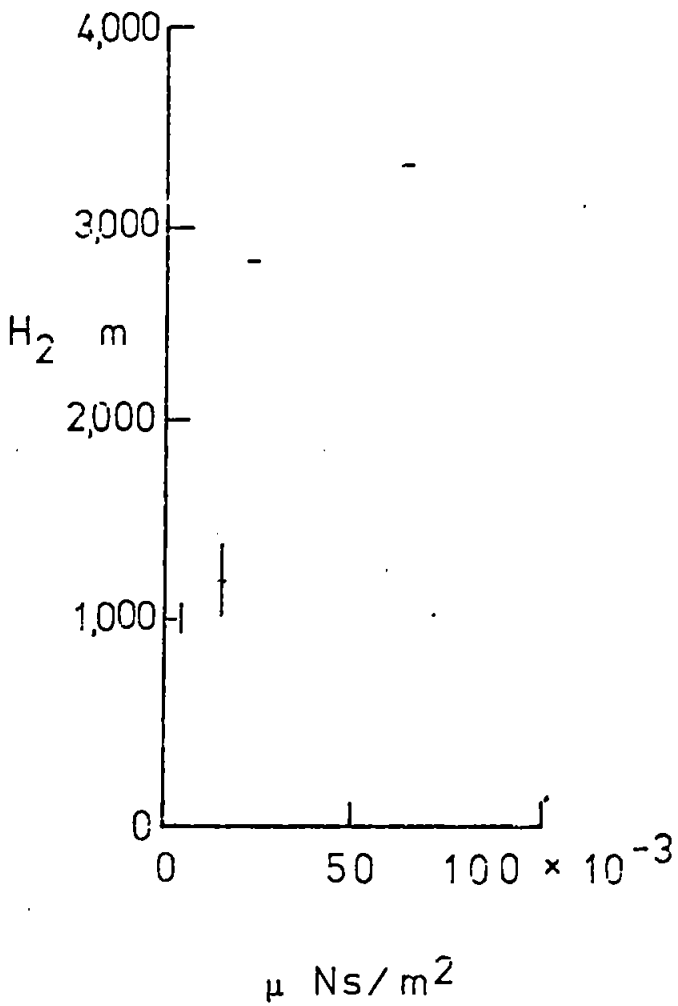
4,000
3,000
2,000
1,000
0
H_2 m
0
50
100×10^{-3}
μ Ns/m^2

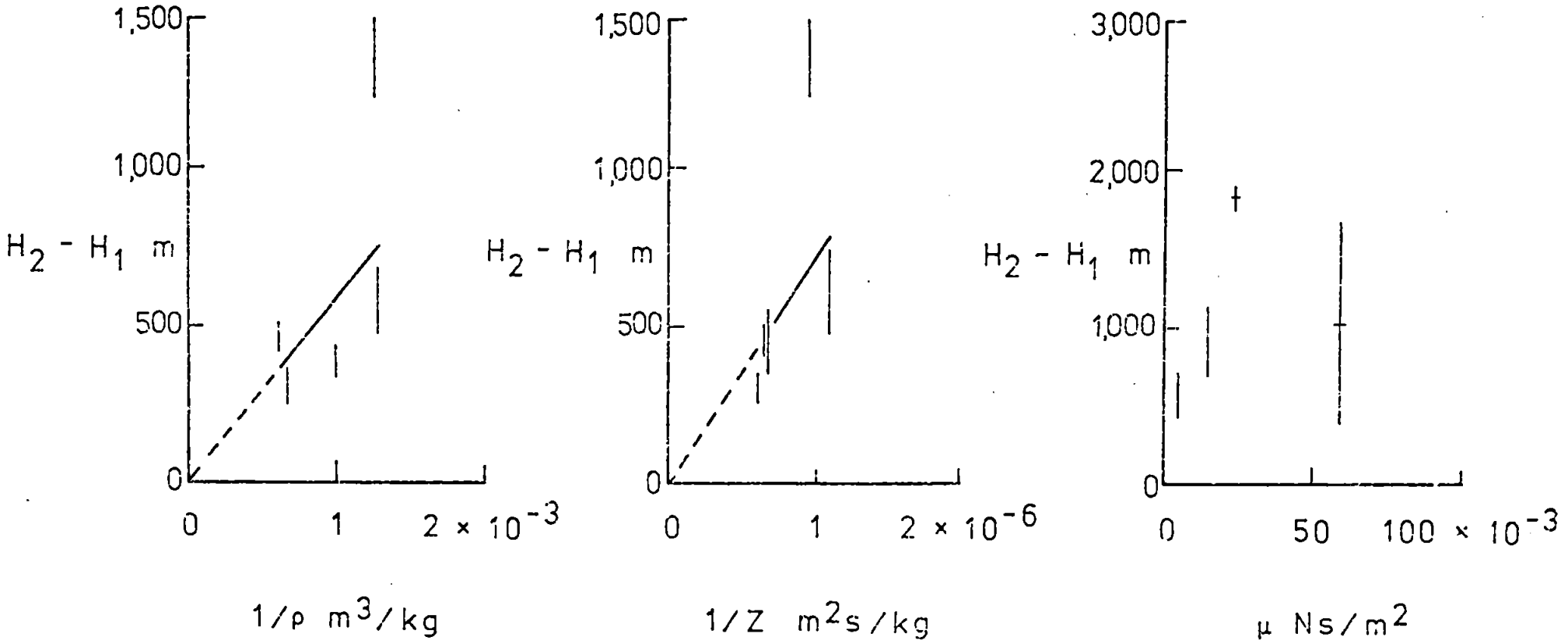
1,500
1,000
500
0
$H_2 - H_1$ m
0
1
2×10^{-3}
$1/\rho$ m^3/kg
1,500
1,000
500
0
$H_2 - H_1$ m
0
1
2×10^{-6}
$1/Z$ m^2s/kg
3,000
2,000
1,000
0
$H_2 - H_1$ m
0
50
100×10^{-3}
μ Ns/m^2

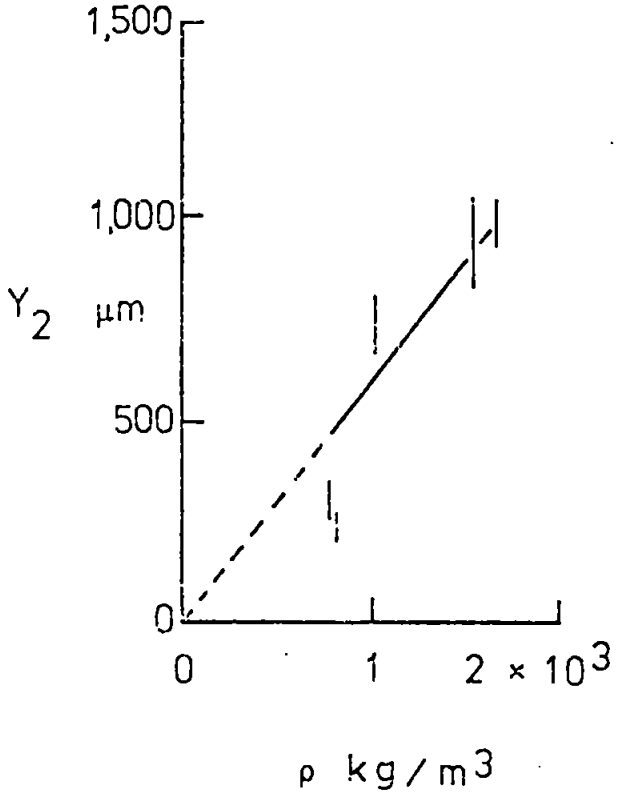
1,500
1,000
500
0
Y_2 µm
0
1
2×10^3
ρ kg/m3

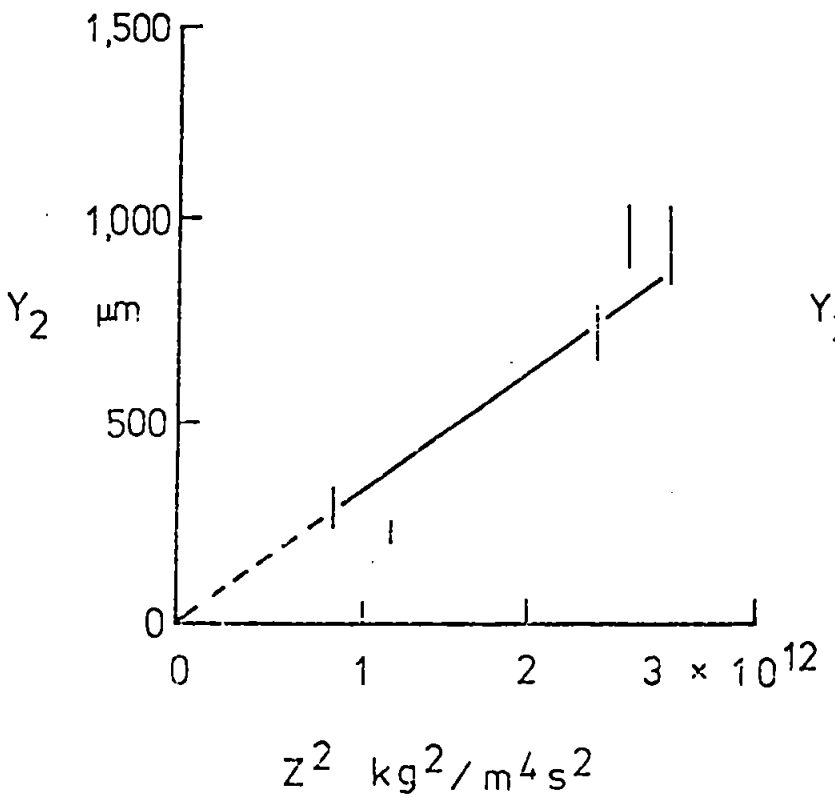
1,500
1,000
500
0
Y_2 µm
0
1
2
3×10^{12}
Z^2 kg^2/m^4s^2

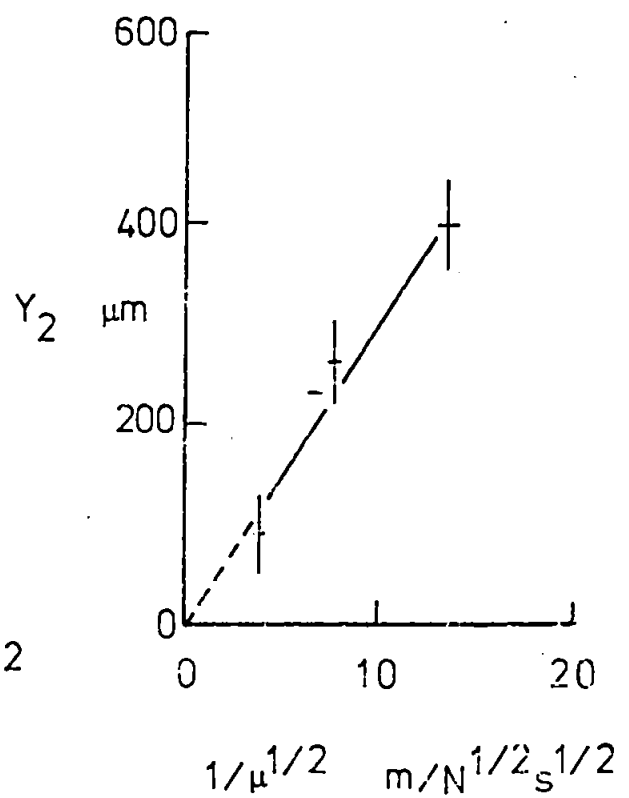
600
400
200
0
Y_2 µm
0
10
20
$1/\mu^{1/2}$ $m/N^{1/2}s^{1/2}$

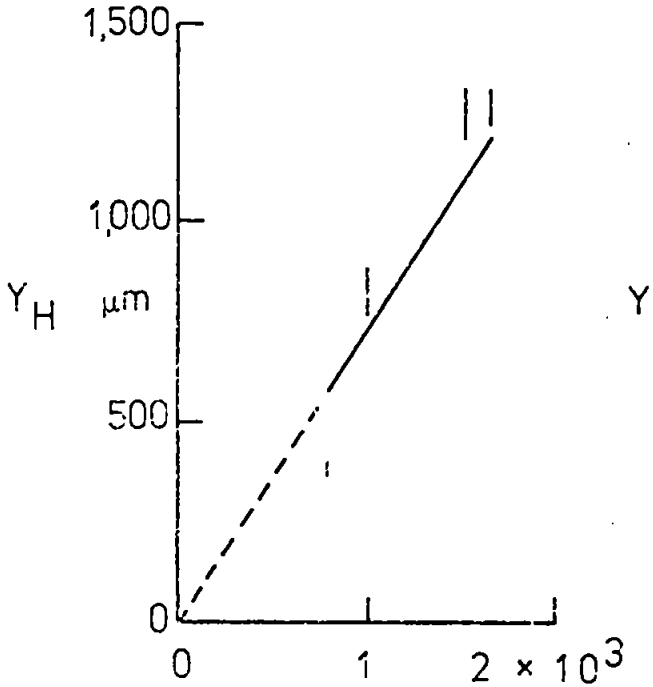
1,500
1,000
500
0
Y_H µm
0
1
2 × 10³
ρ kg/m³

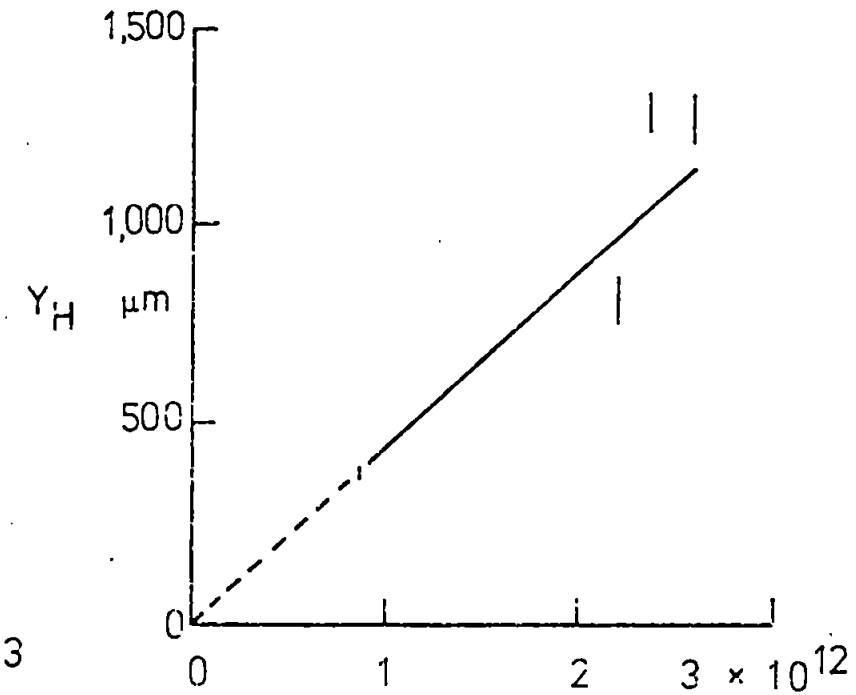
1,500
1,000
500
0
Y_H µm
0
1
2
3 × 10¹²
Z² kg²/m⁴s²

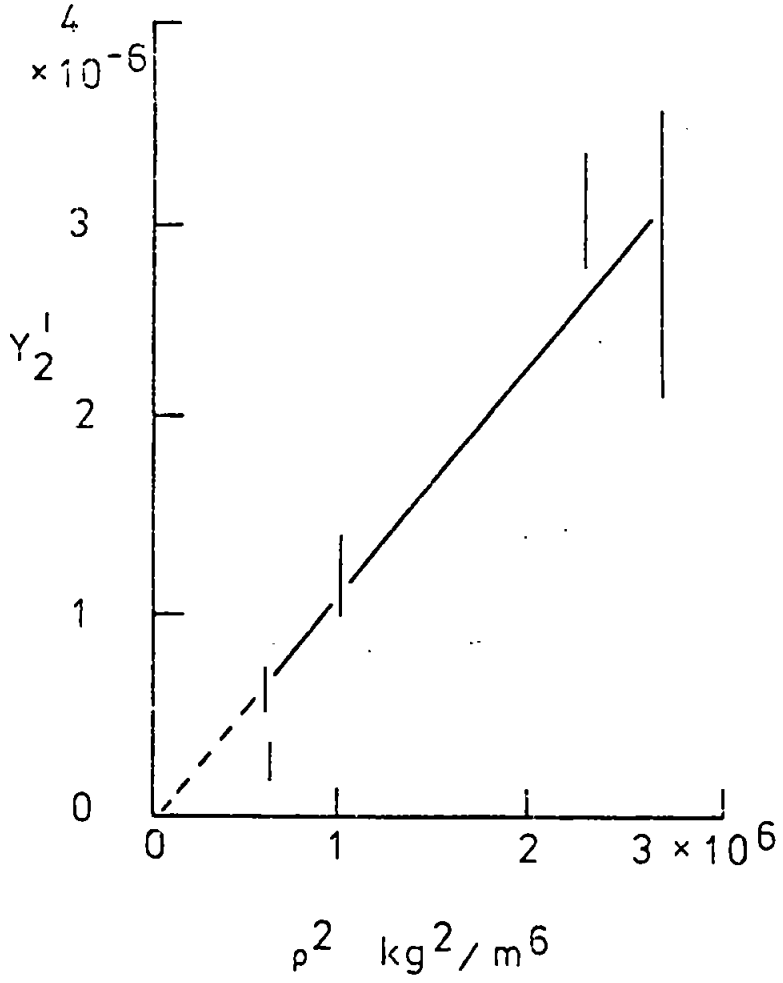
4
× 10⁻⁶
3
2
1
0
Y'2
0
1
2
3 × 10⁶
ρ² kg²/m⁶

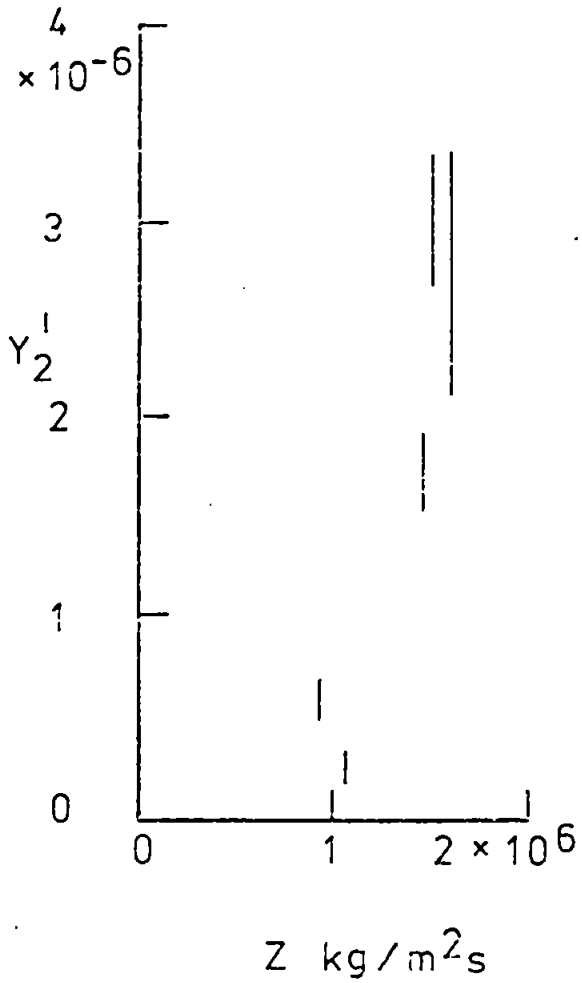
4
× 10⁻⁶
3
2
1
0
Y'2
0
1
2 × 10⁶
Z kg/m²s

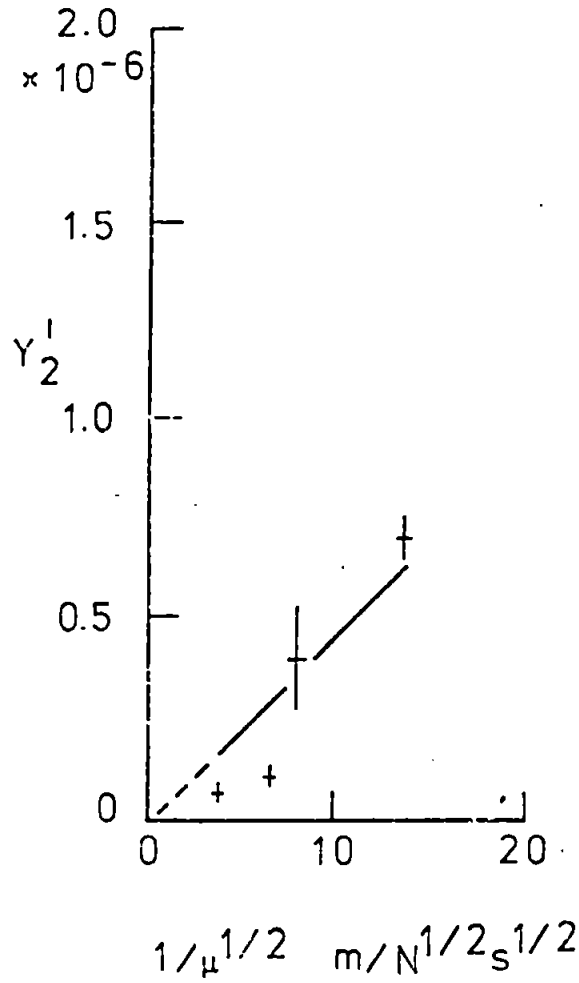
2.0
× 10⁻⁶
1.5
1.0
0.5
0
Y'2
0
10
20
1/μ^1/2 m/N^1/2s^1/2

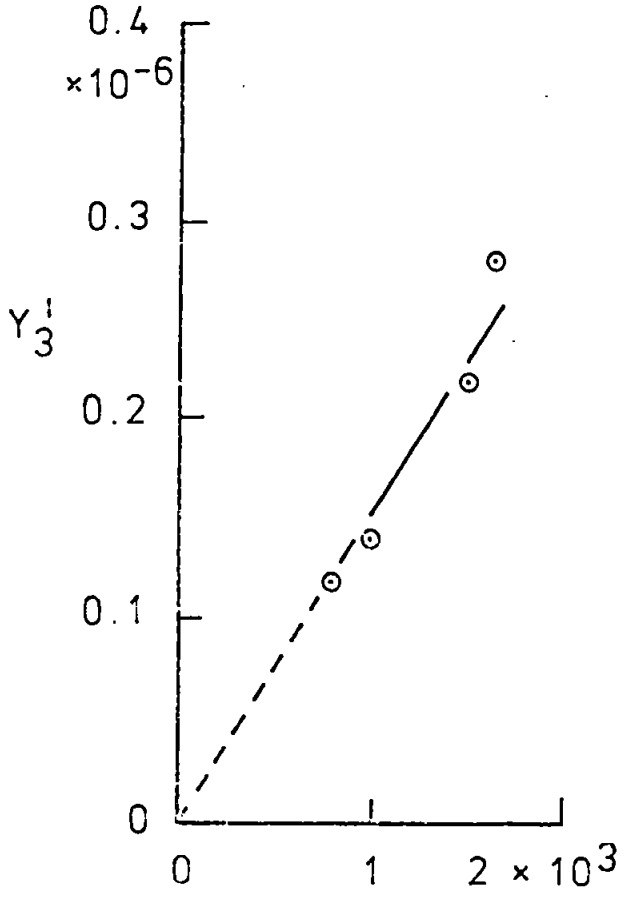
0.4
×10⁻⁶
0.3
0.2
0.1
0
Y'3
0
1
2 × 10³
ρ kg/m³

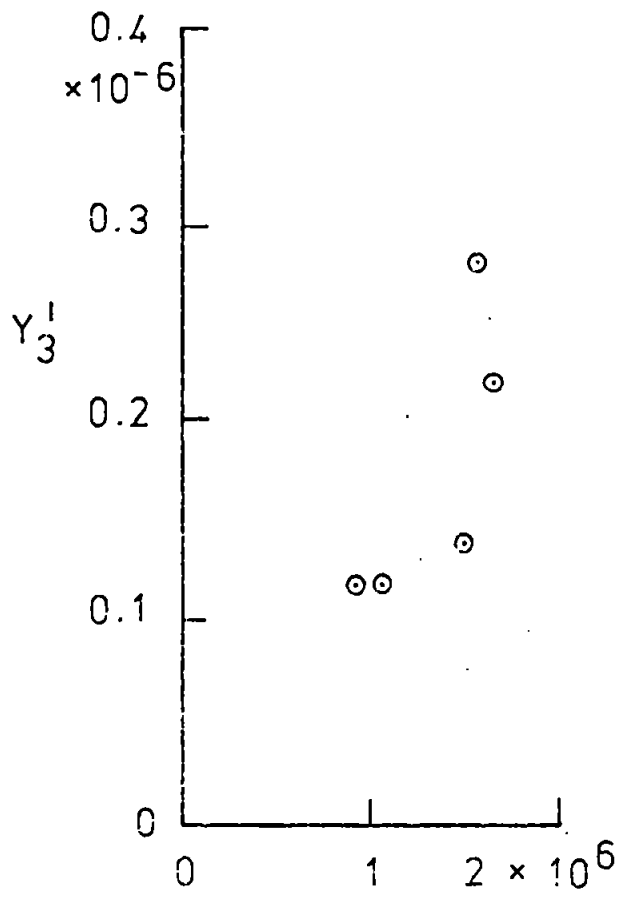
0.4
×10⁻⁶
0.3
0.2
0.1
0
Y'3
0
1
2 × 10⁶
Z kg/m²s

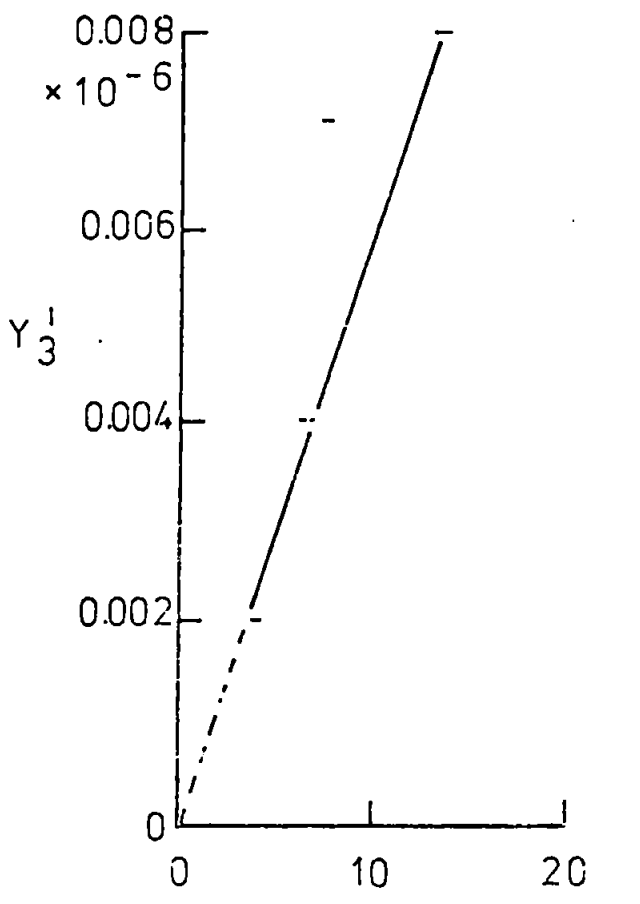
0.008
×10⁻⁶
0.006
0.004
0.002
0
Y'3
0
10
20
1/μ^1/2 m/N^1/2 s^1/2

Table 6.4

Summary of the Relations between Liquid Properties and Erosion Damage Parameters

Damage Parameter	Density	Acoustic Impedance	Viscosity
H_1	No clear trend	No clear trend	$A\mu$ $A = 3.5 \pm 0.2$ $\times 10^{4}$ m^3/Ns
H_2	A/ρ $A = 0.6 \pm 0.1$ $\times 10^{6}$ kg/m^2	A/Z $A = 0.7 \pm 0.1$ $\times 10^{9}$ kg/ms	Increase
$H_2 - H_1$	A/ρ $A = 0.6 \pm 0.1$ $\times 10^{6}$ kg/m^2	A/Z $A = 0.7 \pm 0.1$ $\times 10^{9}$ kg/ms	Increase
Y_2	$A\rho$ $A = 0.6 \pm 0.1$ $\times 10^{-6}$ m^4/kg	AZ^2 $A = 0.35 \pm 0.05$ $\times 10^{-15}$ m^5s^2/kg^2	$A/\mu^{1/2}$ $A = 30 \pm 5$ $\times 10^{-6}$ $N^{1/2}s^{1/2}$
Y_H	$A\rho$ $A = 0.7 \pm 0.2$ $\times 10^{-6}$ m^4/kg	AZ^2 $A = 0.5 \pm 0.1$ $\times 10^{-15}$ m^5s^2/kg^2	
Y_2'	$A\rho^2$ $A = 1.2 \pm 0.1$ $\times 10^{-12}$ m^6/kg^2	Increase	$A/\mu^{1/2}$ $A = 5 \pm 1$ $\times 10^{-8}$ $N^{1/2}s^{1/2}/m$
Y_3'	$A\rho$ $A = 150 \pm 10$ $\times 10^{-12}$ m^3/kg	Increase	$A/\mu^{1/2}$ $A = 0.60 \pm 0.02$ $\times 10^{-9}$ $N^{1/2}s^{1/2}/m$

effect on each stage. It is likely that high viscosity fluids adhere as a thin film to smooth surfaces and lie on the bottom of pits on heavily eroded surfaces. Consequently the surface would be cushioned against the impact forces.

From the correlations illustrated in Fig. 6.8 and summarised in Table 6.4 it may be concluded that a theory developed for predicting the erosion curve under different erosive conditions must include energy transfer, impact pressure and viscosity terms. This is considerably more complex than anything that has been attempted so far.

6.5 Relation between Damage Parameters and Impact Velocity

When water is used as the eroding fluid, it is now generally agreed that the rate of change of the mean depth of erosion during Stage 2, Y_2', is related to the impact velocity, V, by the equation

$$Y_2' = AV^n,$$

where A is a constant for a particular material and n lies between 4 and 6. (See Heymann (1967a, 1970).)

A graph of Y_2' against V for carbon tetracchloride is plotted on a logarithmic scale in Fig. 6.9. (A result for water is also plotted on the same scale. Water was here used in a control experiment.) From the straight line obtained it can be seen that it has the same form as the above expression. The exponent is 4.5 ± 0.5. This is much the same as the result for water despite the fact that water is about 50 percent less dense than carbon tetrachloride. It suggests that the physical properties of the liquid as they affect erosion are independent of flow velocity during impact.

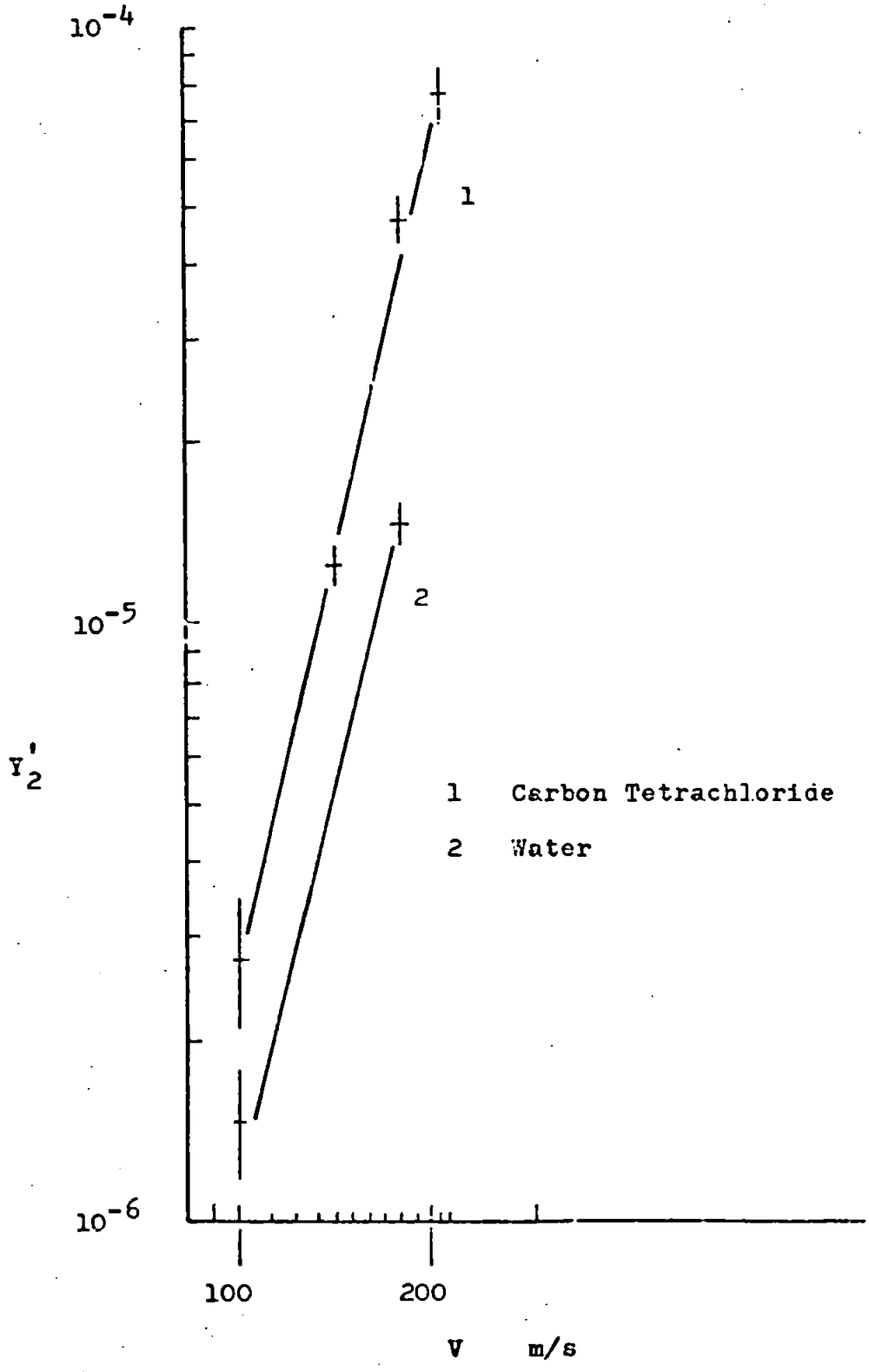

Fig. 6.9 Erosion rate during Stage 2, Y_2', versus impact velocity, V, for carbon tetrachloride and water.

6.6 Dimensional Analysis of Erosion

The results presented in the previous sections can be used to obtain a general expression for the rate of change of the mean depth of erosion during Stage 2. Suppose that Y_2' can be expressed

$$Y_2' = f(\rho, c, \mu, V, d, U),$$

where ρ is the density of the liquid, c is the sound speed in the liquid, μ is the viscosity of the liquid, V is the impact velocity, d is the diameter of the jet and U is an energy property of the material (for example, the strain energy to fracture in a tensile test). When the π-theorem (Buckingham (1915)) is used, the variables fall into three non-dimensional groups to give

$$Y_2' = f(\rho V d/\mu, V/c, \rho V^2/U),$$

where $\rho Vd/\mu$ is the Reynolds number of the flow based on the impact velocity, V/c is the Mach number of the flow based on the impact velocity and $\rho V^2/U$ is the kinetic energy of the fluid per unit volume divided by the energy capacity of the material per unit volume.

The form of the above function can be deduced from the results of the erosion experiments. The Group 1 liquids gave $Y_2' \sim \rho^2$, the Group 2 liquids gave $Y_2' \sim 1/\mu^{1/2}$, and the experiments with both water and carbon tetrachloride gave $Y_2' \sim V^n$, where n lies between 4 and 5. If it is assumed that these three relations hold for all liquids, the equation for Y_2' will be one of the following:

$$Y_2' \sim (\rho Vd/\mu)^{1/2}(V/c)^{1/2}(\rho V^2/U)^{3/2}, \qquad 6.1a$$

for $Y_2' \sim V^4$;

$$Y_2' \sim (\rho V d/\mu)^{1/2}(V/c)(\rho V^2/U)^{3/2}, \qquad 6.1b$$

for $Y_2' \sim V^{4.5}$;

$$Y_2' \sim (\rho V d/\mu)^{1/2}(V/c)^{3/2}(\rho V^2/U)^{3/2}, \qquad 6.1c$$

for $Y_2' \sim V^5$.

It has been assumed that $Y_2' \sim (1/U)^{3/2}$. This is in reasonable agreement with a large number of experimental results (see Heymann (1968a)).

Graphs of these relations are plotted in Figs. 6.10a to 6.10c. It can be seen that Equation 6.1a is the best fit. A check on this relation may be obtained from the result for mercury because it was not used when the straight line was fitted to the results for the other liquids. The measured value of Y_2' for mercury was $200 \pm 30 \times 10^{-6}$, and Equation 6.1a gives $Y_2' = 190 \pm 20 \times 10^{-6}$. The two values are in excellent agreement with one another. Furthermore, the results for water and carbon tetrachloride at the higher impact velocities also fit Equation 6.1a. It can be concluded, therefore, that this equation holds over wide ranges of the variables.

6.7 Energy Analysis of Erosion

By considering the energy transferred from the drop to the solid during the initial, compressible stage of impact, it is possible to derive an expression for the rate of change of the mean depth of erosion during Stage 2 similar in form to Equation 6.1a. Suppose that (i) energy can be absorbed from the fluid up to the time when lateral flow occurs, and (ii) the material must absorb a fixed

Fig. 6.10 Erosion rate during Stage 2, Y_2', versus non-dimensional variables.

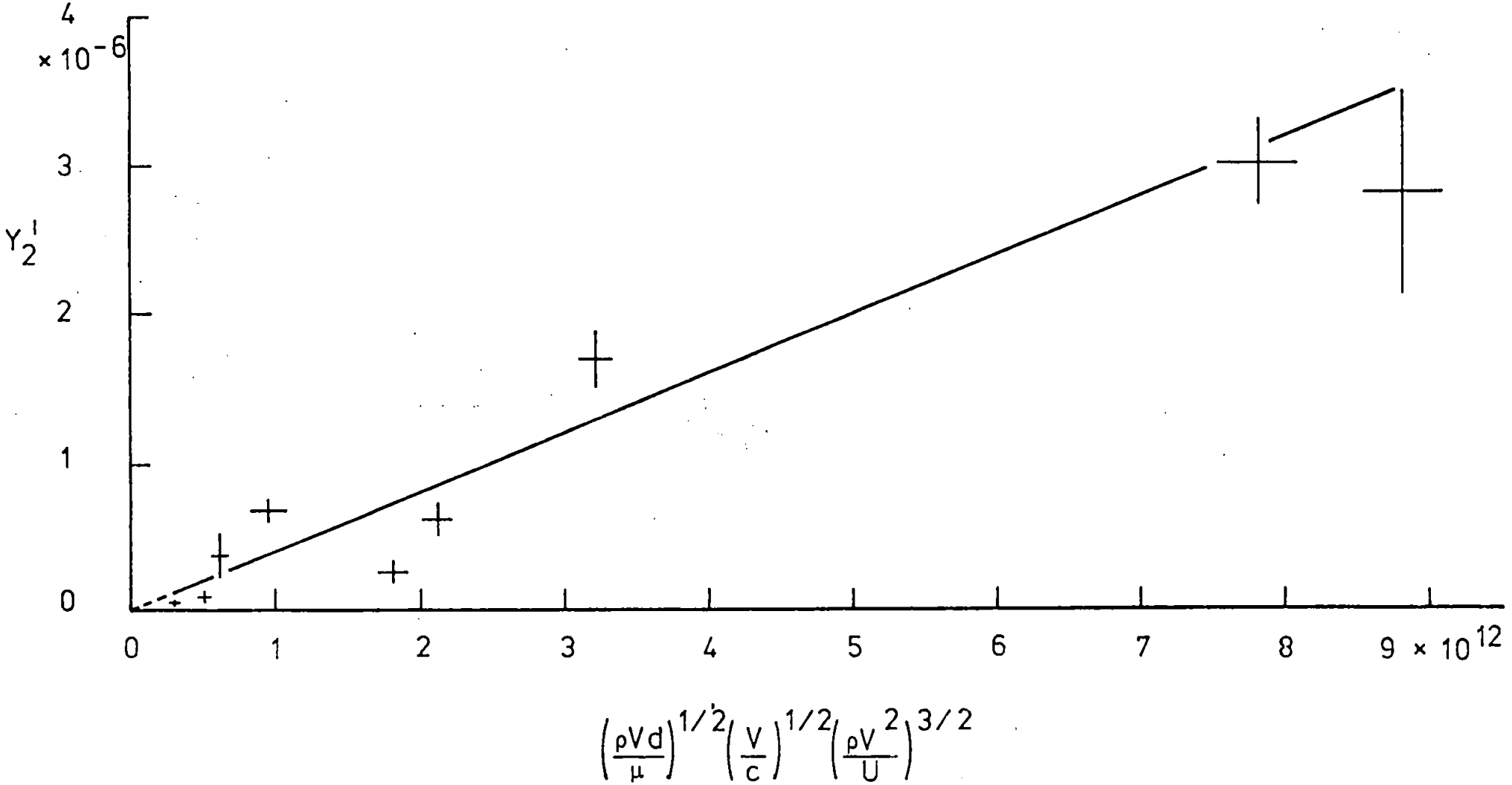
4
× 10⁻⁶
3
2
1
0
Y₂'
0
1
2
3
4
5
6
7
8
9 × 10¹²
(ρVd/μ)^1/2 (V/c)^1/2 (ρV²/U)^3/2

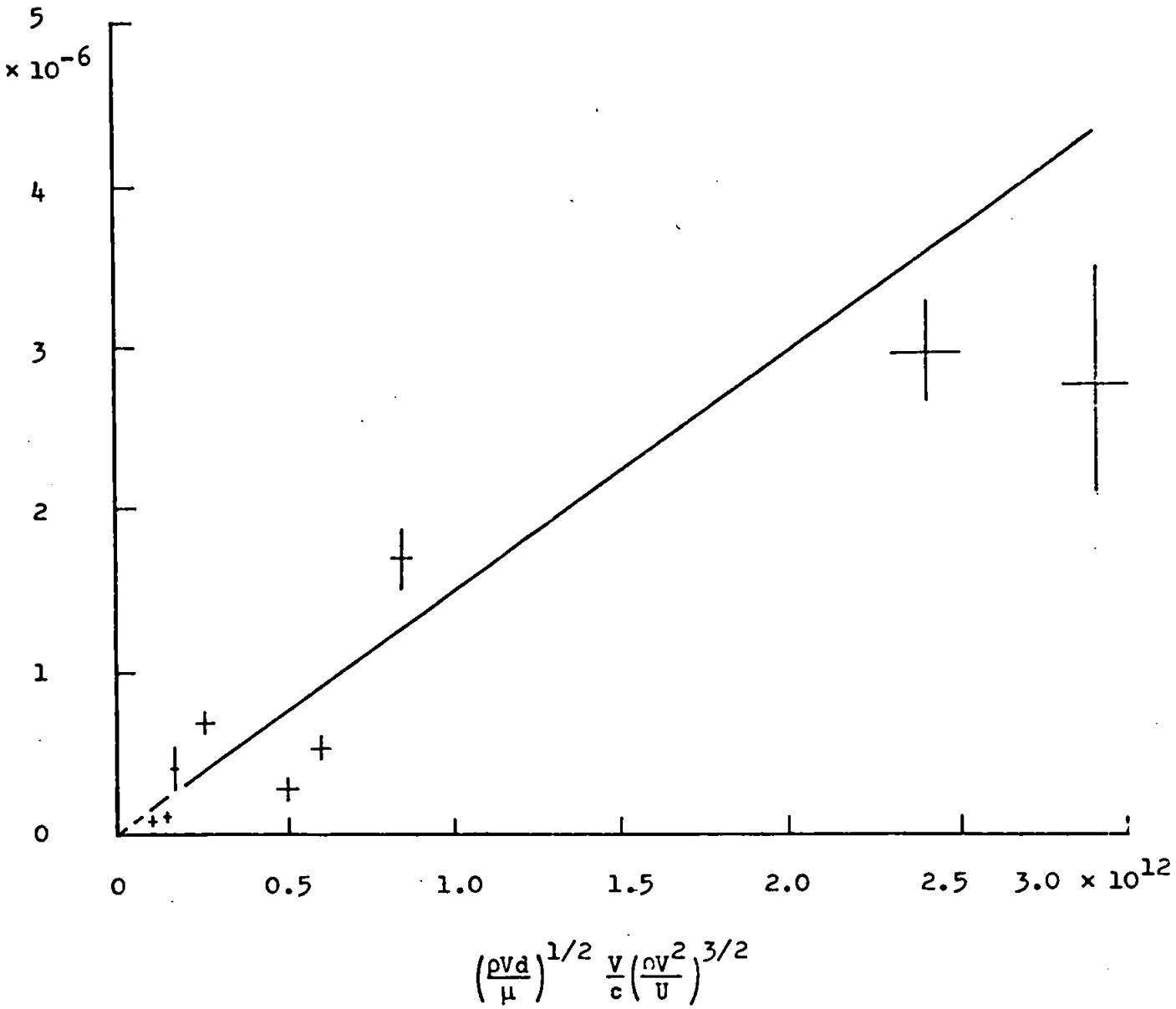
5
× 10⁻⁶
4
3
2
1
0
0
0.5
1.0
1.5
2.0
2.5
3.0 × 10¹²
$\left(\frac{\rho V d}{\mu}\right)^{1/2} \frac{V}{c}\left(\frac{\rho V^2}{U}\right)^{3/2}$

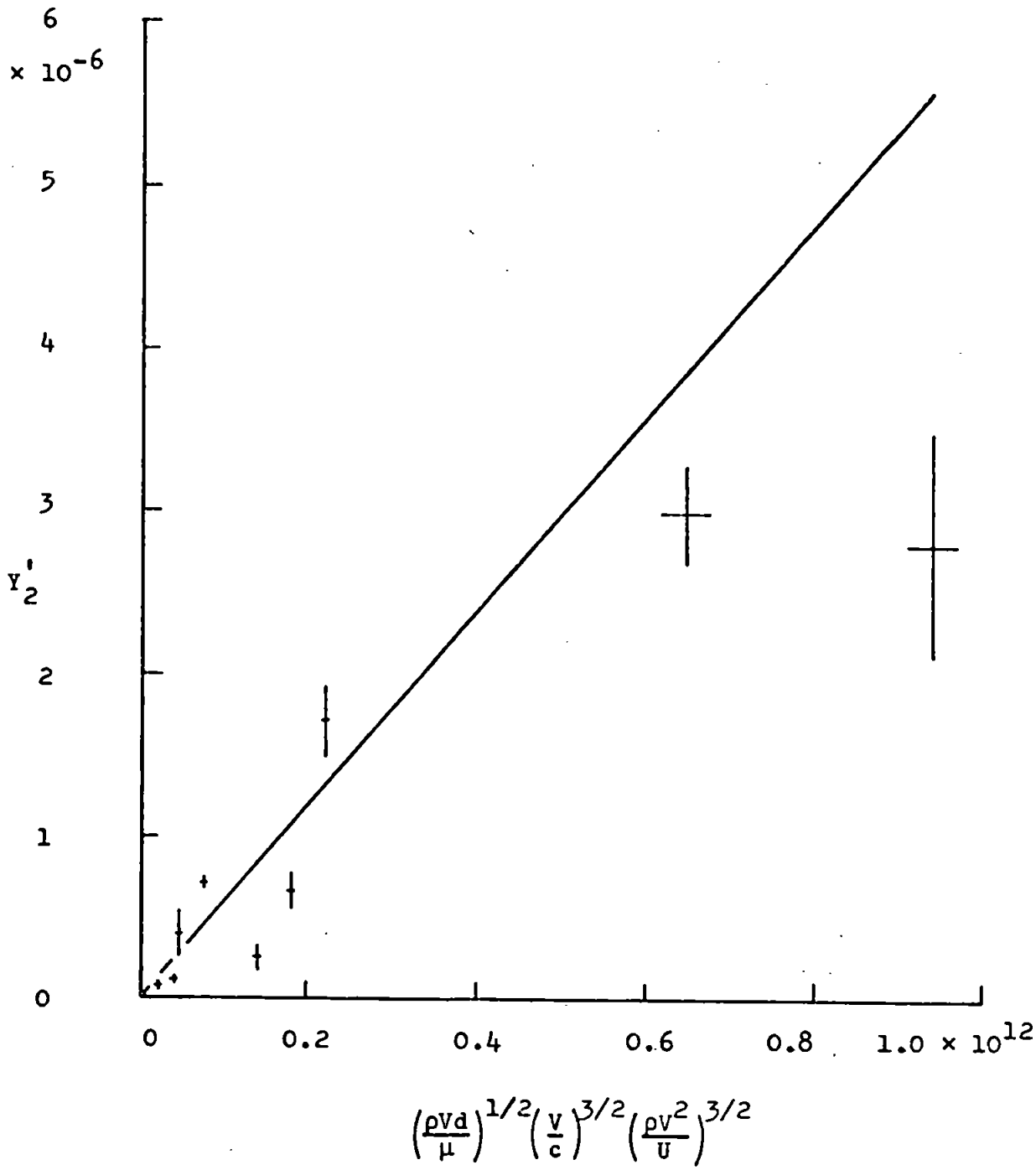
6
× 10⁻⁶
5
4
3
Y'2
2
1
0
0
0.2
0.4
0.6
0.8
1.0 × 10¹²
(ρVd/μ)^1/2 (V/c)^3/2 (ρV²/U)^3/2

amount of energy before any mass loss occurs.

The energy available to damage the solid per impact is

$$E = pA_e t_e V,$$

where p is the average pressure over the contact surface, A_e is the area of the contact surface just before lateral flow from under the edge of the drop occurs, t_e is the time after first contact at which this occurs and V is the impact velocity. In Chapter 3 it is shown that $p = \rho cV$, $A_e = 2R(2V/c)^{1/2}$ and $t_e = R/(4c)$, where R is the radius of the cylindrical drop. When these expressions are substituted into the above equation, it becomes

$$E = 2^{1/2} R^2 \rho V^{5/2} / c^{1/2}.$$

If it is assumed that a fraction, α, of this energy is absorbed in each impact, the energy absorbed by the solid per impact is

$$E_a = \alpha E = \alpha 2^{1/2} R^2 \rho V^{5/2} / c^{1/2}.$$

The fraction α depends on the properties of the material. The energy absorbed by the solid per unit volume of fluid impinged is

$$e_a = E_a/(\pi R^2) = (\alpha 2^{1/2}/\pi)\rho V^{5/2}/c^{1/2}.$$

The total volume of fluid that strikes the surface during Stage 1 is $H_1 2R$. Therefore the total amount of energy absorbed by the solid during Stage 1 is

$$E_T = e_a H_1 2R = (\alpha 8^{1/2}/\pi) R \rho V^{5/2} H_1 / c^{1/2}.$$

But E_T is constant (Assumption 2), therefore

$$H_1 \sim c^{1/2}/(\rho R V^{5/2}). \qquad 6.2$$

This relation gives the correct relation between H_1 and ρ.

During Stage 2 material damaged in Stage 1 is torn from the surface of the solid, and fresh material is exposed to direct impact by the drop. It is reasonable to suppose that the material removed during this period is proportional to the energy absorbed per unit volume of fluid impinged during Stage 1, and that the duration of this stage is inversely proportional to the kinetic energy per unit volume of the outflowing fluid. Thus $Y_2 \sim \rho V^{5/2}/c^{1/2}$ and $(H_2 - H_1) \sim 1/(\rho V^2)$, so that

$$Y_2' = Y_2/(H_2 - H_1) \sim \rho^2 V^{9/2}/c^{1/2}. \qquad 6.3$$

This equation gives the correct relation between Y_2' and both ρ and V. However, neither this equation nor the previous one for H_1 contains the viscosity of the fluid. How could this term be brought into the calculations?

There is a liquid layer on the surface of the solid throughout the erosion experiment. When erosion is carried out in a wheel-and-jet machine, the thickness of the liquid layer during Stage 1 is given by

$$\delta = [3\mu D/(4\pi\rho V)]^{1/2},$$

where D is the diameter of the orbit of the specimen (Pouchot (1968)). Even with the highest viscosity liquid used in these experiments, the layer thickness calculated with this equation is only a fraction of the drop diameter. It is unlikely that such a thin layer will cause a significant reduction in the magnitude of the initial, compressible load. However, the liquid film could reduce the erosive action of the outflowing fluid. It is known that material is torn

from the surface of the solid at places where it has been raised above the mean level by the pounding that it received during Stage 1. (Examples of such sites are the rims of indentations and the edges of exposed grain boundaries - see Hancox and Brunton (1966).) The liquid film could therefore protect the solid both by slowing down the outflowing liquid and by covering up the raised parts of the surface. The solid would therefore not be subjected to the full tearing action of the outflowing fluid until the surface projections had been pushed up through the liquid film. This would lead to increases in the duration of Stages 1 and 2 compared with what they would have been in dry impacts; for a fixed energy transfer to the solid, this would mean a decrease in Y_2'. Although these considerations produce trends that are in agreement with the observed variations of the damage parameters with viscosity, it is not clear how to go further and allow for viscosity in the analysis of erosion, so that it has not been possible to derive general equations for Y_2' and any of the other damage parameters that contain the viscosity of the fluid.

6.8 Summary

It has been shown that liquid properties have a marked effect on the erosion of nickel. Graphs of mean depth of erosion, Y_e, versus mean height of impingement, H_i, were found to have the same shape for most liquids. In general, there were three well-defined stages. The exceptions were as follows: Stage 1 was not found at 210 m/s with carbon tetrachloride and Stages 1 and 3 were not found with mercury.

Measures of erosion damage were defined and related to the density,

acoustic impedance and viscosity of the liquid. Density and acoustic impedance were related to the parameters defining damage during Stages 2 and 3, but were not related to the Stage 1 parameter. Viscosity was related to the parameters defining damage during all stages of erosion.

It has been shown that the erosion rate during Stage 2, Y_2', is proportional to about the 4.5th power of the impact velocity when both water and carbon tetrachloride are used as the eroding fluids. This is similar to the result found for water in other studies of erosion.

A dimensional analysis of the erosion data led to a general expression for the rate of change of the mean depth of erosion during Stage 2; an energy analysis of erosion produced the correct dependence of this parameter on both density and impact velocity.

CHAPTER 7

CONCLUSION

Two problems remain. The maximum impact pressures do not occur at the positions and times given by the theory, and there are not enough measurements in the region of the contact surface up to the time when the liquid flows out from under the drop.

A more refined analysis, in which the full equations of motion are solved and the edges are allowed to move after the initial compression wave is released, will not necessarily lead to the correct solution. Calculations based on the particle-in-cell computer code have been carried out by Huang et al (1971) and fail even to predict that the pressures increase at the edges, let alone determine the places under the drop where this occurs. They made a mistake when they set up the numerical scheme (see Rochester (1977a)), which illustrates that much care needs to be taken with these techniques. In the initial stage of the impact, pressure and velocity changes occur very rapidly, so that in any finite difference scheme the mesh sizes that are used need to be very small; this soon becomes prohibitively expensive. Alternative numerical methods could be tried in the future, in particular either a method based on characteristics, which has the advantage of being similar to the linearised method used here (see the article by Richardson in Alder et al (1964)), or one based on the finite element method, which has recently become very popular (see Zienkiewicz (1971)). This exercise is quite a large undertaking.

If more measurements are required over the contact surface at the beginning of the impact smaller gauges must be built (with a

sensitive width less than 0.3 mm). The gauges used in these experiments were made by chopping up a ceramic plate with a fine ultrasonic drill. The pieces were cut as small as possible. How, then, can smaller devices be made? One method is to try and deposit a piezoelectric material directly onto the impact surface of the bullet. Another is to mount a large ceramic at the base of a fine cone; however, large distortion of the signal would occur as it passed down the cone, so that a way of re-forming the original pulse would have to be devised; furthermore, considerable mechanical problems will arise when a suitable housing for the cone has to be made - the accelerations experienced by the bullet, as it strikes the side of the barrel and runs into the catching box, are very large.

In the future much more emphasis needs to be placed on the development of more realistic theories of erosion damage. It is hoped that the results presented here will assist in this most difficult task. For this is the only real justification for this type of detailed study.

APPENDIX 1

WAVE IMPACTS

Expressions for outward flow velocity and stagnation pressure under a collapsing wedge are developed below, following the analysis of Taylor (1966). The results are then used to interpret some old wave impact data.

Consider a jet velocity U directed downwards at a small angle ϑ onto a horizontal plane. Suppose that the jet is moving from left to right and the plane is moving upwards with velocity V. The velocity of the orifice relative to the plane is V downwards, and the velocity of the edge relative to a fixed point on the plane is $V\cot\vartheta$ to the left. Therefore the velocity of the orifice relative to the edge is $V\operatorname{cosec}\vartheta$ at an angle ϑ to the plane. The velocity of the jet relative to the impact point is therefore $U + V\operatorname{cosec}\vartheta$. The flow is steady in this frame of reference, so that the stagnation pressure is

$$p = \rho_0 U^2(1 + (V/U)\operatorname{cosec}\vartheta)^2/2. \qquad \text{A.1.1a}$$

When U is zero this reduces to

$$p = \rho_0 V^2 \operatorname{cosec}^2\vartheta/2. \qquad \text{A.1.1b}$$

The velocity of the deflected jet relative to a fixed point on the plane is

$$V_j = V\operatorname{cosec}\vartheta + V\cot\vartheta$$

to the left; after a little manipulation this becomes

$$V_j = V\cot(\vartheta/2). \qquad \text{A.1.2}$$

These results can be applied to some old wave impact data, with quite dramatic results. In 1938 three French engineers, de Rouville, Besson and Petry, reported some observations of wave impact loads that they had made on the seawall at Dieppe.[a] They observed maximum pressures as high as 70 tonne/m^2 during a violent storm. Now comes a crucial point: when they were not watching their pressure transducer, they observed that an oncoming wave with a velocity of 6 m/s ejected its crest at 12 m/s and that water was projected up the wall at 77 m/s. These observations appear to be unique, since no-one else has recorded both maximum pressures and the velocities of the water.

Bagnold (1939) assumed that these results, and those of his own experiments carried out in a model tank, were caused by the compression of a shallow air-pocket trapped between the wave and the wall near the crest of the wave as it folded over. Unfortunately his final equation for impact pressure contains the thickness of the air-pocket; he did not measure it in any of his experiments, and he was therefore at liberty to make it any size that he liked - it only had to be chosen so that theory and experiment agreed.

Are these pressures and velocities consistent with the theory developed by Taylor? The flow angle, estimated from the velocity measurements with Equation A.1.2, is 17.7°; the pressure calculated with Equation A.1.1b is then 79 tonne/m^2, remarkably close to the measured pressure of 70 tonne/m^2. It is therefore unnecessary to invoke either the compression of the water or the presence of trapped air to explain these results.

a Rouville, A. de, Besson, P., and Petry, P., Current State of International Studies on Wave Impacts (in French), Annales Pont et Chaussées, 108, 1938.

REFERENCES

Abramowitz, M., and Stegun, I.A., Handbook of Mathematical Functions, Dover, 1965.

Alder, B., Fernbach, S., and Rotenberg, M. (Editors), Methods in Computational Physics, Volume 3, Fundamental Methods in Hydrodynamics, Academic Press, 1964.

Anon., Tufnol Technical Information, Tufnol Ltd., 1954.

Anon., Instrumenting to combat the 'coefficients of ignorance', New Civil Engineer, 18/25 December, 1975.

Bagnold, R.A., Interim Report on Wave-Pressure Research, Journal of the Institution of Civil Engineers, 12, 1939, pp. 202 - 226.

Baker, D.W.C., Jolliffe, K.H., and Pearson, D., The resistance of materials to impact erosion damage, Philosophical Transactions of the Royal Society, A 260, 1966, pp. 193 - 203.

Benjamin, T.B., and Ellis, A.T., The collapse of cavitation bubbles and the pressures thereby produced against solid boundaries, Philosophical Transactions of the Royal Society, A 260, 1966, pp. 221 - 240.

Bowden, F.P., and Brunton, J.H., The deformation of solids by liquid impact at supersonic speeds, Proceedings of the Royal Society, A 263, 1961, pp. 433 - 450.

Bowden, F.P., and Field, J.E., The brittle fracture of solids by liquid impact, by solid impact and by shock, Proceedings of the Royal Society, A 282, 1964, pp. 331 - 352.

Braddick, H.J.J., The Physics of Experimental Method, Chapman and Hall, 1963.

Brunton, J.H., Deformation of Solids by Liquid Impact at Supersonic Speeds, Ph.D. Thesis, Cambridge University, 1959.

Brunton, J.H., Erosion by Liquid Shock, Proceedings of the Second International Conference on Rain Erosion and Allied Phenomena, Royal Aircraft Establishment, 1967, pp. 291 - 309.

Brunton, J.H., Cavitation Damage, Proceedings of the Third International Conference on Rain Erosion and Allied Phenomena, Royal Aircraft Establishment, 1970, pp. 821 - 846.

Brunton, J.H., and Camus, J.J., The Flow of a Liquid Drop during Impact, Proceedings of the Third International Conference on Rain Erosion and Allied Phenomena, Royal Aircraft Establishment, 1970, pp. 327 - 352.

Buckingham, E., Model Experiments and the Forms of Empirical Equations, Transactions of the American Society of Mechanical Engineers, 37, 1915, pp. 263 - 296.

Busch, H., Hoff, G., and Langbein, G., Rain erosion properties of materials, Philosophical Transactions of the Royal Society, A 260, 1966, pp. 168 - 178.

Camus, J.J., A Study of High-Speed Liquid Flow in Impact and Its Effect on Solid Surfaces, Ph.D. Thesis, Cambridge University, 1971.

Canavelis, R., A Study of Cavitation Erosion in Hydraulic Turbomachines (in French), Ph.D. Thesis, University of Paris, 1966.

Camavelis, R., Jet Impact and Cavitation Damage, Transactions of the American Society of Mechanical Engineers, D 90, 1968, pp. 355 - 367.

Chu, W.H., and Abramson, H.N., Hydrodynamic Theories of Ship Slamming - Review and Extension, Journal of Ship Research, 4, 1961, pp. 9 - 21.

Copson, E.T., Partial Differential Equations, Cambridge, 1975.

Cottrill, A., N. Sea gas veterans feeling their age?, New Civil Engineer, 12 June, 1975.

Courant, R., and Hilbert, D., Methods of Mathematical Physics, Volume 2, Interscience, 1962.

Crook, A.W., A study of some impacts between metal bodies by a piezoelectric method, Proceedings of the Royal Society, A 212, 1952, pp. 377 - 390.

Curle, N., and Davies, H.J., Modern Fluid Dynamics, Volume 2, Van Nostrand, 1971.

Denny, D.F., Further Experiments on Wave Pressures, Journal of the Institution of Civil Engineers, 35, 1951, pp. 330 - 345.

Dergarabedian, P., Compressibility Effects during Water Entry, NavOrd Report Number 3523, 1955.

Engel, O.G., Waterdrop Collisions with Solid Surfaces, Journal of Research of the National Bureau of Standards, 54, 1955, pp. 281 - 298.

Fyall, A.A., Single Impact Studies with Liquids and Solids, Proceedings of the Second International Conference on Rain Erosion and Allied Phenomena, Royal Aircraft Establishment, 1967, pp. 428 - 443.

Fyall, A.A., King, R.B., and Strain, R.N.C., Rain Erosion Aspects of Aircraft and Guided Missiles, Journal of the Royal Aeronautical Society, 66, 1962, pp. 447 - 453.

Gardner, F.W., The Erosion of Steam Turbine Blades, Engineer, 58, 1932, pp. 146 - 147, and pp. 202 - 206.

Haller, P. de, Researches into Corrosion Caused by Cavitation (in German), Schweizerische Bauzeitung, 101, 1933, p. 243 and p. 260.

Haller, P. de, Schweizer Archiv, 6, 1940, p. 61.

Hancox, N.L., and Brunton, J.H., The erosion of solids by the repeated impact of liquid drops, Philosophical Transactions of the Royal Society, A 260, 1966, pp. 121 - 139.

Hatfield, H.S., The Inventor and His World, Pelican, 1948.

Heaslet, M.A., and Lomax, H., The Use of Source-Sink and Doublet Distributions Extended to the Solution of Arbitrary Boundary Value Problems in Supersonic Flow, NACA Report Number 900, 1948.

Heymann, F.J., A Survey of Clues to the Relationship between Erosion Rate and Impingement Conditions, Proceedings of the Second International Conference on Rain Erosion and Allied Phenomena, Royal Aircraft Establishment, 1967a, pp. 98 - 157.

Heymann, F.J., On the Time Dependence of the Rate of Erosion due to Impingement or Cavitation, ASTM STP 408, American Society for

Testing and Materials, 1967b, pp. 70 - 110.

Heymann, F.J., Erosion by Cavitation, Liquid Impingement, and Solid Impingement - a Review, Engineering Report Number E - 1460, Development Engineering Department, Westinghouse Electric Corporation, 1968a.

Heymann, F.J., On the Shock Wave Velocity and Impact Pressure in High-Speed Liquid - Solid Impact, Transactions of the American Society of Mechanical Engineers, D 90, 1968b, pp. 400 - 402.

Heymann, F.J., High-Speed Impact between a Liquid Drop and a Solid Surface, Journal of Applied Physics, 40, 1969, pp. 5113 - 5122.

Heymann, F.J., Toward Quantitative Prediction of Liquid Impact Erosion, ASTM STP 474, American Society for Testing and Materials, 1970, pp. 212 - 248.

Heymann, F.J., Progress and Problems in Erosion Prediction - from a Design Engineering Viewpoint, Engineering Report Number E - 1503, Steam Turbine Engineering Department, Westinghouse Electric Corporation, 1974.

Hoff, G., Langbein, G., and Rieger, H., Material Destruction due to Liquid Impact, ASTM STP 408, American Society for Testing and Materials, 1967, pp. 42 - 69.

Holder, D.W., and North, R.J., Schlieren Methods, HMSO, 1963.

Honneger, E., Tests on Erosion Caused by Jets, Brown Boveri Review, 14, 1927, pp. 95 - 104.

Howarth, L. (Editor), Modern Developments in Fluid Dynamics, High Speed Flow, Volume 2, Oxford, 1953.

Huang, Y.C., Hammitt, F.G., and Yang, W., Computer Simulation of High Speed Collision with Rain Drop (Combined Spherical - Cylindrical Shape), Report Number UMICH 03371 - 12 - T, University of Michigan, 1971.

Ippen, A.T. (Editor), Estuary and Coastline Hydrodynamics, McGraw-Hill, 1966.

Jeffrey, A., Magnetohydrodynamics, Oliver and Boyd, 1966.

Johnson, W., and Vickers, G.W., Transient Stress Distribution Caused by Water-Jet Impact, Journal of Mechanical Engineering Science, 15, 1973, pp. 302 - 310.

Karman, T. von, The Impact of Seaplane Floats during Landing, NACA TN 321, 1929.

Kaye, G.W.C., and Laby, T.H., Tables of Physical and Chemical Constants, Longman, 1966.

Kolsky, H., Stress Waves in Solids, Dover, 1963.

Ladenburg, R.W., Lewis, B., Pease, R.N., and Taylor, H.S. (Editors), High Speed Aerodynamics and Jet Propulsion, Volume 9, Physical Measurements in Gas Dynamics and Combustion, Oxford, 1955.

Lesser, M.B., On the Fluid Mechanics of Compressible Liquid Impact - the Rectangular Slug, CERAC Report Number 18, 1973.

Liepmann, H.W., and Roshko, A., Elements of Gasdynamics, Wiley, 1957.

Minikin, R.R., Pressure of Breaking Waves, Dock and Harbour Authority, 1946, pp. 262 - 266.

Nisewanger, C.R., Laboratory Measurements of Pressure versus Time at Water Impact, NavOrd TM 614, 1952.

Ogilvie, T.F., Compressibility Effects in Ship Slamming, Schifftechnik, 10, 1963, pp. 154 - 197.

Pouchot, W.D. (Editor), Comparison of the Erosion Potential for a Potassium Vapour Turbine and a Cesium Vapour Turbine, Report Number WANL - TME - 1730, Astronuclear Laboratory, Westinghouse Electric Corporation, 1968.

Richardson, D.J., The Solution of Two-Dimensional Hydrodynamic Equations by the Method of Characteristics, in Alder et al (Editors), 1964, pp. 295 - 317.

Rochester, M.C., Liquid Impact Erosion - a Review, Report Number CUED/C-MAT/TR 32, Engineering Department, Cambridge University, 1977a.

Rochester, M.C., A Gas-Powered Gun for Use in Drop Impact Studies, Report Number CUED/C-MAT/TR 41, Engineering Department, Cambridge University, 1977b.

Rochester, M.C., Pressure Gauges for Use in Drop Impact Studies, Report Number CUED/C-MAT/TR 42, Engineering Department, Cambridge University, 1977c.

Rochester, M.C., A Cranz-Schardin High-Speed Camera, Report Number CUED/C-MAT/TR 43, Engineering Department, Cambridge University, 1977d.

Rochester, M.C., and Brunton, J.H., The Influence of the Physical Properties of the Liquid on the Erosion of Solids, ASTM STP 567, American Society for Testing and Materials, 1974a.

Rochester, M.C., and Brunton, J.H., Surface Pressure Distribution during Drop Impingement, Proceedings of the Fourth International Conference on Rain Erosion and Allied Phenomena, Royal Aircraft Establishment, 1974b.

Rochester, M.C., Hutchings, I.M., and Camus, J.J., A rectangular-bore gas gun, Journal of Physics E: Scientific Instruments, 10, 1977, pp. 455 - 457.

Savic, P., and Boult, G.T., The Fluid Flow Associated with the Impact of Liquid Drops with Solid Surfaces, Proceedings of the Heat Transfer and Fluid Mechanics Institute, Stanford, 1957, pp. 43 - 73.

Shiffman, M., and Spencer, D.C., The Force of Impact on a Sphere Striking a Water Surface, Applied Mathematics Panel Report Number R/AMG, New York University, 1945.

Skalak, R., and Feit, D., Impact on the Surface of a Compressible Fluid, Transactions of the American Society of Mechanical Engineers, D 88, 1966, pp. 325 - 331.

Taylor, G.I., Oblique impact of a jet on a plane surface, Philosophical Transactions of the Royal Society, A 260, 1966, pp. 96 - 100.

Thomas, G.P., and Brunton, J.H., Drop impingement erosion of metals, Proceedings of the Royal Society, A 314, 1970, pp. 549 - 565.

Wagner, H., On Planing Forces on the Surface of a Liquid (in German), Zeitschrift fur angewandte Mathematik und Mechanik, 12, 1932, pp. 193 - 215.

Ward, G.N., Linearised Theory of Steady High-Speed Flow, Cambridge, 1955.

Zienkiewicz, O.C., The Finite Element Method in Engineering Science, McGraw-Hill, 1971.